FUEL CELLS

Modeling, Control, and Applications

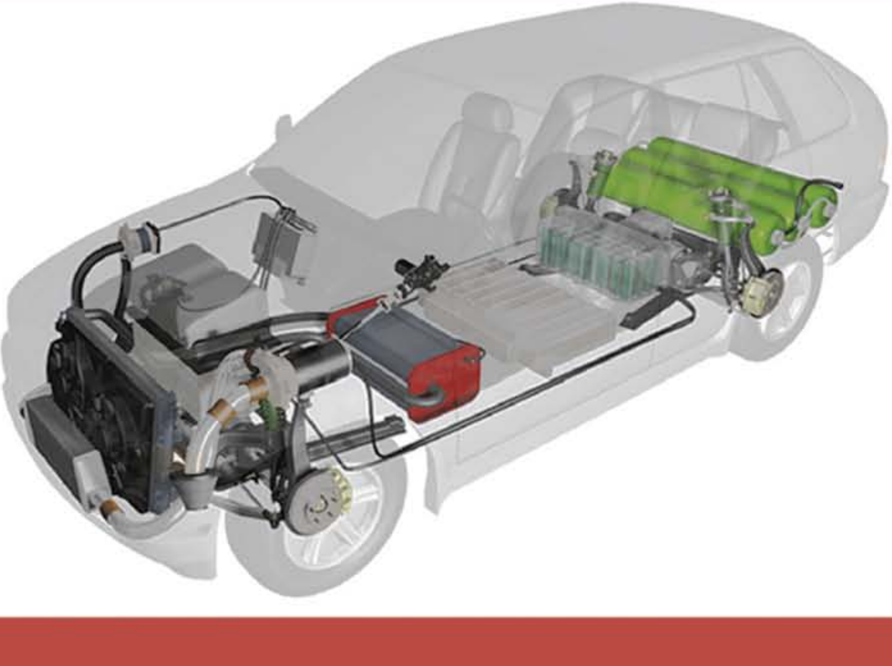

Bei Gou • Woon Ki Na • Bill Diong

CRC Press
Taylor & Francis Group

FUEL CELLS

Modeling, Control, and Applications

POWER ELECTRONICS AND APPLICATIONS SERIES

Muhammad H. Rashid, Series Editor
University of West Florida

PUBLISHED TITLES

Advanced DC/DC Converters
Fang Lin Luo and Hong Ye

Alternative Energy Systems: Design and Analysis with Induction Generators, Second Edition
M. Godoy Simões and Felix A. Farret

Complex Behavior of Switching Power Converters
Chi Kong Tse

DSP-Based Electromechanical Motion Control
Hamid A.Toliyat and Steven Campbell

Electric Energy: An Introduction, Second Edition
Mohamed A. El-Sharkawi

Electrical Machine Analysis Using Finite Elements
Nicola Bianchi

Fuel Cells: Modeling, Control, and Applications
Bei Gou, Woon Ki Na, and Bill Diong

Integrated Power Electronic Converters and Digital Control
Ali Emadi, Alireza Khaligh, Zhong Nie, and Young Joo Lee

Modern Electric, Hybrid Electric, and Fuel Cell Vehicles: Fundamentals, Theory, and Design
Mehrdad Eshani, Yimin Gao, Sebastien E. Gay, and Ali Emadi

Uninterruptible Power Supplies and Active Filters
Ali Emadi, Abdolhosein Nasiri, and Stoyan B. Bekiarov

FUEL CELLS

Modeling, Control, and Applications

Bei Gou • Woon Ki Na • Bill Diong

CRC Press
Taylor & Francis Group
Boca Raton London New York

CRC Press is an imprint of the
Taylor & Francis Group, an **informa** business

MATLAB® and Simulink® are trademarks of The MathWorks, Inc. and are used with permission. The MathWorks does not warrant the accuracy of the text of exercises in this book. This book's use or discussion of MATLAB® and Simulink® software or related products does not constitute endorsement or sponsorship by The MathWorks of a particular pedagogical approach or particular use of the MATLAB® and Simulink® software.

CRC Press
Taylor & Francis Group
6000 Broken Sound Parkway NW, Suite 300
Boca Raton, FL 33487-2742

© 2010 by Taylor and Francis Group, LLC
CRC Press is an imprint of Taylor & Francis Group, an Informa business

No claim to original U.S. Government works

Printed in the United States of America on acid-free paper
10 9 8 7 6 5 4 3 2 1

International Standard Book Number: 978-1-4200-7161-0 (Hardback)

This book contains information obtained from authentic and highly regarded sources. Reasonable efforts have been made to publish reliable data and information, but the author and publisher cannot assume responsibility for the validity of all materials or the consequences of their use. The authors and publishers have attempted to trace the copyright holders of all material reproduced in this publication and apologize to copyright holders if permission to publish in this form has not been obtained. If any copyright material has not been acknowledged please write and let us know so we may rectify in any future reprint.

Except as permitted under U.S. Copyright Law, no part of this book may be reprinted, reproduced, transmitted, or utilized in any form by any electronic, mechanical, or other means, now known or hereafter invented, including photocopying, microfilming, and recording, or in any information storage or retrieval system, without written permission from the publishers.

For permission to photocopy or use material electronically from this work, please access www.copyright.com (http://www.copyright.com/) or contact the Copyright Clearance Center, Inc. (CCC), 222 Rosewood Drive, Danvers, MA 01923, 978-750-8400. CCC is a not-for-profit organization that provides licenses and registration for a variety of users. For organizations that have been granted a photocopy license by the CCC, a separate system of payment has been arranged.

Trademark Notice: Product or corporate names may be trademarks or registered trademarks, and are used only for identification and explanation without intent to infringe.

Library of Congress Cataloging-in-Publication Data

Gou, Bei.
Fuel cells : modeling, control, and applications / Bei Gou, Woon Ki Na, and Bill Diong.
p. cm. -- (Power electronics and applications series)
"A CRC title."
Includes bibliographical references and index.
ISBN 978-1-4200-7161-0 (hard back : alk. paper)
1. Fuel cells. I. Na, Woon Ki. II. Diong, Bill. III. Title. IV. Series.

TK2931.G67 2010
621.31'2429--dc22 2009021692

Visit the Taylor & Francis Web site at
http://www.taylorandfrancis.com

and the CRC Press Web site at
http://www.crcpress.com

Contents

Preface

During the last five years, the University of Texas at Arlington has been independently conducting research on fuel cells as well as collaborating with Texas Christian University. The main research focus has been the modeling of polymer electrolyte membrane (PEM) fuel cells and nonlinear control design using the exact linearization control method.

The present literature pays a lot of attention to the control design of fuel cell interfaces, while the research on control design for the fuel cell itself receives less attention than it should. This may be due to the complexities involved in control design. However, control is very important to fuel cell operation and efficiency, and this book serves as an introduction to this topic.

This book should be of interest to faculty, students, consultants, manufacturers, researchers, and designers in the field of renewable energy, as it provides a detailed discussion on fuel cell modeling, analysis, and nonlinear control with simulation examples and test results. We assume its readers already have a fundamental knowledge of control theory and fuel cell chemical reactions.

It presents a comprehensive description of modeling and control of PEM fuel cells, depicting typical approaches and achievements in the modeling and control design strategies of PEM fuel cells. Both linear and nonlinear models and control designs are included.

For the reader's convenience, this book is organized in a self-contained way to introduce, in sufficient detail, the essence of recent research achievements in the modeling and control design of PEM fuel cells. Mathematical preliminaries in linear control and nonlinear control are provided in the appendix.

The book's organization has been designed to reflect the objective of this book. Chapters 1 and 2 start with a brief introduction to fuel cells and fuel cell power systems and lay down the fundamentals of fuel cell systems and their components. They serve as the background and preparation for the following chapters. Chapter 3 presents the linear and nonlinear modeling of fuel cell dynamics. It serves as preparation for the linear and nonlinear control designs covered in Chapter 4 where it discusses the typical approaches of linear and nonlinear modeling and control design methods for fuel cells. It also serves to compare the linear and nonlinear control designs and their effectiveness. Chapter 5 presents the Simulink implementation of fuel cells, which includes the modeling of PEM fuel cells and control designs and where simulation results of linear and nonlinear controllers are presented and compared. Chapters 6 and 7 discuss the applications of fuel cells in vehicles, utility power systems, and stand-alone systems. Here also, details of typical models and control strategies are presented and discussed. Chapter 8 discusses the modeling and analysis of hybrid renewable energy systems, which include the integration of fuel cells, wind power, and solar power. Details of configuration and control schemes are presented and studied.

We have intended to preserve generality in discussing the advanced technology in the modeling and control of PEM fuel cells and the current applications of fuel cells in vehicles, utility power systems, and stand-alone systems.

We take this opportunity to acknowledge the University of Texas at Arlington (UTA) and Texas Christian University (TCC) as well as the U.S. Department of Energy (DOE) for their support. Our thanks also go to Dr. Kai S. Yeung from the Department of Electrical Engineering at UTA; former graduate students Yunzhi Chen and Dr. Zheng Hui from the same department at UTA; Dr. W. Carter from the Department of Mechanical and Industrial Engineering at the University of Texas at El Paso (UTEP); former graduate student Lu-Ying Chiu from UTEP; and Dr. Randall S. Gemmen from the DOE.

We also wish to express our gratitude to Taylor & Francis Group for giving us the opportunity to publish this book.

Bei Gou
Woonki Na
Bill Diong
Texas

For product information, please contact:

The MathWorks, Inc.
3 Apple Hill Drive
Natick, MA 01760-2098 USA
Tel: 508-647-7000
Fax: 508-647-7001
E-mail: info@mathworks.com
Web: www.mathworks.com

Authors

Dr. Bei Gou received his PhD in electrical engineering from Texas A&M University. He worked as a senior analyst at the Independent System Operator, New England, from 2002 to 2003, and was a power application engineer with ABB System Control at Santa Clara, California, from 2000 to 2002. He joined the faculty of the Department of Electrical Engineering at the University of Texas at Arlington in 2003. His current research areas include power system real-time monitoring, nonlinear control and interface design of fuel cells, blackout and cascading failures, phasor measurements and state estimation, pricing theory for power markets, and power system reliability. Dr. Gou has published more than 70 journal and conference papers. He is the founder of a start-up company—Safe Power Network, LLC and a member of the IEEE Power Engineering Society, the IEEE Power Electronics Society, the IEEE Circuits and Systems Society, the Society of Industrial and Applied Mathematics, and the U.S. National Committee of CIGRE.

Dr. Woonki Na is a senior power electronics and control engineer at Caterpillar, in Peoria, Illinois. He is currently leading a project investigating hybrid AC electric drive systems. Dr. Na received his PhD in electrical engineering from the University of Texas at Arlington in 2008. Previously, he was a power electronics engineer at LG Electronics and at a motor drives company in Seoul, South Korea, for over four years. His research interests include alternative and renewable energy systems, hybrid power and vehicle systems, and power electronics.

Dr. Bill Diong received his BS, MS, and PhD from the University of Illinois, Urbana-Champaign. He gained valuable practical experience as a senior research engineer with Sundstrand Aerospace (now Hamilton-Sundstrand) before returning to academia. Beginning in 1999, he was an assistant professor at the University of Texas at El Paso, where he was appointed the Forrest and Henrietta Lewis Professor of Electrical Engineering from 2000 to 2002. He is currently an associate professor at Texas Christian University, Fort Worth, Texas. His research interests include power electronic systems, advanced power and energy systems, and dynamic systems and control.

1

Introduction

1.1 The Past, Present, and Future of Fuel Cells

1.1.1 What Are Fuel Cells?

A fuel cell operates like a battery by converting the chemical energy from reactants into electricity, but it differs from a battery in that as long as the fuel (such as hydrogen) and an oxidant (such as oxygen) is supplied, it will produce DC electricity (plus water and heat) continuously, as shown in Figure 1.1. In the 1960s, the first practical fuel cells were developed and then used in the U.S. Gemini and Apollo programs for space applications. Since then, fuel cells have also been used increasingly for terrestrial applications although it remains a "new" technology in so far as its commercialization. As some of the fundamental obstacles are being overcome, fuel cells have become more feasible for several applications and are gradually being developed and commercialized.

For example, in 1993, Ballard Power Systems demonstrated fuel cell powered buses. Then all major automotive manufacturers developed fuel cell vehicle prototypes in the late 1990s and the early 2000s, which are undergoing tests in the United States, Japan, and Europe. For stationary power applications, more than 2500 fuel cell stationary power systems have already been installed globally at hospitals, office buildings, utility power plants, and so on. In 2005, Samsung Electronics also unveiled a prototype of fuel cells for portable power applications that can run a laptop about 15 h. However, there remain many challenges to the commercialization of fuel cells. The most significant problems are reducing their cost as well as improving their operating reliability.

The recent increasing impetus in developing and commercializing fuel cells are due to its several advantages. These include "clean" by-products (e.g., water when operated on pure hydrogen), which means it is "zero emission" with extremely low (if any) emission of oxides of nitrogen and sulfur. They also operate quietly, not having any moving parts, even when working with extra fuel processing and supply equipment. Furthermore, they have high power density and high efficiency, typically more than 40% efficiency in electric power production, which is better than traditional combustion engine/generator sets, and the "waste" heat from a fuel cell can be used for heating purposes, thus increasing its overall efficiency. Finally, they can increase national energy security, since different types of fuel cell can

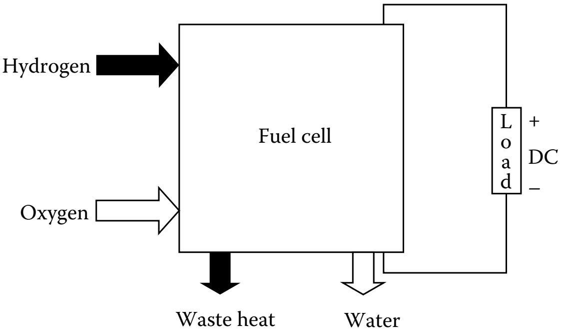

FIGURE 1.1
A fuel cell's inputs and outputs.

operate on various conventional and alternative fuels such as hydrogen, ethanol, methanol, and natural gas, and hydrogen itself can be produced by harnessing a variety of renewable energy sources; such capability can help reduce U.S. dependence on foreign oil.

1.1.2 Types of Fuel Cells

Fuel cells are most commonly classified by the kind of electrolyte being used. These include proton exchange/polymer electrolyte membrane fuel cells (PEMFCs), direct methanol fuel cells (DMFC), alkaline fuel cells (AFC), phosphoric acid fuel cells (PAFC), molten carbonate fuel cells (MCFC), solid oxide fuel cells (SOFC), zinc air fuel cells (ZAFC), and photonic ceramic fuel cells (PCFCs), which vary widely in their required operating temperature. But this book will focus only on PEMFCs, which are low operating temperature fuel cells intended for use in mass-production fuel cell vehicles that are currently under development by the major auto manufacturers, as well as in offices and residences.

1.2 Typical Fuel Cell Power System Organization

The fundamental components of a fuel cell power system are a fuel cell (most commonly a stack or multilayer connection of fuel cells), a fuel and oxidant supply, an electrical load, and an electric power conditioner (see Figure 1.2). The fuel and oxidant supply along with the electric power conditioner are typically lumped together with the fuel reformer, the thermal management subsystem, and the humidification subsystem, when these are present, under the term balance-of-plant.

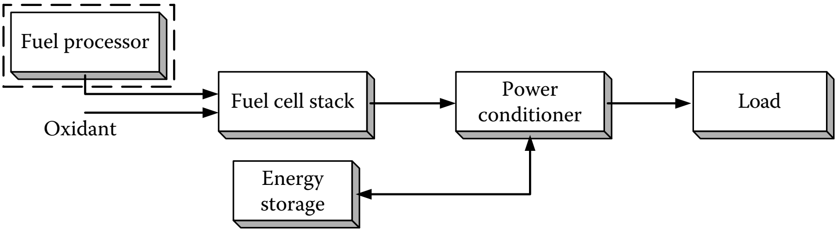

FIGURE 1.2
Block diagram of fuel cell power system interconnection.

1.3 The Importance of Fuel Cell Dynamics

For the successful commercialization of fuel cell vehicles, their performance, reliability, durability, cost, fuel availability and cost, and public acceptance should be considered [1]. The most important disadvantage of fuel cells now is their cost. However, the performance of the fuel cell systems during transients is another key factor. Therefore, during transients, in order to generate a reliable and efficient power response and to prevent membrane damage as well as detrimental degradation of the fuel cell stack voltage and oxygen depletion, it is necessary to design better control schemes to achieve optimal air and hydrogen inlet flow rates—i.e., fuel cell control system that can perform air and hydrogen pressure regulation and heat/water management precisely based on the current drawn from the fuel cell [2,3].

This book essentially addresses the issue of fuel cells' slow transient response to load changes, which is important since the dynamic behavior of a fuel cell is integral to the overall stability and performance of the power system formed by the fuel supply, fuel cell stack, power conditioner, and electrical load. Present-day fuel cells have transient (dynamic) responses that are much slower than the dynamic responses of the typical power conditioner and load to which they are attached. As such, the fuel cell's inability to change its electrical output (current) as quickly as the electrical load changes has significant implications on the overall power system design. In particular, some form of energy storage with quick charge/discharge capability is needed to function as firm power backup during electrical load increases if the fuel flow to the fuel cell is not being kept constant at its maximum level (which is wasteful and inefficient). The slower the fuel cell's response, the larger the amount of energy storage that is needed with the attendant increases in its size, weight, and cost; it also reduces the number of suitable energy storage options (ultracapacitor, flywheel, battery, etc.). Therefore, the fuel cell's dynamic response is of significant importance, particularly in mobile applications.

1.4 Organization of This Book

Chapter 2 describes PEMFCs and the fuel cell power system balance-of-plant components in more detail. Then Chapter 3 describes the modeling of a PEMFC's dynamic behavior as an initial step towards prescribing controller designs to improve its transient behavior. This is followed by Chapter 4, which presents a few methods of control design for PEMFCs. Chapter 5 features the Simulink® implementations of fuel cell models and controllers. Finally, Chapters 6, 7 and 8 discuss three important applications of fuel cells where dynamic response is important; for vehicles and for fixed-voltage stand-alone and hybrid power generation systems. To make this a more complete book for the reader, we have also included several appendices briefly reviewing topics such as linear and nonlinear feedback control.

References

1. F. Barbir and T. Gomez, Efficiency and economics of PEM fuel cells, *International Journal of Hydrogen Energy*, 22(10/11), 1027–1037, 1997.
2. A.M. Borbely and J.G. Kreider, *Distributed Generation: The Power Paradigm for the New Millennium*, New York: CRC Press, 2001.
3. F. Barbir, *PEM Fuel Cells: Theory and Practice*, New York: Elsevier Academic Press, 2005.

2

Fundamentals of Fuel Cells

2.1 Introduction

The PEMFC, also called solid polymer fuel cell, was first developed by General Electric in the United States during the 1960s, for use by NASA on their first manned space vehicles [1]. This type of fuel cell depends primarily on a special polymer membrane that is coated with highly dispersed catalyst particles. Hydrogen is fed to the membrane's anode side (possibly at a pressure greater than atmospheric pressure) where the catalyst causes the hydrogen atoms to release their electrons and become H^+ ions (protons):

$$2H_2 \rightarrow 4H^+ + 4e^- \tag{2.1}$$

as shown in Figure 2.1. The proton exchange membrane (PEM) only allows the H^+ ions to pass through it, while the electrons are collected and utilized as electricity by an outside electrical circuit (doing useful work), before they reach the cathode side. There the electrons and the hydrogen ions diffusing through the membrane combine with the supplied oxygen (typically from air) to form water, a reaction that releases energy in the form of heat:

$$4e^- + 4H^+ + O_2 \rightarrow 2H_2O \tag{2.2}$$

This water by-product must be removed to prevent the cell from being flooded and rendered inoperative (more details later). In addition, any unused hydrogen and oxygen (air) are exhausted from the cell anode and cathode outlets, respectively. For this reaction to proceed continuously, the electrons produced at the anode must flow through a circuit external to the fuel cell, and the protons must flow through the PEM as shown in Figure 2.1.

The reaction in a single fuel cell produces an output voltage of around 0.7 V; for general applications, several individual cells are connected in series to form a fuel cell stack to produce the desired voltage additively. The required operating temperature for PEMFCs is only 50°C–100°C, which enables fast start-up of operation. Thus, the PEMFC is particularly attractive for transportation applications, and also as a small- or mid-size distributed electric power generator because it has a high power density, a solid electrolyte, a long stack life, and low corrosion. Other advantages include its clean by-products (pure water when hydrogen is the fuel, which means "zero-emission"), high energy

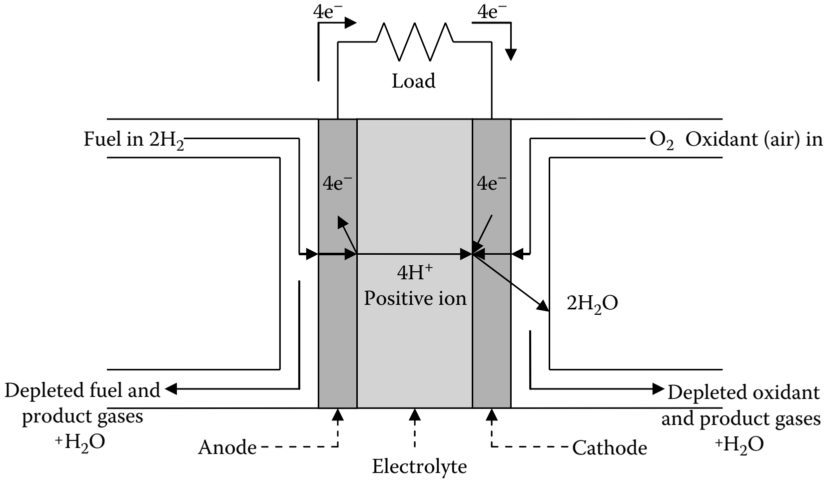

FIGURE 2.1
Electrochemical reaction in the PEMFC. (From Na, W., Dynamic modeling, control and optimization of PEM fuel cell system for automotive and power system applications, PhD thesis, The University of Texas at Arlington, 2008. With permission.)

efficiency of more than 40% typically in electric power production, and quiet operation [3]. Hence PEMFCs are very likely be used to power automobiles, aircraft (auxiliary power), homes and small offices, and portable electronics (as replacements for rechargeable batteries).

2.2 PEMFC Components

The main parts of a practical PEMFC are illustrated in Figure 2.2. The membrane electrode assembly (MEA) consists of the polymer membrane together with the electrodes and gas diffusion layers. Each electrode

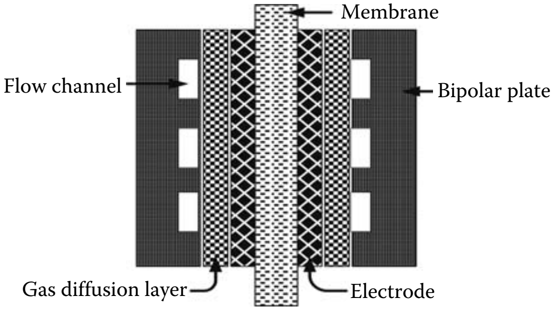

FIGURE 2.2
The main functional parts of a PEMFC.

essentially consists of a layer of catalyst particles (usually platinum deposited on the surface of larger particles of carbon support powder), and is affixed to either the membrane or the gas diffusion layer. The gas diffusion layer is made of a porous and electrically conductive material, such as carbon cloth, to enable the reactants to diffuse into and out of the MEA, and to collect the resulting current by providing electric contact between the electrode and the outside bipolar plate. Furthermore, it allows the water formed at the cathode to exit to the gas channels.

The bipolar plates, also called flow field plates, distribute the reactant gas over the surface of the electrodes through flow channels on their surfaces; different channel geometries are available. They also collect the current and form the supporting structure of the fuel cell. For good electrical and thermal conductivity, plus physical strength and chemical stability, solid graphite is usually used as the material for these plates.

The composition and functions of the various PEMFC parts are further discussed in the following sections.

2.2.1 Membrane

The electrolyte membrane is the key part in any PEMFC. A proton conducting polymer is used as the electrolyte, thus giving rise to this type of fuel cell's name. The basic material used for the membrane is polyethylene, which has been modified by substituting fluorine for hydrogen to yield polytetrafluoroethylene. The bonds between the fluorine and the carbon make the membrane very durable and chemical-resistant (inert). The basic electrolyte is then complemented with sulfonic acid; the HSO_3 group added is ionically bonded (see Figure 2.3). The result is the ability to attract H^+ ions into the electrolyte. This material, made by the DuPont Co. and sold under the trade name Nafion®, has been very significant in the development of PEMFCs.

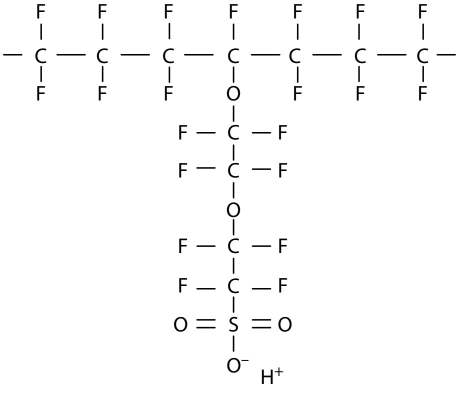

FIGURE 2.3
Structure of a sulfonated fluoroethylene.

The main properties of these polymer membranes [3] are as follows:

- They are resistant to chemical attacks.
- They have very strong bonds, so they can be made into very thin films.
- They are acidic.
- They can absorb a lot of water.
- The H^+ ions they attract are well-conducted through them if the membranes are adequately hydrated (but not flooded).

2.2.2 Membrane Electrode Assembly

The performance of the PEMFC is largely determined by the MEA, which is the central part of the fuel cell. The MEA, as illustrated in Figure 2.4, consists of the electrolyte membrane sandwiched between the anode and cathode electrodes. These electrodes include the catalyst particles and the gas diffusion layers.

Since the fuel oxidation and the oxygen reduction reactions are kinetically slow, a noble metal such as platinum or one of its alloys is used as the catalyst to increase the reaction rate; this catalyst is used at both the anode and the cathode. The platinum is formed into small particles which are spread onto the surfaces of larger particles of the carbon support. The most common carbon support used is a carbon-based powder XC72® (Cabot). The platinum spread into the carbon is highly divided to increase the surface area that it is in contact with the reactants, so as to maximize its catalytic effect. In the early days of PEMFC development, this catalyst was used at loadings of about

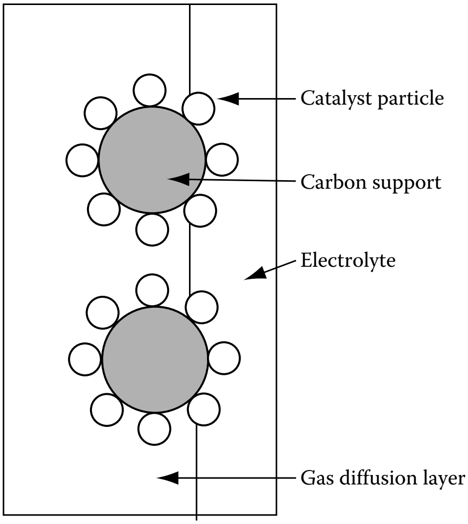

FIGURE 2.4
Membrane electrode assembly.

50 mg of platinum per cm^2 [4] but that has now been reduced to less than 1 mg of platinum per cm^2 [5], thus significantly lowering a PEMFCs overall cost.

The catalyst particles and carbon support are affixed to a porous gas diffusion layer made of an electrically conductive material such as carbon cloth or carbon paper. This carbon cloth or carbon paper diffuses the reactant gases to the surfaces of the catalyst particles, while diffusing the water produced at the cathode away from the electrolyte membrane. In addition, it also provides the electrical connection between the electrode and its corresponding current-conducting bipolar plate.

2.2.3 Bipolar Plates

The bipolar (also known as field flow) plates that form a significant part of the weight and volume of a PEMFC are used to bring the reactant gases via machined flow channels (grooves) to the MEA. They help distribute the reactants onto the surface of the electrodes. In addition, they collect the current produced by the electrochemical reaction. The bipolar plates require good electrical and thermal conductivity, good mechanical strength, and chemical stability. Graphite is the most common material used for these plates at present, although extensive research is performed to develop new materials that can reduce the bipolar plate weight, thereby increasing the fuel cell's power density.

It is important to note that the geometry of the flow channels varies depending on the needs and design of each fuel cell. The specific geometry is also a significant factor in a PEMFCs operating performance. Figure 2.5 illustrates the different geometries used for the bipolar plates.

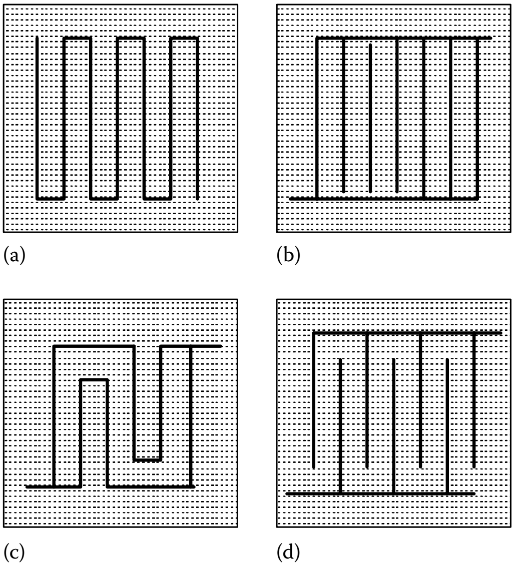

FIGURE 2.5
Different geometries of the flow channels (a) serpentine, (b) parallel, (c) parallel serpentine, and (d) discontinuous.

2.2.4 Heating or Cooling Plates

These plates may be used to either heat the PEMFC or cool it in order to keep its temperature close to the one that yields optimal operating performance. Heating plates typically rely on the use of electricity and ohmic (resistive) heating. Cooling plates are used when air cooling is insufficient; then liquid, such as water, is actively circulated through these plates to cool the stack.

2.3 The Balance-of-Plant Components

A practical fuel cell stack may get the hydrogen fuel from a pressurized tank through regulated valves, or the hydrogen is obtained indirectly from a hydrogen-rich fuel like natural gas via a fuel processor called the reformer. The additional components, such as the above, that may be needed in operating a PEMFC stack are collectively known as the balance-of-plant (BOP). They help with the functions of fuel storage and processing, water management, thermal management, and power conditioning, to achieve the design requirements of the fuel cell system. These are only briefly described below as they are not the main focus of the rest of this book.

2.3.1 Water Management

Without adequate water management, an imbalance will occur between water production by and water removal from the fuel cell. It is critical to ensure that all parts of the cell are sufficiently hydrated, since adherence of the membrane to the electrode and also membrane lifetime will be adversely affected if dehydration occurs. Furthermore, high water content in the electrolyte membrane ensures high ionic conductivity, which improves the overall operating efficiency of the fuel cell. Since the electrochemical reaction produces heat, which increases evaporation, humidifiers are used to (pre) humidify the incoming gases, particularly on the anode side. The humidifier may be as simple as a bubbler or else something more sophisticated like a membrane humidifier or water evaporator [4].

Due to the PEMFCs operation at less than 100°C and at atmospheric pressure, water is produced at the cathode as a liquid. While sufficient hydration is important for optimal PEMFC operation as noted above, this water must not be allowed to flood the electrode because it would impede gas diffusion to that electrode and reduce the cell's operating performance.

2.3.2 Thermal Management

Most PEMFCs at present use cast carbon composite plates for current collection and distribution, gas distribution, and also thermal management. Active air cooling can be achieved through the use of fans. Liquid cooling requires the use of pumps to circulate the fluid through the cooling plates of the stack. These fans and pumps are typically driven by electric motors.

2.3.3 Fuel Storage and Processing

Currently, the most common way to store hydrogen for use as PEMFC fuel is as a gas requiring pressurized cylinders or tanks. Then pressure-reducing regulators are also needed. Storing hydrogen in liquid form requires "only" adequate insulation, but this is a more inefficient way of storing and transporting hydrogen than as a gas.

An alternative to using hydrogen as the primary fuel is to use a hydrocarbon or an alcohol compound as the source of hydrogen. But then a fuel processor or reformer is needed to chemically convert that hydrocarbon or alcohol to a hydrogen-rich gas. Furthermore, as PEM and reformer catalysts are prone to inactivation by sulfur and CO (and also CO_2 to a lesser extent), other subsystems are also needed to remove the sulfur from the primary fuel and the CO from the hydrogen-rich reformate. All of these various components add weight, volume, and expense to the overall system, and reduce its efficiency.

2.3.4 Power Conditioning

The power conditioner is an electronic system that is needed to convert the variable low DC voltage produced by a fuel cell into usable DC power (typically at a regulated higher voltage) or AC power, as appropriate to meet the operating requirements of the intended application. Various types of power converters, such as DC–DC converters and DC–AC inverters, may be employed in fuel cell power conditioning systems.

For powering DC loads, typically a step-up DC–DC converter (to increase the voltage level) is employed. On the other hand, a switch-mode DC–AC inverter is typically used to convert a PEMFCs output DC voltage to regulated AC voltage at 60 Hz (or other) frequency. A filter at the output of such an inverter attenuates the switching frequency harmonics and produces a high-quality sinusoidal voltage suitable for typical AC loads.

For many important applications, such as powering vehicle propulsion, a 5:1 or better peak-to-average power capability [4] is desired, e.g., compare the power needed for accelerating a vehicle as compared to cruising at constant speed. Since present-day fuel cells typically cannot change their power output as quickly as most of these load demand changes, they are thus designed to satisfy the average power requirements and then any additional amount of power must be supplied from another energy source such as a battery or an ultracapacitor. The power conditioning unit must therefore also provide the means for interfacing to this energy storage device and a control scheme is needed to properly coordinate its charging and discharging based on the fuel cell output and load demand conditions.

References

1. *Fuel Cell Handbook*, 7th ed., Morgantown, WV: EG&G Technical Services, Inc., for U.S. Department of Energy, Office of Fossil Energy, National Energy Technology Laboratory, November 2004.
2. W. Na, Dynamic modeling, control and optimization of PEM fuel cell system for automotive and power system applications, PhD thesis, The University of Texas at Arlington, May 2008.
3. J. Larminie and A. Dicks, *Fuel Cell Systems Explained*, 2nd ed., Chichester, U.K.: John Wiley & Sons, 2003.
4. G. Hoogers (ed.), *Fuel Cell Technology Handbook*, Boca Raton, FL: CRC Press, 2003.
5. H.A. Gasteiger, J.E. Panels, and S.G. Yan, Dependence of PEM fuel cell performance on catalyst loading, *Journal of Power Sources*, 127, 162–171, 2004.

3

Linear and Nonlinear Models of Fuel Cell Dynamics

3.1 Introduction

For preliminary fuel cell power system planning, stability analysis, control strategy synthesis, and evaluation, an appropriate dynamic model of a fuel cell system is desired. Since the existing control-oriented models [1–3] do not contain all water components, which are one of the important factors of fuel cell systems [4], it is difficult to design an accurate dynamic fuel cell model based on the existing models. The main motivation for developing dynamic models of PEMFCs is to facilitate the design of control strategies with such objectives as to ensure good load-following performance, to prevent fuel cell stack damage, and to prolong the stack life by controlling the anode and cathode gas pressures. In this chapter, various models of PEMFCs are described. Using these models of PEMFCs, appropriate controllers of fuel cell systems can be designed as described in Chapter 5.

3.2 Nomenclature

E_0	Cell open circuit potential at standard pressure
N	Number of cells in stack
E	Fuel cell (stack) output voltage
L	Sum of cell voltage losses
i	Cell output current density
i_n	Cell internal current density corresponding to internal current losses
i_o	Cell exchange current density corresponding to activation losses
i_l	Cell limiting current density corresponding to concentration losses
r	Cell area-specific resistance corresponding to resistive losses
a	Constant associated with cell activation losses (slope of Tafel line)

b	Constant associated with cell concentration losses
T	Stack operating temperature
P_{H_2}	Partial pressure of hydrogen inside cell anode
P_{O_2}	Partial pressure of oxygen inside cell cathode
$P_{H_2O_a}$	Partial pressure of water vapor inside cell anode
$P_{H_2O_c}$	Partial pressure of water vapor inside cell cathode
P_{N_2}	Partial pressure of nitrogen inside cell cathode
P_{cathode}	Summation of partial pressures inside cell cathode
R	Universal gas constant (8.3144J/mol-K)
F	Faraday's constant (96,439C/mol)
P_{std}	Standard pressure (101,325Pa)
P_{op}	An assumed constant cell operating pressure
$\mathrm{H}_{2\text{in}}, \mathrm{H_2O}_{\text{Ain}}$	Anode inlet molar flow rates of hydrogen and water vapor
Anode_{in}	Summation of anode inlet molar flow rates
$\mathrm{O}_{2\text{in}}, \mathrm{N}_{2\text{in}}, \mathrm{H_2O}_{\text{Cin}}$	Cathode inlet molar flow rates of oxygen, nitrogen, and water vapor
Cath_{in}	Summation of cathode inlet molar flow rates
$\mathrm{H}_{2\text{out}}, \mathrm{H_2O}_{\text{Aout}}$	Anode outlet molar flow rates of hydrogen and water vapor
$\mathrm{O}_{2\text{out}}, \mathrm{N}_{2\text{out}}, \mathrm{H_2O}_{\text{Cout}}$	Cathode outlet molar flow rates of oxygen, nitrogen, and water vapor
$\mathrm{H}_{2\text{used}}, \mathrm{O}_{2\text{used}}, \mathrm{H_2O}_{\text{Cproduced}}$	Molar usage and production rates of hydrogen, oxygen, and water vapor (in cathode)
I	Cell output current
A_c	Cell-active area
V_A	Volume of the cell anode channels
V_C	Volume of the cell cathode channels
$F_{H_2}, F_{O_2}, F_{H_2O_c}$	Pressure fractions of hydrogen, oxygen, and water vapor (in cathode) inside the fuel cell
Y_{H_2}	Molar fraction of H_2 at the anode inlet
Y_{O_2}	Molar fraction of O_2 at the cathode inlet
$Y_{H_2O_c}$	Molar fraction of water vapor at the cathode inlet
$\Delta P_{H_2}, \Delta P_{O_2}, \Delta P_{H_2O_c}$	Perturbations of the partial pressures of hydrogen, oxygen, and water vapor (in cathode) inside the fuel cell
$\Delta \mathrm{H}_{2\text{in}}, \Delta \mathrm{O}_{2\text{in}}, \Delta \mathrm{H_2O}_{\text{Cin}}$	Perturbations of the inlet flow rates of hydrogen, oxygen, and water vapor (to cathode)
Δi	Perturbation of the output current density
ΔE	Perturbation of the fuel cell stack output voltage

3.3 Nonlinear Models of PEM Fuel Cell Dynamics

3.3.1 Unified Model of Steady-State and Dynamic Voltage–Current Characteristics

The performance of a fuel cell can be expressed by the polarization curve, which describes the cell voltage–load current (*V–I*) characteristics of the fuel cell that are highly nonlinear [1–9]. Optimization of fuel cell operating points, design of the power conditioning units, design of simulators for fuel cell stack systems, and design of system controllers depend on such characteristics [10]. Therefore, the modeling of the *V–I* characteristics of fuel cells is important.

It is observed that the known steady-state *V–I* characteristics computed from the formulated electrochemical modeling are divided into two components: one of which is named as the steady component including the thermodynamic potential and the ohmic overvoltage; the other is named as the transient component consisting of the activation and concentration overvoltages. Then, the former is fitted by a low-order least squares polynomial and the latter is described by a high-order least squares polynomial. The coefficients in the polynomials can be estimated by using the least squares technique. The sum of these two components can be used to accurately model the steady-state *V–I* characteristics of PEM fuel cells. Furthermore, by introducing the first-order time delay to describe the dynamic response of PEM fuel cells, the developed mathematical modeling can also be used to accurately predict the dynamic *V–I* characteristics.

For PEM fuel cells, steady-state *V–I* characteristics of a fuel cell are determined by [1,4,5]:

$$V_{\mathrm{cell}} = E_{\mathrm{N}} - V_{\mathrm{a}} - V_{\mathrm{c}} - V_{\mathrm{ohm}} = V_{\mathrm{st}} - V_{\mathrm{tr}}$$

where

V_{cell} represents the output voltage of the fuel cell

E_{N} represents the reversible voltage of the fuel cell (also named as the thermodynamic potential)

V_{a} represents the voltage drop due to the activation of the anode and cathode (also named as the activation overvoltage)

V_{c} denotes the voltage drop resulting from the reduction in concentration of the reactants' gases or from the transport of mass of oxygen and hydrogen (also named as the concentration overvoltage)

V_{ohm} denotes the ohmic voltage drop resulting from the resistance of the conduction of protons through the solid electrolyte and of the electrons through its path (also named as the ohmic overvoltage)

$V_{\mathrm{st}} = E_{\mathrm{N}} - V_{\mathrm{ohm}}$ is the steady component of the cell voltage

$V_{\mathrm{tr}} = V_{\mathrm{a}} + V_{\mathrm{c}}$ is the transient component of the cell voltage

The unified mathematical model of the steady-state and dynamic voltage–current characteristics of fuel cells is

$$\begin{aligned} v_{\text{cell}}(t) &= \sum_{k=0}^{2} p_k (I_{\text{cell}} - I_{\text{st}})^k - \sum_{k=0}^{5} q_k (I_{\text{cell}} - I_{\text{tr}})^k \\ &\quad - \left[\sum_{k=0}^{5} q_k (I_{\text{cell}t} - T_{\text{tr}})^k - (I_{\text{cell}} - I_{\text{tr}})^k \right] \left(1 - e^{-t/T_{\text{C}}}\right) \end{aligned}$$

where

$$V_{\text{st}}(I_{\text{cell}}) = \sum_{k=0}^{2} p_k (I_{\text{cell}} - I_{\text{st}})^k$$

$$I_{\text{st}} = \sum_{m=0}^{N_{\text{st}}-1} \frac{I_{\text{cell}m}}{N_{\text{st}}}$$

$$V_{\text{tr}}(I_{\text{cell}}) = \sum_{k=0}^{5} q_k (I_{\text{cell}} - I_{\text{tr}})^k$$

$$I_{\text{tr}} = \sum_{m=0}^{N_{\text{tr}}-1} \frac{I_{\text{cell}m}}{N_{\text{tr}}}$$

I_{cell} is the cell current

p_k are the coefficients determined by using the least squares technique

$I_{\text{cell}m}$ are the known discrete current values

N_{st} is the number of the given discrete current data for the steady component ($N_{\text{st}} \geq 3$)

q_k are the coefficients determined by using the least squares technique

N_{tr} is the number of the given discrete current data for the transient component ($N_{\text{tr}} \geq 6$)

3.3.2 Simulation Results

The Ballard Mark V PEM fuel cell is used to test the proposed model (Figures 3.1 and 3.2). Tables 3.1 and 3.2 show the computed coefficients in the steady and transient component polynomials, respectively. These coefficients are computed by using the least squares technique, based on the data from the formulated electrochemical modeling and the parameters of the Ballard Mark V PEM fuel cell listed in Table 3.3.

3.3.3 Nonlinear Model of PEM Fuel Cells for Control Applications

A PEM fuel cell consists of a polymer electrolyte membrane sandwiched between two electrodes (anode and cathode) in Figure 3.3. In the electrolyte, only ions can pass by, and electrons are not allowed to go through. So, the flow of electrons needs a path like an external circuit from the anode to the cathode to produce electricity because of potential difference between the anode and cathode. The overall electrochemical reactions for a PEM fuel

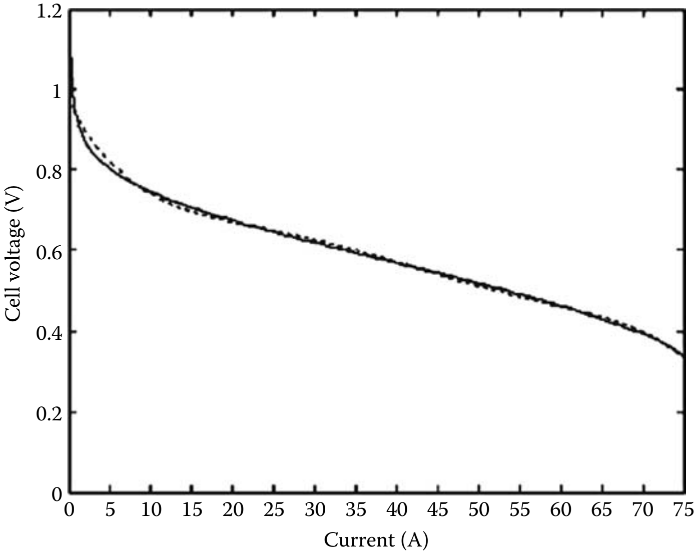

FIGURE 3.1
Computed and given steady-state *V–I* characteristics for the Ballard Mark V PEM fuel cell (dotted curve—computed values and solid curve—given data).

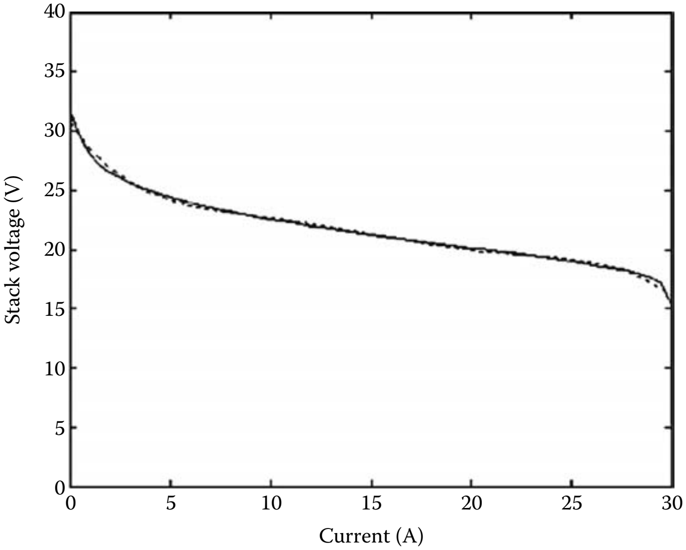

FIGURE 3.2
Polarization *V–I* curve (Ballard Mark V PEMFC at 70°C).

TABLE 3.1

Steady Coefficients for the Ballard Mark V PEM Fuel Cell

k	0	1	2
p_k	.110149E+01	−.297366E−02	−.183457E−04

TABLE 3.2

Transient Coefficients for the Ballard Mark V PEM Fuel Cell

k	0	1	2	3	4	5
q_k	.516228E+00	.298822E−02	.265448E−04	−.323092E−05	−.603896E−07	.349527E−08

Source: Larminie, J. and Dicks, A., *Fuel Cell Systems Explained*, Wiley, New York, 2002. With permission.

TABLE 3.3

PEMFCs Ballard Mark V Voltage Parameters

Parameter	Value and Definition
N	Cell number: 35
V_o	Open-cell voltage: 1.032 [V]
R	Universal gas constant [J/mol-K]: 8.314 [J/mol-K]
T	Temperature of the fuel cell [K]: 353 [K]
F	Faraday constant [C/mol]: 96,485 [C/mol]
α	Charge transfer coefficient: 0.5
M	Constant in the mass transfer voltage: 2.11×10^{-5} [V]
N	Constant in the mass transfer voltage: 8×10^{-3} [cm^2/mA]
R_{ohm}	2.45×10^{-4} [kΩ cm^2]
A_{fc}	Fuel cell active area: 232 [cm^2]
I_0	Exchange current density [A/cm^2]
I_n	Internal current density [A/cm^2]

cell fed with hydrogen-containing anode gas and oxygen-containing cathode gas are as follows:

$$\text{Anode: } 2H_2 \leftrightarrow 4H^+ + 4e^-$$

$$\text{Cathode: } O_2 + 4H^+ + 4e^- \leftrightarrow 2H_2O$$

$$\text{Overall reaction: } 2H_2 + O_2 \leftrightarrow 2H_2O + \text{electricity} + \text{heat}$$

In practice, a 5 kW fuel cell stack, such as a Ballard MK5-E PEMFC stack, uses a pressurized hydrogen tank at 10 atm and oxygen taken from atmospheric

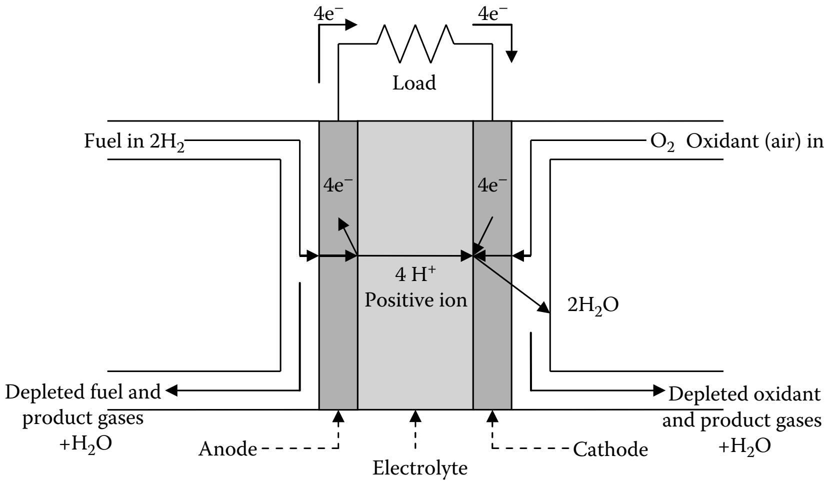

FIGURE 3.3
Schematic of fuel cell operation.

air [11,12]. In case of using reformer, on the anode side, a fuel processor called reformer that generates hydrogen through reforming methane or other fuels like natural gas can be used instead of the pressurized hydrogen tank.

A pressure regulator and purging of the hydrogen component are also required. On the cathode side, an air supply system containing a compressor, an air filter, and an airflow controller are required to maintain the oxygen partial pressure [2,4,7,13]. On both sides, a humidifier is needed to prevent dehydration of fuel cell membrane [2,4,7]. In addition, a heat exchanger, a water tank, a water separator, and a pump may be needed for water and heat management in the fuel cell systems [2,4,7].

To produce a higher voltage, multiple cells have to be connected in series. Typically, a single cell produces voltage between 0 and 1 V based on the polarization *I*–*V* curve, which expresses the relationship between the stack voltage and the load current [2,4,7]. Figure 3.4 shows that their relationship is nonlinear and mainly depends on current density, cell temperature, reactant partial pressure, and membrane humidity [2,4,7].

The output stack voltage V_{st} [4] is defined as a function of the stack current, reactant partial pressures, fuel cell temperature, and membrane humidity:

$$V_{\mathrm{st}} = E - V_{\mathrm{activation}} - V_{\mathrm{ohmic}} - V_{\mathrm{concentration}} \tag{3.1}$$

In the above equation,

$E = N_{\mathrm{O}} \cdot \left[V_{\mathrm{O}} + (RT/2F)\ln\left(P_{\mathrm{H_2}}\sqrt{P_{\mathrm{O_2}}}\,/P_{\mathrm{H_2O_c}}\right)\right]$ is the thermodynamic potential of the cell or reversible voltage based on Nernst equation [4]

$V_{\mathrm{activation}}$ is the voltage loss due to the rate of reactions on the surface of the electrodes

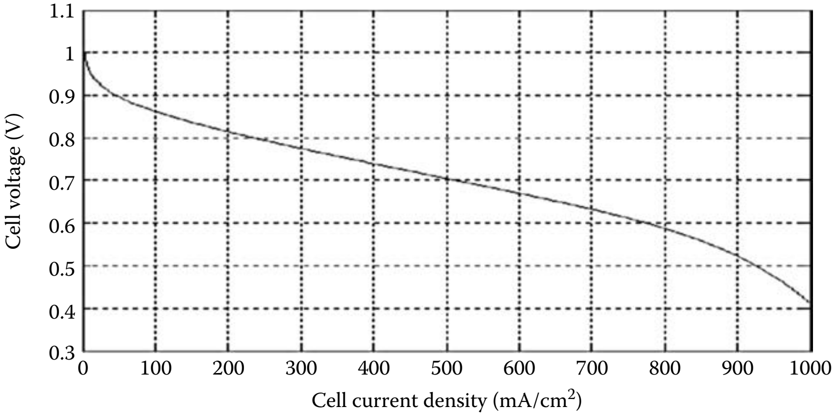

FIGURE 3.4
Polarization *V–I* curve (Ballard Mark V PEMFC at 70°C). (From Larminie, J. and Dicks, A., *Fuel Cell Systems Explained*, Wiley, New York, 2002. With permission.)

V_{ohmic} is the ohmic voltage drop from the resistances of proton flow in the electrolyte

$V_{\text{concentration}}$ is the voltage loss from the reduction in concentration gases or the transport of mass of oxygen and hydrogen

Their equations are given as follows:

$$V_{\text{activation}} = N \cdot \frac{RT}{2\alpha F} \cdot \ln\left(\frac{I_{\text{fc}} + I_{\text{n}}}{I_{\text{o}}}\right) \tag{3.2}$$

$$V_{\text{ohm}} = N \cdot I_{\text{fc}} \cdot R_{\text{ohm}} \tag{3.3}$$

$$V_{\text{concentration}} = N \cdot m \exp(n \cdot I_{\text{fc}}) \tag{3.4}$$

In Equation 3.1, P_{H_2}, P_{O_2}, and $P_{H_2O_c}$ are the partial pressures of hydrogen, oxygen, and water, respectively. Subscript "c" means the water partial pressure, which is vented from the cathode side.

3.4 State Space Dynamic Model of PEMFCs

To derive a simplified nonlinear dynamic PEMFC model, the following assumptions are made:

- Due to slower dynamics of the stack temperature, the average stack temperature is assumed to be constant.
- The relative humidity can be well controlled to a little over 100%, and thereby the liquid water always forms the stack. This liquid water is

perfectly managed by the water tank and water separator, and the water flooding effects can be controlled.

- A continuous supply of reactants is fed to the fuel cell to allow operation at a sufficiently high flow rate.
- The mole fractions of inlet reactants are assumed to be constant in order to build the simplified dynamic PEMFC model. In other words, pure hydrogen (99.99%) is fed to the anode, and the air that is uniformly mixed with nitrogen and oxygen by a ratio of, say, 21:79, is supplied to the cathode.
- The full state has to be measured to utilize feedback linearization [14].

The ideal gas law and the mole conservation rule are employed. Each partial pressure of hydrogen, the water from the anode, and the oxygen, nitrogen, and water from the cathode are defined as state variables of the PEMFC. The relationship between inlet gases and outgases is described in Figure 3.5 [15].

The partial-pressure derivatives are given by the following equations:

Anode mole conservation

$$\begin{aligned}\frac{\mathrm{d}P_{H_2}}{\mathrm{d}t} &= \frac{RT}{V_A}\left(H_{2\mathrm{in}} - H_{2\mathrm{used}} - H_{2\mathrm{out}}\right)\\ \frac{\mathrm{d}P_{H_2O_A}}{\mathrm{d}t} &= \frac{RT}{V_A}\left(H_2\,O_{\mathrm{Ain}} - H_2\,O_{\mathrm{Aout}} - H_2O_{\mathrm{mbr}} + H_2O_{\mathrm{back}} - H_2O_{\mathrm{l,Aout}}\right)\end{aligned} \tag{3.5a}$$

Cathode mole conservation

$$\begin{aligned}\frac{\mathrm{d}P_{O_2}}{\mathrm{d}t} &= \frac{RT}{V_C}\left(O_{2\mathrm{in}} - O_{2\mathrm{used}} - O_{2\mathrm{out}}\right)\\ \frac{\mathrm{d}P_{N_2}}{\mathrm{d}t} &= \frac{RT}{V_C}\left(N_{2\mathrm{in}} - N_{2\mathrm{out}}\right)\\ \frac{\mathrm{d}P_{H_2O_C}}{\mathrm{d}t} &= \frac{RT}{V_C}\left(H_2O_{\mathrm{Cin}} + H_2O_{\mathrm{Cproduced}} - H_2O_{\mathrm{Cout}} + H_2O_{\mathrm{mbr}} - H_2O_{\mathrm{mbr}} - H_2O_{\mathrm{l,Cout}}\right)\end{aligned} \tag{3.5b}$$

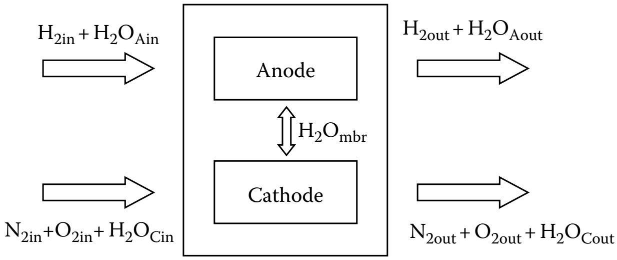

FIGURE 3.5
Gas flows of PEMFCs.

where $H_{2\text{in}}, O_{2\text{in}}, N_{2\text{in}}, H_2O_{\text{Ain}}$, and H_2O_{Cin} are the inlet flow rates of hydrogen, oxygen, nitrogen, the anode-side water, and the cathode-side water, respectively. In addition, $H_{2\text{out}}, O_{2\text{out}}, N_{2\text{out}}, H_2O_{\text{Aout}}$, and H_2O_{Cout} are the outlet flow rates of each gas. $H_{2\text{used}}, O_{2\text{used}}$, and $H_2O_{\text{Cproduced}}$ are the usage and the production of the gases, respectively. In general, the membrane water inlet flow rate H_2O_{mbr} across the membrane is a function of the stack current and the membrane water content λ_m. By assuming that $\lambda_m = 14$ [7,16], H_2O_{mbr} is defined as a function of the current density only, and $H_2O_{\text{mbr}} = 1.2684(N \cdot A_{\text{fc}} \cdot I_{\text{fc}})/F$ [7,16], where A_{fc} (cm^2) is the fuel cell active area, N is the number of the fuel cells, and I_{fc} is the fuel cell current density. Furthermore, in order to describe a more accurate dynamic model, the back-diffusion of water from the cathode to the anode can be defined with $H_2O_{\text{v,back}} = \gamma \cdot H_2O_{\text{v,mbr}}$ [2]. The back-diffusion coefficient β is measured as 6×10^{-6}(cm^2/s) with the water content being $\lambda_m = 14$ [2]. The flow rates of liquid water leaving the anode and cathode are given by $H_2O_{\text{l,Aout}}$ and $H_2O_{\text{l,Cout}}$, which are dependent upon the saturation state of each gas [7]. To estimate the liquid water, the maximum mass of vapor has to be calculated from the vapor saturation pressure as follows:

$$m_{\text{v,max,A or C}} = \frac{p_{\text{vs}} V_{\text{A or C}}}{R_v T_{\text{st}}} \tag{3.6}$$

The saturation pressure p_{vs} is calculated from an equation presented in [17]:

$$\log_{10}(p_{\text{vs}}) = -1.69 \times 10^{-10} T^4 + 3.85 \times 10^{-7} T^3 - 3.39 \times 10^{-4} T^2 + 0.143T - 20.92 \tag{3.7}$$

where the saturation pressure p_{vs} is in kPa and temperature T is in Kelvin. If the mass of water calculated in Equations 3.5a and b is greater than the maximum mass of vapor in Equation 3.6, the liquid water formation occurs simultaneously. The mass of liquid water and vapor is calculated as follows [7]:

Logic 1

if $m_{\text{w,A or C}} \le m_{\text{v,max A or C}} \rightarrow m_{\text{v,A or C}} = m_{\text{w,A or C}}, m_{\text{l,A or C}} = 0$;
if $m_{\text{w,A or C}} > m_{\text{v,max A or C}} \rightarrow m_{\text{v,A or C}} = m_{\text{v,max A or C}}$;
$m_{\text{l,A or C}} = m_{\text{w, A or C}} - m_{\text{v, max A or C}}$.

Thereby, $\beta_{\text{A or C}}$ can be used to estimate the liquid water formation in Equation 3.8. According to logic 1, if $m_{\text{w,A or C}} \le m_{\text{v,max A or C}}$, then $\beta_{\text{A or C}} = 0$; otherwise $\beta_{\text{A or C}} = 1$, and therefore $H_2O_{\text{l,Aout}}$ and $H_2O_{\text{l,Cout}}$ are defined by

$$H_2O_{\text{l,A or C out}} = \beta_{\text{a or c}} \left| \frac{p_{H_2O_{\text{A or C}}} V_{\text{A or C}}}{R_v T_{\text{st}}} - \frac{p_{\text{vs}} V_{\text{A or C}}}{R_v T_{\text{st}}} \right| \Bigg/ M_{H_2O} \tag{3.8}$$

where M_{H_2O} is the water molar mass, 18.02 g/mol. All units of flow rates, usage, and the production of gases are defined in mol/s. However, because the liquid water is considered based on our assumption that each relative humidity stays over 100%, $\beta_{\mathrm{a\ or\ c}}$ will be 1, which means that $p_{\mathrm{H_2O_{A\ or\ C}}} > P_{\mathrm{vs}}$ during the simulation. V_{a} and V_{c} are the anode and cathode volumes, respectively, and their units are m^3. According to the basic electrochemical relationships, the usage and production of the gases are functions of the cell current density I_{fc} [4], as follows:

$$\mathrm{H}_{2\,\mathrm{used}} = 2\mathrm{O}_{2\,\mathrm{used}} = \mathrm{H_2O}_{\mathrm{Cproduced}} = \frac{N \cdot A_{\mathrm{fc}} \cdot I_{\mathrm{fc}}}{2F} \tag{3.9}$$

For simplicity, let us define

$$\frac{N \cdot A_{\mathrm{fc}}}{2F} = C_1 \quad \text{and} \quad 1.2684\frac{N \cdot A_{\mathrm{fc}}}{F} = C_2$$

Thus, in Equations 3.5a and b, $\mathrm{H_2O_{mbr}}$ and $\mathrm{H_2O_{v,back}}$ can be simplified with C_1 and C_2. With the measured inlet flow rates and the stack current, the outlet flow rates are given by the summation of the anode and cathode inlet flow rates, that is, $\mathrm{Anode_{in}}$ and $\mathrm{Cath_{in}}$, minus the usage and production of gases as well as the pressure fraction proposed by [13]. The $\mathrm{Anode_{in}}$ is defined by $\mathrm{H_{2in}} + \mathrm{H_2O_{Ain}}$, and the $\mathrm{Cath_{in}}$ is defined by $\mathrm{O_{2in}} + \mathrm{N_{2in}} + \mathrm{H_2O_{Cin}}$.

The outlet flow rates on the anode side are

$$\begin{aligned} \mathrm{H}_{2\mathrm{out}} &= (\mathrm{H}_{2\mathrm{in}} - C_1 \cdot I_{\mathrm{fc}})F_{\mathrm{H_2}} \\ \mathrm{H_2O}_{\mathrm{Aout}} &= (\mathrm{H_2O}_{\mathrm{Ain}} - C_2 \cdot I_{\mathrm{fc}} + \gamma \cdot C_2 \cdot I_{\mathrm{fc}})F_{\mathrm{H_2O_A}} \end{aligned} \tag{3.10}$$

and the outlet flow rates on the cathode side are

$$\begin{aligned} \mathrm{O}_{2\mathrm{out}} &= \left(\mathrm{O}_{2\mathrm{in}} - \frac{C_1}{2} I_{\mathrm{fc}}\right)F_{\mathrm{O_2}} \\ \mathrm{N}_{2\mathrm{out}} &= \mathrm{N}_{2\mathrm{in}} \cdot F_{\mathrm{N_2}} \\ \mathrm{H_2O}_{\mathrm{Cout}} &= (\mathrm{H_2O}_{\mathrm{Cin}} + C_1 \cdot I_{\mathrm{fc}} + C_2 \cdot I_{\mathrm{fc}} - \gamma \cdot C_2 \cdot I_{\mathrm{fc}})F_{\mathrm{H_2O_C}} \end{aligned} \tag{3.11}$$

where $F_{\mathrm{H_2}}$, $F_{\mathrm{H_2O_A}}$, $F_{\mathrm{O_2}}$, $F_{\mathrm{N_2}}$, and $F_{\mathrm{H_2O_C}}$ are the pressure fractions of gases inside the fuel cell, given as follows [18]:

$$\begin{aligned} &F_{\mathrm{H_2}} = \frac{P_{\mathrm{H_2}}}{P_{\mathrm{H_2}} + P_{\mathrm{H_2O_A}}}; \quad F_{\mathrm{H_2O_A}} = \frac{P_{\mathrm{H_2O_A}}}{P_{\mathrm{H_2}} + P_{\mathrm{H_2O_A}}}; \quad F_{\mathrm{O_2}} = \frac{P_{\mathrm{O_2}}}{P_{\mathrm{O_2}} + P_{\mathrm{N_2}} + P_{\mathrm{H_2O_C}}}; \\ &F_{\mathrm{N_2}} = \frac{P_{\mathrm{N_2}}}{P_{\mathrm{O_2}} + P_{\mathrm{N_2}} + P_{\mathrm{H_2O_C}}}; \quad F_{\mathrm{H_2O_C}} = \frac{P_{\mathrm{H_2O_C}}}{P_{\mathrm{O_2}} + P_{\mathrm{N_2}} + P_{\mathrm{H_2O_C}}} \end{aligned} \tag{3.12}$$

To analyze the transient behavior of fuel cells, we take into account the pressure fraction of each gas proposed by Chiu et al. [18]. In [18], only the three pressure fractions $F_{\mathrm{H_2}}$, $F_{\mathrm{O_2}}$, and $F_{\mathrm{H_2O_C}}$ are considered, but in our study, by considering all pressure fractions of gases, a more accurate dynamic fuel cell model is achieved and a better analysis of the transient behavior of fuel cells is possible than in previous studies [3,7,18,19]. The state equations (Equations 3.13 and 3.14) are obtained by substituting Equations 3.10 and 3.12 into Equations 3.5a and b.

The new state equations on the anode side are

$$\frac{\mathrm{d}P_{H_2}}{\mathrm{d}t} = \frac{RT}{V_A}\left[H_{2\mathrm{in}} - C_1 \cdot I_{\mathrm{fc}} - (H_{2\mathrm{in}} - C_1 \cdot I_{\mathrm{fc}})F_{H_2}\right]$$

$$\frac{\mathrm{d}P_{H_2O_a}}{\mathrm{d}t} = \frac{RT}{V_A}\left[H_2O_{\mathrm{Ain}} - (H_2O_{\mathrm{Ain}} - C_2 \cdot I_{\mathrm{fc}} + C_2 \cdot I_{\mathrm{fc}})F_{H_2O_A} - C_2 \cdot I_{\mathrm{fc}} + \gamma \cdot C_2 \cdot I_{\mathrm{fc}}\right] \tag{3.13}$$

and the state equations on the cathode side are

$$\frac{\mathrm{d}P_{O_2}}{\mathrm{d}t} = \frac{RT}{V_C}\left[O_{2\mathrm{in}} - \frac{C_1}{2} I_{\mathrm{fc}} - \left(O_{2\mathrm{in}} - \frac{C_1}{2} I_{\mathrm{fc}}\right)F_{O_2}\right]$$

$$\frac{\mathrm{d}P_{N_2}}{\mathrm{d}t} = \frac{RT}{V_C}\left[N_{2\mathrm{in}} - N_{2\mathrm{in}} \cdot F_{N_2}\right] \tag{3.14}$$

$$\frac{\mathrm{d}P_{H_2O_C}}{\mathrm{d}t} = \frac{RT}{V_C}\left[H_2O_{\mathrm{Cin}} + C_1 \cdot I_{\mathrm{st}} - (H_2O_{\mathrm{Cin}} + C_1 \cdot I_{\mathrm{st}} + C_2 \cdot I_{\mathrm{st}} - C_2 \cdot I_{\mathrm{st}})F_{H_2O_C} + C_2 \cdot I_{\mathrm{st}} - \gamma \cdot C_2 \cdot I_{\mathrm{st}}\right]$$

Because the initial mole fractions Y_{H_2}, Y_{O_2}, and Y_{N_2} are set to be 0.99, 0.21, and 0.79, respectively [3,7,19], the input values $H_{2\mathrm{in}}, O_{2\mathrm{in}}$, and $N_{2\mathrm{in}}$ are defined by the mole fractions, which are given as

$$\begin{aligned} H_{2\mathrm{in}} &= Y_{H_2} \cdot \mathrm{Anode}_{\mathrm{in}} \\ O_{2\mathrm{in}} &= Y_{O_2} \cdot \mathrm{Anode}_{\mathrm{in}} \\ N_{2\mathrm{in}} &= Y_{N_2} \cdot \mathrm{Cath}_{\mathrm{in}} \end{aligned} \tag{3.15}$$

The water inlet flow rates on the anode and the cathode are expressed in terms of the relative humidity, saturation pressure, and total pressure on each side, as follows [2]:

$$\begin{aligned} H_2O_{\mathrm{Ain}} &= \frac{\varphi_a P_{\mathrm{vs}}}{P_A - \varphi_a P_{\mathrm{vs}}} \cdot \mathrm{Anode}_{\mathrm{in}} \\ H_2O_{\mathrm{Cin}} &= \frac{\varphi_c P_{\mathrm{vs}}}{P_C - \varphi_c P_{\mathrm{vs}}} \cdot \mathrm{Cath}_{\mathrm{in}} \end{aligned} \tag{3.16}$$

where φ_a and φ_c are the relative humidity on the anode and the cathode sides, respectively; $P_A = P_{H_2} + P_{H_2O_A}$ is the summation of partial pressures of the anode; and $P_C = P_{O_2} + P_{N_2} + P_{H_2O_C}$ is the summation of partial pressures of the cathode. P_{vs} is the saturation pressure, which can be found in the thermodynamics tables [20]. The relative humidity φ_a and φ_c are defined from the water injection input u_{a_h} for the anode and u_{c_h} for the cathode. Furthermore, Anode_{in} and Cath_{in} are defined as the products of the input control variables u_a and u_c and the conversion factors k_a and k_c [11,18] on each side, which are translated from standard liters per minute (SLPM) to mol/s. In other words

$$\begin{aligned}\text{Anode}_{in} &= u_a \cdot k_a \\ \text{Cath}_{in} &= u_c \cdot k_c\end{aligned} \tag{3.17}$$

where the conversion factors k_a and k_c are 0.065 mol/s, respectively. The hydrogen and the air stoichiometric ratios are assumed to be constant to keep the reactants flowing through the stack [20]. Hence, both of these reactants are able to be fed to the fuel cell continuously and the fuel cell control system can be mainly dependent upon the input control variables u_a and u_c. First, the anode gas pressure $P_a = P_{H_2} + P_{H_2O_A}$ and the cathode gas pressure $P_c = P_{N_2} + P_{O_2} + P_{H_2O}$ will be controlled by u_a and u_c, respectively, to avoid unwanted pressure fluctuation and prevent MEA damage; thus it can lead to prolong the fuel cell stack life [15]. In terms of control for the relative humidity on both sides, the first-order time-delay water injection inputs u_{a_h} and u_{c_h} will be applied because the water injection system has a very slow time constant τ_d of about 70 s [21]. Thus, in our dynamics model of PEMFC, the first-order time-delay model for the water injection is considered and the state equation from the relationship between the water injection input and relative humidity is derived as follows:

$$\varphi_a = \frac{1}{1+\tau_d s} u_{a\_h}; \quad \varphi_b = \frac{1}{1+\tau_d s} u_{b\_h} \tag{3.18}$$

where φ is relative humidity. As seen in Equation 3.16, because each water input is a function of humidity, the water injection inputs also affect the pressure controls. So, we can establish a dynamic model of PEMFCs and the details of control design will be described in Chapter 4.

3.5 Electrochemical Circuit Model of PEM Fuel Cells

3.5.1 Equivalent Circuit

Another important modeling method of PEM fuel cells is to use equivalent electrical circuits. The benefit of this kind of models is that the analysis, simulation or study of PEM fuel cells can be simplified by using equivalent electrical circuits to replace PEM fuel cells. In this section, we will introduce a typical electrical circuit as proposed in [22].

A mathematical approach is presented for building a dynamic model for a PEM fuel cell stack. The following assumptions are made [2,4,8,18,23]:

- One-dimensional treatment.
- Ideal and uniformly distributed gases.
- Constant pressures in the fuel cell gas flow channels.
- The fuel is humidified and the oxidant is humidified air. Assume the effective anode water vapor pressure is 50% of the saturated vapor pressure while the effective cathode water pressure is 100%.
- The fuel cell works under 100°C and the reaction product is in liquid phase.
- Thermodynamic properties are evaluated at the average stack temperature, temperature variations across the stack are neglected, and the overall specific heat capacity of the stack is assumed to be a constant.
- Parameters for individual cells can be lumped together to represent a fuel cell stack.

A schematic diagram of a PEM fuel cell and its internal voltage drops is shown in Figure 3.6. For details of the working of PEM fuel cell, the reader is referred to [18,23,24].

After the effective partial pressures of H_2 and O_2 are studied, and the instantaneous change in the effective partial pressures of hydrogen and oxygen is also considered through the ideal gas equations as given in [25], the fuel cell output voltage can be written as follows [22]:

$$V_{\text{out}} = E - V_{\text{c}} - V_{\text{act1}} - V_{\text{ohm}}$$

where

E is the reversible potential of each cell (in volt)

V_{c} is the voltage across the capacitor

$V_{\text{act}} = V_{\text{act 1}} + V_{\text{act 2}}$, where $V_{\text{act 1}} = \eta_0 + a(T - 29)$ is the voltage drop affected only by the fuel cell internal temperature, while $V_{\text{act 2}} = bT\ln(I)$ is both current and temperature dependent

V_{ohm} is the overall ohmic voltage drop

According to the above voltage output equation, an equivalent circuit is obtained, as in Figure 3.7.

In the above circuit, C is the equivalent capacitor due to the double-layer charging effect.

3.5.2 Simulation Results

To validate the models built in Simulink and PSPICE, real input and output data were measured on the 500 W SR-12 Avista Labs PEM fuel cell. The Chroma 63 112 programmable electronic load was used as a current load.

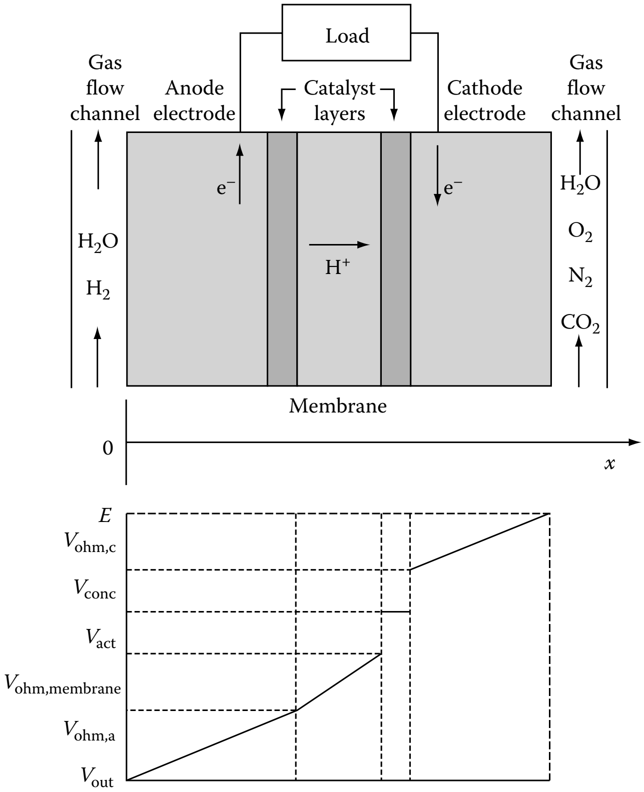

FIGURE 3.6
Schematic diagram of a PEM fuel cell and voltage drops across it.

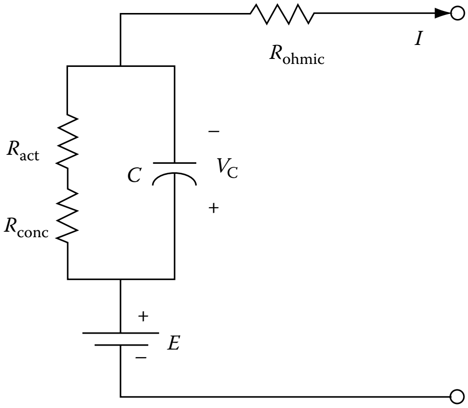

FIGURE 3.7
Equivalent circuit of PEM fuel cell.

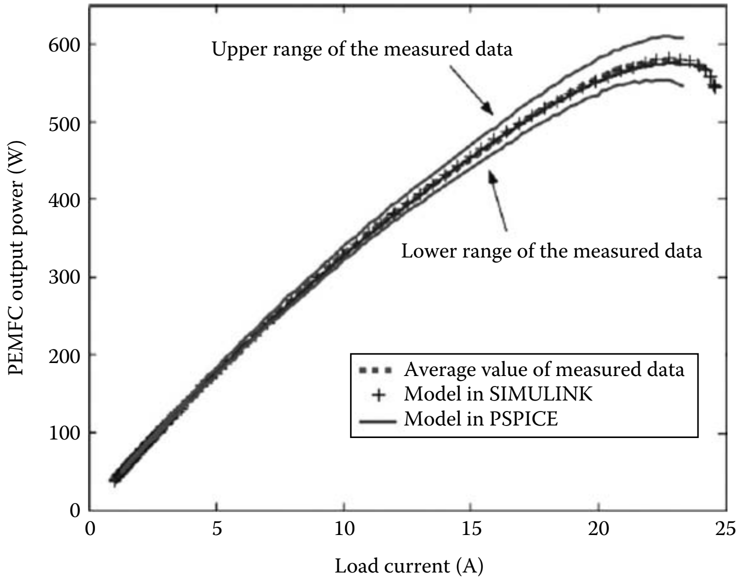

FIGURE 3.8
P–I characteristics of SR-12 and models.

Current signals were measured by LEM LA100-P current transducers; the output voltage was measured by a LEM LV25-P voltage transducer, and the temperature was measured by a k-type thermocouple together with an analog connector. The current, voltage, and temperature data were all acquired by a 12-b Advantech data-acquisition card in a PC (Figures 3.8 and 3.9).

3.6 Linear Model of PEM Fuel Cell Dynamics

We restrict our attention to models of PEMFC "dynamic" behavior and so will not focus on models of their "static" behavior, as described by [26–28]. Of course, the static equations are obtainable as a limiting case from the dynamic equations, and the differences between the modeling performances of those derived static equations can be compared, as in [29]. These steady-state models are able to simulate solely the cells' steady-state behavior, and cannot be used for describing and for model-based feedback control of transient conditions that are important for some specific applications. This is the case, especially, for vehicle applications, given the rapid changes of mechanical and electrical quantities.

Furthermore, our focus is on the fuel cell stack itself, and thus we will not be describing the behavior of the balance of plant (systems), which include the hydrogen and air supplies, the thermal management unit, humidifiers, etc.

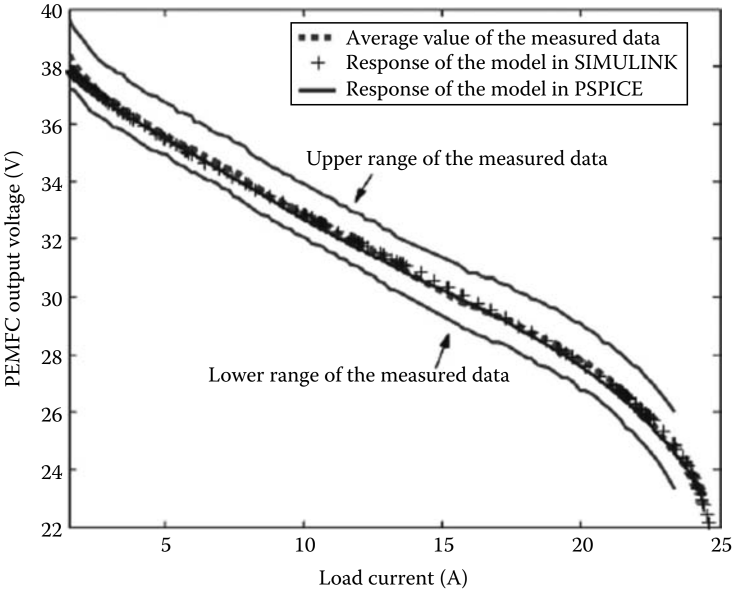

FIGURE 3.9
V–I characteristics of SR-12 and models.

Since the PEMFCs dynamic behavior is inherently nonlinear, any linear model of those dynamics is only an approximation of the original nonlinear equations. The different linear approximating models studied thus far include the following.

3.6.1 Chiu et al. Model

This was one of the earliest proposed linear models of PEMFC dynamic behavior [18]. It is based upon a set of nonlinear dynamic equations as the starting point. In order to linearize these equations, a small-perturbation method was used to model the fuel cell dynamics around particular operating points as an approximating linear system. Such a model is useful for transient response analysis and for control design by linear system techniques subject to the constraint of small perturbations.

The output voltage of the PEMFC is defined as in Larminie and Dicks [30], which gives the stack voltage equation as

$$E = N\left(E_0 + \frac{R*T}{2F}\ln\left\{\frac{P_{H_2}(P_{O_2}/P_{std})^{1/2}}{P_{H_2O_c}}\right\} - L\right) \tag{3.19}$$

where E, N, E_0, T, and L denote the stack output voltage, number of cells in stack, cell open-circuit voltage at standard pressure, operating temperature, and voltage losses, respectively. In addition, P_{H_2}, P_{O_c}, and V_{ohm} $P_{H_2O_c}$ represent the partial pressure of each gas inside the cell. Also R is the universal gas constant, F is Faraday's constant, and P_{std} is the standard pressure. Note the implicit assumption in the equation that all the cells in a stack are identical.

The PEMFCs voltage losses L consist of the following:

- Activation losses—due to the slowness of the reactions taking place in the cell, which can be minimized by maximizing the catalyst contact area for reactions.
- Internal current losses—due to the leakage of electrons passing through the membrane to the cathode side instead of being collected to be utilized, which has a significant effect on the open-circuit voltage.
- Resistive losses—caused by current flow through the resistance of the whole electrical circuit including the membrane and various interconnections, with the biggest contributor being the membrane; effective water management to keep it hydrated reduces its ohmic loss.
- Mass transport or concentration losses—caused by gas concentration changes at the surface of the electrodes.

Hence, the voltage losses L can be expressed as

$$L = (i + i_n)r + a\ln\left(\frac{i + i_n}{i_o}\right) - b\ln\left(1 - \frac{i + i_n}{i_l}\right) \tag{3.20}$$

where

i is the output current density

i_n is the internal current density related to internal current losses

i_o is the exchange current density related to activation losses

i_l is the limiting current density related to concentration losses

r is the area-specific resistance related to resistive losses

a and b are constants

3.6.1.1 Fuel Cell Small-Signal Model

From Equations 3.19 and 3.20 we can see that there are some nonlinear terms in the equations. In order to linearize the cell voltage equation, we use a small-perturbation method to model the fuel cell dynamics around particular operating points as an approximately linear system. Then, we can easily obtain the dynamic response of the cell's output voltage at these operating points for small input variable perturbations.

3.6.1.1.1 State Equations

First, we define the partial pressures of hydrogen, oxygen, and water (on the cathode side) as the three state variables of the system. Since the water management is a factor to affect the performance, we have to use humidifiers on

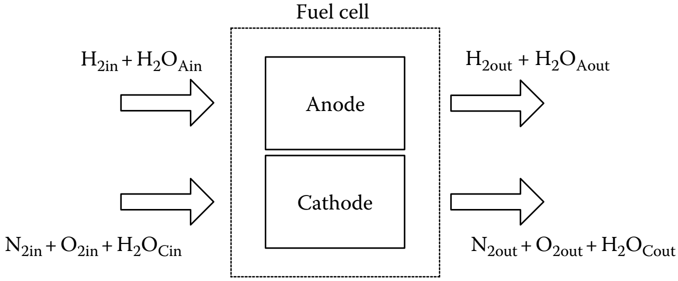

FIGURE 3.10
Illustration of gas flows of the PEMFC.

both the anode and cathode sides to control the humidity inside the cell. The consideration of water on the cathode side is more complicated than on the anode side because it includes not only the water supplied from the humidifiers, but also the by-product of the reaction. Figure 3.10 illustrates the various gas/vapor flows in and out of the cell.

Based on the ideal gas law $P*V = n*R*T$, the partial pressure of each gas is proportional to the amount of the gas in the cell, which is equal to the gas inlet flow rate minus gas consumption and gas outlet flow rate. Thus the state equations are

$$\frac{\mathrm{d}P_{H_2}}{\mathrm{d}t} = \frac{R*T}{V_A}(H_{2in} - H_{2used} - H_{2out}) \tag{3.21}$$

$$\frac{\mathrm{d}P_{O_2}}{\mathrm{d}t} = \frac{R*T}{V_C}(O_{2in} - O_{2used} - O_{2out}) \tag{3.22}$$

$$\frac{\mathrm{d}P_{H_2O_c}}{\mathrm{d}t} = \frac{R*T}{V_C}\left(H_2O_{Cin} + H_2O_{Cproduced} - H_2O_{Cout}\right) \tag{3.23}$$

where H_{2in}, O_{2in}, and H_2O_{Cin} are inlet flow rates of hydrogen, oxygen, and water on the cathode side, respectively; H_{2out}, O_{2out}, and H_2O_{Cout} are outlet flow rates of each gas. Furthermore, H_{2used}, O_{2used}, and $H_2O_{Cproduced}$ represent usage and production of the gases, which are related to output current I by

$$H_{2used} = 2O_{2used} = H_2O_{Cproduced} = 2K_rI = 2K_rA_ci \tag{3.24}$$

where
$K_r = N/4F$
A_c is the cell active area
i is the cell current density

Since we can measure the inlet flow rates and output current, we can define the outlet flow rates by the equations

$$H_{2\text{out}} = (\text{Anode}_{\text{in}} - 2K_r A_c i)F_{H_2} \tag{3.25}$$

$$O_{2\text{out}} = (\text{Cath}_{\text{in}} - K_r A_c i)F_{O_2} \tag{3.26}$$

$$H_2O_{\text{Cout}} = (\text{Cath}_{\text{in}} + 2K_r A_c i)F_{H_2O_c} \tag{3.27}$$

where Anode_{in} and Cath_{in} are the summations of anode inlet flows and cathode inlet flows, respectively, as defined by $\text{Anode}_{\text{in}} = H_{2\text{in}} + H_2O_{\text{Ain}}$ and $\text{Cath}_{\text{in}} = N_{2\text{in}} + O_{2\text{in}} + H_2O_{\text{Cin}}$, while F_{H_2}, F_{O_2}, and $F_{H_2O_c}$ are the pressure fractions of each gas inside the fuel cell. At this juncture, we point out the subtle but significant difference between the proposed model and the original U.S. Department of Energy (DoE) model [31] for defining the pressure fractions.

For the original DoE model,

$$F_{H_2} = \frac{P_{H_2}}{P_{op}} \tag{3.28}$$

$$F_{O_2} = \frac{P_{O_2}}{P_{op}} \tag{3.29}$$

$$F_{H_2O_c} = \frac{P_{H_2O_c}}{P_{op}} \tag{3.30}$$

but for the model proposed by [32],

$$F_{H_2} = \frac{P_{H_2}}{P_{H_2} + P_{H_2O_a}} \tag{3.31}$$

$$F_{O_2} = \frac{P_{O_2}}{P_{N_2} + P_{O_2} + P_{H_2O_c}} \tag{3.32}$$

$$F_{H_2O_c} = \frac{P_{H_2O_c}}{P_{N_2} + P_{O_2} + P_{H_2O_c}} \tag{3.33}$$

In the original DoE model, it is assumed that the cell anode and cathode pressures remain constant and equal at P_{op}, which is the steady-state operating pressure. But because we are using the model to analyze the transient behavior of fuel cells, we have to account for the perturbation of each gas pressure as soon as we change some conditions. Thus, we use the summation of the gas partial pressures in Equations 3.31 through 3.33 instead of assuming a constant operating pressure.

In order to get the state equation matrices, we substitute Equations 3.24 through 3.33 into Equations 3.21 through 3.23 and then differentiate both sides.

For example, we substitute Equations 3.25 and 3.28 into Equation 3.21, which becomes

$$\frac{\mathrm{d}P_{\mathrm{H_2}}}{\mathrm{d}t}=\frac{R*T}{V_{\mathrm{A}}}\left[H_{2\mathrm{in}}-2K_{\mathrm{r}}A_{\mathrm{c}}i-(\mathrm{Anode}_{\mathrm{in}}-2\,\mathrm{K}_{\mathrm{r}}A_{\mathrm{c}}i)\frac{P_{\mathrm{H_2}}}{P_{\mathrm{op}}}\right]$$

Then, performing linearization (first-order approximation) about the given steady-state operating point yields

$$\begin{aligned}\frac{\mathrm{d}\Delta P_{\mathrm{H_2}}}{\mathrm{d}t}=\frac{R*T}{V_{\mathrm{A}}}\Bigg[&-\left(\frac{H_{2\mathrm{in}}}{Y_{\mathrm{H_2}}}-2K_{\mathrm{r}}A_{\mathrm{c}}i\right)\frac{1}{P_{\mathrm{op}}}\Delta P_{\mathrm{H_2}}\\&+\left(1-\frac{P_{\mathrm{H_2}}}{Y_{\mathrm{H_2}}P_{\mathrm{op}}}\right)\Delta H_{2\mathrm{in}}-2K_{\mathrm{r}}A_{\mathrm{c}}\frac{P_{\mathrm{op}}-P_{\mathrm{H_2}}}{P_{\mathrm{op}}}\Delta i\Bigg]\end{aligned}\tag{3.34}$$

where $\Delta P_{\mathrm{H_2}}$, $\Delta \mathrm{H}_{2\mathrm{in}}$, and Δi are the perturbations of each variable, and $Y_{\mathrm{H_2}}$ is the molar fraction of $\mathrm{H_2}$ at the anode inlet defined by $\mathrm{H}_{2\mathrm{in}}/\mathrm{Anode}_{\mathrm{in}}$. Moreover, the state and input variables in the equation need to be replaced by their steady-state values at the chosen operating point.

Following this example, we obtained the remaining equations for the DoE and Chiu et al. models as

(i) Original DoE model

$$\begin{aligned}\frac{\mathrm{d}\Delta P_{\mathrm{O_2}}}{\mathrm{d}t}=\frac{R*T}{V_{\mathrm{C}}}\Bigg[&-(\mathrm{Cath}_{\mathrm{in}}-K_{\mathrm{r}}A_{\mathrm{c}}i)\frac{1}{P_{\mathrm{op}}}\Delta P_{\mathrm{O_2}}-K_{\mathrm{r}}A_{\mathrm{c}}\frac{P_{\mathrm{op}}-P_{\mathrm{O_2}}}{P_{\mathrm{op}}}\Delta i\\&+\left(1-\frac{P_{\mathrm{O_2}}}{(Y_{\mathrm{O_2}}+Y_{\mathrm{H_2O_c}})P_{\mathrm{op}}}\right)\Delta \mathrm{O}_{2\mathrm{in}}-\frac{P_{\mathrm{O_2}}}{(Y_{\mathrm{O_2}}+Y_{\mathrm{H_2O_c}})P_{\mathrm{op}}}\Delta \mathrm{H_2O}_{\mathrm{Cin}}\Bigg]\end{aligned}\tag{3.35}$$

$$\begin{aligned}\frac{\mathrm{d}\Delta P_{\mathrm{H_2O_c}}}{\mathrm{d}t}=\frac{R*T}{V_{\mathrm{C}}}\Bigg[&-(\mathrm{Cath}_{\mathrm{in}}+2K_{\mathrm{r}}A_{\mathrm{c}}i)\frac{1}{P_{\mathrm{op}}}\Delta P_{\mathrm{H_2O_c}}-\frac{P_{\mathrm{H_2O_c}}}{(Y_{\mathrm{O_2}}+Y_{\mathrm{H_2O_c}})P_{\mathrm{op}}}\Delta \mathrm{O}_{2\mathrm{in}}\\&+\left(1-\frac{P_{\mathrm{H_2O_c}}}{(Y_{\mathrm{O_2}}+Y_{\mathrm{H_2O_c}})P_{\mathrm{op}}}\right)\Delta \mathrm{H_2O}_{\mathrm{Cin}}+2K_{\mathrm{r}}A_{\mathrm{c}}\frac{P_{\mathrm{op}}-P_{\mathrm{H_2O_c}}}{P_{\mathrm{op}}}\Delta i\Bigg]\end{aligned}\tag{3.36}$$

where $Y_{\mathrm{O_2}}$ is the mole fraction of $\mathrm{O_2}$ at the cathode inlet defined by $\mathrm{O}_{2\mathrm{in}}/\mathrm{Cath}_{\mathrm{in}}$, and $Y_{\mathrm{H_2O_c}}$ is the mole fraction of water at the cathode inlet defined by $\mathrm{H_2O}_{\mathrm{Cin}}/\mathrm{Cath}_{\mathrm{in}}$; so $\mathrm{Cath}_{\mathrm{in}}=\mathrm{O}_{2\mathrm{in}}+\mathrm{H_2O}_{\mathrm{Cin}}/Y_{\mathrm{O_2}}+Y\mathrm{H_2O_c}$.

(ii) Chiu et al. model

$$\begin{aligned}\frac{\mathrm{d}\Delta P_{\mathrm{H_2}}}{\mathrm{d}t} = \frac{R*T}{V_{\mathrm{A}}}\Bigg[&-(\mathrm{Anode_{in}} - 2K_{\mathrm{r}}A_{\mathrm{c}}i)\frac{P_{\mathrm{H_2O_a}}}{(P_{\mathrm{H_2}}+P_{\mathrm{H_2O_a}})^2}\Delta P_{\mathrm{H_2}}\\ &+\left(1-\frac{P_{\mathrm{H_2}}}{Y_{\mathrm{H_2}}(P_{\mathrm{H_2}}+P_{\mathrm{H_2O_a}})}\right)\Delta H_{2\mathrm{in}} - 2K_{\mathrm{r}}A_{\mathrm{c}}\frac{P_{\mathrm{H_2O_a}}}{P_{\mathrm{H_2}}+P_{\mathrm{H_2O_a}}}\Delta i\Bigg]\end{aligned} \tag{3.37}$$

$$\begin{aligned}\frac{\mathrm{d}\Delta P_{\mathrm{O_2}}}{\mathrm{d}t} = \frac{R*T}{V_{\mathrm{C}}}\Bigg[&-(\mathrm{Cath_{in}} - K_{\mathrm{r}}A_{\mathrm{c}}i)\frac{P_{\mathrm{N_2}}+P_{\mathrm{H_2O_c}}}{P_{\mathrm{cathode}}^{\;2}}\Delta P_{\mathrm{O_2}} + (\mathrm{Cath_{in}} - K_{\mathrm{r}}A_{\mathrm{c}}i)\frac{P_{\mathrm{O_2}}}{P_{\mathrm{cathode}}^{\;2}}\Delta P_{\mathrm{H_2O_c}}\\ &+\left(1-\frac{P_{\mathrm{O_2}}}{(Y_{\mathrm{O_2}}+Y_{\mathrm{H_2O_c}})P_{\mathrm{cathode}}}\right)\Delta \mathrm{O}_{2\mathrm{in}} - \frac{P_{\mathrm{O_2}}}{(Y_{\mathrm{O_2}}+Y_{\mathrm{H_2O_c}})P_{\mathrm{cathode}}}\Delta H_2O_{\mathrm{C\,in}}\\ &-K_r\,A_c\frac{P_{\mathrm{N_2}}+P_{\mathrm{H_2O_c}}}{P_{\mathrm{cathode}}}\Delta i\Bigg]\end{aligned} \tag{3.38}$$

$$\begin{aligned}\frac{\mathrm{d}\Delta P_{\mathrm{H_2O_c}}}{\mathrm{d}t} = \frac{R*T}{V_{\mathrm{C}}}\Bigg[&(\mathrm{Cath_{in}} - 2K_{\mathrm{r}}A_{\mathrm{c}}i)\frac{P_{\mathrm{H_2O_c}}}{P_{\mathrm{cathode}}^{\;2}}\Delta P_{\mathrm{O_2}} - (\mathrm{Cath_{in}} + 2K_{\mathrm{r}}A_{\mathrm{c}}i)\frac{P_{\mathrm{N_2}}+P_{\mathrm{O_2}}}{P_{\mathrm{cathode}}^{\;2}}\Delta P_{\mathrm{H_2O_c}}\\ &-\frac{P_{\mathrm{H_2O_c}}}{(Y_{\mathrm{O_2}}+Y_{\mathrm{H_2O_c}})P_{\mathrm{cathode}}}\Delta \mathrm{O}_{2\mathrm{in}} + \left(1-\frac{P_{\mathrm{H_2O_c}}}{(Y_{\mathrm{O_2}}+Y_{\mathrm{H_2O_c}})P_{\mathrm{cathode}}}\right)\Delta \mathrm{H_2O_{C\,in}}\\ &+2K_{\mathrm{r}}A_{\mathrm{c}}\frac{P_{\mathrm{N_2}}+P_{\mathrm{O_2}}}{P_{\mathrm{cathode}}}\Delta i\Bigg]\end{aligned} \tag{3.39}$$

where

$P_{H_2O_a}$ is the partial pressure of water vapor in anode
P_{N_2} is the partial pressure of the nitrogen in cathode
$P_{\mathrm{cathode}} = P_{N_2} + P_{O_2} + P_{H_2O_c}$

For the fuel cell output, we substitute Equation 3.20 into Equation 3.19 and differentiate both sides. Then we obtain a linear equation for the perturbation of the stack output voltage ΔE in response to the system state changes due to input perturbations at particular operating points as

$$\Delta E = N\left[\frac{R*T}{2F}\frac{1}{P_{\mathrm{H_2}}}\Delta P_{\mathrm{H_2}} + \frac{R*T}{4F}\frac{1}{P_{\mathrm{O_2}}}\Delta P_{\mathrm{O_2}} - \frac{R*T}{2F}\frac{1}{P_{\mathrm{H_2O_c}}}\Delta P_{\mathrm{H_2O_c}} - \left(r + \frac{a}{i+i_{\mathrm{n}}} + \frac{b}{i_{\mathrm{l}} - i - i_{\mathrm{n}}}\right)\Delta i\right] \tag{3.40}$$

3.6.1.1.2 Linear State-Space Model

From Equations 3.34 through 3.40, we can form a linear small-signal state space model of the hydrogen PEMFC described by

$$\Delta = \boldsymbol{A}\,\Delta x + \boldsymbol{B}\,\Delta u$$

$$\Delta y = \boldsymbol{C}\,\Delta x + \boldsymbol{D}\,\Delta u$$

$$\Delta x = [\Delta P_{\mathrm{H_2}} \quad \Delta P_{\mathrm{O_2}} \quad \Delta P_{\mathrm{H_2O_c}}]^{\mathrm{T}}$$

$$\Delta u = [\Delta \mathrm{H}_{2\mathrm{in}} \quad \Delta \mathrm{O}_{2\mathrm{in}} \quad \Delta \mathrm{H_2O}_{\mathrm{Cin}} \quad \Delta i]^{\mathrm{T}}$$

$$\Delta y = \Delta E$$

where the three system states in Δx are the perturbations of the partial pressures of hydrogen, oxygen, and water vapor inside the cells, and the four inputs in Δu are the perturbations of the inlet flow rates of hydrogen, oxygen, water vapor, and also the output current density, while the system output Δy is the perturbation of the fuel cell stack voltage.

For the DoE model, the matrices ***A***, ***B***, ***C***, and ***D*** are

$$\boldsymbol{A} = RT\begin{bmatrix} -(\mathrm{Anode_{in}} - 2K_{\mathrm{r}}A_{\mathrm{c}}i)\dfrac{1}{V_{\mathrm{A}}P_{\mathrm{op}}} & 0 & 0 \\ 0 & -(\mathrm{Cath_{in}} - K_{\mathrm{r}}A_{\mathrm{c}}i)\dfrac{1}{V_{\mathrm{C}}P_{\mathrm{op}}} & 0 \\ 0 & 0 & -(\mathrm{Cath_{in}} + 2K_{\mathrm{r}}A_{\mathrm{c}}i)\dfrac{1}{V_{\mathrm{C}}P_{\mathrm{op}}} \end{bmatrix} \tag{3.41}$$

$$\boldsymbol{B} = RT\begin{bmatrix} \dfrac{1}{V_{\mathrm{A}}} - \dfrac{P_{\mathrm{H_2}}}{V_{\mathrm{A}}Y_{\mathrm{H_2}}P_{\mathrm{op}}} & 0 & 0 & -2K_{\mathrm{r}}A_{\mathrm{c}}\dfrac{P_{\mathrm{op}} - P_{\mathrm{H_2}}}{V_{\mathrm{A}}P_{\mathrm{op}}} \\ 0 & \dfrac{1}{V_{\mathrm{C}}} - \dfrac{P_{\mathrm{O_2}}}{V_{\mathrm{C}}(Y_{\mathrm{O_2}} + Y_{\mathrm{H_2O_c}})P_{\mathrm{op}}} & -\dfrac{P_{\mathrm{O_2}}}{V_{\mathrm{C}}(Y_{\mathrm{O_2}} + Y_{\mathrm{H_2O_c}})P_{\mathrm{op}}} & -K_{\mathrm{r}}A_{\mathrm{c}}\dfrac{P_{\mathrm{op}} - P_{\mathrm{O_2}}}{V_{\mathrm{C}}P_{\mathrm{op}}} \\ 0 & -\dfrac{P_{\mathrm{H_2O_c}}}{V_{\mathrm{C}}(Y_{\mathrm{O_2}} + Y_{\mathrm{H_2O_c}})P_{\mathrm{op}}} & \dfrac{1}{V_{\mathrm{C}}} - \dfrac{P_{\mathrm{H_2O_c}}}{V_{\mathrm{C}}(Y_{\mathrm{O_2}} + Y_{\mathrm{H_2O_c}})P_{\mathrm{op}}} & 2K_{\mathrm{r}}A_{\mathrm{c}}\dfrac{P_{\mathrm{op}} - P_{\mathrm{H_2O_c}}}{V_{\mathrm{C}}P_{\mathrm{op}}} \end{bmatrix}$$

$$\boldsymbol{C} = N\frac{RT}{2F}\begin{bmatrix} \dfrac{1}{P_{\mathrm{H_2}}} & \dfrac{1}{2P_{\mathrm{O_2}}} & -\dfrac{1}{P_{\mathrm{H_2O_c}}} \end{bmatrix}$$

$$\boldsymbol{D} = N\begin{bmatrix} 0 & 0 & 0 & -\left(r + \dfrac{a}{i + i_{\mathrm{n}}} + \dfrac{b}{i_1 - i - i_{\mathrm{n}}}\right) \end{bmatrix}$$

For the Chiu et al. model, the matrices ***A, B, C,*** and ***D*** are

$$\boldsymbol{A} = RT\begin{bmatrix} -(\text{Anode}_{\text{in}} - 2K_\text{r}A_\text{c}i)\dfrac{P_{\text{H}_2\text{O}_\text{a}}}{V_A\left(P_{\text{H}_2} + P_{\text{H}_2\text{O}_\text{a}}\right)^2} & 0 & 0 \\ 0 & -(\text{Cath}_{\text{in}} - K_\text{r}A_\text{c}i)\dfrac{P_{\text{N}_2} + P_{\text{H}_2\text{O}_\text{c}}}{V_\text{C}P_{\text{cathode}}{}^2} & (\text{Cath}_{\text{in}} - K_\text{r}A_\text{c}i)\dfrac{P_{\text{O}_2}}{V_\text{C}P_{\text{cathode}}{}^2} \\ 0 & (\text{Cath}_{\text{in}} + 2K_\text{r}A_\text{c}i)\dfrac{P_{\text{H}_2\text{O}_\text{c}}}{V_\text{C}P_{\text{cathode}}{}^2} & -(\text{Cath}_{\text{in}} + 2K_\text{r}A_\text{c}i)\dfrac{P_{\text{N}_2} + P_{\text{O}_2}}{V_\text{C}P_{\text{cathode}}{}^2} \end{bmatrix}$$

$$\boldsymbol{B}=R*T\begin{bmatrix} \dfrac{1}{V_\text{A}} - \dfrac{P_{\text{H}_2}}{V_\text{A}Y_{\text{H}_2}\left(P_{\text{H}_2} + P_{\text{H}_2\text{O}_\text{a}}\right)} & 0 & 0 & -2K_\text{r}A_\text{c}\dfrac{P_{\text{H}_2\text{O}_\text{a}}}{V_\text{A}\left(P_{\text{H}_2} + P_{\text{H}_2\text{O}_\text{a}}\right)} \\ 0 & \dfrac{1}{V_\text{C}} - \dfrac{P_{\text{O}_2}}{V_\text{C}(Y_{\text{O}_2} + Y_{\text{H}_2\text{O}_\text{c}})P_{\text{cathode}}} & -\dfrac{P_{\text{O}_2}}{V_\text{C}(Y_{\text{O}_2} + Y_{\text{H}_2\text{O}_\text{c}})P_{\text{cathode}}} & -K_rA_\text{c}\dfrac{P_{\text{N}_2} + P_{\text{H}_2\text{O}_\text{c}}}{V_\text{C}P_{\text{cathode}}} \\ 0 & -\dfrac{P_{\text{H}_2\text{O}_\text{c}}}{V_\text{C}(Y_{\text{O}_2} + Y_{\text{H}_2\text{O}_\text{c}})P_{\text{cathode}}} & \dfrac{1}{V_\text{C}} - \dfrac{P_{\text{H}_2\text{O}_\text{c}}}{V_\text{c}(Y_{\text{O}_2} + Y_{\text{H}_2\text{O}_\text{c}})P_{\text{cathode}}} & 2K_\text{r}A_\text{c}\dfrac{P_{\text{N}_2} + P_{\text{O}_2}}{V_\text{C}P_{\text{cathode}}} \end{bmatrix} \tag{3.42}$$

$$\boldsymbol{C} = N\frac{RT}{2F}\begin{bmatrix} \dfrac{1}{P_{\text{H}_2}} & \dfrac{1}{2P_{\text{O}_2}} & -\dfrac{1}{P_{\text{H}_2\text{O}_\text{c}}} \end{bmatrix}$$

$$\boldsymbol{D} = N\begin{bmatrix} 0 & 0 & 0 & -\left(r + \dfrac{a}{i + i_\text{n}} + \dfrac{b}{i_1 - i - i_\text{n}}\right) \end{bmatrix}$$

3.6.1.2 Correspondence of Simulation and Test Results

MATLAB® was used to perform simulations of PEMFC dynamic response based on the small-signal linear state-space models described above. The values of the fuel cell models′ main parameters, corresponding to a PEMFC stack (comprised of four cells) that was tested at the DoE National Energy Technology Lab in Morgantown, WV, are listed in Table 3.4. From auxiliary tests, it was also estimated that the coefficient of Δi in Equation 3.40, yielding the instantaneous voltage change for a unit perturbation in current density, equaled 30.762 μΩ m^2. Furthermore, the state variables′ steady-state values

TABLE 3.4

Fuel Cell Parameters

Cell active area A_c = 136.7 cm^2
Volume of anode V_A = 6.495 cm^3
Volume of cathode V_C = 12.96 cm^3
Number of cells N = 4
Operating pressure (for original DoE model) P_{op} = 101 kPa

at the chosen operating point of 40 A load current were calculated from the input and output steady-state values, and then substituted into the matrices ***A***, ***B***, ***C***, and ***D***.

The following figures compare the responses between the test fuel cell stack, the original DoE model, and the Chiu et al. model. They are of the output voltage response to a step change of the load current with the input flow rates held constant. For the first test case with the results shown in Figure 3.11, the stack was operating at a steady-state condition with $H_{2in} = 3{,}664\,\text{mL/min}$, $N_{2in} + O_{2in} = 11{,}548\,\text{mL/min}$ (assumed to be equally distributed between the four cells), $T = 338.5\,\text{K}$, and load current of 40 A, when the load current was abruptly increased to 50 A at the fifth second. The measured stack output voltage (with data acquisition rate of 0.2 samples/s) shows a rapid decrease followed by a steady state that appears to be a constant accompanied by some "noise." Simulations of this load current perturbation from the 40 A operating value were then performed using the DoE and the Chiu et al. small-signal dynamic models described by Equations 3.41 and 3.42, respectively. As shown in Figure 3.11, the Chiu et al. model predicts the transient response starting from the output voltage operating value of 2.813 V (the voltage drop at the instant of current change being given by $30.762^*\Delta i$) and also the steady-state response of the measured output voltage better than the DoE model.

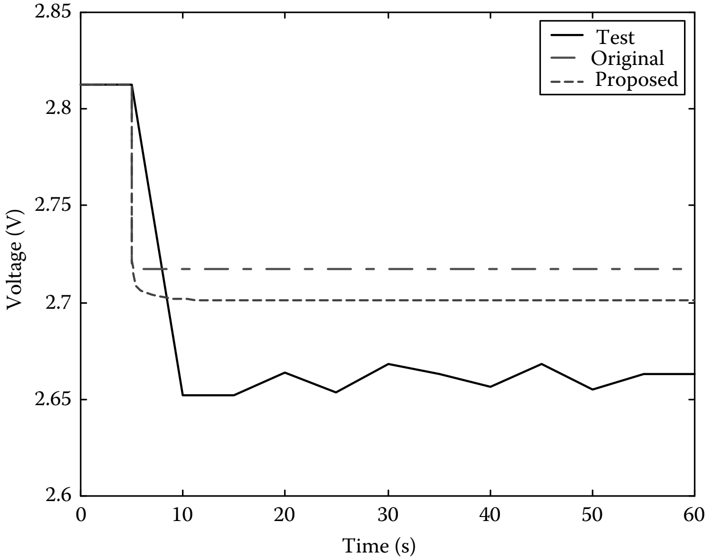

FIGURE 3.11
Comparison of simulated and test results. Operating condition: H_{2in} = 3664 mL/min, N_{2in} + O_{2in} = 11,548 mL/min, T (operating or cell temperature) = 338.5 K; Perturbation: I at 40 A then stepped up to 50 A at fifth second.

Note that the discrepancy in steady-state values is mainly due to the nonlinear functions found in the exact output voltage equation (Equation 3.19), that is, the linear models used are only a fair approximation of the stack's exact behavior due to the fairly large perturbation involved in this test, as to be expected.

For the second test case with the results shown in Figure 3.12, the stack was operating at a steady-state condition with $H_{2in} = 3000$ mL/min, $N_{2in} + O_{2in} = 10{,}000$ mL/min (assumed to be equally distributed between the four cells), $T = 338.5$ K, and load current of 40 A, when the load current was abruptly increased to 42 A at 0.1 s. The measured stack output voltage (with data acquisition rate of 100 samples/s) shows a rapid decrease followed by a gradual increase accompanied by some "noise." Simulations of this (smaller) load current perturbation from the 40 A operating value were then performed again using the DoE and the Chiu et al. small-signal dynamic models. As shown in Figure 3.12, the Chiu et al. model again predicts the transient response and the steady-state response of the output voltage better than the DoE model. However, their difference has been reduced as has the difference between them and the measured response, which was expected because of the smaller perturbation from the chosen operating point.

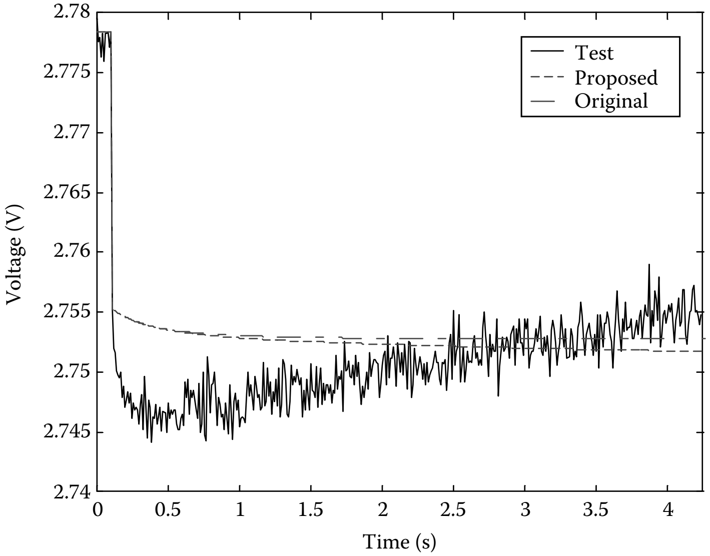

FIGURE 3.12
Another comparison of simulated and test results. Operating condition: H_{2in} = 3000 mL/min, $N_{2in} + O_{2in}$ = 10,000 mL/min, T (operating or cell temperature) = 338.5 K; Perturbation: I at 40 A then stepped up to 42 A at 0.1th second.

Note that the test response showing the output voltage slowly increasing over time after the initial drop was also observed consistently at various operating conditions after a load increase; this was more noticeable for smaller perturbations (when a finer voltage scale was used) than for larger perturbations. But the phenomenon does not appear to represent an undershoot and subsequent recovery as they pertain to a linear dynamic system. It may be that the membrane conductivity changes as its level of hydration increases after a load change leading to the gradual increase in cell voltage. This will need to be addressed in future research.

3.6.2 Page et al. Model

A different approach from [32] was adopted toward obtaining a linear model of PEMFC dynamics in [33]. This approach is based upon acquisition of test data from a single cell or a multiple-cell stack, followed by a least squares estimation of the parameters (component values) for the proposed equivalent circuit model (Figure 3.13). But this is an input–output model where the equivalent circuit internal variables do not actually correspond to actual physical quantities.

3.6.3 University of South Alabama's Model

A partially linearized model of PEMFC dynamics is applied, where the partial pressures of the hydrogen, oxygen, and water in the fuel cell were each modeled as having first-order dynamics [34,35]. But the PEMFC output voltage still depends nonlinearly on these partial pressures in their model.

3.6.4 Other Models

Pasricha and Shaw [36] also adopt a small-signal approach toward modeling the dynamics of PEMFCs, but choose to ignore the dynamics of all variables except temperature, as being the dominant (slowest evolving) system variable. In any case, this approach does not lead to a strictly linear model of PEMFC dynamics.

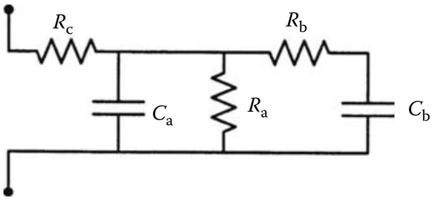

FIGURE 3.13
Page et al. equivalent circuit model.

In [37], the dynamic model presented (essentially amounting to a single equivalent capacitance) was not validated with respect to transient responses from actual PEMFCs, although the steady-state values predicted by the model were compared to the polarization curves of actual PEMFCs.

3.7 Parametric Sensitivity of PEMFC Output Response

There is significant motivation to identify which fuel cell parameters have greater impact on the cell's steady state and transient responses so as to facilitate improved simulations and designs (internal modifications as opposed to external controller designs) of such cells. A sensitivity analysis was described in [38] using a PEMFC electrochemical model and data from a 500 W PEMFC stack manufactured by BCS Technology [39]. The goal was to identify the relative importance of each parameter to the fuel cell model simulation's accuracy. To investigate this, the parametric sensitivity of the fuel cell electrochemical model was calculated using a multiparametric sensitivity analysis approach. To represent the fuel cell stack electrochemical behavior, a first-order (one capacitor) electrical circuit was used to model the fuel cell dynamic behavior. But the main focus was on fuel cell "steady-state" response and evaluating the parameters effects on the stack polarization curve. To evaluate accuracy of the model's "dynamic" response, since the charge double-layer effect is responsible for a delay in the fuel cell voltage change after a change in its current, the parameter used to describe this behavior is an equivalent capacitance, so its effect on the model's step response (representing a real-world current interruption test) was studied. This capacitance does not influence the stack polarization curve, because each point of this curve is obtained after the voltage has reached its steady-state value. As expected, the results of the transient response analysis were similar to that of a basic RC circuit.

The remainder of this section describes the results obtained by [40,41] from a sensitivity analysis performed on an input–output transfer function (which is a linear systems concept) that is derived from the linear small-signal model of PEM fuel cell dynamics previously described in Section 3.6.1 [42]. These provide greater insight into the issue of which physical parameters have the greater impact on fuel cell dynamic response.

The transfer function being investigated represents the fuel cell's output voltage response (system output) to a perturbation of the load current (system input), which is equivalent to its output impedance. It is well known that this impedance has long been studied, usually through AC measurements termed impedance spectroscopy, as a means to characterize a cell's physical processes, electrical properties, and transient response [43–45]. But in this chapter, we describe a slightly different use of PEMFC output impedance.

Sensitivity is defined mathematically as the partial derivative of a function with respect to one of its parameter divided by the ratio of the function to that parameter. Here, it gauges the effect of a unit change in a given fuel cell parameter on the cell's input–output transfer function (for small load current changes). The sensitivity of the PEMFCs dynamic response can be evaluated for the following parameters: cell active area, parameter associated with cell activation losses (slope of Tafel line), parameter associated with cell concentration losses, cell limiting current density (corresponding to concentration losses), cell internal current density (corresponding to internal current losses), cell exchange current density (corresponding to activation losses), number of cells in stack, cell area-specific resistance (corresponding to resistive losses), stack operating temperature (actually an operating condition parameter), cell anode volume, and cell cathode volume. Several plots are presented in the following to illustrate and compare these sensitivity functions.

3.7.1 Fuel Cell Dynamic Response and Sensitivity Analysis

Now note that the fuel cell's output impedance represents its output voltage response to a perturbation of the load current, which is the system transfer function of main practical interest. This impedance function can be obtained from Equation 3.42 as

$$\begin{aligned} G_{\mathrm{Vi}}(s) &= C(sI_3 - A)^{-1}B_4 + D_4 \\ &= \frac{c_{11}b_{14}}{s-a_{11}} + \frac{(c_{13}a_{32} + c_{12}(s-a_{33}))b_{24} + (c_{12}a_{23} + c_{13}(s-a_{22}))b_{34}}{(s-a_{22})(s-a_{33}) - a_{23}a_{32}} + d_4 \end{aligned} \quad (3.43)$$

where

s represents complex frequency

I_3 is the 3 × 3 identity matrix

B_4 and D_4 represent the fourth columns of B and D, respectively

m_{ij} refers to the element in the ith row and jth column of the corresponding matrix M

3.7.1.1 The Sensitivity Function

A sensitivity analysis can be performed on the PEMFC output impedance. This analysis quantitatively characterizes the effect that each particular parameter and operating point variable of the fuel cell have on that impedance. Such information can then be used for prescribing design changes to a fuel cell system in order to improve its dynamic behavior.

The sensitivity function is defined here as the ratio of the partial derivative of the transfer function (Equation 3.43) with respect to a particular parameter to the transfer function divided by that parameter, i.e.,

$$S_\theta = \frac{\partial G_{\mathrm{Vi}}}{\partial \theta} \Bigg/ \frac{G_{\mathrm{Vi}}}{\theta} \quad (3.44)$$

where θ represents any parameter or operating point variable of the fuel cell. It shows how sensitive the system is to different parameters and variables as a function of frequency.

As examples, we present the sensitivity functions for $G_{\mathrm{Vi}}(s)$ with respect to $\mathrm{H}_{2\mathrm{in}}$ and for $G_{\mathrm{Vi}}(s)$ with respect to V_{A}, which were among the simplest of the derived functions, as

$$S_{\mathrm{H}_{2\mathrm{in}}} = \mathrm{Num}_{\mathrm{H}_{2\mathrm{in}}}(s) / \mathrm{Den}_{\mathrm{H}_{2\mathrm{in}}}(s) \tag{3.45}$$

$$\mathrm{Num}_{\mathrm{H}_{2\mathrm{in}}}(s) = 2 * A_{\mathrm{c}} * \mathrm{H}_{2\mathrm{in}} * K_1{}^2 * K_2 * P_{\mathrm{anode}} * P_{\mathrm{H_2O_a}}{}^2 * R * T * Y_{\mathrm{H}_2} \tag{3.46}$$

$$\begin{aligned}
\mathrm{Den}_{\mathrm{H}_{2\mathrm{in}}}(s) = {} & F * P_{\mathrm{H}_2} * (\mathrm{H}_{2\mathrm{in}} * K_1 * P_{\mathrm{H_2O_a}} * I * K_1 * K_2 * P_{\mathrm{H_2O_a}} * Y_{\mathrm{H}_2} + P_{\mathrm{anode}}{}^2 * s * Y_{\mathrm{H}_2})^2 \\
& *[-4 * L(2 * A_{\mathrm{c}} * K_1 * K_2 * P_{\mathrm{anode}} * P_{\mathrm{H_2O_a}} * R * T * Y_{\mathrm{H}_2})/(F * P_{\mathrm{H}_2} \\
& *(\mathrm{H}_{2\mathrm{in}} * K_1 * P_{\mathrm{H_2O_a}} - I * K_1 * K_2 * P_{\mathrm{H_2O_a}} * Y_{\mathrm{H}_2} + P_{\mathrm{anode}}{}^2 * s * Y_{\mathrm{H}_2})) \\
& + (A_{\mathrm{c}} * K_2 * K_3 * P_{\mathrm{cath}} * (P_{\mathrm{H_2O_c}} + P_{\mathrm{N}_2}) * R * T * Y_{\mathrm{O}_2} * (-(P_{\mathrm{cath}}{}^2 * s * Y_{\mathrm{O}_2}) \\
& - K_3 * (P_{\mathrm{N}_2} - P_{\mathrm{O}_2}) * (\mathrm{O}_{2\mathrm{in}} + I * K_2 * Y_{\mathrm{O}_2})))/(F * P_{\mathrm{O}_2} * (2 * P_{\mathrm{cath}}{}^4 * s^2 * Y_{\mathrm{O}_2}{}^2 \\
& + K_3 * P_{\mathrm{cath}}{}^2 * s * Y_{\mathrm{O}_2} * (2 * \mathrm{O}_{2\mathrm{in}} * (P_{\mathrm{H_2O_c}} + 2 * P_{\mathrm{N}_2} + P_{\mathrm{O}_2}) - I * K_2 \\
& *(P_{\mathrm{H_2O_c}} - P_{\mathrm{N}_2} - 2 * P_{\mathrm{O}_2}) * \mathrm{Y}_{\mathrm{O}_2}) + K_3{}^2 * P_{\mathrm{N}_2} * (P_{\mathrm{cath}}) * (2 * \mathrm{O}_{2\mathrm{in}}{}^2 + I * K_2 * \mathrm{O}_{2\mathrm{in}} \\
& * Y_{\mathrm{O}_2} + K_2{}^2 * Y_{\mathrm{O}_2}{}^2))) + (I * A_{\mathrm{c}} * K_2 * K_3 * P_{\mathrm{cath}} * (P_{\mathrm{N}_2} + P_{\mathrm{O}_2}) * R * T * Y_{\mathrm{O}_2} \\
& *(4 * I * P_{\mathrm{cath}}{}^2 * s * Y_{\mathrm{O}_2} + K_3 * (P_{\mathrm{H_2O_c}} + 2 * P_{\mathrm{N}_2}) * (2 * I * \mathrm{O}_{2\mathrm{in}} + K_2 * Y_{\mathrm{O}_2}))) \\
& /(F * P_{\mathrm{H_2O_c}} * (2 * P_{\mathrm{cath}}{}^4 * s^2 * Y_{\mathrm{O}_2}{}^2 + K_3 * P_{\mathrm{cath}}{}^2 * s * Y_{\mathrm{O}_2} * (2 * \mathrm{O}_{2\mathrm{in}} \\
& *(P_{\mathrm{H_2O_c}} + 2 * P_{\mathrm{N}_2} + P_{\mathrm{O}_2}) - I * K_2 * (P_{\mathrm{H_2O_c}} - P_{\mathrm{N}_2} - 2 * P_{\mathrm{O}_2}) * Y_{\mathrm{O}_2}) \\
& + K_3{}^2 * P_{\mathrm{N}_2} * (P_{\mathrm{cath}}) * (2 * \mathrm{O}_{2\mathrm{in}}{}^2 + I * K_2 * \mathrm{O}_{2\mathrm{in}} * Y_{\mathrm{O}_2} + K_2{}^2 * Y_{\mathrm{O}_2}{}^2))))]
\end{aligned} \tag{3.47}$$

and

$$S_{V_{\mathrm{A}}} = \mathrm{Num}_{V_{\mathrm{A}}}(s) / \mathrm{Den}_{V_{\mathrm{A}}}(s) \tag{3.48}$$

$$\mathrm{Num}_{V_{\mathrm{A}}}(s) = -2 * A_{\mathrm{c}} * K^2 * P_{\mathrm{anode}}{}^3 * P_{\mathrm{H_2O_a}} * R^2 * s * T^2 * V_{\mathrm{A}} \tag{3.49}$$

$$\begin{aligned}
\mathrm{Den}_{\mathrm{VA}}(\mathrm{s}) = {} & F * P_{\mathrm{H}_2} * (F_{\mathrm{in}} * P_{\mathrm{H_2O_a}} * R * T - I * K_2 * P_{\mathrm{H_2O_a}} * R * T + P_{\mathrm{anode}}{}^2 * \mathrm{s} * V_{\mathrm{A}})^2 * [4 * L \\
& + (A_{\mathrm{c}} * K_2 * K_3 * P_{\mathrm{cath}} * (P_{\mathrm{H_2O_c}} + P_{\mathrm{N}_2}) * R * (A_{\mathrm{in}} * K_3 * (P_{\mathrm{N}_2} - P_{\mathrm{O}_2}) + \mathrm{I} * K_2 * K_3 \\
& *(P_{\mathrm{N}_2} - P_{\mathrm{O}_2}) + P_{\mathrm{cathode}}{}^2 * s) * T)/(F * P_{\mathrm{O}_2} * (2 * A_{\mathrm{in}}{}^2 * K_3{}^2 * P_{\mathrm{N}_2} * (P_{\mathrm{cath}}) + K_2{}^2 * K_3{}^2 \\
& * P_{\mathrm{N}_2} * (P_{\mathrm{cath}}) - \mathrm{I} * K_2 * K_3 * P_{\mathrm{cath}}{}^2 * (P_{\mathrm{H_2O_c}} - P_{\mathrm{N}_2} - 2 * P_{\mathrm{O}_2}) * s + 2 * P_{\mathrm{cath}}{}^4 * s^2 + A_{\mathrm{in}} \\
& * K_3 * (I * K_2 * K_3 * P_{\mathrm{N}_2} * (P_{\mathrm{cath}}) + 2 * P_{\mathrm{cath}}{}^2 * (P_{\mathrm{H_2O_c}} + 2 * P_{\mathrm{N}_2} + P_{\mathrm{O}_2}) * s))) \\
& + (A_{\mathrm{c}} * K_2 * K_3 * P_{\mathrm{cath}} * (P_{\mathrm{N}_2} + P_{\mathrm{O}_2}) * R * (2 * A_{\mathrm{in}} * K_3 * (P_{\mathrm{H_2O_c}} + 2 * P_{\mathrm{N}_2}) - I * K_2 \\
& * K_3 * (P_{\mathrm{H_2O_c}} + 2 * P_{\mathrm{N}_2}) + 4 * P_{\mathrm{cath}}{}^2 * s) * T)/(F * P_{\mathrm{H_2O_c}} * (2 * \mathrm{A}_{\mathrm{in}}{}^2 * K_3{}^2 * P_{\mathrm{N}_2} * (P_{\mathrm{cath}}) \\
& + K_2{}^2 * K_3{}^2 * P_{\mathrm{N}_2} * (P_{\mathrm{cath}}) - I * K_2 * K_3 * P_{\mathrm{cath}}{}^2 * (P_{\mathrm{H_2O_c}} - P_{\mathrm{N}_2} - 2 * P_{\mathrm{O}_2}) * s \\
& + 2 * P_{\mathrm{cath}}{}^4 * s^2 + A_{\mathrm{in}} * K_3 * (\mathrm{I} * K_2 * K_3 * P_{\mathrm{N}_2} * (P_{\mathrm{cath}}) + 2 * P_{\mathrm{cath}}{}^2 * (P_{\mathrm{H_2O_c}} \\
& + 2 * P_{\mathrm{N}_2} + P_{\mathrm{O}_2}) * \mathrm{s}))) + (2 * A_{\mathrm{c}} * K_2 * P_{\mathrm{anode}} * P_{\mathrm{H_2O_a}} * \mathrm{R}^2 * T^2)/(F * P_{\mathrm{H}_2} * (F_{\mathrm{in}} * P_{\mathrm{H_2O_a}} \\
& * \mathrm{R} * T - \mathrm{I} * K_2 * P_{\mathrm{H_2O_a}} * R * T + P_{\mathrm{anode}}{}^2 * s * V_{\mathrm{A}}))]
\end{aligned}$$

where

$$K_1 = (R*T)/V_A, K_2 = 2*K_r, K_3 = (R*T)/V_c, P_{\mathrm{anode}} = P_{H_2} + P_{H_2O_a},$$
$$P_{\mathrm{cath}} = P_{O_2} + P_{N_2} + P_{H_2O_c}, F_{\mathrm{in}} = H_{2\mathrm{in}}/Y_{H_2}, A_{\mathrm{in}} = O_{2\mathrm{in}}/Y_{O_2}.$$

3.7.1.2 Sensitivity Function Plots

The various sensitivity functions for the PEMFCs output impedance were evaluated using MATLAB and then plotted. Since the calculated sensitivity functions are complicated expressions and the parameters and input variables are many, only a few representative plots are presented here.

The baseline parameter and input values that were used are given in Table 3.5. These correspond to a PEMFC stack at the DoE's National

TABLE 3.5

Fuel Cell Parameter and Input Values for Sensitivity Analysis

Parameter or Input	Description	Value
N	Number of cells in stack	4
T	Stack operating temperature	338.6 K
$H_{2\mathrm{in}}$	Anode inlet flow rate of hydrogen	3,000 mL/min
$\mathrm{Air}_{\mathrm{in}}$	Cathode inlet flow rate of air	10,000 mL/min
I	Cell output current	40.25 A
A_c	Cell active area	136.7 cm^2
i	Cell output current density	2926 A/m^2
V_A	Volume of the cell anode channels	6.495 cm^3
V_C	Volume of the cell cathode channels	12.96 cm^3
L	Sum of cell voltage losses	−36 μV/cell (for a 2.2 A change)
a	Constant associated with cell activation losses (slope of Tafel line)	0.06 V
b	Constant associated with cell concentration losses	0.05 V
i_n	Cell internal current density corresponding to internal current losses	20 A/m^2
i_o	Cell exchange current density corresponding to activation losses	
i_l	Cell limiting current density corresponding to concentration losses	9000 A/m^2
r	Cell area-specific resistance corresponding to resistive losses	3 μΩ m^2
Y_{H_2}	Molar fraction of H_2 at the anode inlet	0.9
Y_{O_2}	Molar fraction of O_2 at the cathode inlet	0.189 (=0.9*0.21)

Energy Technology Laboratory, Morgantown, WV, that underwent testing in 2003. This stack had four cells and ran on air (rather than pure oxygen).

These sensitivity function plots for the DoE NETL model were derived for the anode and cathode volume, cell's active area, output current density, cell's temperature, inlet flow of hydrogen, inlet flow of air, and voltage loss constants, based on the NETL fuel cell's parameter values and one set of operating conditions.

We first present the output impedance sensitivity plot with respect to the fuel cell's anode volume (Figure 3.14). From the plot, we can notice that the overall impedance function is more sensitive to changes in the anode volume at frequencies around 1 rad/s.

We next present the output impedance sensitivity plot with respect to the fuel cell's cathode volume (Figure 3.15). From the plot, we can notice that the overall impedance function is more sensitive to changes in the cathode volume at frequencies around 1 rad/s.

We next present the output impedance sensitivity plot with respect to the fuel cell's active area (Figure 3.16). From the plot, we can notice that the overall impedance function is more sensitive to changes in the cell's active area at low frequencies.

We next present the output impedance sensitivity plot with respect to the fuel cell's output current density (Figure 3.17). From the plot, we can notice that the overall impedance function is more sensitive to changes in the cell's output current density at frequencies above 10 rad/s.

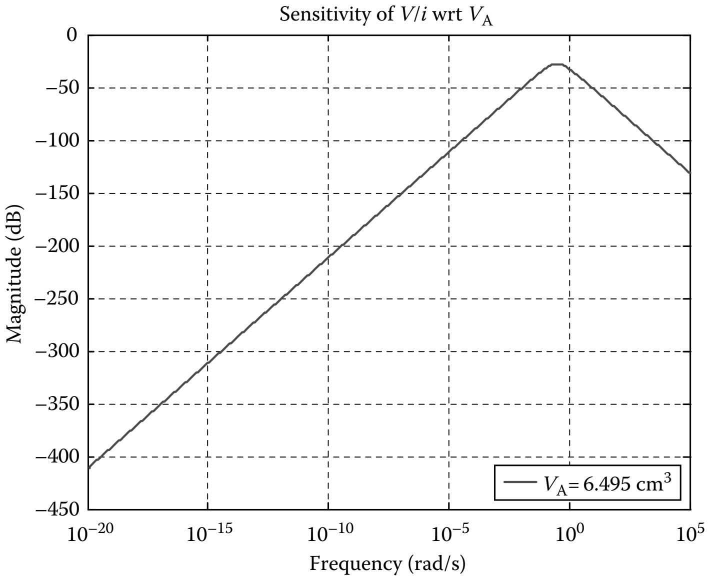

FIGURE 3.14
Output impedance sensitivity plot with respect to cell anode volume.

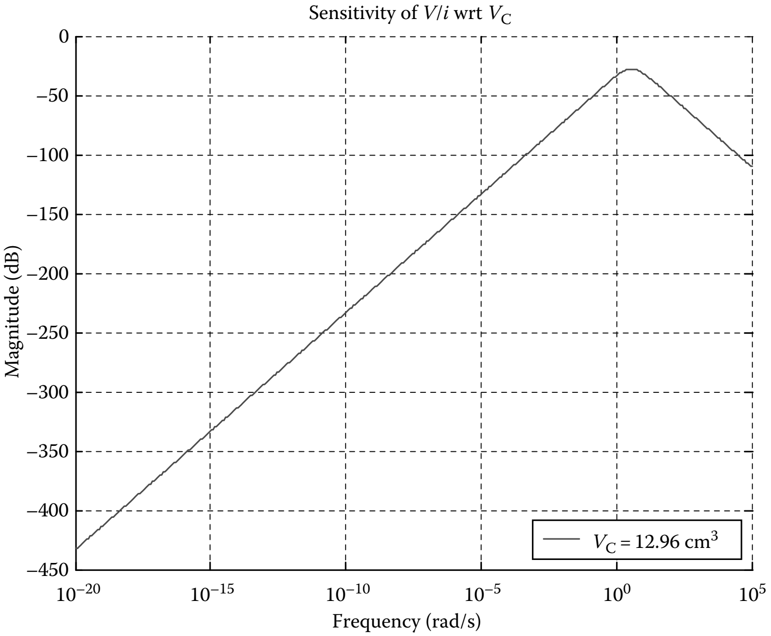

FIGURE 3.15
Output impedance sensitivity plot with respect to cell cathode volume.

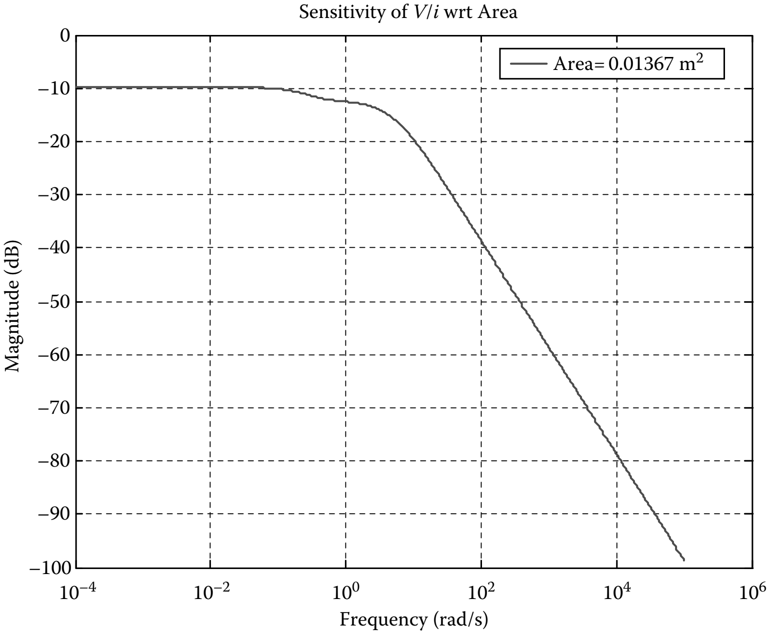

FIGURE 3.16
Output impedance sensitivity plot with respect to cell's active area.

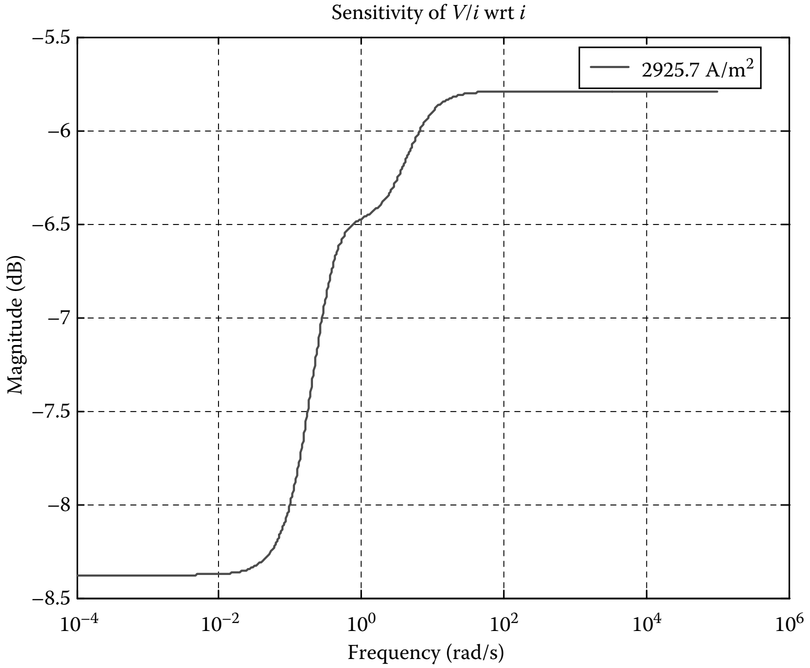

FIGURE 3.17
Output impedance sensitivity plot with respect to output current density.

We next present the output impedance sensitivity plot with respect to the inlet flow rate of hydrogen (Figure 3.18). From the plot, we can notice that the overall impedance function is more sensitive to changes in the flow rate of hydrogen at a frequency range below 10 rad/s.

We next present the output impedance sensitivity plot with respect to the inlet flow rate of air (Figure 3.19). From the plot, we can notice that the overall impedance function is more sensitive to changes in the flow rate of oxygen at frequencies below about 1 rad/s.

We next present the output impedance sensitivity plot with respect to the fuel cell's temperature (Figure 3.20). From the plot, we can notice that the overall impedance function is more sensitive to changes in temperature at frequencies around 0.1 rad/s.

We next present the output impedance sensitivity plot with respect to the voltage losses constant a (Figure 3.21). From the plot, we can notice that the overall impedance function is more sensitive to changes in the voltage losses constant a at frequencies above 10 rad/s.

We next present the output impedance sensitivity plot with respect to the voltage losses constant b (Figure 3.22). From the plot, we can notice that the overall impedance function is more sensitive to changes in the voltage losses constant b at frequencies above 10 rad/s.

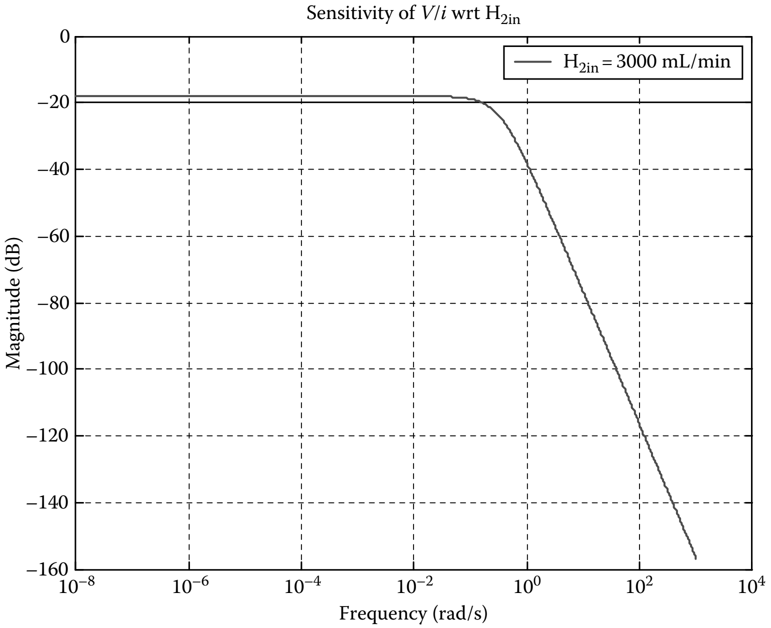

FIGURE 3.18
Output impedance sensitivity plot with respect to the hydrogen inlet flow.

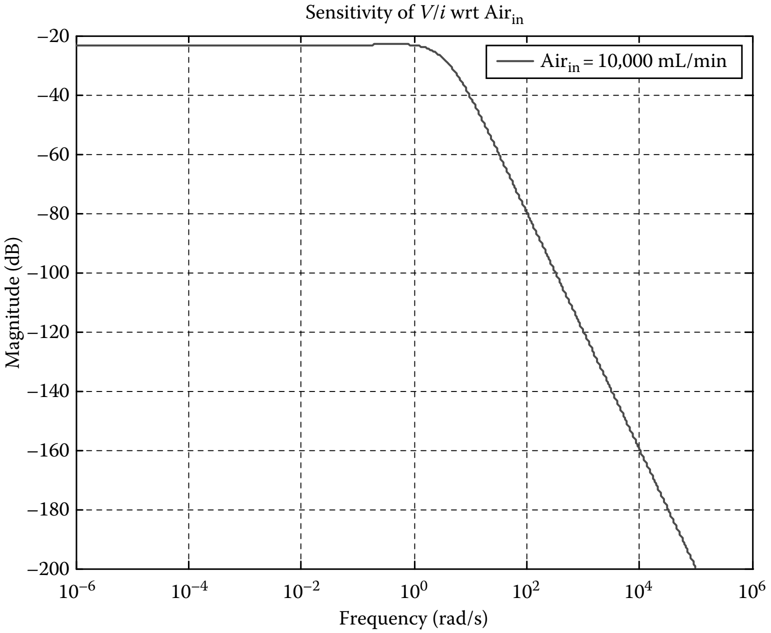

FIGURE 3.19
Output impedance sensitivity plot with respect to the air inlet flow.

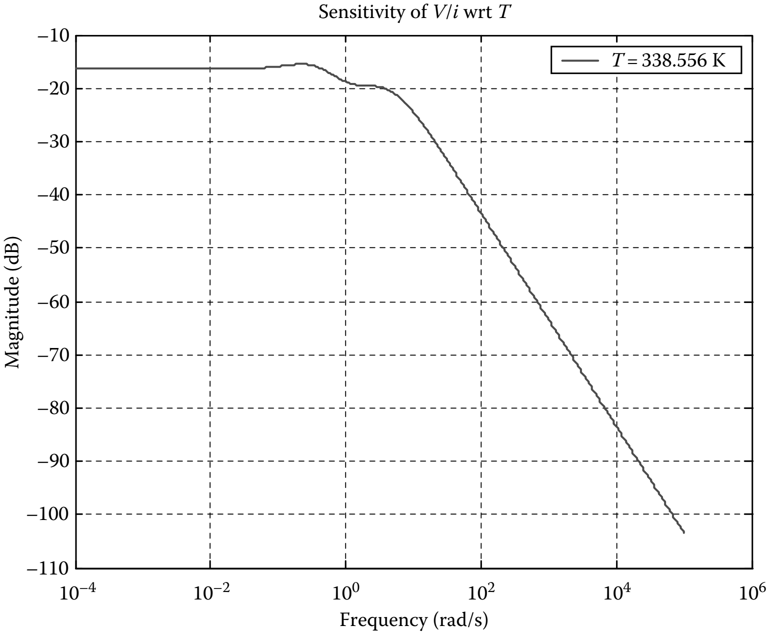

FIGURE 3.20
Output impedance sensitivity plot with respect to the cell temperature.

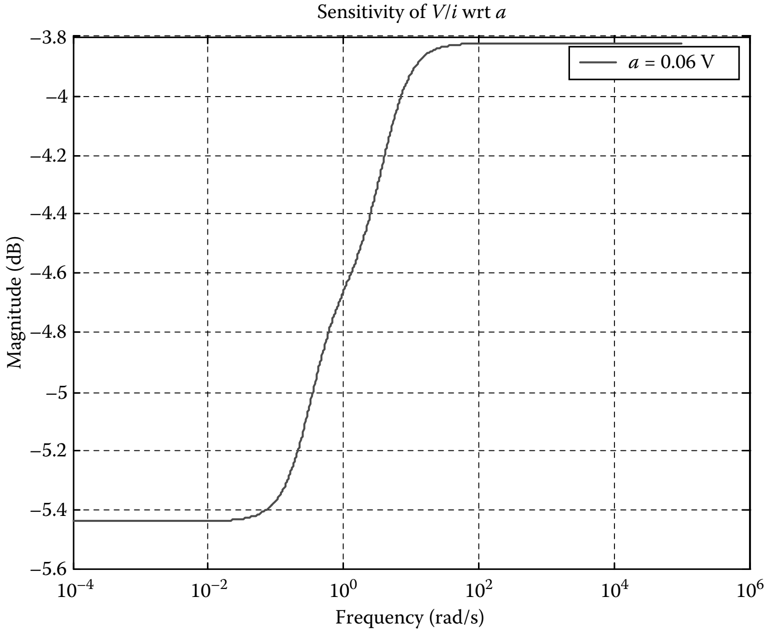

FIGURE 3.21
Output impedance sensitivity plot with respect to the voltage losses constant a.

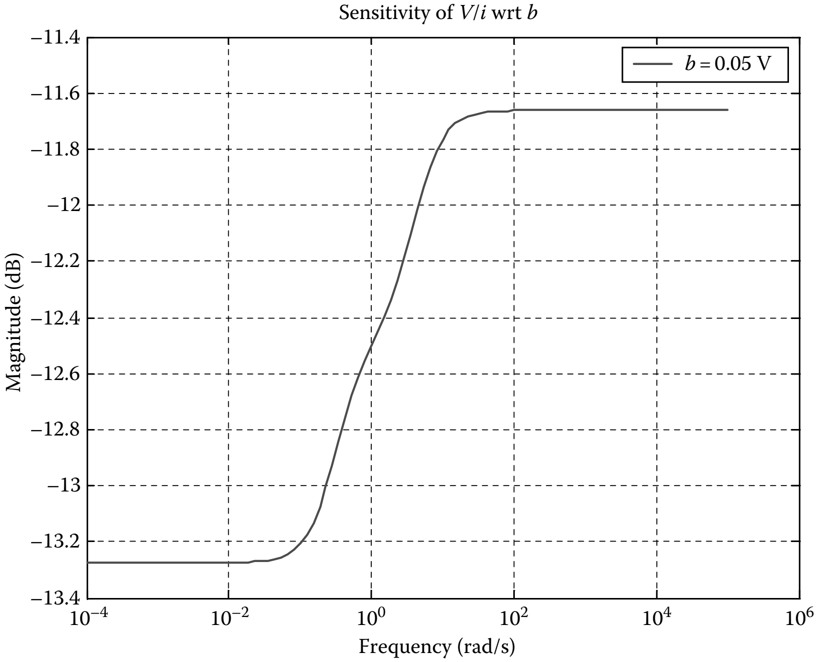

FIGURE 3.22
Output impedance sensitivity plot with respect to the voltage losses constant *b*.

We next present the output impedance sensitivity plot with respect to the internal and fuel crossover current density constant i_n (Figure 3.23). From the plot, we can notice that the overall impedance function is more sensitive to changes in the internal current density at frequencies above 10 rad/s.

We next present the output impedance sensitivity plot with respect to the limiting current density constant i_l (Figure 3.24). From the plot, we can notice that the overall impedance function is more sensitive to changes in the limiting current density at frequencies above 10 rad/s.

We next present the output impedance sensitivity plot with respect to the specific area resistance *r* (Figure 3.25). From the plot, we can notice that the overall impedance function is more sensitive to changes in the specific area resistance *r* at frequencies above 10 rad/s.

Comparing plots of the output impedance sensitivities with respect to the cell's anode volume and to its cathode volume in Figures 3.14 and 3.15, respectively, note that the plots are somewhat similar to each other. However, the magnitude of the function for cathode volume is greater at higher frequencies above 1 rad/s than the corresponding function for anode volume, and vice versa for frequencies below 1 rad/s. Hence, we infer that the high frequency component of the cell's dynamic response is more sensitive to changes in its cathode volume than to its anode volume under typically expected operating conditions. Considering the impedance sensitivity function with respect to

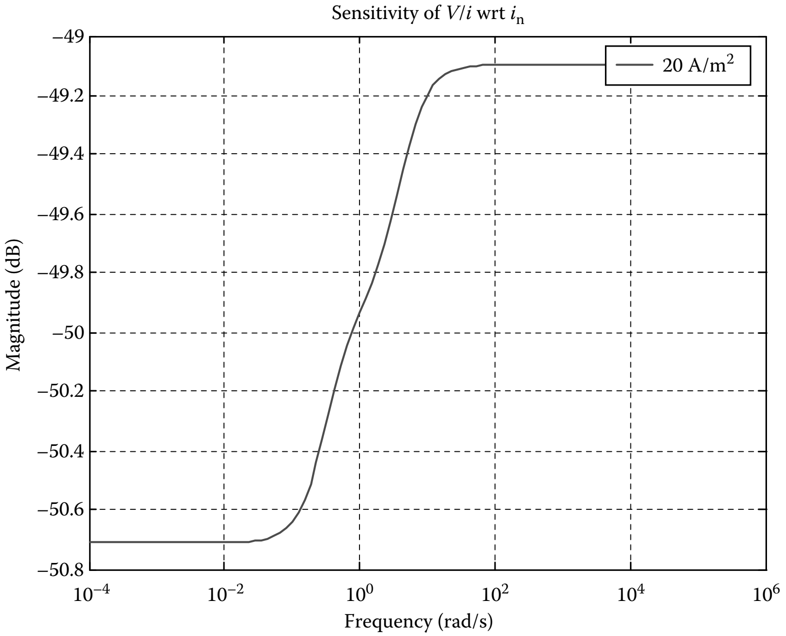

FIGURE 3.23
Output impedance sensitivity plot with respect to the internal current density constant i_n.

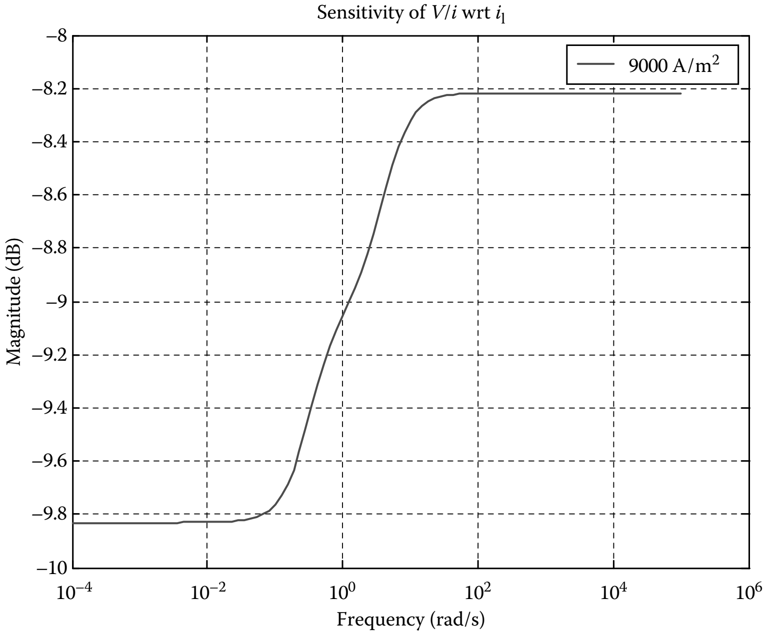

FIGURE 3.24
Output impedance sensitivity plot with respect to the limiting current density constant i_l.

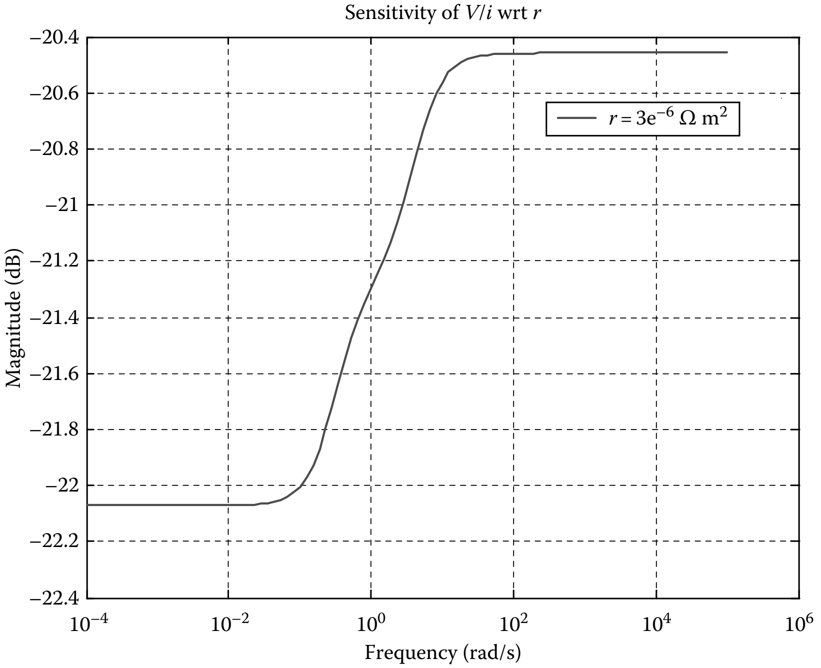

FIGURE 3.25
Output impedance sensitivity plot with respect to the specific area resistance *r*.

the fuel cell active area, as graphed by Figure 3.16, we can see that the overall impedance function is also more sensitive to changes in the fuel cell's active area at lower frequencies than at frequencies higher than about 1 rad/s. The impedance sensitivity functions with respect to the inlet flow rates of hydrogen and air are shown in Figures 3.18 and 3.19. From these plots, we can see that the impedance is more sensitive to changes in the flow rate of hydrogen at a frequency range lower than 0.1 rad/s. On the other hand, for the flow rate of air, the impedance has higher sensitivity at frequencies below about 1 rad/s.

3.7.2 Summary

In this section, we have described the results obtained from a sensitivity analysis performed on an input–output transfer function that is derived from the linear small-signal model of PEMFC dynamics proposed by [42]. These results provide greater insight into the important design issue of which fuel cell parameters have greater impact on the cell's dynamic response. As one example, it was determined that the fuel cell's dynamic response at higher frequencies is typically more sensitive to changes in its cathode volume than to its anode volume, which implies that the former is a more significant parameter for influencing the higher frequency component of transient response than the latter.

References

1. A.M. Borbely and J.G. Kreider, *Distributed Generation: The Power Paradigm for the New Millennium*, New York: CRC Press, 2001.
2. F. Barbir, *PEM Fuel Cells: Theory and Practice*, New York: Elsevier Academic Press, 2005.
3. J. Purkrushpan, A.G. Stefanopoulou, and H. Peng, Control of fuel cell breathing, *IEEE Control Systems Magazine*, April 2004.
4. J. Larminie and A. Dicks, *Fuel Cell Systems Explained*, New York: Wiley, 2002.
5. K. Rajashekrara, Propulsion system strategies for fuel cell vehicles, SAE paper 2000-01-0369, 2000.
6. F. Barbir and T. Gomez, Efficiency and economics of PEM fuel cells, *International Journal of Hydrogen Energy*, 22(10/11), 1027–1037, 1997.
7. J. Purkrushpan and H. Peng, *Control of Fuel Cell Power Systems: Principles, Modeling, Analysis and Feedback Design*, Germany: Springer, London 2004.
8. J. Purkrushpan, A.G. Stefanopoulou, and H. Peng, Modeling and control for PEM fuel cell stack systems, *Proceedings of American Control Conference*, Anchorage, AK, 2002, pp. 3117–3122.
9. J.C. Amphlett, R.M. Baumert, R.F. Mann, B.A. Peppy, P.R. Roberge, and A. Rodrigues, Parametric modeling of the performance of a 5-kW proton exchange membrane fuel cell stack, *Journal of Power Sources*, 49, 349–356, 1994.
10. X.D. Xue, K.W.E. Cheng, and D. Sutanto, Unified mathematical modeling of steady-state and dynamic voltage–current characteristics for PEM fuel cells, *Electrochimica Acta*, 52(3), 1135–1144, 2006.
11. M.J. Khan and M.T. Labal, Modeling and analysis of electro chemical, thermal, and reactant flow dynamics for a PEM fuel cell system, *Fuel cells*, 4, 463–475, 2005.
12. Ballard Power System, Inc., Canada, at http://www.ballard.com.
13. M.Y. El-Sharkh, A. Rahman, M.S. Alamm, A.A. Sakla, P.C. Byrne, and T. Thomas, Analysis of active and reactive power control of a stand-alone PEM fuel cell power plant, *IEEE Transactions on Power Delivery*, 19(4), 2022–2028, 2004.
14. J.J.E. Slotine and W. Li, *Applied Nonlinear Control*, Englewood Cliffs, NJ: Prentice Hall, 1991.
15. Woonki Na and Bei Gou, Feedback linearization based nonlinear control for PEM fuel cells, *IEEE Transactions on Energy Conversion*, 23(1), 179–190, 2008.
16. J. Sun and V. Kolmannovsky, Load governor for fuel cell oxygen starvation protection: A robust nonlinear reference governor approach, *IEEE Transactions on Control Systems Technology*, 3(6), 911–913, 2005.
17. S. Basu, M.W. Renfro, and B.M. Cetegen, Spatially resolved optical measurements of water partial pressure and temperature in a PEM fuel cell under dynamic operating conditions, *Journal of Power Sources*, 162(1), 286–293, 2006.
18. L.Y. Chiu, B. Diong, and R.S. Gemmen, An improved small-signal model of the dynamic behavior of PEM fuel cells, *IEEE Transactions on Industry Applications*, 40(4), 970–977, 2004.

19. M.J. Khan and M.T. Labal, Dynamic modeling and simulation of a fuel cell generator, *Fuel Cells*, 1, 97–104, 2005.
20. R.E. Sonntag, C. Borgnakke, and G.J.V. Wylen, *Fundamentals of Thermodynamics*, New York: Wiley, 1998.
21. M.P. Nielsen, P. Pedersen, C.A. Andesen, M.O. Christen, and A.R. Korgaard, Design and control of fuel cell system for transport application, Project Report, Aalborg University, 2002.
22. C. Wang, M.H. Nehrir, and S.R. Shaw, Dynamic models and model validation for PEM fuel cells using electrical circuits, *IEEE Transactions on Energy Conversion*, 20(2), 442–451, 2005.
23. J.M. Correa, F.A. Farret, and L.N. Canha, An analysis of the dynamic performance of proton exchange membrane fuel cells using an electrochemical model, *IECON'01, The 27th Annual Conference of the IEEE Industrial Electronics Society*, Vol. 1, pp. 141–146, 2001.
24. C.J. Hatiziadoniu, A.A. Lobo, F. Pourboghrat, and M. Daneshdoot, A simplified dynamic model of grid connected fuel-cell generators, *IEEE Transactions on Power Delivery*, 17(2), 467–473, 2002.
25. A. Sakhare, A. Davari, and A. Feliachi, Fuzzy logic control of fuel cell for stand-alone and grid connection, *Journal of Power Sources*, 135(1–2), 165–176, 2004.
26. J.C. Amphlett, R.M. Baumert, R.F. Mann, B.A. Peppley, and P.R. Roberge, Performance modeling of the Ballard Mark IV solid polymer electrolyte fuel cell, 1. Mechanistic model development, *Journal of the Electrochemical Society*, 142(1), 1–8, 1995.
27. J.C. Amphlett, E.K. De Oliveira, R.F. Mann, P.R. Roberge, and A. Rodrigues, Dynamic interaction of a proton exchange membrane fuel cell and a lead-acid battery, *Journal of Power Sources*, 65, 173–178, 1997.
28. F. Grasser and A. Rufer, A fully analytical PEM fuel cell system model for control applications, *IEEE Transactions on Industry Applications*, 43(6), 1499–1506, 2007.
29. S. Pasricha, M. Keppler, S.R. Shaw, and M.H. Nehrir, Comparison and identification of static electrical terminal fuel cell models, *IEEE Transaction on Energy Conversion*, 22(3), 746–754, 2007.
30. J. Larminie and A. Dicks, *Fuel Cell Systems Explained*, New York: John Wiley & Sons, 2000.
31. R.S. Gemmen, Analysis for the effect of inverter ripple current on fuel cell operating condition, *Journal of Fluids Engineering*, 125(3), 576–585, 2003.
32. S.C. Page, A.H. Anbuky, S.P. Krumdieck, and J. Brouwer, Test method and equivalent circuit modeling of a PEM fuel cell in a passive state, *IEEE Transaction on Energy Conversion*, 22(3), 764–773, 2007.
33. M.Y. El-Sharkh, A. Rahman, M.S. Alam, A.A. Sakla, P.C. Byrne, and T. Thomas, Analysis of active and reactive power control of a stand-alone PEM fuel cell power plant, *IEEE Transactions on Power Systems*, 19(4), 2022–2028, 2004.
34. M. Uzunoglu and M.S. Alam, Dynamic modeling, design, and simulation of a combined PEM fuel cell and ultracapacitor system for stand-alone residential applications, *IEEE Transaction on Energy Conversion*, 21(3), 767–775, 2006.
35. S. Pasricha and S.R. Shaw, A dynamic PEM fuel cell model, *IEEE Transaction on Energy Conversion*, 21(2), 484–490, 2006.
36. J.M. Correa, F.A. Farret, L.N. Canha, and M.G. Simoes, An electrochemical-based fuel-cell model suitable for electrical engineering automation approach, *IEEE Transactions on Industrial Electronics*, 51(5), 1103–1112, 2004.

37. J.M. Correa, F.A. Farret, V.A. Popov, and M.G. Simoes, Sensitivity analysis of the modeling parameters used in simulation of proton exchange membrane fuel cells, *IEEE Transactions on Energy Conversion*, 20(1), 211–218, 2005.
38. BCS Technology Co., *Data Sheet for a 500 W FC Stack*, 2001.
39. L. Lorandi, E. Hernandez, and B. Diong, Parametric sensitivity analysis of fuel cell dynamic response, *SAE Transactions Journal of Aerospace*, 113, 2024–2032, 2004.
40. E. Hernandez, Parametric sensitivity analysis and circuit modeling of PEM fuel cell dynamics, MS thesis, University of Texas at El Paso, December 2004.
41. R.S. Gemmen, E. Liese, J.G. Rivera, and J. Brouwer, Development of dynamic modeling tools for solid oxide and molten carbonate hybrid fuel cell gas turbine systems, *Proceedings of the ASME/IGTI Turbo Expo*, 2000.
42. K. Sedghisigarchi and A. Feliachi, Control of grid-connected fuel cell power plant for transient stability enhancement, *Proceedings of the IEEE Power Engineering Society Winter Meeting*, pp. 383–388, 2002.
43. E. Liese, and R.S. Gemmen, Dynamic modeling results of a 1 MW molten carbonate fuel cell/gas turbine power system, *Proceedings of the ASME/IGTI Turbo Expo*, pp. 341–349, 2002.

4

Linear and Nonlinear Control Designs for Fuel Cells

4.1 Introduction

Fuel cell-based power systems present a wide range of challenging problems for control and systems integration. Considerable research and development efforts have been devoted to fuel cell operation and systems, in particular, in the area of PEMFCs for mobile and stationary applications. Control plays a critical role in the fuel cell operation and systems. The objective of a control system is to modify the natural response of the fuel cell electrochemical reactor and maintain desired operation in case of uncertainties and disturbances. Moreover, the control system attempts to diagnose abnormal operation, monitors heath of stack, and adapts operation to address material and electrode degradation. A wide range of operating conditions that the fuel cell system needs to operate also makes the controls challenging.

Due to the complexity of the fuel cell system, control strategies are applied in various aspects, including compressor motor control, pressure control, humidity control, temperature control, ratio control, control of output voltage and current, etc. Both linear and nonlinear control approaches have been developed for fuel cell systems in the literature. This chapter introduces the linear and nonlinear control designs for PEMFCs, and the modeling of fuel cells is also covered accordingly.

4.2 Linear Control Design for Fuel Cells

A robust control strategy is critical to satisfy high power density demand in PEMFCs. In this section, we introduce a linear ratio control strategy based on the distributed parameter model of fuel cells that includes the effect of spatial variations.

4.2.1 Distributed Parameter Model of Fuel Cells

Figure 4.1 shows the distributed parameter model of fuel cells proposed in [1]. In the model, a fuel cell is modeled along its channel. The model considers

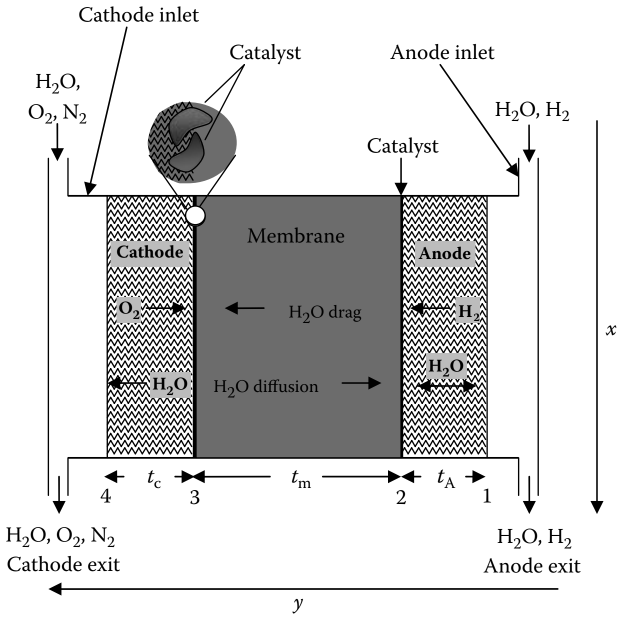

FIGURE 4.1
Schematic diagram of fuel cell channel.

the heat transfer between the solid and the two gas channels, and between the solid and the cooling water. The water content is also modeled to calculate the condensation and evaporation, water drag through the membrane, and water generation at the cathode. The energy balance on the solid is modeled dynamically, but all the other equations are assumed to be at quasi-steady state for a given solid temperature profile.

Based on the work in [1,2], the energy balance equation is given by [3]:

$$\rho_s C_{p,s}\frac{\partial T_s}{\partial t} = k_s\frac{\partial^2 T_s}{\partial x^2} + \frac{U_g A_g}{f}(T_a + T_C - 2T_s) + \frac{U_W A_{cool}}{f}(T_{cool} - T_s) - \frac{e}{f}\left(\frac{\Delta H}{2F} + V_{cell}\right)$$
$$+\frac{1}{f}\Delta H_{vap}(T_s)\left(\frac{dM^1{}_{W,a}(x)}{dx} + \frac{dM^1{}_{W,C}(x)}{dx}\right)$$

with the following boundary conditions:

$$k_s \left.\frac{\partial T_s}{\partial x}\right|_{x=0} = U_C(T_s - T_{inf})$$

$$k_s \left.\frac{\partial T_s}{\partial x}\right|_{x=L} = -U_C(T_s - T_{inf})$$

The V_{cell} is given as

$$V_{\text{cell}} = V_{\text{OC}}^0 + \frac{RT_s}{nF}\ln\left(\frac{P_{\text{H}_2}P_{\text{O}_2}^{0.5}}{P_{\text{H}_2\text{O}}}\right) - \frac{RT_s}{F}\ln\left(\frac{I(x)}{i_0 P_{\text{O}_2}(x)}\right) - \frac{I(x)t_{\text{m}}}{\sigma_{\text{m}}(x)}$$

4.2.2 Linear Control Design and Simulations for Fuel Cells

4.2.2.1 Power Control Loop

For the power control loop, the average power density in the PEMFC is controlled by manipulating the inlet molar flow rate of hydrogen and the inlet molar flow rate of oxygen. Here we only cover the control using the inlet molar flow rate of hydrogen [3].

The control scheme is given in Figure 4.2. The controller for the hydrogen flow to the power density loop is designed by using the internal model control (IMC)-based proportional integral derivative (PID) method. The resulting controller is of PI form. The performance of the PI controller along with the manipulated variable actions are shown in Figure 4.3. The settling time for this control strategy is approximately 275 s. This large settling time could be attributed to severe nonlinearities present in the PEMFC.

4.2.2.2 Power and Solid Temperature Control Loop

The rate of reaction has to be kept at a high value to achieve maximum power density. However, the high rate of reaction increases the heat produced from the reaction, which finally increases the solid temperature of the PEMFC. Furthermore, increasing the solid temperature beyond a specific value will adversely affect the conductivity of the membrane and also the catalyst activity, which in turn affects the rate of reaction. Therefore, it is necessary to control the average solid temperature within specified limits.

The linear control design is given in Figure 4.4. To control the average solid temperature, the steady-state relative gain array (RGA) analysis recommends that the inlet coolant flow rate be the manipulated variable. The

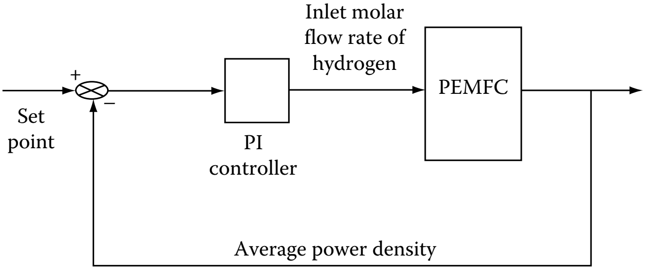

FIGURE 4.2
Schematic of power control loop using the inlet molar flow rate of hydrogen as the manipulated variable.

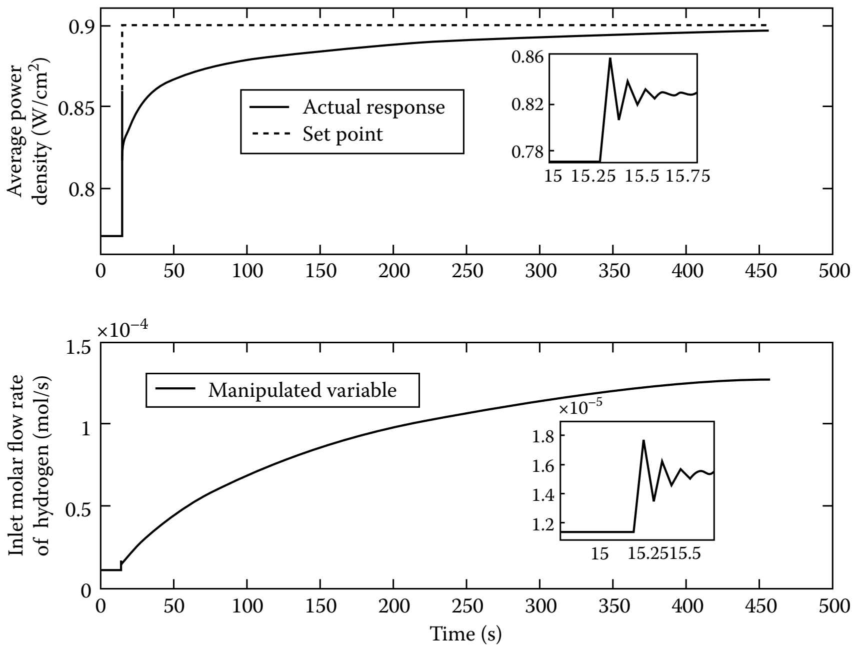

FIGURE 4.3
Performance of the power control loop using the inlet molar flow rate of hydrogen as the manipulated variable.

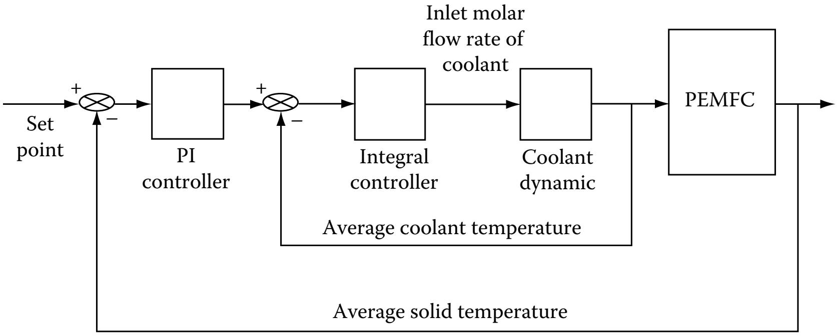

FIGURE 4.4
Schematic of the cascade control loop using the inlet molar flow rate of coolant as the manipulated variable.

average solid temperature is controlled by using a cascade control loop with the inlet molar flow rate of coolant as the manipulated variable.

This strategy in Figure 4.4 provides an additional advantage of disturbance rejection. The performance of the cascade control design is shown in Figure 4.5. Further simulation results can be found in [3].

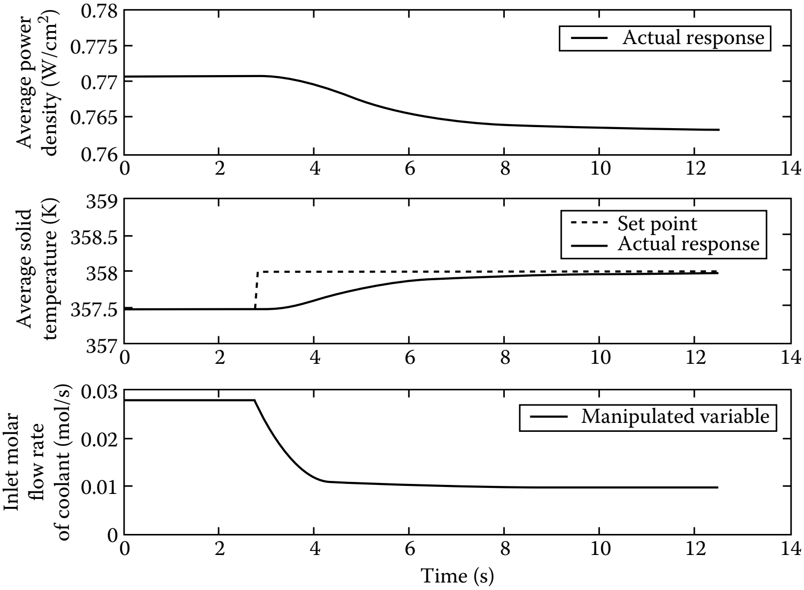

FIGURE 4.5
Performance of cascade control using the inlet molar flow rate of coolant as the manipulated variable.

4.2.2.3 MIMO Control Strategy

The PEMFCs can also be considered a multi-input and multi-output (MIMO) system where the average power density and average solid temperature are the two controlled outputs. The MIMO control design is shown in Figure 4.6.

Figure 4.7 shows that the response of the MIMO controller is faster than that of the single-input and single-output (SISO) controller. The settling time for the MIMO controller is approximately 90 s, while the settling time for the SISO controller is 275 s. In addition, the MIMO control strategy also avoids the unwanted effect of a rise in temperature.

A simulation using air instead of oxygen at the cathode was taken and its performance is shown in Figure 4.8. The results demonstrate that the MIMO control strategy can provide satisfactory control performance for hydrogen–air fuel cells.

4.2.2.4 Ratio Control

A ratio control strategy was also implemented in [3] to avoid the problem of oxygen starvation and to satisfy the maximum power density demand. In the ratio control design, the inlet molar flow rate of oxygen is used as a dependent manipulated variable and changed in a constant ratio with respect to the inlet molar flow rate of hydrogen.

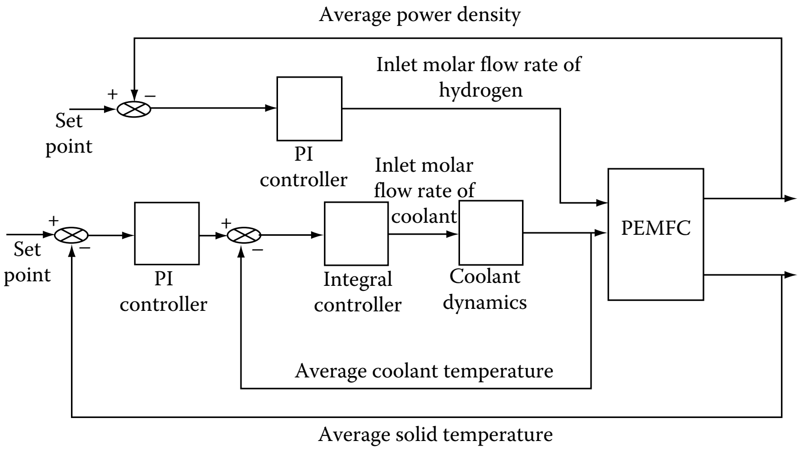

FIGURE 4.6
MIMO control schematic.

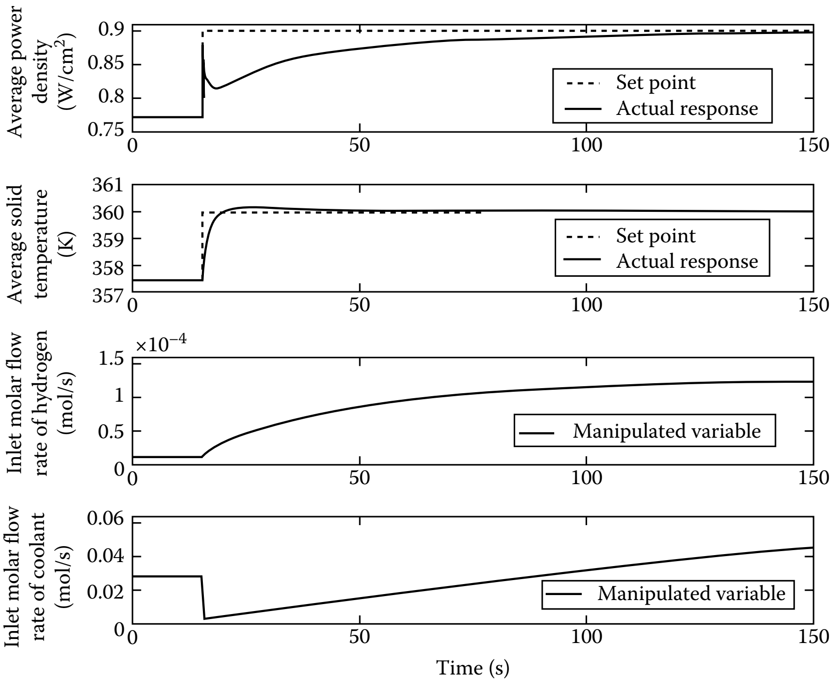

FIGURE 4.7
Performance of the proposed MIMO control strategy in response to changes in the set points for the average power density and the average solid temperature.

The ratio control design is given in Figure 4.9. In this strategy, the measured manipulated variable is the inlet molar flow rate of hydrogen. The inlet flow rate of oxygen is changed in proportion to the inlet flow rate of hydrogen.

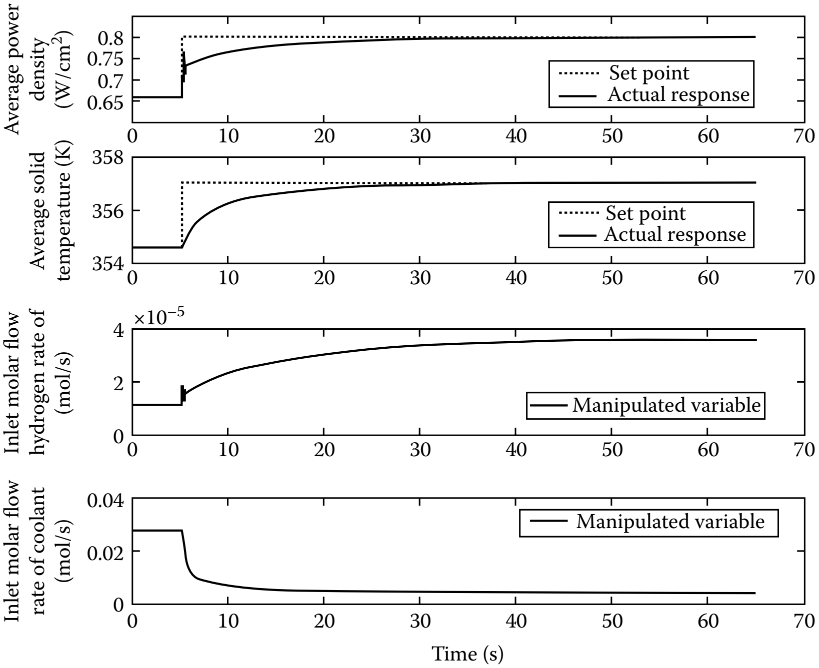

FIGURE 4.8
Performance of the proposed MIMO control strategy in response to changes in the set points for the average power density and the average solid temperature using air at the cathode.

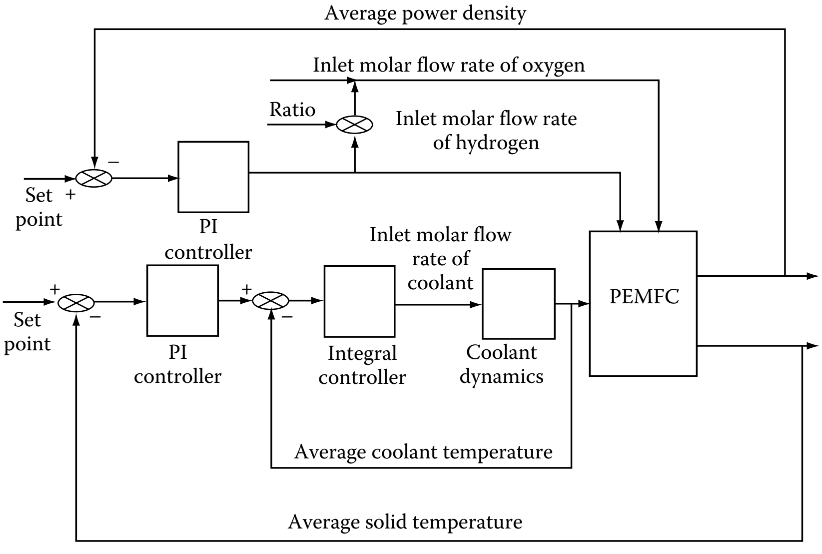

FIGURE 4.9
Schematic for ratio control along with cascade control for temperature.

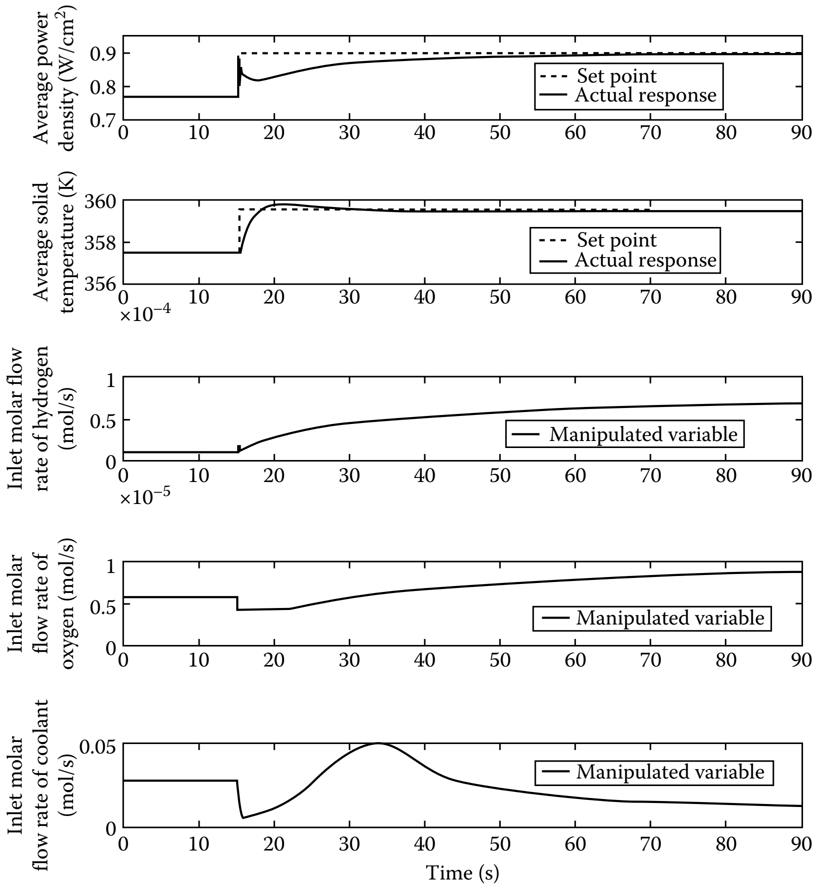

FIGURE 4.10

Performance of the multivariable controller with ratio control for oxygen in response to changes in the set points of the average power density and the average solid temperature.

Figure 4.10 shows the performance of the ratio control strategy. To improve the performance of ratio control, the average solid temperature is also controlled using the previously described cascade control strategy. Simulation results show that the response of this ratio controller is faster than the MIMO strategy using only hydrogen as the manipulated variable. The ratio controller is faster because, on loop closure, the initial input molar flow rate of oxygen is lower than that of the base case flow rate. Figure 4.11 shows that in the proposed ratio control strategy, the problem of oxygen starvation has been circumvented due to an increase in the input molar flow rate of oxygen.

In summary, simulation results show that the ratio control strategy provides a faster response than a MIMO control strategy. This ratio control

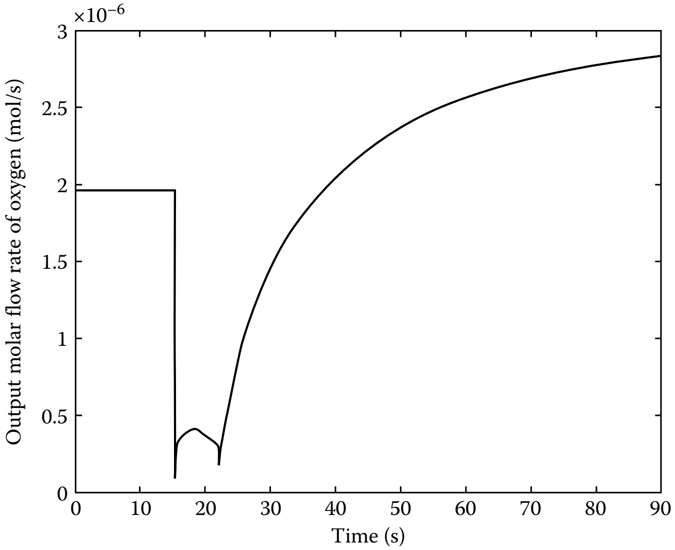

FIGURE 4.11
Output flow rate of oxygen from the PEMFC with ratio control, corresponding to the results shown in Figure 4.27.

strategy is able to circumvent the problem of oxygen starvation, and the increase in average solid temperature is small as compared to the MIMO control strategy.

Methekar et al. [3] state that a ratio control strategy is able to overcome the problem of oxygen starvation; however, the performance of the linear controllers is slow due to the presence of nonlinearities in the dynamic response of the PEMFC. Hence, a nonlinear controller is essential and necessary for effective control of the PEMFC over a wide range of power densities.

4.3 Nonlinear Control Design for Fuel Cells

An MIMO dynamic nonlinear model of PEMFC is derived in this section, and it is then used to design a nonlinear controller by using feedback linearization in order to minimize the difference ΔP between the hydrogen and oxygen partial pressures. The main purpose of keeping ΔP in a certain small range is to protect the membrane from damage and therefore prolong the fuel cell stack life [4,5]. In addition, the pressures have a bigger impact on the performance of the fuel cells than other parameters [4,5]. Because the fuel cell voltage is a function of the pressures, each pressure needs to be appropriately controlled to avoid a detrimental degradation of the fuel cell voltage. To achieve this goal, it is necessary to minimize the pressure deviation between the anode and the cathode by using precise actuators like an accurate valve controller. Normally, the optimal pressure controller consists of a pressure sensor and a solenoid flow-control valve. In this book, we mainly focus on developing a pressure control algorithm for the whole fuel cell system instead of designing the pressure sensors and flow controllers inside the fuel cell. Furthermore, the fuel cell voltage is not considered a control output because of the characteristics of the *V–I* polarization curve, which makes it difficult to perform voltage control in a short period of time and, normally, the fuel cell system needs a secondary energy storage for a short period of time control. Therefore, only the partial pressures of hydrogen and oxygen are chosen as the outputs. The stack current is considered a disturbance to the system instead of an external input [5].

Consider the following MIMO nonlinear system with a disturbance:

$$\begin{gathered}\dot{X} = f(X) + \sum_{i=1}^{m} g_i(X)u_i + p(X)d, \quad i = 1, 2, \ldots, m \\ y_1 = h_1(X) \\ \vdots \\ y_m = h_m(X)\end{gathered} \tag{4.1}$$

where

$X \subset R^n$ is the state vector

$U = [\mathrm{u}_1, \mathrm{u}_2, \ldots, \mathrm{u}_\mathrm{m}] \subset R^m$ is the input or control vector

$y \subset R^P$ is the output vector

$f(x)$ and $g(x)$, $i = 1, 2, \ldots, m$, are n-dimensional smooth-vector fields

d represents the disturbance variables

$p(x)$ the dimensional vector field directly related to the disturbance

Consider the following MIMO nonlinear system with a disturbance, and the nonlinear dynamic system model of PEMFC is rewritten as follows:

$$\begin{gathered}\dot{X} = f(x) + g_1(x)u_1 + g_2(x)u_2 + p(x)d \\ \begin{bmatrix} y_1 \\ y_2 \end{bmatrix} = \begin{bmatrix} x_1 \\ x_3 \end{bmatrix} = \begin{bmatrix} h_1(x) \\ h_2(x) \end{bmatrix}\end{gathered} \tag{4.2}$$

where

$$X = \begin{bmatrix} P_{\mathrm{H_2}} \\ P_{\mathrm{H_2O_A}} \\ P_{\mathrm{O_2}} \\ P_{\mathrm{N_2}} \\ P_{\mathrm{H_2O_C}} \end{bmatrix}; \quad U = \begin{bmatrix} u_\mathrm{a} \\ u_\mathrm{c} \end{bmatrix}; \quad Y = \begin{bmatrix} P_{\mathrm{H_2}} \\ P_{\mathrm{O_2}} \end{bmatrix}; \quad d = I_{\mathrm{fct}}$$

$$f(x) = 0; \quad g_1(x) = RT \cdot \lambda_{H_2} \begin{bmatrix} \dfrac{k_a \cdot Y_{H_2}}{V_A} - \dfrac{k_a}{V_A} \dfrac{x_1}{x_1 + x_2} \\ \dfrac{k_a \cdot \varphi_a P_{vs}}{V_A(x_1 + x_2 - \varphi_a P_{vs})} - \dfrac{k_a}{V_A} \dfrac{x_1}{x_1 + x_2} \\ 0 \\ 0 \\ 0 \end{bmatrix}$$

$$g_2(x) = RT \cdot \lambda_{air} \begin{bmatrix} 0 \\ 0 \\ \dfrac{k_c \cdot Y_{O_2}}{V_C} - \dfrac{k_c}{V_C} \dfrac{x_3}{x_3 + x_4 + x_5} \\ \dfrac{k_c \cdot Y_{N_2}}{V_C} - \dfrac{k_c}{V_C} \dfrac{x_4}{x_3 + x_4 + x_5} \\ \dfrac{k_c \cdot \varphi_c P_{vs}}{V_C(x_3 + x_4 + x_5 - \varphi_c P_{vs})} - \dfrac{k_c}{V_C} \dfrac{x_5}{x_3 + x_4 + x_5} \end{bmatrix}$$

$$p(x) = RT \begin{bmatrix} -\dfrac{C_1}{V_A} + \dfrac{C_1 \cdot x_1}{V_A(x_1 + x_2)} \\ \dfrac{C_1 \cdot x_2}{V_A(x_1 + x_2)} - \dfrac{C_1}{V_A} \\ -\dfrac{C_1}{2V_C} + \dfrac{C_1 \cdot x_2}{2V_C(x_3 + x_4 + x_5)} \\ 0 \\ -\dfrac{C_1}{V_C} - \dfrac{C_1 \cdot x_5}{V_C(x_3 + x_4 + x_5)} - \dfrac{C_2 \cdot x_5}{V_C(x_3 + x_4 + x_5)} + \dfrac{C_2}{V_C} \end{bmatrix}$$

Equation 4.2 implies that the input–output behavior of the system is nonlinear and coupled. Two steps are needed in order to achieve the control objective:

- Obtaining a nonlinear control law that not only can compensate nonlinearities but also can decouple and linearize the input and output behaviors.
- Imposing the poles of the closed loop so that the outputs P_{H_2} and P_{O_2} track asymptotically the desired trajectory by adding a PI controller.

Equation 4.2 presents an MIMO nonlinear system that makes us ready to develop a nonlinear control law. Normally, the disturbance *d* in Equation 4.2 cannot be directly used in the control design because an additional necessary condition—that the disturbance is able to be measured and the feed-forward action is allowed—has to be satisfied [6,7]. Otherwise, the linearized map between the new input v and the output y does not exist. The condition renders the following control law by using the measurement of the disturbance:

$$U = -A^{-1}(x)b(x) + A^{-1}(x)v - A^{-1}(x)p(x)d \tag{4.3}$$

As shown in Equation 4.2, $f(x) = 0$ leads to $b(x) = L_f^r h(x) = 0$, and so the control law is written as

$$U = A^{-1}(x)v - A^{-1}(x)p(x)d \tag{4.4}$$

Because each control variable u shows up after the first derivative of each $y_1 = x_1$ and $y_2 = x_3$, the relative degree vector $[r_1\ r_2]$ is $[1\ 1]$ and the decoupling matrix $A(x)$ is defined as

$$A(x) = \begin{bmatrix} L_{g_1}h_1(x) & L_{g_2}h_1(x) \\ L_{g_1}h_2(x) & L_{g_2}h_2(x) \end{bmatrix} \tag{4.5}$$

where

$$A(x) = \begin{bmatrix} \dfrac{k_a \cdot Y_{H_2} \cdot \lambda_{H_2}}{V_A} - \dfrac{k_a \cdot \lambda_{H_2}}{V_A}\dfrac{x_1}{x_1 + x_2} & 0 \\ 0 & \dfrac{k_c \cdot Y_{O_2} \cdot \lambda_{air}}{V_C} - \dfrac{k_c \cdot \lambda_{air}}{V_C}\dfrac{x_3}{x_3 + x_4 + x_5} \end{bmatrix}$$

which is nonsingular at $x = x_0$. Additionally, the matrix v and $p(x)$ in Equation 4.4 are given as follows:

$$v = \begin{bmatrix} \dot{y}_1 \\ \dot{y}_2 \end{bmatrix}; \quad p(x) = RT \begin{bmatrix} -\dfrac{C_1}{V_A} + \dfrac{C_1 \cdot x_1}{V_A(x_1 + x_2)} \\ -\dfrac{C_1}{2V_C} + \dfrac{C_1 \cdot x_2}{2V_C(x_3 + x_4 + x_5)} \end{bmatrix} \tag{4.6}$$

The control law given in Equation 4.4 yields a decoupled and linearized input–output behavior (see Figure 4.1):

$$\begin{aligned} \dot{P}_{H_2} &= v_1 \\ \dot{P}_{O_2} &= v_2 \end{aligned} \tag{4.7}$$

The outputs P_{H_2} and P_{O_2} are decoupled in terms of the new inputs v_1 and v_2. Thus, two linear subsystems, which are between the input v_1 and the hydrogen partial pressure $y_1 = P_{H_2}$, and between the input v_2 and the oxygen partial pressure $y_2 = P_{O_2}$, are obtained. Furthermore, note that $\dot{y}_1 = \dot{x}_1$ and $\dot{y}_2 = \dot{x}_3$, and so in order to ensure that y_1 and y_2 are adjusted to the desired value 3 [atm] of y_{1_S} and y_{2_S}, the stabilizing controller is designed by linear control theory using the pole-placement strategy [8]. The new control inputs are given by

$$\begin{bmatrix} v_1 \\ v_2 \end{bmatrix} = \begin{bmatrix} \dot{y}_{1\_S} - k_{11}e_1 \\ \dot{y}_{2\_S} - k_{21}e_2 \end{bmatrix} \tag{4.8}$$

where $e_1 = y_1 - y_{1\_S}$ and $e_2 = y_2 - y_{2\_S}$.

Even though the nonlinear system PEMFC is exactly linearized by feedback linearization, there may exist a tracking error in the variation of the parameters, especially when the load changes. To eliminate this tracking error, the integral terms are added in the closed-loop error equation as in [7,8]:

$$\begin{bmatrix} v_1 \\ v_2 \end{bmatrix} = \begin{bmatrix} \dot{y}_{1\_S} - k_{11}e_1 - k_{12}\int e_1\,\mathrm{d}t \\ \dot{y}_{2\_S} - k_{21}e_2 - k_{22}\int e_2\,\mathrm{d}t \end{bmatrix} \tag{4.9}$$

From Equation 4.9, the error dynamics can be obtained as follows:

$$\begin{aligned} \ddot{e}_1 + k_{11}\dot{e}_1 + k_{12}e_1 &= 0 \\ \ddot{e}_2 + k_{21}\dot{e}_2 + k_{22}e_2 &= 0 \end{aligned} \tag{4.10}$$

By appropriately choosing the roots of the characteristics of $s^2 + k_{11}s + k_{12}$ and $s^2 + k_{21}s + k_{22}$, asymptotic tracking is achieved, so that $P_{H_2} \to y_{1\_s}$ and $P_{O_2} \to y_{2\_S}$, as $t \to \infty$. The overshoots also become small by choosing $k_{11}^2 \gg 4k_{12}$ and $k_{21}^2 \gg 4k_{22}$ [7,8].

As shown in Figure 4.12, the main objective of this control scheme is to design a nonlinear controller by appropriately defining a transformation mapping that transforms the original nonlinear system into a linear and controllable (closed) system, at which point a linear controller can be designed using the pole-placement technique for tracking purposes. However, the control law in Equation 4.4 will be unobservable because the entire dynamics

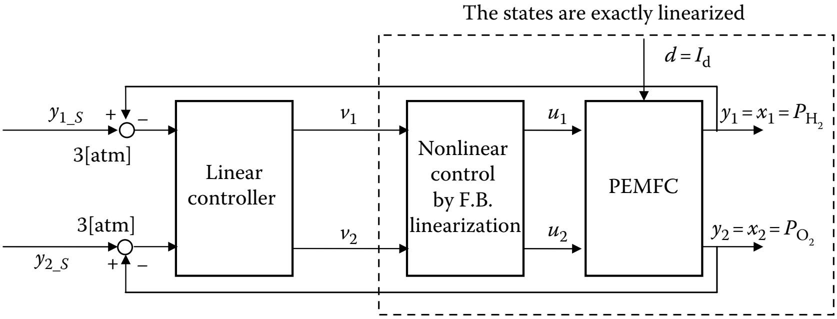

FIGURE 4.12
Overall control block diagram of PEMFC.

has five orders (P_{H_2}, …, $P_{H_2O_C}$), whereas only two orders (P_{H_2} and P_{O_2}) are observed in the outputs. So, we may have a problem of internal dynamics. In other words, the internal dynamics of $P_{H_2O_A}$, P_{N_2}, and $P_{H_2O_C}$ must be stable so that the states of the tracking controllers in Equation 4.9 are held in a bounded region during tracking. Otherwise, with external as well as internal dynamics, this control law cannot enhance the overall system performance. However, it is difficult to directly determine the internal dynamics of the system because it is nonlinear, nonautonomous, and coupled to the external closed-loop dynamics, as seen in Equations 4.1 through 4.10. Here simulation is used to verify whether each state remains within the reasonable bounded area [9]. A comparison between the simulation results and experimental data in [10] was used to verify the performance of the control law.

4.4 Nonlinear Control Design for Interface

For the interface design of the fuel cell nonlinear controller, several main components have to be considered, especially in a fuel cell vehicle system. The following are the main components of a fuel cell vehicle [11]:

- A fuel cell processor: gasoline or methanol reformer (in case of using a direct hydrogen, a hydrogen storage tank is required).
- The fuel cell stack, which can produce electricity and includes an air compressor to provide pressurized oxygen to the fuel cell.
- A cooling system, which can maintain the proper operating temperature.
- A water management system, which can manage the humidity and the moisture in the system and keep the fuel cell membrane saturated and, at the same time, prevent the water from being accumulated at the cathode.
- A DC–DC converter, which can condition the output voltage of the fuel cell stack.
- An inverter system, which can convert the DC to variable voltage and the variable frequency to power for the propulsion motor.
- A battery or an ultracapacitor, which can provide supplemental power for the start-up of the system and can store excessive energy during deceleration. For the power management, a bidirectional converter can be used between the DC–DC converter and the battery.

As seen in Figure 4.13, if using methanol or gasoline instead of the direct hydrogen, the fuel storage tank is needed before the reformer. For the direct hydrogen, a hydrogen tank is required. Both storage tanks should be fit into the vehicle as small as possible by considering safety against hazards.

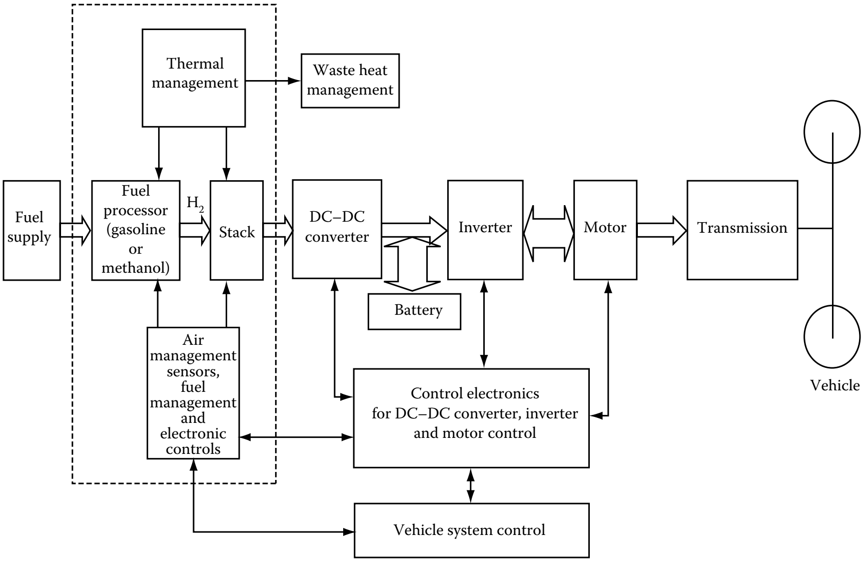

FIGURE 4.13
A typical fuel cell vehicle system. (From Rajashekrara, K., Propulsion system strategies for fuel cell vehicles, SAE paper 2000-01-0369. With permission.)

When high power demand is required, such as acceleration, the battery will provide the required power. When low power is required, the fuel cell can generate the power and even charge the battery. Figure 4.14 shows the fuel cell converter control system. In Figure 4.14, a DC–DC boost converter is used to boost the fuel cell voltage to the required battery voltage of about 300 V for the propulsion inverter. The DC–DC converter has to be designed

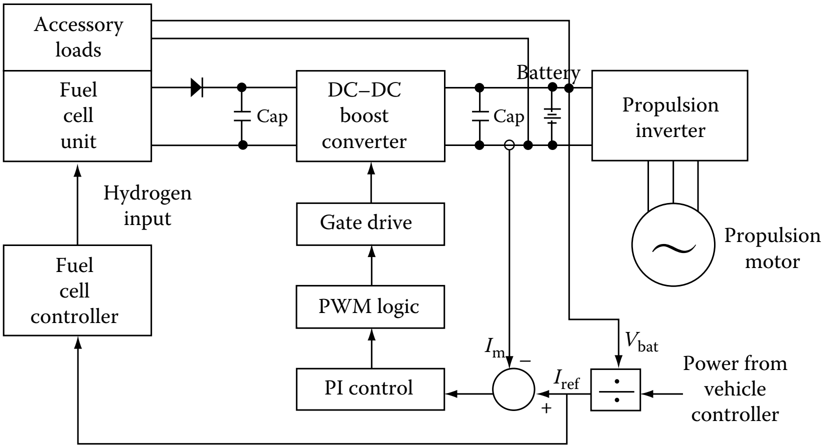

FIGURE 4.14
Fuel cell converter control system.

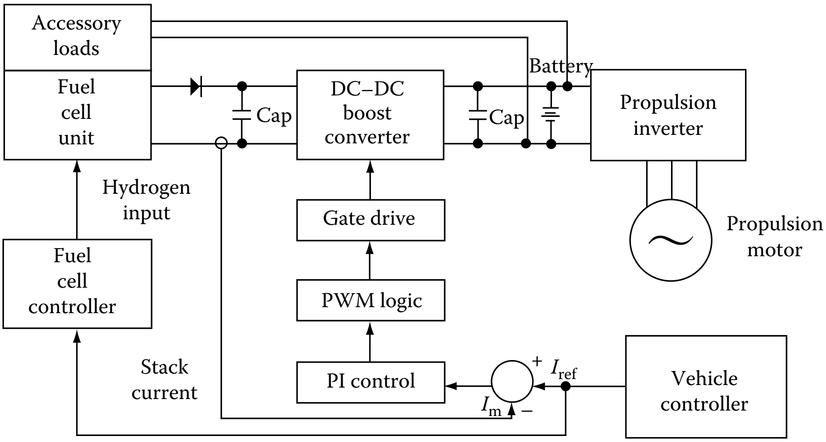

FIGURE 4.15
Modified fuel cell converter control system. (From Rajashekrara, K., Propulsion system strategies for fuel cell vehicles, SAE paper 2000-01-0369. With permission.)

based on the maximum power capacity of the fuel cell stack. The blocking diode is needed at the output of the fuel cell stack so as to prevent the reversal current flowing into the stack, which leads to damage to the fuel cell stack.

The power command from the vehicle controller is divided by the battery voltage and, therefore, it can generate the current reference, which is used for the DC–DC boost converter and the fuel cell controller. In the DC–DC boost converter, the reference signal is compared with the measured current to derive the duty cycle for controlling the output power of the DC–DC boost converter. Based on the battery voltage change, the fuel output power varies in a wide range. In the fuel cell controller, since the fuel cell output power is proportional to the hydrogen and oxygen flow rates, it has a wide bandwidth to stabilize the system under all operating conditions [11]. Hence, in order to have a constant power output in a wide range, a modified fuel cell converter system is proposed [11]. By directly measuring the fuel cell current in Figure 4.15, this fuel cell current is compared with the reference current, and the error in these currents can derive the duty cycle of the DC–DC converter and produce a constant current and voltage; thus the power remains constant and makes the system stabilized in a wide range.

4.5 Analysis of Control Design

Several nonlinear control approaches are compared with a PID controller, which is used to control the gas pressure loop for both input gases: hydrogen and oxygen. Among them are the feedback linearization-based-nonlinear

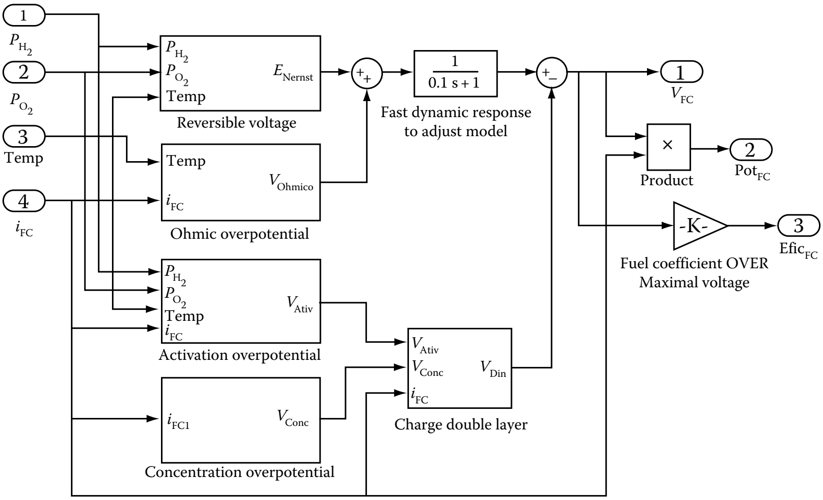

FIGURE 4.16
Dynamic MATLAB/Simulink PEMFC model. (From Anderson, C.A. et al., Design and control of fuel cells system for transport application, Aalborg University, Project Report, 2002. With permission.)

control for both input gases [12] and the neural network-based optimal control (NOC) for the gas pressures. More details about these control designs can be found in [13]. Using the electrochemical and thermodynamic relationships in a PEMFC, a dynamic MATLAB®/Simulink® model of PEMFC was built [13] using the NOC scheme, which is shown in Figure 4.16. In this model, four inputs are fed to the fuel cell. The PID pressure control Simulink model can be found in Figure 4.17 [13]. According to the simulation results in Figures 4.18 and 4.19, NOC can tune the gain automatically using

$$U(t) = \alpha \cdot (V_{ref}(t) - V(t))^2 + \beta \cdot (P_{H_2}(t) - P_{H_2}(t-1))^2 \tag{4.11}$$

This cost criterion $U(t)$ shows that the error between the desired state and the actual state must be minimized. As seen in Equation 4.11, fine tuning of the parameters α and β is required in order to have the minimum cost.

4.6 Simulation of Nonlinear Control for PEMFC

As to the feedback linearization-based nonlinear control of PEMFC derived in Equation 4.4, the dynamic PEMFC model and control method are tested through simulation in the MATLAB/Simulink environment [9]. For simplicity, the fuel processor, water and heat management, and air compressor models, are not considered in the simulation. Experimental data in [10] are used to justify the validity of the proposed dynamic PEMFC model.

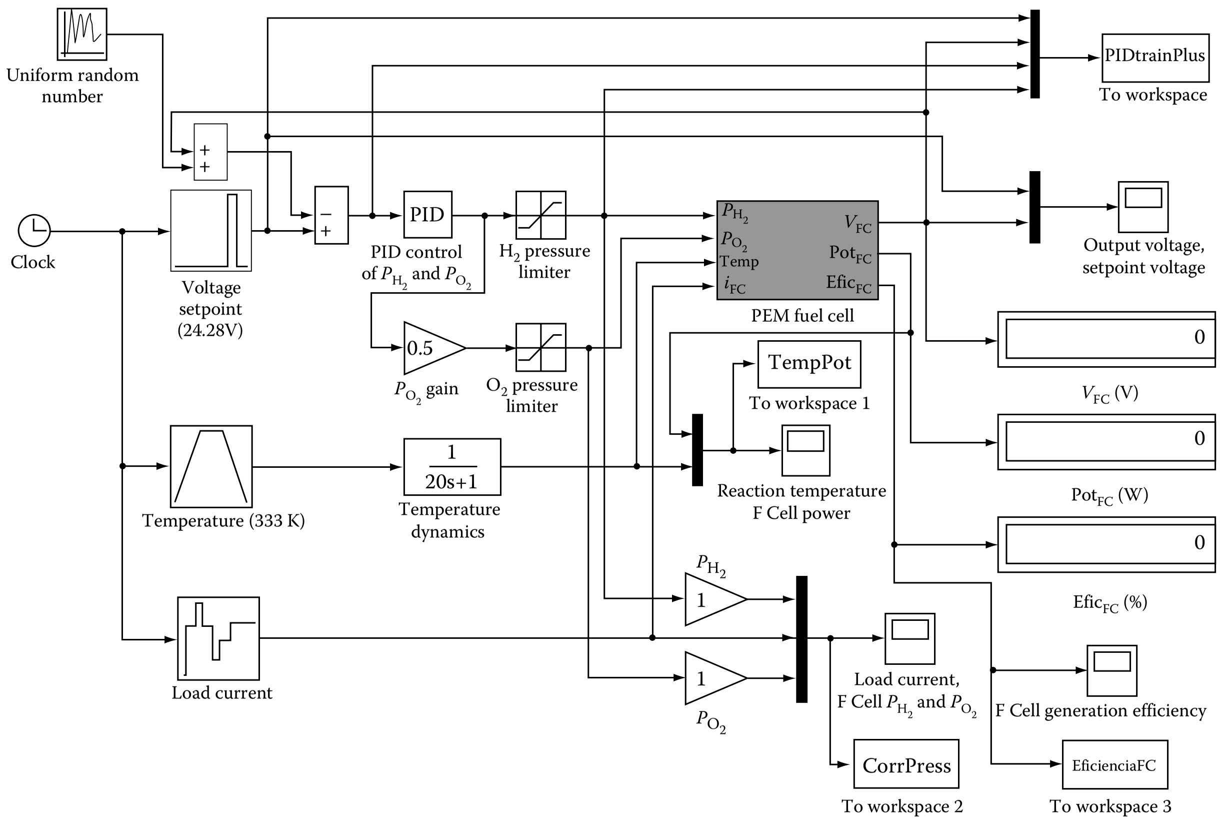

FIGURE 4.17
PID pressure control.

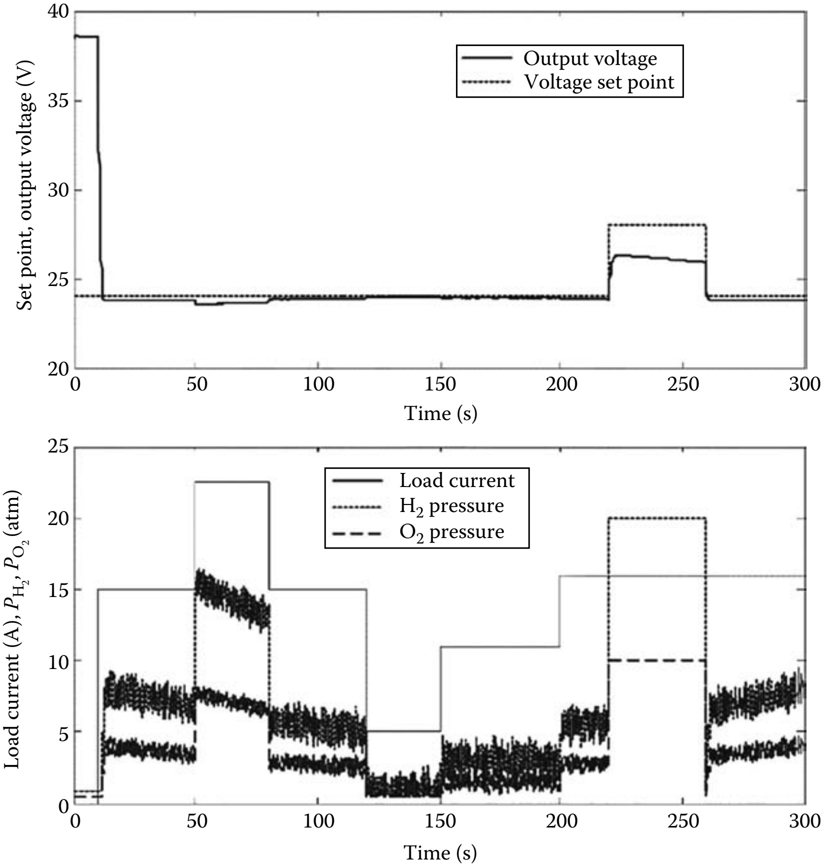

FIGURE 4.18
PEMFC PID control: set point, output voltage, hydrogen pressure, oxygen pressure, and load current.

The fuel cell system Ballard MK5-E-based PGS105B system shown in Figure 4.19 is used to test the feedback linearization-based nonlinear controller. This system has a total of 35 cells, connected in series, with a cell surface area of 232 cm^2. The membrane electrode assembly consists of a graphite electrode and a Dow™ membrane. The reactant gases (hydrogen and air) are humidified inside the stack, and the hydrogen is recirculated at the anode side while the air flows through the cathode side. The hydrogen pressure is regulated to 3 atm at the anode inlet by a pressure regulator, and a back-pressure regulator at the air outlet also maintains 3 atm through the Ballard fuel cell stack. The oxidant flow rate is automatically adjusted to a constant value of 4.5 L/s, based on a programmable load, via a mass flow meter to ensure sufficient water removal at the cathode. Hydrogen is replenished at the same rate as it is consumed. The stack temperature measured

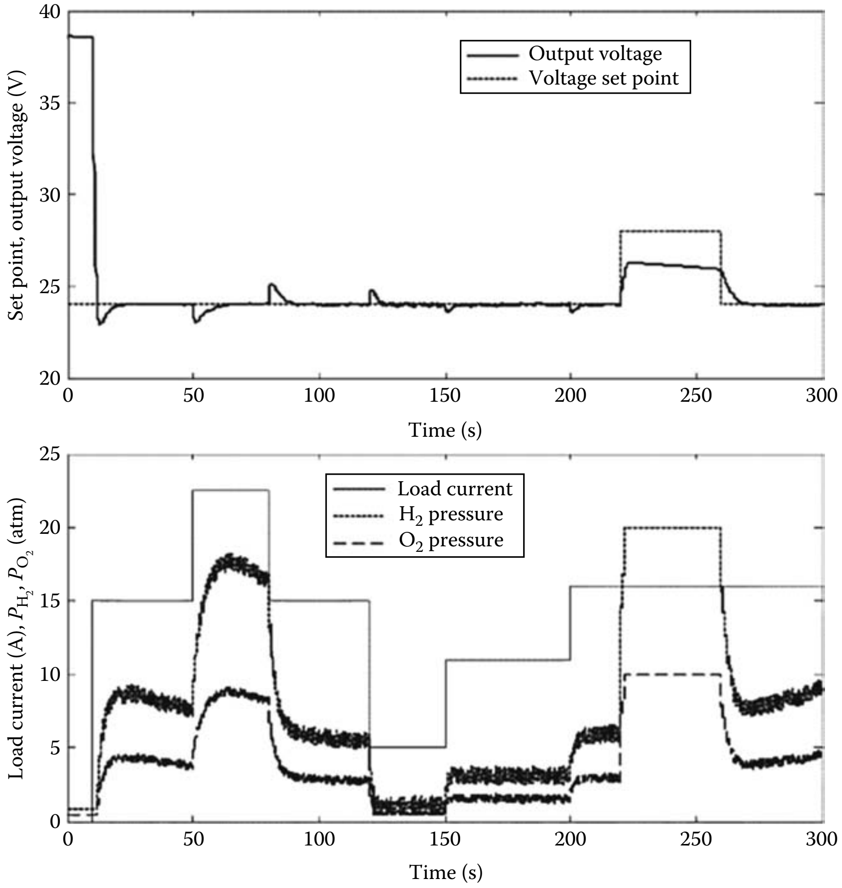

FIGURE 4.19

PEMFC neural optimal control: set point, output voltage, hydrogen pressure, oxygen pressure, and load current. (From Anderson, C.A. et al., Design and control of fuel cells system for transport application, Aalborg University, Project Report, 2002. With permission.)

at the air outlet is maintained between 72°C and 75°C to produce the maximum power output. A simplified diagram of the Ballard system is depicted in Figure 4.20. The PGS105 system is more likely to be a presetting control system instead of a feedback control system. In the case of outer ranges of settings, the system automatically shuts down, and a higher-level control system is thus needed. The outline of the experimental setup of the nonlinear controller is explained in [9]. To implement this control scheme in the practical system, the sensors to measure the states P_{H_2}, …, $P_{H_2O_C}$; the stack current; and the voltage must be installed, and a main controller such as a digital signal processor (DSP) needs to be implemented based on the nonlinear control law obtained using the tool of feedback linearization. With the help of the DSP, the fuel cell can communicate with the electronics rack and the PC for user interface monitoring, as shown in Figure 4.21. The safety

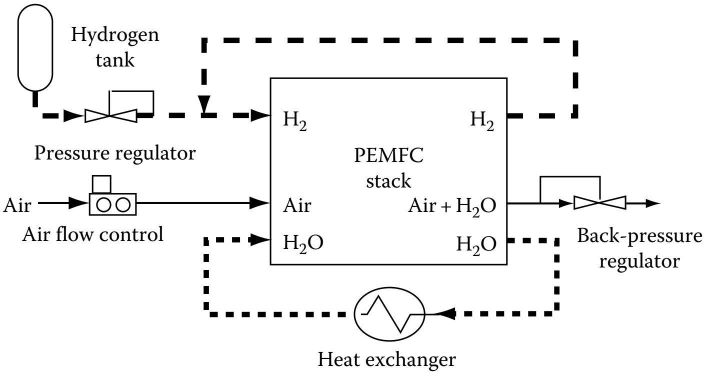

FIGURE 4.20
PEMFC stack based on PGS105B system. (From Hamelin, J. et al., *Int. J. Hydrogen Energ.*, 26, 625, 2001. With permission.)

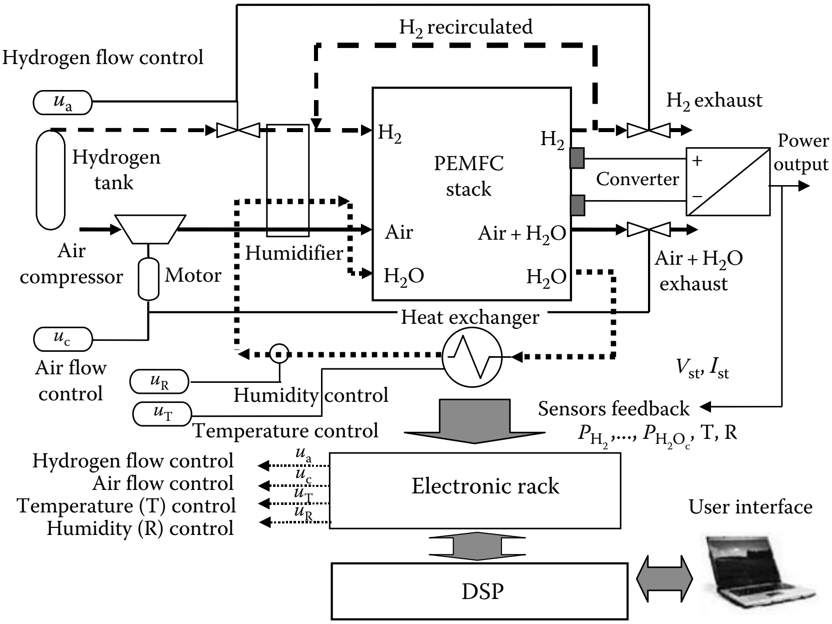

FIGURE 4.21
Simplified experiment setup for the PEMFC nonlinear control. (From Na, W.K. and Gou, B., *IEEE Trans. Energ. Convers.*, 23(1), 179, 2008. With permission.)

concerns for the fuel cell system must be solved with high priority before a control scheme is implemented. At least, the safety issues related to low cell voltage, stack overload, high temperature, hydrogen leaking, and pressure differences between the anode and the cathode must be considered in the fuel cell control system, to prevent a fatal accident and severe damage to the fuel cell system.

To control the entire fuel cell system, sensors and temperature and humidity control actuators must be added to the system. In the simulation, since the temperature and the humidity in the system have a very slow response time, a perfectly controlled humidifier and heat exchanger are assumed to be applied. In addition, an automatic purge controller for the hydrogen exhaust is required, and with respect to the air and water exhaust, the back-pressure regulator must be coordinated with the air inlet flow-rate input as well as the hydrogen inlet flow-rate input to maintain the pressures for hydrogen and air at the same level. By assuming that the electrical capacitor is 1 F [12] and the sum of the activation and concentration resistances is from 0.2 to 0.3 Ω [13], the time constant of the fuel cell stack is approximately from 0.2 to 0.3 s. With the use of a fast actuator on the cathode side, whose performance setting time is 10%–90% of 50 ms, and another actuator on the anode side whose performance setting time is 10%–90% of less than 20 ms, it becomes possible to maintain the anode and cathode pressures at a certain level. To ensure this performance, the anode pressure controller must be three times faster than the one on the cathode side as the anode pressure follows the cathode side pressure [13]. Currently, these fast actuators are available in the market [14], yet, in reality, due to the uncertainties in the fuel cell model parameters and inaccuracy in the measurements, we may encounter a serious obstacle to achieve the desired responses. Moreover, the time delays of actuators, sensors, compressor, and sampling period for the DSP are unavoidable for the design of the nonlinear control of PEMFCs. Even though we could not exactly calculate the time delays, they still can be compensated for by adapting a lead compensator in practical systems. However, since the lead compensation is very sensitive to noise, a multiple first-order, low-pass noise filter is recommended [13]. In the simulation in [12], the time delays and other problems like uncertainty and inaccuracy in measurements are not considered.

The nominal values of the parameters for the simulation are shown in Table 4.1.

Experimental data from Hamelin et al. [10] were used to justify the validity of the proposed dynamic model of PEMFCs. The voltage and the current—the most important variables—were used for this comparison. In [10], a load profile with rapid variations between 0 and 150 A was imposed on the PGS105B system. The corresponding stack current and voltage transients are plotted in Figure 4.22, where the experimental data [10] are indicated by solid lines.

The details of the load profile are shown in Figure 4.23, where the load resistances were changed from 0.145 to 4.123 Ω during the simulation period. Figure 4.22 shows a good agreement between the experimental data and the simulated results, except for the time periods (13 s, 15 s) and (25 s, 29 s). The main reason for the voltage difference during these periods is the internal resistance variation of the PEMFC systems [12]. The rapid current increase can cause an immediate voltage drop across the internal resistor of the fuel cell, which is closely related to the temperature change that adversely affects this resistance. In this simulation, the stack temperature was assumed to be constant at 353 K. A small discrepancy between the simulation results and

TABLE 4.1

PEMFC Parameters for the Simulation

Parameter	Value and Definition
N	Cell number: 35
V_o	Open cell voltage: 1.032 [V]
R	Universal gas constant: 8.314 [J/mol-K]
T	Temperature of the fuel cell: 353 [K]
F	Faraday constant: 96485 [C/mol]
α	Charge transfer coefficient: 0.5 [Ref 9]
M	Constant in the mass transfer voltage: 2.11×10^{-5} [V]
N	Constant in the mass transfer voltage: 8×10^{-3} [cm^2/mA]
R	2.45×10^{-4} [$k\Omega$ cm^2]
A_{fc}	Fuel cell active area: 232 [cm^2]
V_a	Anode volume: 0.005 [m^3] [Ref 15]
V_c	Cathode volume: 0.01 [m^3] [Ref 15]
k_a	Anode conversion factor: 7.034×10^{-4} [mol/s]
k_c	Cathode conversion factor: 7.036×10^{-4} [mol/s]
P_{vs}	The saturation pressure: 32 [kPa] at the temperature 353 [K]

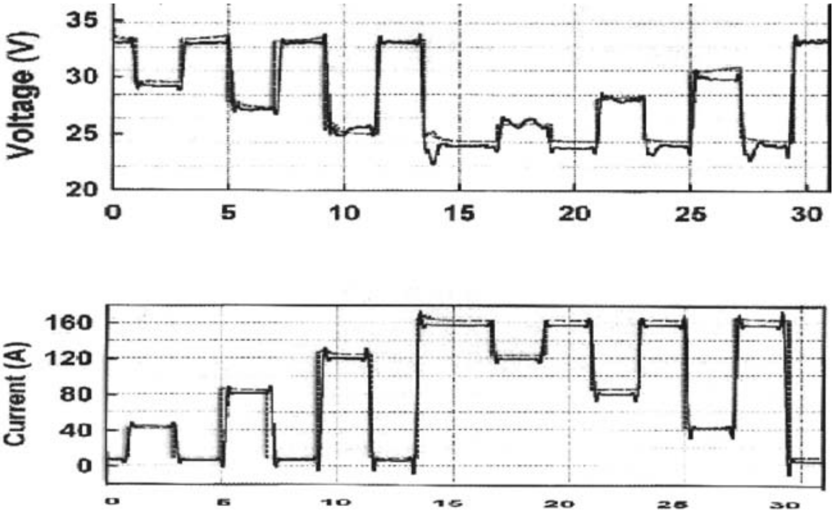

FIGURE 4.22
Voltage and current under load variations.

experimental data is inevitable under the rapid current changes. In order to compare the efficiency of the nonlinear controller, a linear controller (PI controller) is used in the fuel cell system.

To achieve fewer overshoot results, the feedback gains k_{11}, k_{21}, k_{12}, and k_{22} in Equation 4.10 have to be tuned to 5 and 1, which are the optimal values in their

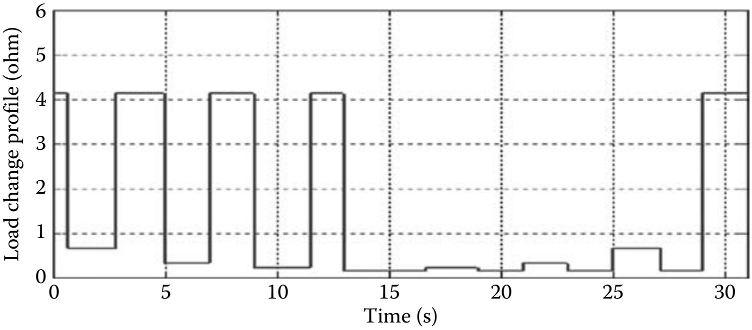

FIGURE 4.23
Load variation profile.

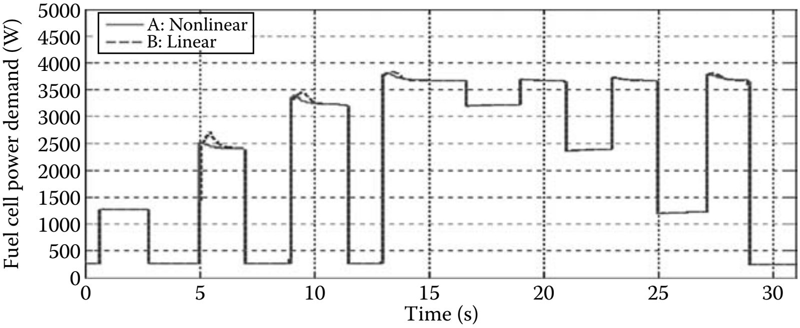

FIGURE 4.24
Fuel cell power demand under load variations.

feasible ranges [0.1, 10] for k_{11} and k_{21} and [0, 10] for k_{12} and k_{22}, and being beyond the ranges can easily cause a violation of the MATLAB simulation limits.

For the voltage, current, and power shown in Figures 4.22 and 4.24, the discrepancies between the nonlinear control and the linear control are not obvious due to the fast response times, which are less than a few milliseconds. However, other simulation results in Figures 4.25 through 4.29 indicate that better transient performances are observed when using a nonlinear controller because the linear controller is more dependent upon the operating point, while the nonlinear controller is independent of the operating point due to the feedback linearization control design based on the differential geometry [16]. Figure 4.26 shows that the oxygen partial pressure has much bigger overshoot than the hydrogen partial pressure, which implies that the oxygen partial pressure is more sensitive to the load variation than the hydrogen partial pressure. Figure 4.27 displays the absolute value of the difference between the hydrogen and oxygen partial pressures. It is found in Figure 4.27 that the nonlinear controller has a better transient response than the linear controller. Generally, an increase in the stack current causes a decrease in the reactant pressures as more fuel consumption is required. However, the flow rates vary

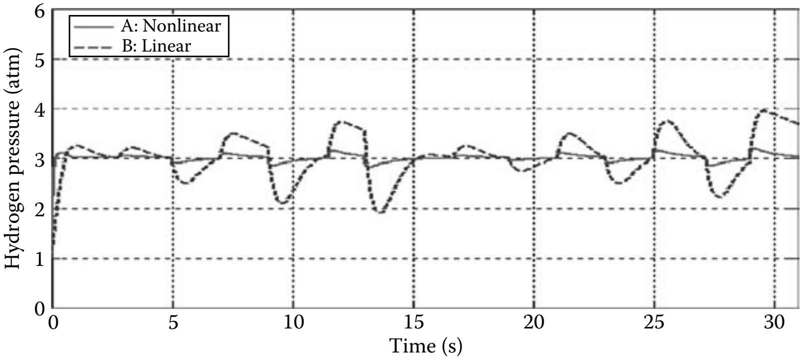

FIGURE 4.25
Variations of hydrogen pressure.

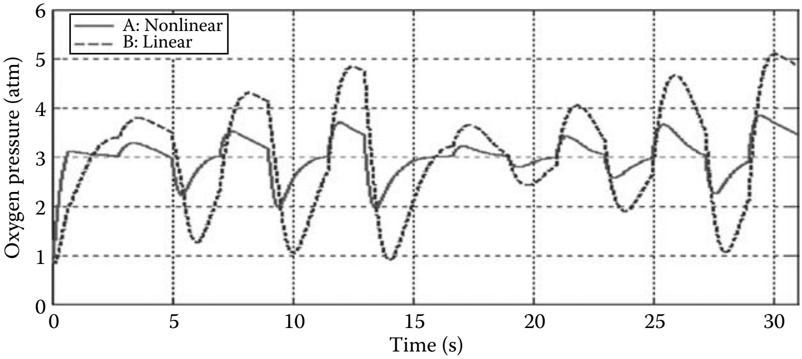

FIGURE 4.26
Variations of oxygen pressure.

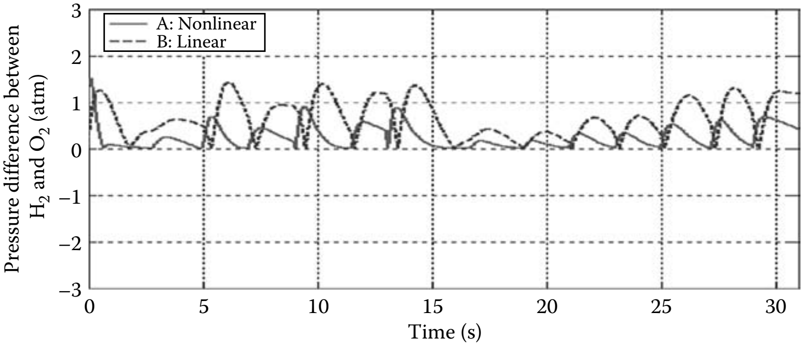

FIGURE 4.27
Variations of pressure differences of H_2 and O_2.

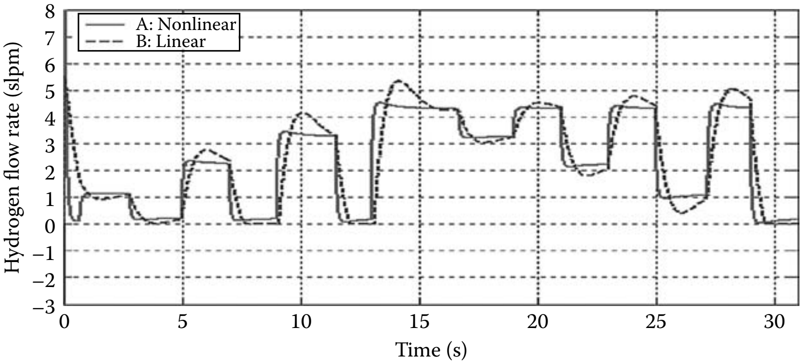

FIGURE 4.28
Variations of hydrogen flow rate.

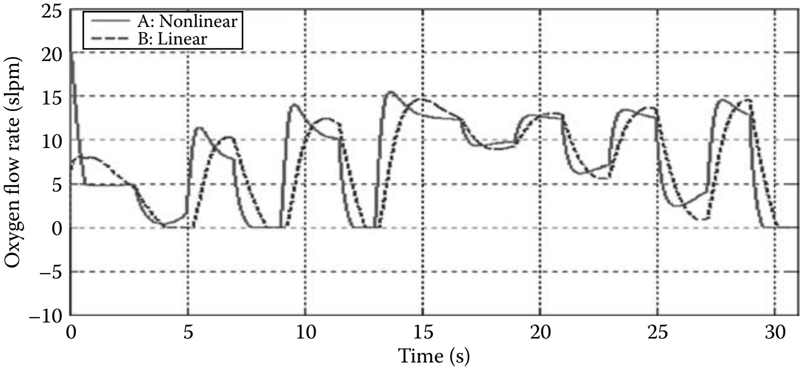

FIGURE 4.29
Variations of oxygen flow rate.

with the stack current in the same way and compensate for the increased fuel consumption.

Figures 4.28 and 4.29 give the responses of the hydrogen and the oxygen flow rates under load variations. The hydrogen flow rate varies between 0 and 5 slpm, while the oxygen flow rate varies from 0 to 16 slpm. It is observed that the oxygen flow rate has much bigger variations than hydrogen because the oxygen flow rate is more sensitive to the load variation than the hydrogen flow rate, as was seen with the pressure variations.

Although the nonlinear controller has slightly more overshoot in the oxygen flow rate than the linear controller in Figure 4.28, it shows that the response time of the nonlinear controller is faster than the linear controller. Figures 4.20 through 4.32 show that the states $P_{H_2O_A}$, $P_{H_2O_c}$, and P_{N_2} are stable under load variations.

Figures 4.31 and 4.32 show that the nonlinear controller behaves approximately in the same way as the linear controller, under the water partial pressure on the cathode side and the nitrogen partial pressure on the anode side.

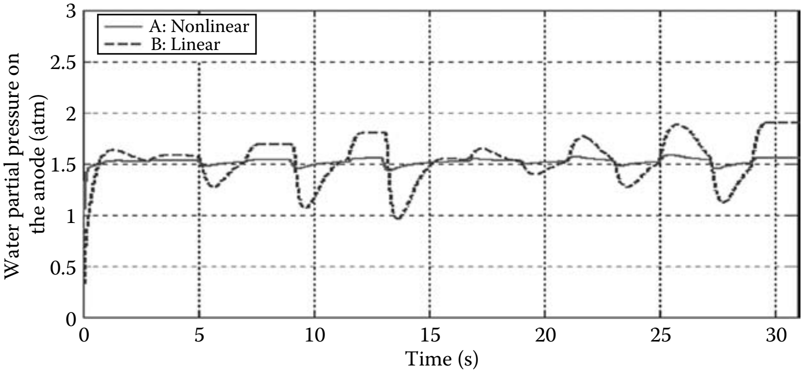

FIGURE 4.30
Variations of water partial pressure on the anode.

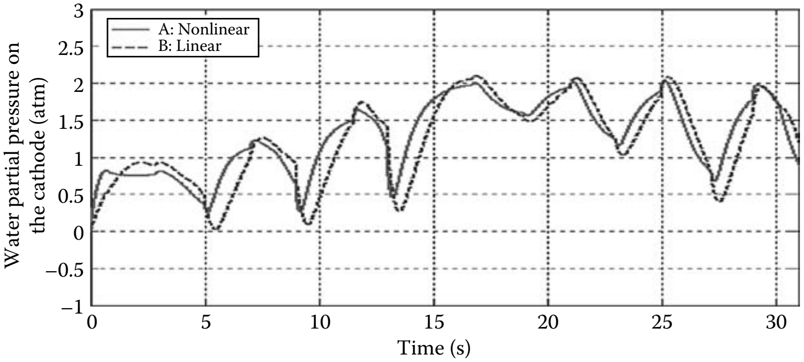

FIGURE 4.31
Variations of water partial pressure on the cathode.

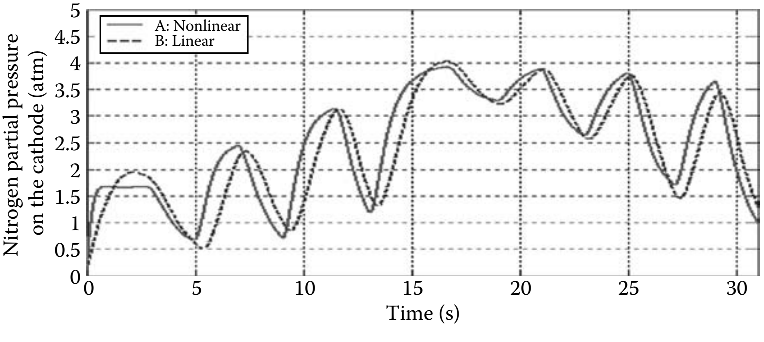

FIGURE 4.32
Variations of nitrogen partial pressure on the cathode.

In addition, even though no tracking controllers are considered in the design of the nonlinear and linear controllers, Figures 4.20 through 4.32 show that $P_{H_2O_A}$, P_{N_2}, and $P_{H_2O_c}$ vary within bounded ranges (0–4 atm) with the load variations, which implies that the internal dynamics problem of the nonlinear tracking controller in our design is not a concern. It is observed that the water partial pressure on the anode side remains a little more stable than the water partial pressure at the cathode and the nitrogen pressure. Furthermore, the water partial pressure on the anode side follows a pattern similar to that of the hydrogen partial pressure because of the high mole fraction of hydrogen, which is about 99%. Therefore, it can be concluded that the load variations have more influence on the cathode side than on the anode side, which implies a more sophisticated control strategy than the one proposed in this chapter needs to be applied on the cathode side.

References

1. J.S. Yi and T.V. Nguyen, An along-the-channel model for proton exchange membrane fuel cells, *Journal of Electrochemical Society*, 145(4), 1149–1159, 1998.
2. J. Golbert and D. Lewin, Model-based control of fuel cells: (1) Regulatory control, *Journal of Power Sources*, 135, 135–151, 2004.
3. R.N. Methekar, V. Prasad, and R.D. Gudi, Dynamic analysis and linear control strategies for proton exchange membrane fuel cell using a distributed parameter model, *Journal of Power Sources*, 165, 152–170, 2007.
4. W.C. Yang, B. Bates, N. Fletcher, and R. Pow, Control challenges and methodologies in fuel cell vehicle development, SAE paper 98C054, 1998.
5. J. Pukrushpan, A.G. Stefanopoulou, and H. Peng, Control of fuel cell breathing, *IEEE Control Systems Magazine*, 24(2), 30–46, 2004.
6. A. Isidori, *Nonlinear Control Systems*, 3rd ed., London: Springer Verlag, 1995.
7. M.A. Henson and D.E. Seborg, Critique of exact linearization strategies for process control, *Journal of Process Control*, 1, 122–139, 1991.
8. J.J.E. Slotine and W. Li, *Applied Nonlinear Control*, Englewood Cliffs, NJ: Prentice Hall, 1991.
9. W.K. Na and B. Gou, Feedback linearization based nonlinear control for PEM fuel cells, *IEEE Transactions on Energy Conversion*, 23(1), 179–190, 2008.
10. J. Hamelin, K. Abbossou, A. Laperriere, F. Laurencelle, and T.K. Bose, Dynamic behavior of a PEM fuel cell stack for stationary application, *International Journal of Hydrogen Energy*, 26, 625–629, 2001.
11. K. Rajashekrara, Propulsion system strategies for fuel cell vehicles, SAE paper 2000-01-0369, 2000.
12. J. Larminie and A. Dicks, *Fuel Cell Systems Explained*, New York: Wiley, 2002.
13. C.A. Anderson, M.O. Christensen, A.R. Korsgaad, M. Nielsen, and P. Pederson, Design and control of fuel cells system for transport application, Project Report, Aalborg University, 2002.
14. Burkert, http://www.bci,buerkert.com/product.
15. M.J. Khan and M.T. Labal, Dynamic modeling and simulation of a fuel cell generator, *Fuel Cells*, 1, 97–104, 2005.
16. B.W. Bequette, Nonlinear control of chemical process: A review, *Industrial and Engineering Chemistry Research*, 30, 1391–1413, 1991.

5

Simulink Implementation of Fuel Cell Models and Controllers

5.1 Introduction

The dynamic fuel cell models and controllers were developed using MATLAB®/Simulink® environment. Simulink is a toolbox extension of the MATLAB program by Mathworks Inc. Simulink is a very powerful tool in modeling and mathematical representation. We can choose a suitable integration method and set up the run-time and initial conditions in the Simulink environment. Systems are drawn on screen by block diagrams in Simulink. Elements of the block diagrams, such as transfer functions, summing junction, etc., as well as virtual input and output devices: function generators and oscilloscopes, are available. Because Simulink provides a graphical user interface, it is easy to build the block diagrams, perform simulations, and analyze the results. In Simulink, models are hierarchical so you can view a system at a high level, and details in each block can be viewed by double-click on the blocks.

The Simulink simulations in the CD-ROM attached in this book were developed in MATLAB version 6.5. The details of Simulink implementation of the fuel cell model and controllers as well as related elements are described in this chapter.

5.2 Simulink Implementation of the Fuel Cell Models

The following assumptions are made to develop a fuel cell model in Simulink:

- Due to a slow response time of the stack temperature (about 102 s [1]), the operating stack temperature is assumed to be constant.
- The fuel cell is well humidified on both the anode and cathode sides.
- For water management, it is assumed that the liquid water does not leave the stack and that it evaporates into the cathode or anode gas if humidity on either side drops below 100% [2].

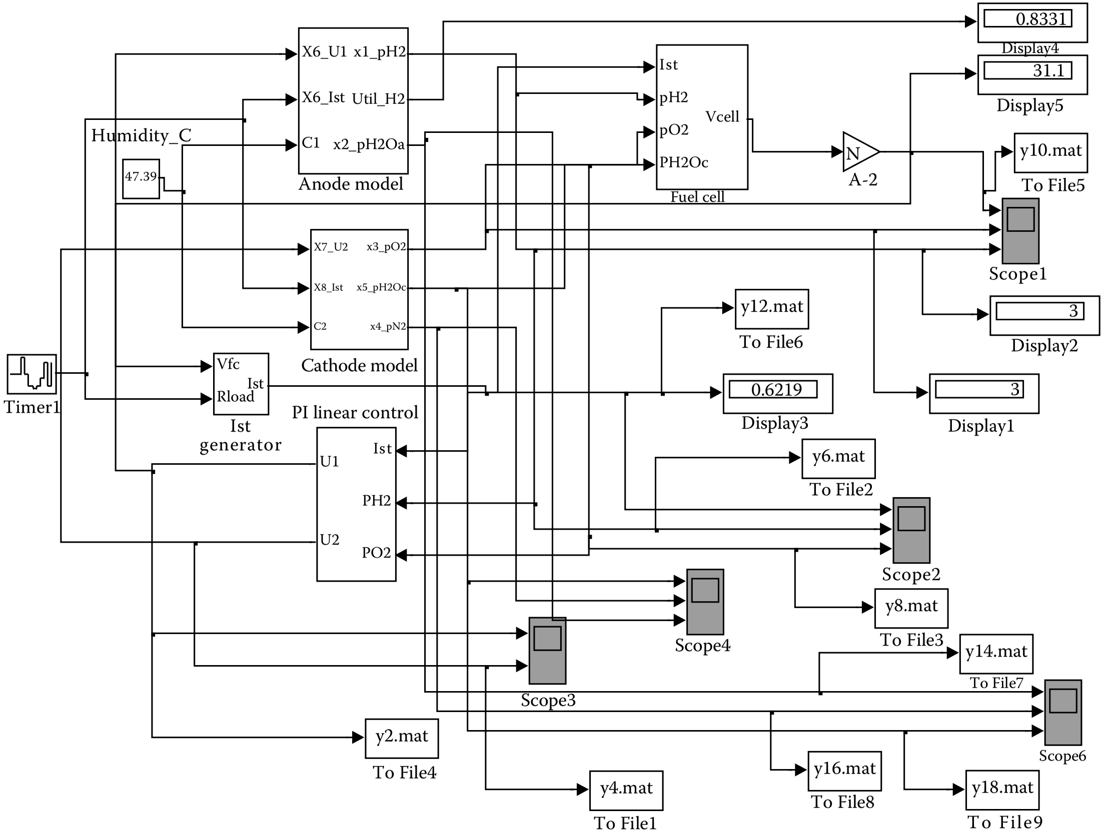

FIGURE 5.1
PEMFC system block diagram.

- Humidifier and temperature controllers are assumed to be perfectly working [3].
- The mole fractions of the inlet reactants are assumed to be constant to build the simplified dynamic PEMFC model (Figure 5.1). In other words, pure hydrogen (99.99%) is fed to the anode, and the air that is uniformly mixed with nitrogen and oxygen by a ratio of, say, 21:79 is supplied to the cathode side [3].
- The ideal gas law and mole conservation rule are applied by supposing that all gases are ideal.

Therefore, the water management and temperature control are not a concern in this simulation. PEM fuel cell system composes of four blocks which are anode model, cathode model, fuel cell voltage model, and control block.

Let us consider the fuel cell voltage model block first. The output fuel cell stack voltage V_{st} [1] is defined as a function of the stack current, reactant partial pressures, fuel cell temperature, and membrane humidity:

$$V_{st} = E - V_{activation} - V_{ohmic} - V_{concentration} \tag{5.1}$$

In the above equation,

$E = N_o\left[V_o + (RT/2F)\ln\left(P_{H_2}\sqrt{P_{O_2}}/P_{H_2O_c}\right)\right]$ is the thermodynamic potential of the cell or reversible voltage based on Nernst equation (Equation 5.1)

$V_{activation}$ is the voltage loss due to the rate of reactions on the surface of the electrodes

V_{ohmic} is the ohmic voltage drop from the resistances of proton flow in the electrolyte

$V_{concentration}$ is the voltage loss from the reduction in concentration gases or the transport of a mass of oxygen and hydrogen

Their values are given as follows:

$$V_{activation} = N \cdot \frac{RT}{2\alpha F} \cdot \ln\left(\frac{I_{fc} + I_n}{I_o}\right) \tag{5.2}$$

$$V_{ohm} = N \cdot I_{fc} \cdot r \tag{5.3}$$

$$V_{concentration} = N \cdot m \exp(n \cdot I_{fc}). \tag{5.4}$$

In Equation 5.1, P_{H_2}, P_{O_2}, and $P_{H_2O_c}$ are the partial pressures of hydrogen, oxygen, and water, respectively. Subscript "c" means the water partial pressure, which is vented from the cathode side.

A detailed explanation of each voltage loss is given in [2], and other voltages are also described in [1,3], where the fuel cell voltage is mainly expressed by the combination of physical and empirical relationships in which parametric coefficients of the membrane water content, humidity, and temperature, as well as the reactant concentrations are involved (Table 5.1). In this book, the

TABLE 5.1

Cell Voltage Parameters

Parameter	Value and Definition
N	Cell number
V_o	Open cell voltage [V]
R	Universal gas constant [J/g-mol-K]
T	Temperature of the fuel cell [K]
F	Faraday constant [C/mol]
α	Charge transfer coefficient
I_{fc}	Output current density [A/cm^2]
I_0	Exchange current density [A/cm^2]
I_n	Internal current density [A/cm^2]
m and n	Constants in the mass transfer voltage
r	Area-specific resistance [kΩ cm^2]

Source: Khan, M.J. and Labal, M.T., *Fuel Cells*, 4, 463, 2005. With permission.

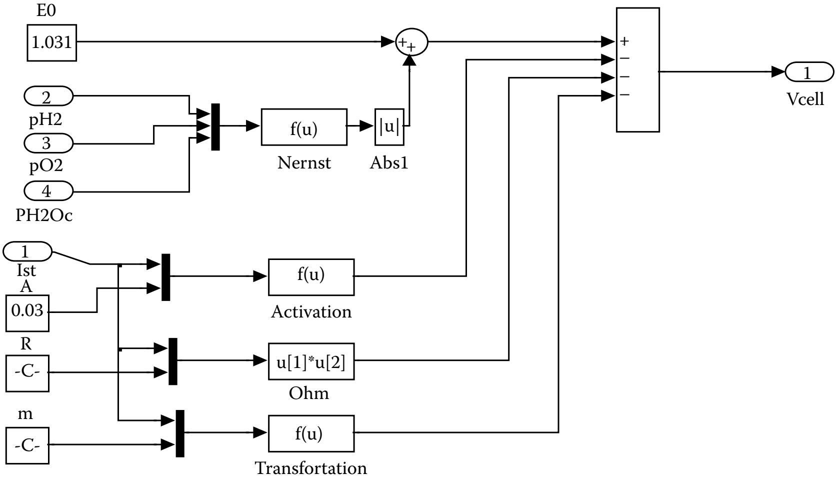

FIGURE 5.2
Fuel cell voltage model block.

general voltage formulation as given in Equation 5.1 will be used because water and temperature factors are assumed to be constant due to their slow response time. According to Equation 5.1, the fuel cell voltage block is built as shown in Figure 5.2.

The reactant flow rates at the anode and cathode sides are determined by the partial pressures and the stack current. Using the ideal gas law, each partial pressure block can be modeled as shown in Figure 5.3. As seen in Figure 5.3, the anode block consists of the hydrogen and water models.

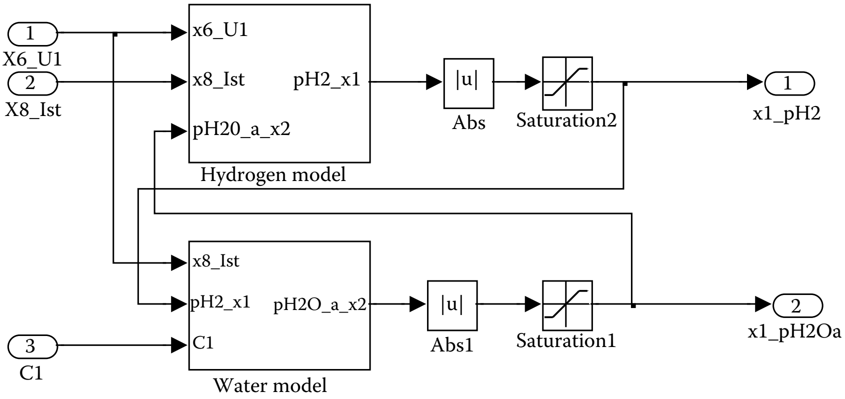

FIGURE 5.3
Anode model.

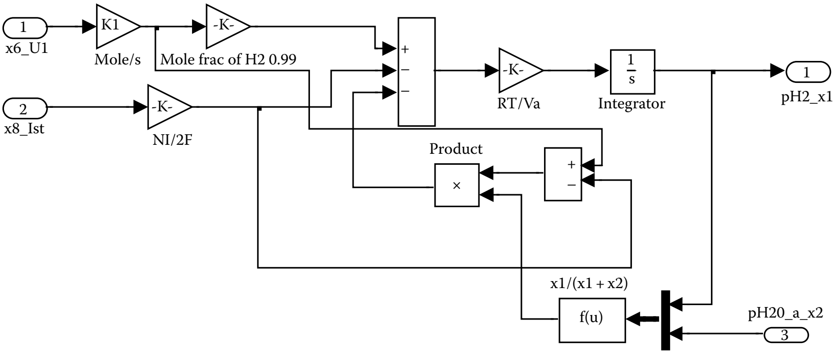

FIGURE 5.4
Hydrogen model.

There are many limiters placed in the output of each pressure and even in the controller outputs to prevent problems caused by algebraic loops and extreme numerical values [1]. The detailed hydrogen and water models are shown in Figures 5.4 and 5.5, respectively.

The cathode model consists of the oxygen, water, and nitrogen models, as seen in Figures 5.6 through 5.9.

In the anode block, the hydrogen inlet flow rate (SLPM) is converted in to mol/s using a conversion factor (1 standard liter per minute: 7.034×10^{-4} mol/s); the mole fraction of H_2 is assumed to be 99%. In the cathode block, air is uniformly mixed with nitrogen and oxygen in a ratio 21:79, with conversion factor 7.034×10^{-4} mol/s [1]. In order to analyze data in a short time, a fast ode solver is used. The ode45 method is based on Dormand–Prince, which is an explicit, one-step Runge–Kutta that is recommended as a first

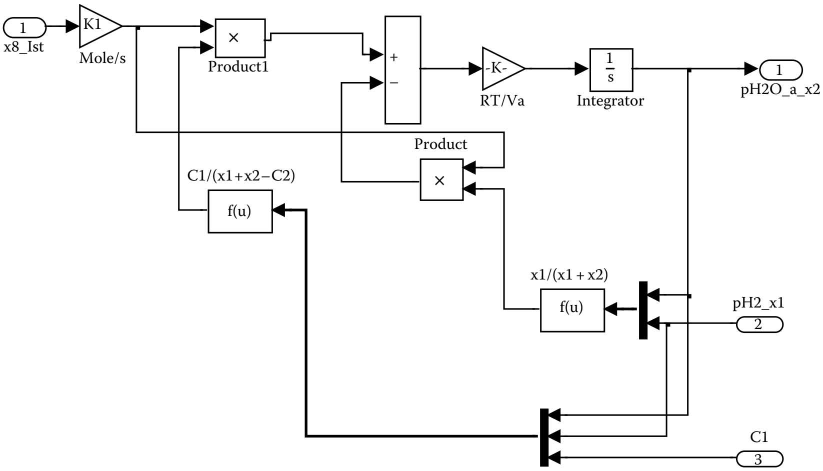

FIGURE 5.5
Water model at the anode side.

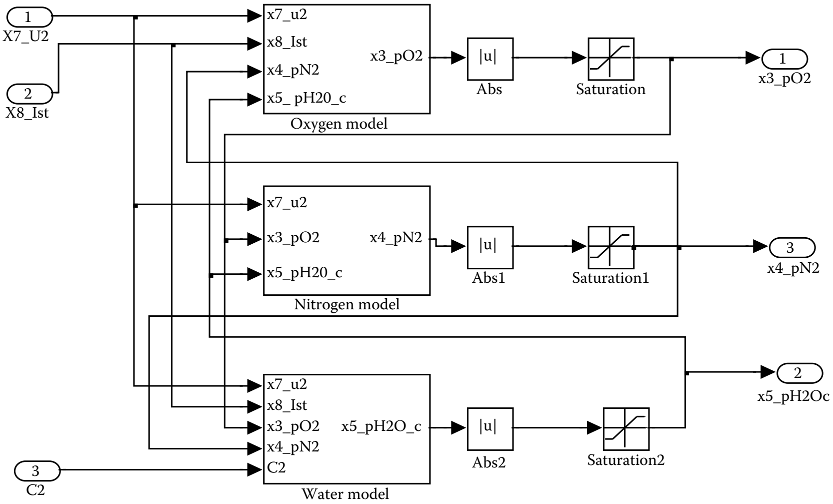

FIGURE 5.6
Cathode model.

try method [4]. All simulations results are obtained and shown within 10 s even though the setup time is 100 s. During the time duration 0–0.5 s, the unrealistic values of the simulations can be seen due to the inadequacies of initial conditions.

The stack current is generated by the fuel cell voltage, V_{fc} and the load block, R_{load}. The road block is made by the timer; its time matrix [0, 15.0, 20.0, 25.0, 30.0, 35.0, 40.0, 45.0, 50, 55 s] corresponds to the amplitude resistor matrix [1, 0.6, 0.3, 0.175, 0.3, 1, 2.5, 5, 1, 5 Ω].

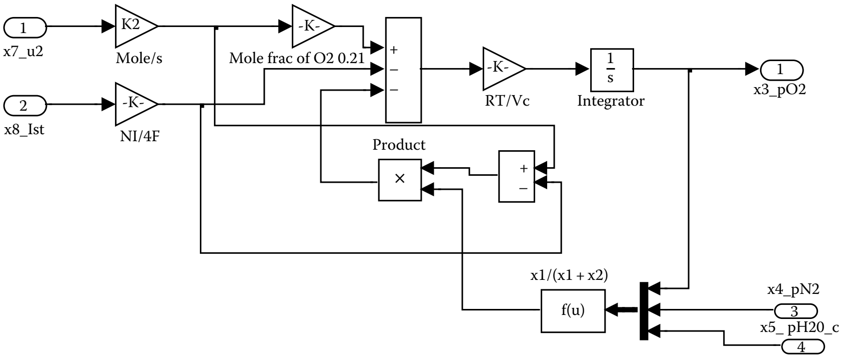

FIGURE 5.7
Oxygen model.

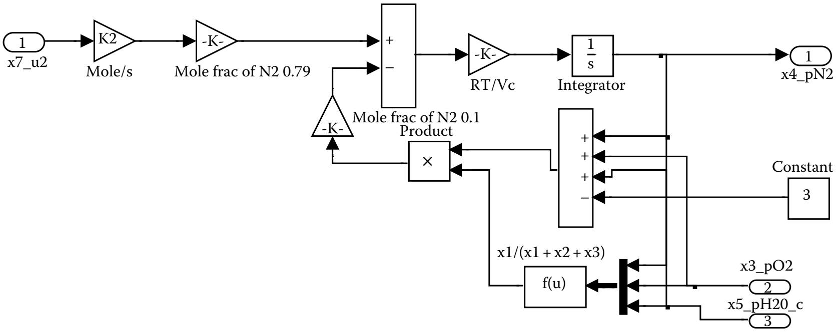

FIGURE 5.8
Nitrogen model.

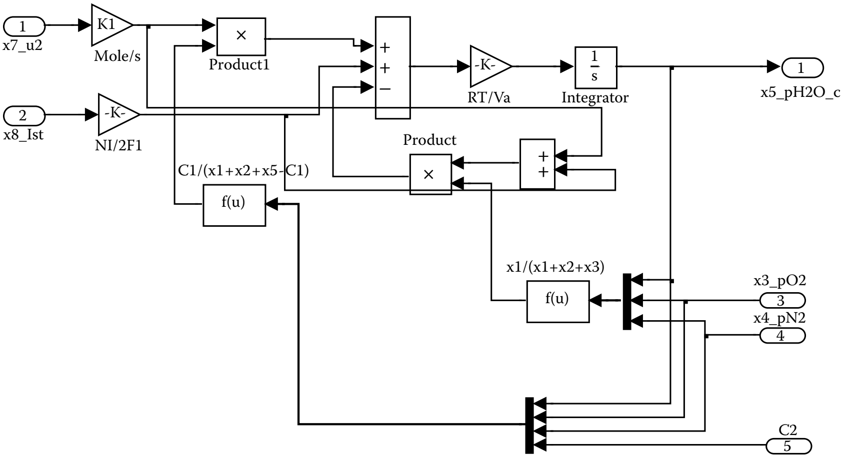

FIGURE 5.9
Water model at the cathode side.

5.3 Simulink Implementation of the Fuel Cell Controllers

For pressure control of the fuel cell system, the hydrogen and oxygen pressures are sensed and then compared with the reference pressure, 3 atm, in the linear PI controllers in Figure 5.10. In the case of feed-forward control, the stack current is fed to the controller, but in this simulation, the feed-forward control is not used (Figure 5.11).

Figure 5.12 shows a PI controller for the pressure control. Through trial and error, the optimized PI gain of 5 is obtained.

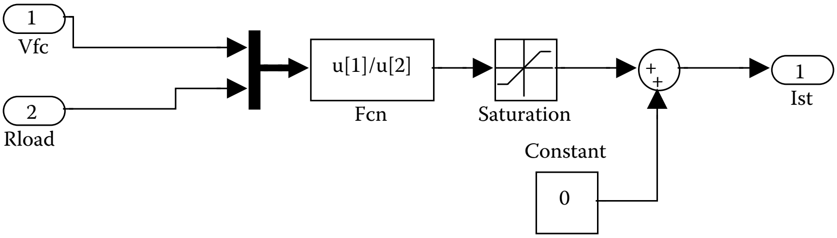

FIGURE 5.10
The load and current block.

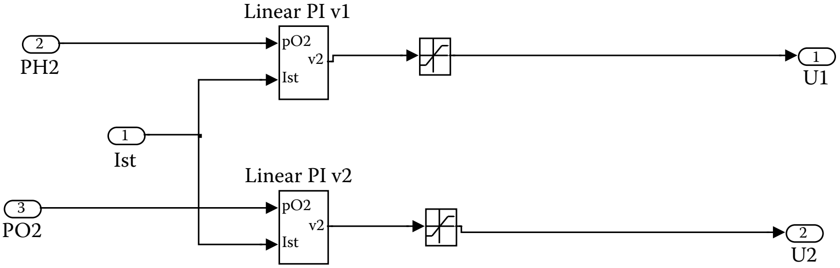

FIGURE 5.11
The linear controller block.

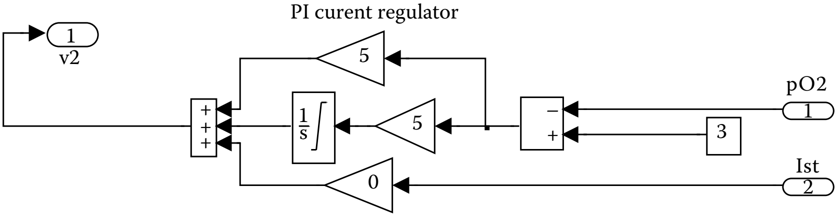

FIGURE 5.12
The linear PI controller block.

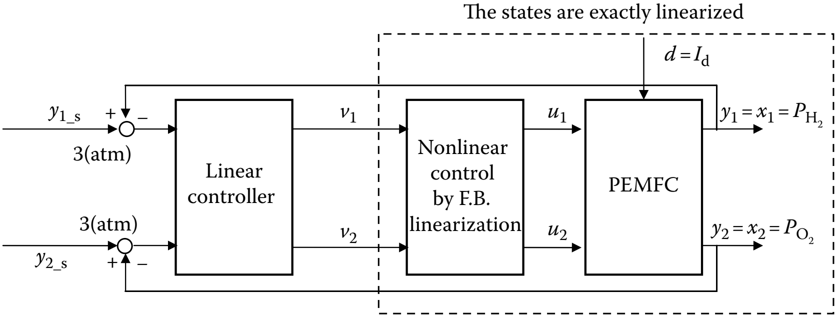

FIGURE 5.13
Nonlinear control block diagram of PEMFC.

For the design of the nonlinear pressure controller, feedback linearization algorithm is adapted as shown in Figure 5.13. The nonlinear control law is derived by using the decoupling matrix in Section 4.4.

The nonlinear control law vector U is obtained by feedback linearization, and the linear controller block is also used in this block to generate a control input V vector in Figure 5.13.

To implement the nonlinear controller law, the multiplexer and other math functions in the Simulink are used. A filter is used before generating the nonlinear control law, which can remove sudden variations in the anode and cathode flow rates (Figure 5.14).

5.4 Simulation Results

For the simulations, the load profile is generated using a timer in the Simulink. The details of load profile are shown in Figure 5.15.

In terms of the fuel cell voltage control, the fuel cell voltage will be kept varying based on the load profile as in Figure 5.16, because the fuel cell system cannot compensate for a fast power demand, such as an acceleration and deceleration, or other fast load changes of the fuel cell vehicle without a secondary power source such as battery or ultracapacitor.

Based on the load change, the current varies from 6.5 to 160 A, and the fuel cell system can generate up to 4.6 kW.

For the voltage, current (Figure 5.17), and power (Figure 5.18), the discrepancies between the nonlinear control and the linear control are not obvious due to the fast response time, which is less than a few milliseconds, as reported in [5].

In Figures 5.19 and 5.20, the hydrogen flow rate varies between 0 and 5 SLPM, while the oxygen flow rate varies from 0 to 14 SLPM. It can be seen

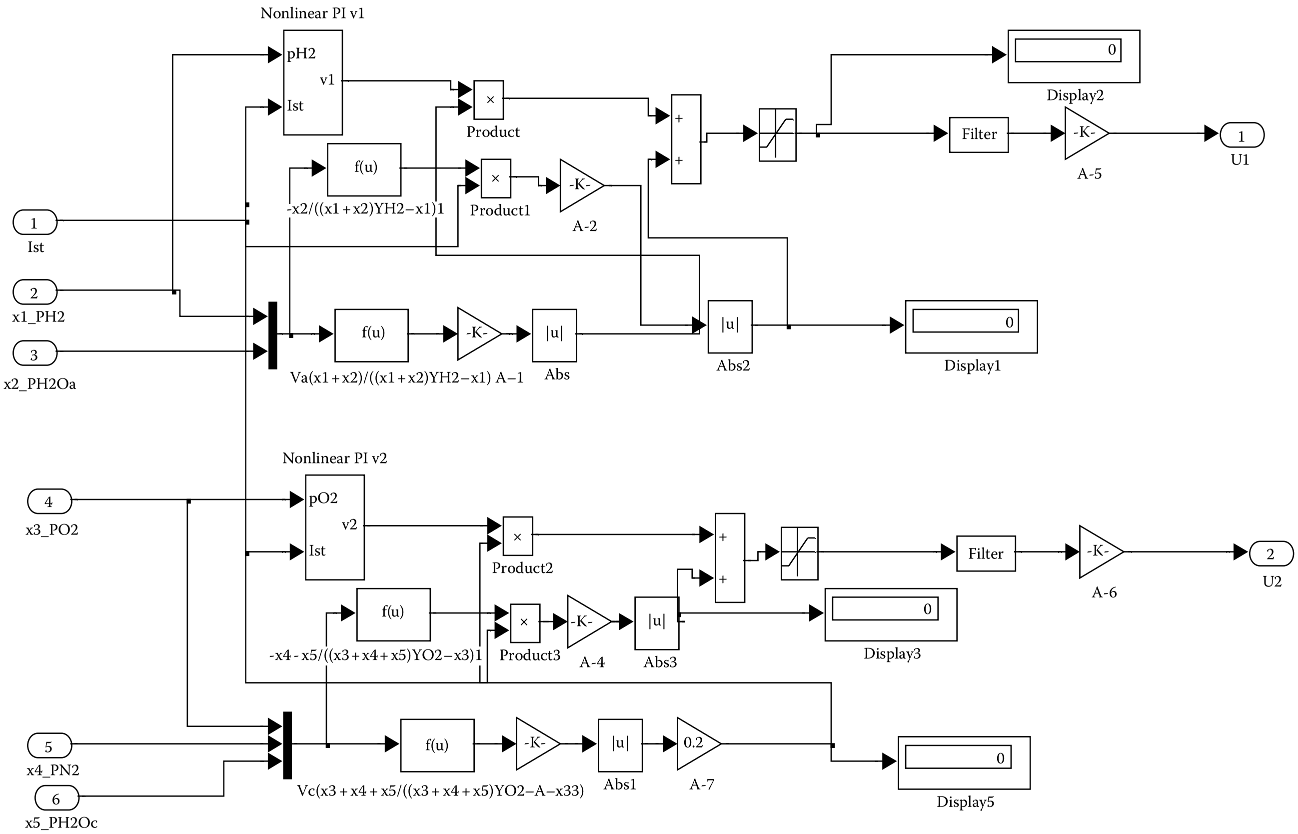

FIGURE 5.14
The nonlinear controller block using feedback linearization.

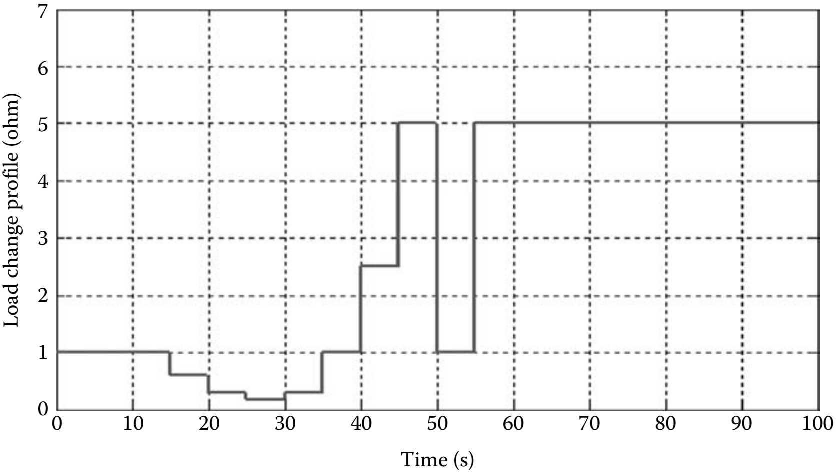

FIGURE 5.15
Load variation profile.

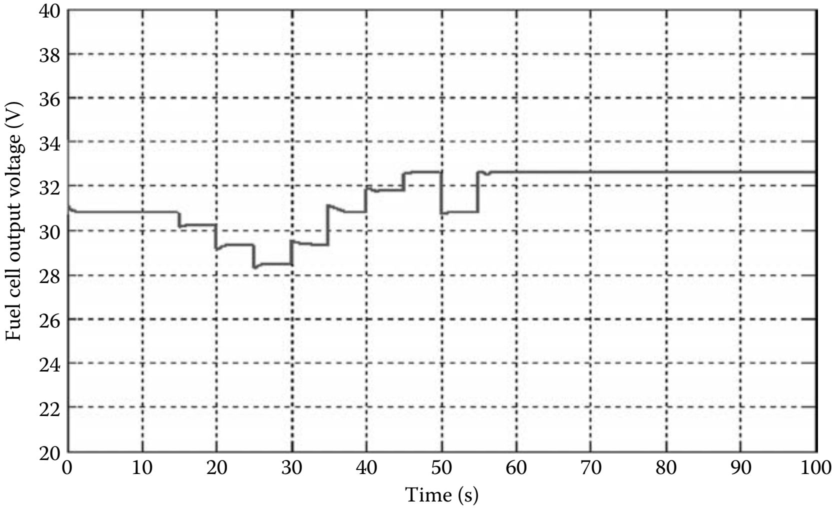

FIGURE 5.16
Fuel cell voltage under load variations.

that the oxygen flow rate has much larger variations than that of the hydrogen because the oxygen flow rate is more sensitive to the load variation than the hydrogen flow rate.

According to Figures 5.21 and 5.22, the results show that the linear and nonlinear controllers for the pressure of the fuel cell system keep tracking

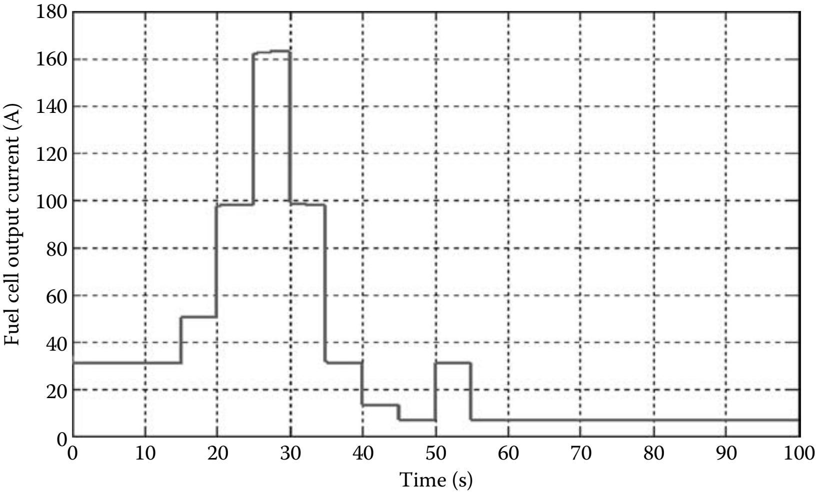

FIGURE 5.17
Fuel cell current under load variations.

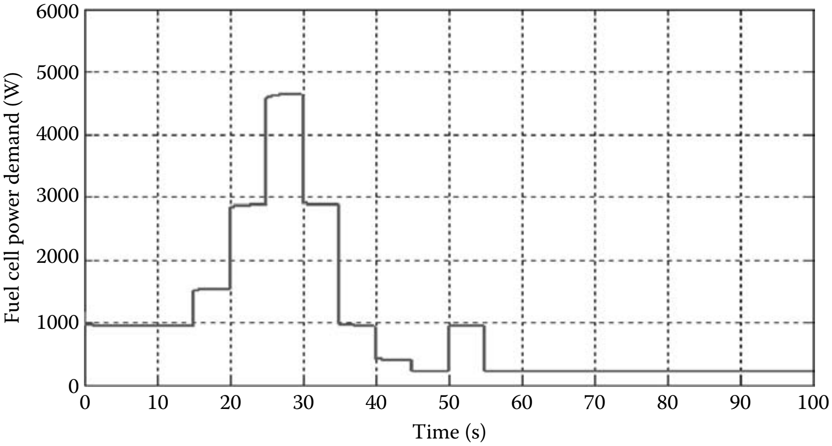

FIGURE 5.18
Fuel cell power under load variations.

the reference value 3 atm. These simulation files can be found in the attached CD. The load profile is likely to be changed and different results can be obtained based on the new load profile.

In this section, a 5 kW PEM fuel cell dynamic model has been built in MATLAB/Simulink, and its linear and nonlinear controllers and simulation

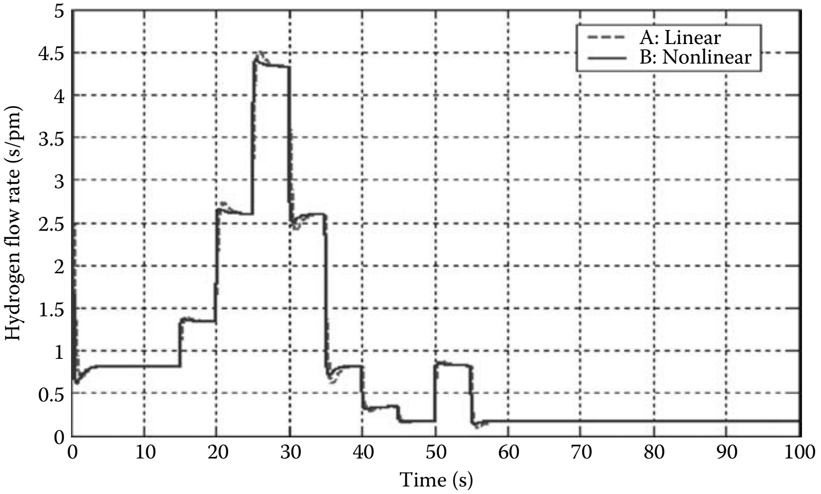

FIGURE 5.19
Variations of hydrogen flow rate.

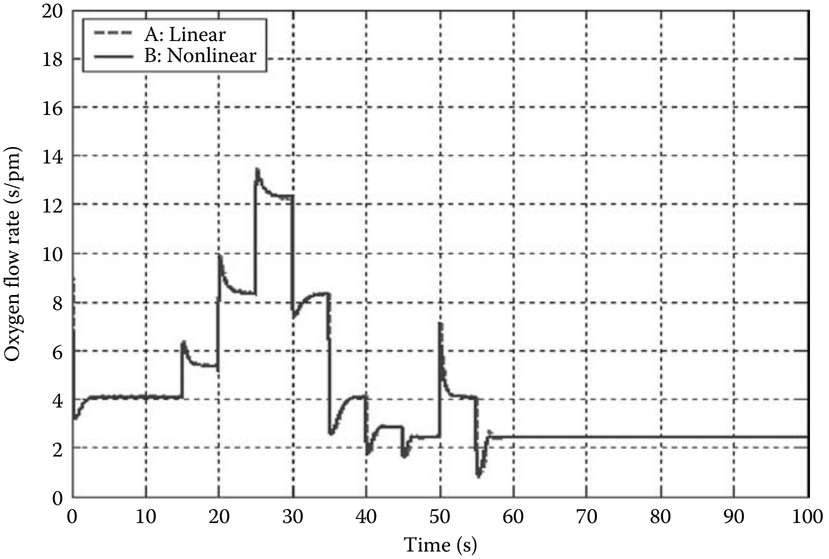

FIGURE 5.20
Variations of oxygen flow rate.

results have been analyzed and discussed. As seen in Figure 5.16, the fuel cell system should be coordinated with a secondary energy system to avoid a voltage drop due to a load change. To integrate this fuel cell system with a secondary energy system, power electronics devices and electrical components

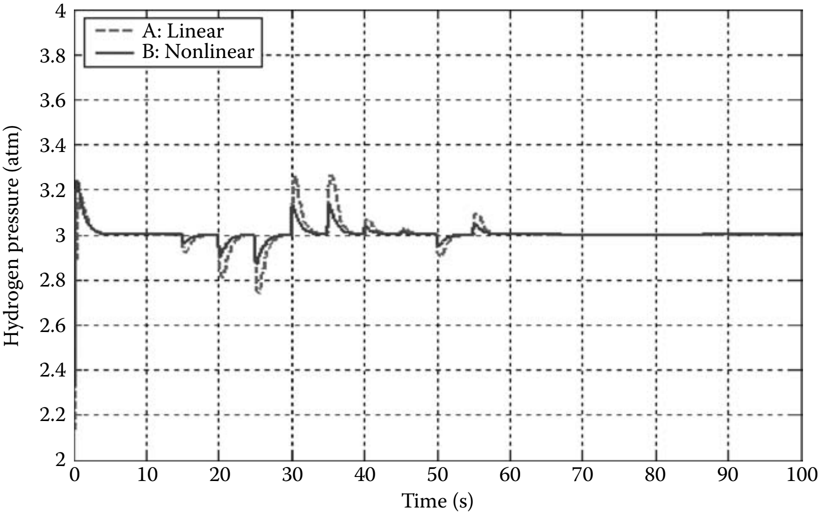

FIGURE 5.21
Variations of hydrogen pressure.

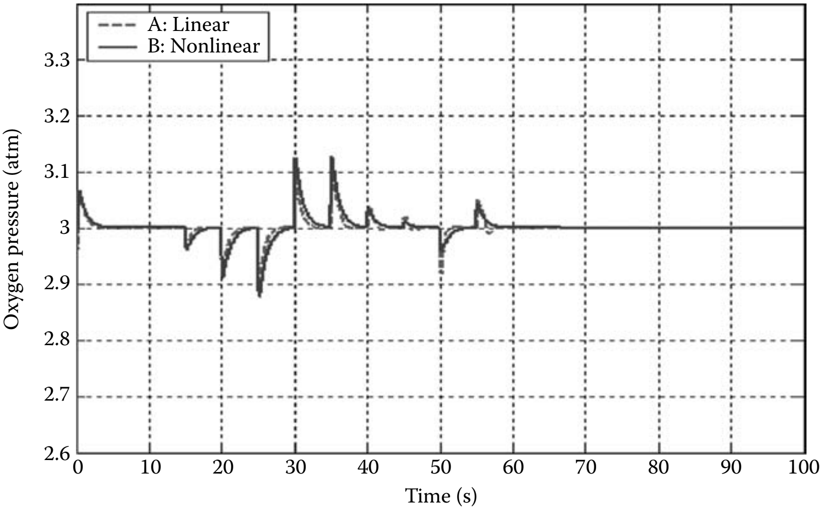

FIGURE 5.22
Variations of oxygen pressure.

such as capacitor, resistor, and reactor are needed. Since the switching devices make the simulation slower, it is easier to have a conversion error due to its high switching frequency over 1 kHz. For example, for 30 s simulation duration, it takes over 5–6 h to finish the simulation, and this book does not deal with the hybrid power fuel cell system simulation.

References

1. M.J. Khan and M.T. Labal, Modeling and analysis of electro chemical, thermal, and reactant flow dynamics for a PEM fuel cell system, *Fuel Cells*, 4, 463–475, 2005.
2. J. Larminie and A. Dicks, *Fuel Cell Systems Explained*, New York: Wiley, 2002.
3. J. Purkrushpan and H. Peng, *Control of Fuel Cell Power Systems: Principle, Modeling, Analysis and Feedback Design*, Germany: Springer, 2004.
4. C.-M. Ong, *Dynamic Simulation of Electric Machinery using Matlab/Simulink*, New Jersey: Prentice Hall, 1998.
5. C.A. Anderson, M.O. Christensen, A.R. Korsgaad, M. Nielsen, and P. Pederson, Design and control of fuel cells system for transport application, Project Report, Aalborg University, 2002.

6

Applications of Fuel Cells in Vehicles

6.1 Introduction

Fossil fuels including coal, oil, and gas, which we heavily depend on, can cause air pollution and greenhouse gas problems. Recent study [1] shows that about 18% of CO_2 (carbon dioxide), greenhouse gas, is emitted by motor vehicles. The development of fuel cell vehicles is very important to our environment and even our economy, especially for a soaring oil price at present. The fuel cell system is widely regarded as one of the most promising energy sources, thanks to its high energy efficiency, extremely low emission of oxides of nitrogen and sulfur, very low noises, and the cleanness of its energy production. Furthermore, a fuel cell system can operate with other conventional and alternative fuels, such as hydrogen, ethanol, methanol, and natural gas. Based on the types of electrolytes currently used, fuel cells are classified into PEMFCs, solid oxide fuel cells (SOFCs), phosphoric acid fuel cells (PAFCs), molten carbonate fuel cells (MCFCs), alkaline fuel cells (AFCs), direct methanol fuel cells (DMFCs), zinc air fuel cells (ZAFCs), and photonic ceramic fuel cells (PCFCs) [1].

To date, PEMFCs have been considered the most promising candidate for the fuel cell vehicle and small- and mid-size distributed generators because of their high power density, solid electrolyte, long stack life, and low corrosion. PEMFCs can operate at low temperatures (50°C–100°C), which enables fast start-up. PEMFCs are hence particularly attractive for transportation applications that require rapid start-up and fast dynamic responses over transient times (stopping and running, acceleration, and deceleration).

The fuel cell has higher efficiency than an internal combustion engine (ICE). It is noted in [2] that the efficiency of a fuel cell vehicle using direct hydrogen from natural gas is two times greater than that of an ICE vehicle. However, for the commercialization of fuel cell vehicles, their performance, reliability, durability, cost, fuel availability and cost, and public acceptance should be considered [3]. Especially, the performance of the fuel cell systems during transients, the cost of fuel cells, and availability of hydrogen for the success of commercialization of fuel cell vehicles are critical issues. In this chapter, fuel cell vehicle components are discussed in Section 6.2. Hybrid fuel cell system design and control for electric vehicles are presented in Sections 6.3 and 6.4, respectively. The fault diagnosis of hybrid fuel cell system is discussed in Section 6.5.

6.2 Fuel Cell Vehicle Components

Fuel cell power electric vehicle (FCV) uses hydrogen fuel as the major source of electric power to drive its electric traction motor through a fuel cell system. There are three major components in the FCV system. The first is the fuel cell and fuel cell subsystem, the second is the hydrogen storage or the fuel processor, and the third is the electric drive system.

6.2.1 Fuel Cell and Fuel Cell Subsystem

Since the principle of fuel cell operation has already covered in Chapter 2, this section will mainly focus on the fuel cell subsystems—gas flow management, water management, and heat management systems.

6.2.1.1 Gas Flow Management Subsystem

Oxygen and hydrogen are fed to the fuel cell system at an appropriate rate according to the current drawn from the load. Oxygen on the cathode side is often supplied with a higher stoichiometric flow rate because the cathode reaction is much slower than the anode reaction. Since the fuel cell voltage heavily relies on the air stoichiometric flow rate, the role of the compressor is very important to blow more air through the system. Another issue is related to the pressure control between the anode and cathode sides, which is to prevent the membrane from collapsing. With the help of a fast actuator on the cathode side whose performance setting time is 10%–90% of 50 ms, and another actuator on the anode side whose performance setting time is 10%–90% of less than 20 ms, it becomes possible to maintain the anode and cathode pressures at a certain level. To ensure this performance, the anode pressure controller must be three times faster than the one on the cathode side because the anode pressure follows the cathode side pressure [4]. An air compressor with an optimal speed can supply varying amounts of air for the power demand. Since an electric motor driving the compressor produces parasitic power loss, the compressor must be coordinated with the power management system in the fuel cell system, in order to reduce the power loss. For the direct hydrogen fuel cell system, hydrogen needs to be controlled at 100% relative humidity by the humidifier before entering the anode side of the fuel cell stack for proper operation. The recirculation of hydrogen is needed to improve the utilization of hydrogen. In order to avoid accumulation of gas and impurities at the inserts, a purging valve of hydrogen is also required.

6.2.1.2 Water Management Subsystem

To achieve high efficiency of a PEMFC, water management is crucial to the fuel cell system. Water management system has three main functions:

1. Proper hydration of the membrane
2. Removal of the produced water in the stack
3. Cooling of the stack to control the operating temperature

First, proper hydration of the membrane is related to the membrane conductivity, which greatly affects the stack performance at high power density operation. Second, proper removal of the produced water in each cell can keep the air flow passage from being blocked by the accumulated water and therefore avoid cell performance degradation. For the cooling of the system, it is closely related to the temperature control, which will be considered in the following section.

6.2.1.3 Heat Management Subsystem

The heat management, one of the important factors for the fuel cell mechanism and the warranty to maintain the stack temperature to the desired level, is directly related to the fuel cell performance [1,5,6].

Figure 6.1 shows that the polarization curve is shifted upward as the temperature increases. A number of control-oriented fuel cell models [4–21] have been developed under the assumption that the operating temperature is constant. Although controlling the temperature is vital for the fuel cell operation, those models proposed in [4–21] do not consider the temperature as a state variable due to its complexity. In [22], the temperature is defined as one of state variables and a control strategy is developed based on the transient thermal model of PEMFC [11,12,15].

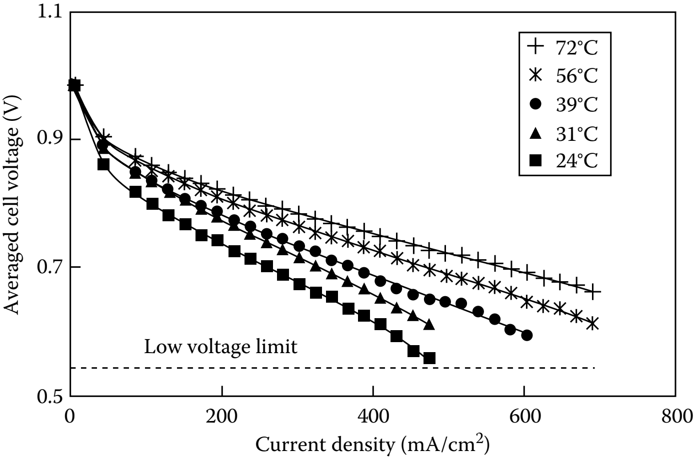

FIGURE 6.1
Polarization curves for difference temperatures. (From Larminie, J. and Dicks, A., *Fuel Cell Systems Explained*, Wiley, New York, 2002. With permission.)

Several thermal models of PEMFC have been reported in [11,12,15]. However, those models are not proposed for the purpose of control design, but for the mathematical analysis and their experimental validation instead. Based on the transient thermal models in [11,12,15], the control-oriented dynamic thermal model is developed in this section.

A transient energy balance is described by

$$\dot{Q}_{\text{stack}} = C_{\text{t}} \frac{\mathrm{d}T_{\text{s}}}{\mathrm{d}t} = P_{\text{tot}} - P_{\text{elec}} - \dot{Q}_{\text{cool}} - \dot{Q}_{\text{loss}} \tag{6.1}$$

where

$\dot{Q}_{\text{stack}}$ is the rate of heat absorption (J/s) by the stack
C_{t} is the thermal capacitance (J/C)
P_{tot} is the total power released by chemical reaction (W)
P_{elec} is the power consumed by the load (W)
$\dot{Q}_{\text{cool}}$ is the heat flow rate of the cooling system (heat exchanger)
$\dot{Q}_{\text{loss}}$ is the heat flow rate through the stack surface

The total energy can be calculated using the rate of hydrogen consumption:

$$P_{\text{tot}} = \dot{m}_{\text{H}_2\text{\_used}} \Delta H = \frac{\text{NI}_{\text{fc}}}{2F} \Delta H \tag{6.2}$$

where

ΔH is the enthalpy change for hydrogen (285.5 kJ mol/s)
$\dot{m}_{\text{H}_2\text{\_used}}$ is the hydrogen consumption rate

The electrical power output is given by

$$P_{\text{elec}} = V_{\text{st}} I_{\text{fc}} \tag{6.3}$$

The rate of heat removal by the cooling water is directly related to the water flow in the heat exchanger. The relationship is given as follows [4]:

$$\dot{Q}_{\text{cool}} = \dot{m}_{\text{cool\_water}} \cdot c_p \cdot \Delta T_{\text{s}} \tag{6.4}$$

where

$\dot{m}_{\text{cool\_water}}$ is the water pump flow (SLPM)
c_p is the specific heat coefficient of water (4182 J/kg K)
ΔT_{s} is the allowable temperature rise (10 K)

The water pump flow can be described by the time delay and conversion factor:

$$\dot{m}_{\text{cool\_water}} = \frac{k_{\text{c}}}{(1+\tau_{\text{c}} s)} u_{\text{cl}} \tag{6.5}$$

where τ_c is the time delay constant, 70 s, k_c is the conversion factor with a value 1.5, which means that if the control input u_{cl} for the heat exchanger ranges 0–10(V), $\dot{m}_{cool\_water}$ takes a value in the range between 0 and 15 (SLPM) with a 70 s delay.

The heat loss by the stack surface is calculated by the following equation:

$$\dot{Q}_{loss} = hA_{stack} \cdot (T_s - T_{amb}) = \frac{T_s - T_{amb}}{R_t} \tag{6.6}$$

where

hA_{stack}, stack heat transfer coefficient, is 17 W/K [11,12,15]

T_{amb} is the ambient temperature of about 25°C (298.15 K) ± 5%

R_t, the thermal resistance of the stack, which is the reciprocal of hA_{stack}, is 0.0588 K/W

The thermal time constant of the fuel cell is given by

$$\tau = R_t C_t = \frac{MC}{hA_{stack}} \tag{6.7}$$

where MC is the product of stack mass and average specific heat, 35 kJ/K, the thermal capacitance C_t is 35 kJ/K, and τ is 2059 s [10].

Equation 6.7 shows that the thermal equivalent circuit model can be developed by using the circuit analogy [17]:

$$C\frac{dv}{dt} = i \tag{6.8}$$

where the stack temperature corresponds to voltage, the energy flows (P_{tot}, P_{elec}, $\dot{Q}_{cool}$, and $\dot{Q}_{loss}$) correspond to current, and the thermal capacitance C_t corresponds to the capacitance.

In Figure 6.2, load variations cause the changes of the fuel cell stack temperature, and the fuel cell voltage and current are used as external inputs

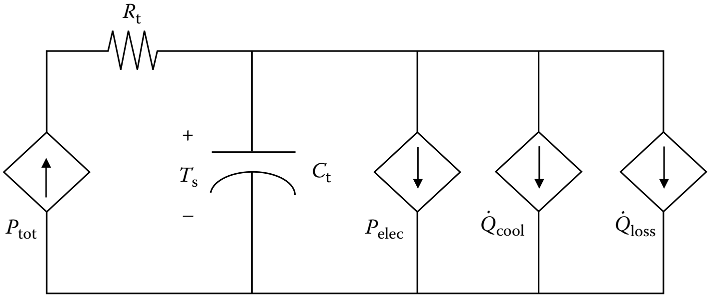

FIGURE 6.2
The thermal equivalent circuit of the fuel cell.

or disturbances, and then the stack temperature can be used as an output when designing the controller. The total power, P_{tot} depends on the hydrogen consumption which is based on the load changes and the electrical power, while P_{elec} depends on the load current. The cooling power $\dot{Q}_{cool}$ and the heat loss by the stack surface $\dot{Q}_{loss}$ are functions of the fuel cell stack temperature change. For this reason, four dependent energy flow sources have to be considered in the thermal equivalent circuit of the fuel cell shown in Figure 6.2.

6.2.2 Hydrogen Storage and Fuel Processor

The PEMFC needs to be supplied with hydrogen, which is the most abundant resource on Earth. It is a colorless and odorless gas, an ideal energy source because it has a very high energy density for its weight compared to an equivalent amount of gasoline, which means hydrogen generally produces much more energy than gasoline. For direct hydrogen fuel cell system, compressed gas or cryogenic liquid storage tank, or metal hydride energy storage (ES) needs to be installed in the vehicle.

The most common way to store hydrogen is to simply compress it in cylinders with high pressure to increase its density. The major concerns of compressed storage are the required large volume and the weight of gas containers which are normally made from steel alloy. Aluminum can be possibly used to make the body of the cylinder, but it is easy to be broken and currently expensive. Typically, storage pressures are between 200 and 450 bars (3000–6000 psi) [6]. In practice, storage densities are between 3% and 4% of hydrogen. The volume of these storage tanks ranges from 30 to 300 L [6].

At a temperature of 20 K and vapor pressure of 0.5 MPa, liquid hydrogen can be obtained. Cryogenic liquid hydrogen storage can be used if a large amount of hydrogen is needed. This cryogenic technology has been demonstrated in vehicle applications by Bavarian Motor Works (BMW), and shows that it can reach a storage efficiency of 14.2%. The main concerns of this technology are to maintain hydrogen at such low temperatures and to minimize hydrogen boil-off.

Metal hydride, in which metal atoms bond with hydrogen, is another means to store hydrogen. To release hydrogen from metal hydride, temperature over 100°C is required and therefore, it is not a good option for low-temperature PEMFC application. Even though metal hydride can take a large amount of hydrogen per unit volume, it has the problem of high alloy cost and low gravimetric hydrogen density, and it is heavy and sensitive to gases impurities.

Hydrogen can also be produced from hydrocarbon fuel such as natural gas, gasoline, or methanol through chemical processes: steam reformation, partial oxidation, and autothermal reformation [6]. A fuel processor is required for these chemical processes. Using fuel processor in vehicle applications causes

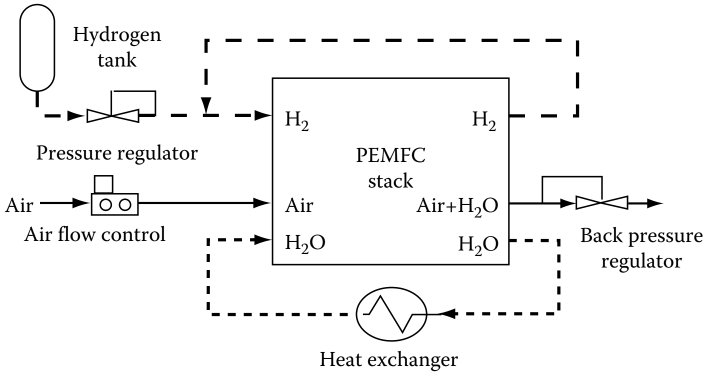

FIGURE 6.3
PEMFC stack based on PGS105B system. (From Hamelin, J. et al., *Int. J. Hydrogen Energ.*, 26, 625, 2001. With permission.)

another problem of slow dynamics due to the slow heat transfer processes, mass transfer and mixing delays [23]. To compensate the slow dynamics, a battery or an ultracapacitor is necessary for the ES during start-up, acceleration, and deceleration in the vehicle operations.

As an example of the practical fuel cell system using direct hydrogen tank, the Ballard MK5-E-based PGS105B system shown in Figure 6.3 is used to test the proposed nonlinear controller. This Ballard MK-5E system has a total of 35 cells, connected in series with a cell surface area of 232 cm^2. The membrane electrode assembly consists of a graphite electrode and a Dow™ membrane. The reactant gases (hydrogen and air) are humidified inside the stack, and the hydrogen is recirculated at the anode while the air flows through the cathode. The hydrogen pressure is regulated to 3 atm at the anode inlet by a pressure regulator and the Ballard fuel cell stack is maintained at 3 atm through a back pressure regulator at the air outlet. The oxidant flow rate is automatically adjusted to a constant value of 4.5 L/s for a programmable load, via a mass flowmeter to ensure sufficient water removal at the cathode. Hydrogen is replenished at the same rate as it is consumed. The stack temperature measured at the air outlet is maintained in a range from 72°C to 75°C by internal water to produce the maximum power output. The simplified diagram of the Ballard system is depicted in Figure 6.3. PGS105 system is more likely to be a presetting control system instead of a feedback control system. If it is out of the ranges of setting, the system is automatically shut down. The safety concern for the fuel cell system and the person operating this system must be handled with a high priority before a control scheme is implemented. For instance, a low cell voltage, stack overload, high temperature, hydrogen leaking detector, and pressure difference between the anode and the cathode must be considered in the fuel cell control system to prevent a fatal accident and severe damage to the fuel cell system.

6.2.3 Electric Drives Subsystem

A fuel cell vehicle is an "electric drive" vehicle. The rotating torque of the traction motor in the FCV is powered by electricity generated by the fuel cell. Induction motors, permanent magnet (PM) synchronous motors, and switched reluctance motors (SRMs) can be used for FCV applications [23]. More details about control and integration of electric drives system in FCV will be explained in the following sections.

6.3 Hybrid Electric Vehicles and Fuel Cell System Design for Electric Vehicles

Today, combustion engine/hybrid electric vehicles (HEVs) such as the Toyota Prius and Honda Civic Hybrid are very successful. However, HEV still heavily depends on oil. FCVs will, therefore, be the next wave of electric-drive vehicles after HEV, even though the issues of hydrogen refueling infrastructure and high cost of PEMFC have to be solved before commercialization. Before presenting the fuel cell vehicle architecture, it is necessary to describe hybrid vehicle architectures for a better understanding of the fuel cell vehicle technology because, generally, FCVs also belong to the HEVs. Since hybrid vehicle uses ICE and electric motor/generator, there are several series and parallel configurations. These hybrid vehicle technologies can increase the efficiency and fuel economy through the use of regenerating energy during braking and storing energy from the ICE coasting.

6.3.1 Series Hybrid Electric Vehicles

In series hybrid vehicles, the ICE mechanical output is first converted into electricity by a generator and the onboard battery charger uses dynamic braking energy from the motor to charge the battery (Figure 6.4). So, the converted electricity either charges the battery or can bypass the battery to propel the wheels via the same electric motor and mechanical transmission.

In series hybrid vehicles, ICE is operated at its optimal speed and torque according to its speed–torque characteristics, because it is fully decoupled from the driven train wheel. Hence, low fuel consumption and high efficiency can be achieved. The disadvantage of the series hybrid vehicle is that it has low efficiency compared to other parallel and combination configurations because it has two energy conversion stages (ICE/generator and generator/motor).

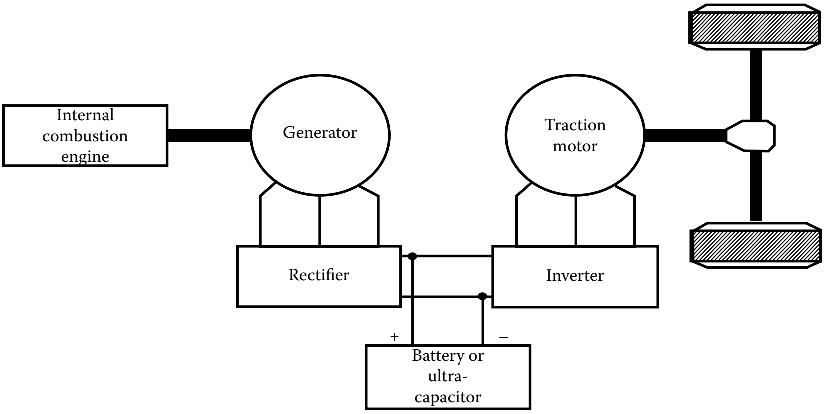

FIGURE 6.4
Series hybrid vehicle configuration. (From Emadi, A. et al., *IEEE Trans. Power Electron.*, 21(3), 567, 2006. With permission.)

There are six possible different operation modes in a series HEV [25]:

1. Battery alone mode: engine is off, vehicle is powered by the battery only
2. Engine alone mode: power from ICE/G
3. Combined mode: both ICE/G set and battery provide power to the traction motor
4. Power split mode: ICE/G power is split to drive the vehicle and charge the battery
5. Stationary charging mode
6. Regenerative braking mode

6.3.2 Parallel Hybrid Electric Vehicles

As shown in Figure 6.5, ICE and motor are connected in parallel to drive the wheels in the parallel HEV. It allows to choose from the three options: (1) both ICE and motor, (2) ICE alone, and (3) motor alone.

Normally at low speeds, the motor-alone drive strategy is preferred because it has a high efficiency than the ICE; the ICE is used at high speeds. Similar to a series HEV, during regenerating braking, the electric motor can be used as a generator to charge the battery and this battery can also absorb power from the ICE when the output power is greater than the required power.

The advantage of the parallel HEV is that it has fewer energy conversion stages than the series HEV, which leads to less power loss in the parallel HEV. Another advantage over the series HEV is that a smaller ICE and a smaller motor can be possible as long as enough battery energy is

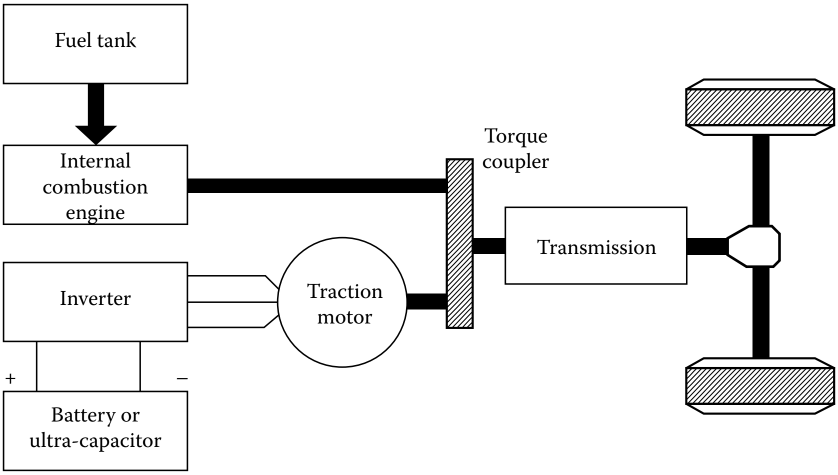

FIGURE 6.5
Parallel hybrid vehicle configuration. (From Emadi, A. et al., *IEEE Trans. Power Electron.*, 21(3), 567, 2006. With permission.)

provided. The following are the possible different operation modes of a parallel hybrid [25]:

1. Motor alone mode: engine is off, vehicle is powered by the motor only
2. Engine alone mode: vehicle is propelled by the engine only
3. Combined mode: both ICE and motor provide power to the drive the vehicle
4. Power split mode: ICE power is split to drive the vehicle and charge the battery (motor becomes generator)
5. Stationary charging mode

6.3.3 Series–Parallel Hybrid Electric Vehicles

To achieve both advantages of the series and parallel HEVs, their combination is considered in Figures 6.6 and 6.7. An additional mechanical link between the generator and the electric motor can be seen in Figure 6.6. Although the complex hybrid in Figure 6.7 is similar to the series—parallel HEV, the main difference is that the complex hybrid has a bidirectional power flow of the generator and the motor, but the series and parallel HEVs have unidirectional power from the generator.

Even though these drive strategies suffer from higher complexity and cost problems, many hybrid vehicles still use the combination configurations to adopt the advantages of series and parallel HEVs.

The following are the possible different operation modes of a complex hybrid:

1. Motor alone mode: engine is off, vehicle is powered by the motor only
2. Engine alone mode: vehicle is propelled by the engine only

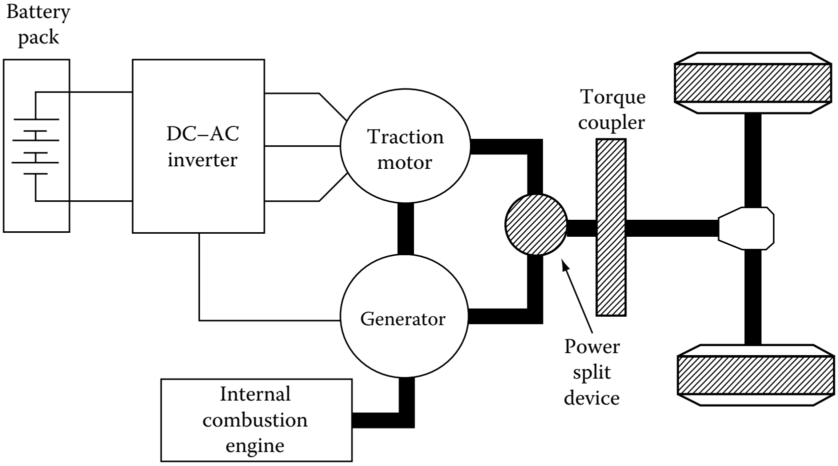

FIGURE 6.6
Series–parallel hybrid vehicle configuration. (From Emadi, A. et al., *IEEE Trans. Power Electron.*, 21(3), 567, 2006. With permission.)

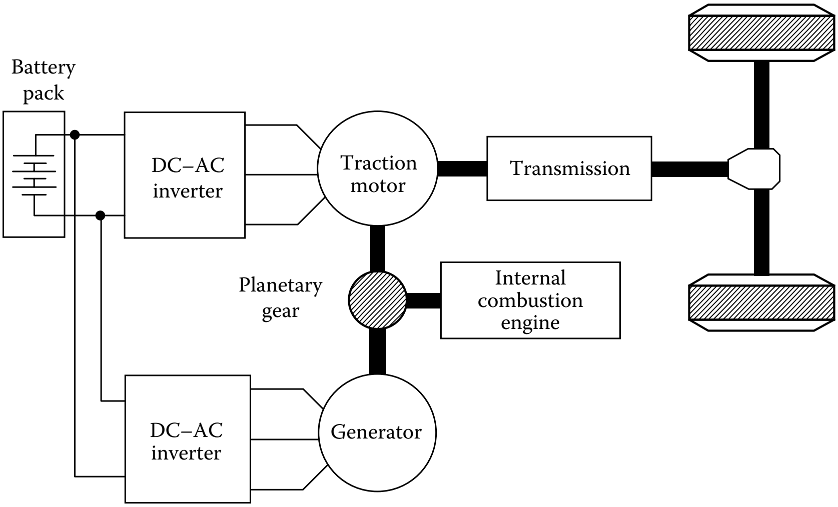

FIGURE 6.7
Complex hybrid vehicle configuration. (From Emadi, A. et al., *IEEE Trans. Power Electron.*, 21(3), 567, 2006. With permission.)

3. Combined mode: both ICE and motor provide power to the drive the vehicle
4. Power split mode: ICE power is split to drive the vehicle and charge the battery (motor becomes generator)
5. Generating mode (if battery is necessary to be charged, the generator is in active mode)

6.3.4 Fuel Cell Vehicle

As seen in Figures 6.8 and 6.9, FCV can be considered as a series type hybrid vehicle. A typical hybrid FCV is shown in Figures 6.8 and 6.9 where the direct hydrogen supply to fuel cell stack is employed. The hydrogen gas that feeds the fuel cell stack is stored in high-pressure tanks in the vehicle. The flow rates of hydrogen and oxygen vary according to the current drawn in the stack. The fuel cell output is fed to the power control unit (power converters)

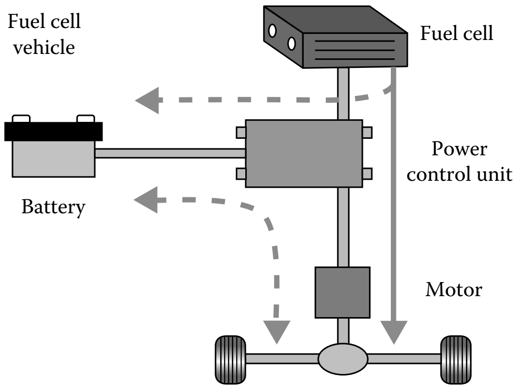

FIGURE 6.8
Hybrid FCV configuration (Toyota).

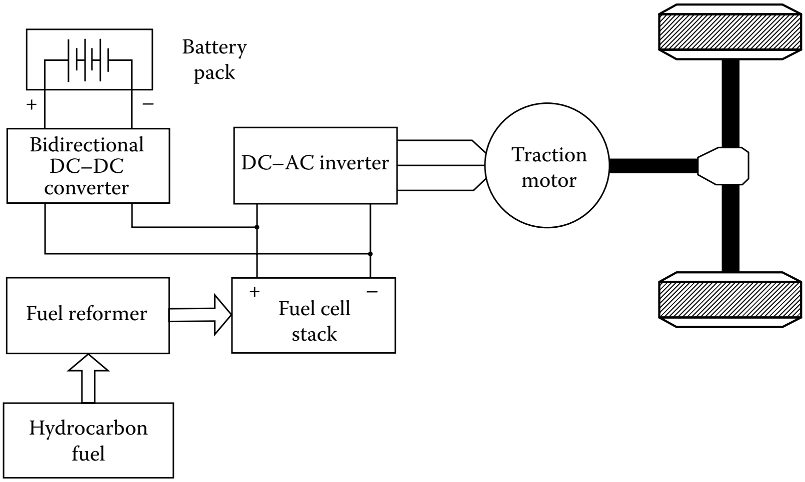

FIGURE 6.9
Typical hybrid FCV configuration. (From Emadi, A. et al., *IEEE Trans. Power Electron.*, 21(3), 567, 2006. With permission.)

to control the traction motor and the distribution of electric power from the fuel cell secondary ES (battery or ultracapacitor). Secondary ES not only provides additional power to the motor when accelerating, but also stores the power generated by braking. The traction motor generates the force to propel the vehicle.

Power conditioners in the power control unit must have minimal losses and higher efficiency up to 80%. This section discusses how to design and coordinate the energy management systems, including ES, electric motors, electric motor controller/inverter, and auxiliaries for FCV.

6.3.4.1 Energy Management Systems for Fuel Cell Vehicles

Detailed schematic diagram of the energy management system of the fuel cell vehicle is shown in Figure 6.10.

The fuel cell voltage is transferred to a higher level using DC–DC boost converter. The output of the boost converter is fed to a three phase DC–AC inverter. Because traction motor needs AC voltage, the DC–AC inverter converts the voltage from DC to AC with three phase variable voltage/frequency. The fuel cell power is also provided to the load of the electric-driven components in the balance-of-plant (BOP) systems such as pumps, fans, blowers, actuators, and so on, through another DC–DC converter in Figure 6.10. The fuel cell system needs to be equipped with a battery system to start up or

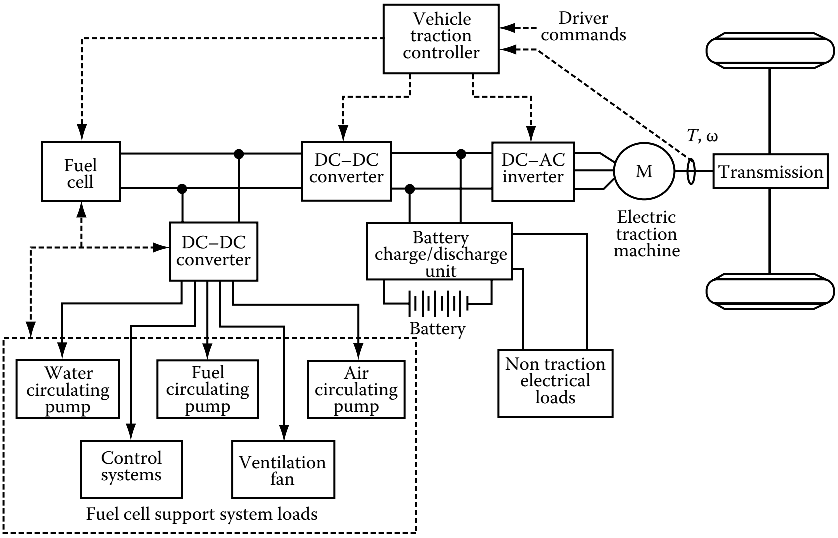

FIGURE 6.10
Detailed schematic diagram of the energy management system of the FCV. (From Emadi, A. et al., *IEEE Trans. Power Electron.*, 21(3), 567, 2006. With permission.)

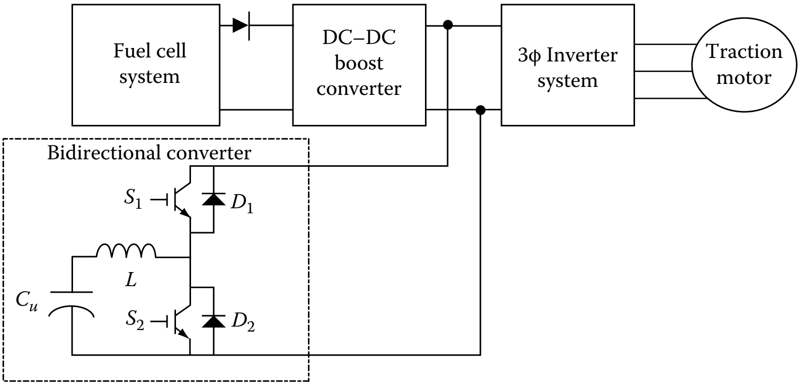

FIGURE 6.11
Energy management configuration in the FCV.

to supply peak load demand. The battery or ultracapacitor, serving as the secondary power source, can be used for both load leveling and regenerative brake energy capture. This secondary power source can be charged during the steady states from the fuel cell system and be discharged during the transient period when the fuel cell system responds to sudden load changes. The charging and discharging processes are carried out by the battery discharge/charge unit through the bidirectional DC–DC converter. For simplicity of the control design for the bidirectional converter, a simple buck/boost converter is used in Figure 6.11.

In the boost mode, the switch S2 and the diode D1 are on and then the ultracapacitor or battery can release the energy from the ES; in the buck mode, the switch S1 and the diode D2 are on and the energy from the braking can be stored in the ES unit.

6.3.4.2 Electric Motors and Motor Controller/Inverter for Fuel Cell Vehicle

A FCV consists of high-voltage components at a range of 300–400 V, such as traction motor, inverter drive systems, battery, DC–DC converter, and so on.

The power demand of the FCV electric motor ranges from 75 to 120 kW. With great progress in power electronics and microcontroller-based controllers, compact, cost effective and high-efficient inverters make the utilization of AC induction motor and brushless PM (BPM) motor in FCVs possible. In general, both of these motors provide high efficiency over a wide range of operations, but these motors require complicated control schemes such as space vector pulse width modulation (SVPWM) to produce the desired torque through processing of the feedback signals of the current and rotor position when compared to DC brush motors. Traction motor plays an important role in the FCV. The main characteristics of traction motor for vehicle applications are [26]:

- High torque density and power density
- High torque for starting at low speeds and hill climbing, and high power for high-speed cruising
- Wide speed range, with a constant power operating range of around three to four times the base speed being a good compromise between the peak torque requirement of the machine and the volt–ampere rating of the inverter
- High efficiency over wide speed and torque ranges, including low torque operation
- Intermittent overload capability, typically twice the rated torque for short durations
- High reliability and robustness appropriate for the vehicle environment
- Acceptable cost

The PM synchronous or PM brushless motors, induction motors, and SRMs in Figure 6.12 are used for traction applications.

Torque/power–speed characteristics required for traction applications are shown in Figure 6.13. Idealized torque/power–speed characteristics for these applications are illustrated in Figure 6.14.

In Figure 6.14, three torque/power regions are observed. In the constant torque region I, the maximum torque capability especially at low speed ranges is determined by the current rating of the inverter and the ratio of magnitude of inverter output voltage to inverter frequency is adjusted to maintain air-gap flux approximately constant in this region [27]. As the maximum available voltage of the inverter is reached, the constant torque region I is switched to the constant power region II. In this region, the stator voltage

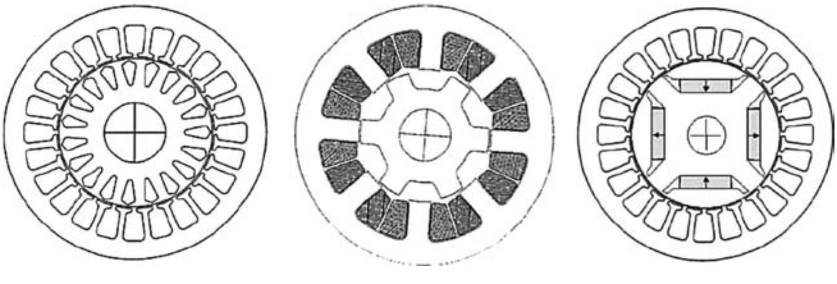

FIGURE 6.12
Main traction machine technologies [30]: (a) IM, induction machine; (b) SRM, switched reluctance machine; (c) PMM, permanent magnet machine.

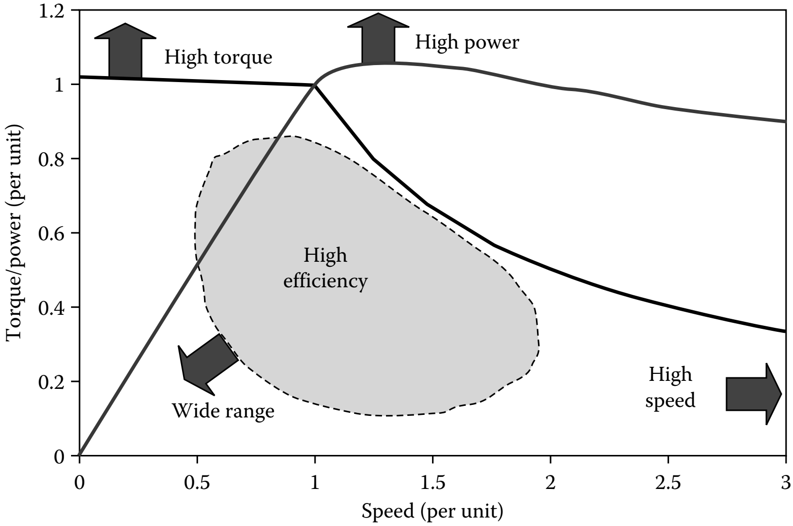

FIGURE 6.13
Torque/power requirements for traction machines. (From Zhu, Z.Q. and Howe, D., *Proc. IEEE*, 95(4), 746, 2007. With permission.)

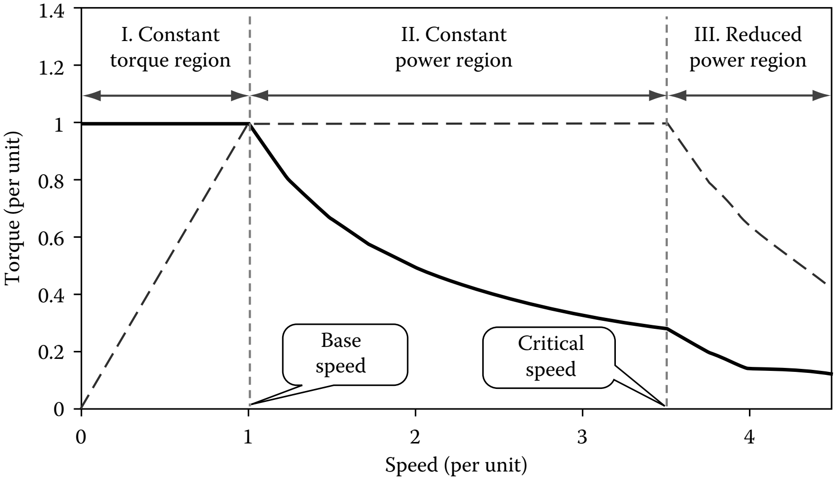

FIGURE 6.14
Idealized torque/power–speed characteristics for traction applications. (From Zhu, Z.Q. and Howe, D., *Proc. IEEE*, 95(4), 746, 2007. With permission.)

is held at its rated value and the stator current is regulated to obtain constant power [28]. The motor operates in flux-weakening due to the inverter voltage and current limits. As the frequency continuously keeps increasing in this mode, it operates with reduced air-gap flux by increasing slip to maintain the stator current at its limit. When slip is reached to a value corresponding to the pull-out torque, region II is switched to region III. In region III, the stator voltage is held at its rated value and the slip speed is regulated just below its pull-out torque value. Slip will be kept just below its pull-out torque value. The torque and the power reduce due to the increasing influence of the back electromotive force (EMF). In traction applications, a wide range of speed control and control beyond constant power range are also needed.

Since induction motors are simple and robust as well as having a wide speed range, it is desirable for traction application. Good dynamic torque control performance can be achieved by field-oriented control (vector control) or direct torque control because an induction machine can be modeled with *d–q* model so as to behave just like a DC machine [25]. However, the efficiency of an induction motor is lower than a PM motor due to the rotor loss and its size bigger than the same power- and speed-rated PM motor. The PM motor has a high efficiency, high torque, and high power density, but has a short constant range which can limit its field weakening capability when compared with an induction motor. The SRM is also a good candidate for traction application due to its simple and rugged construction, simple control, ability of extremely high speed operation, and harzard-free operation [25]. But, SRM has not been widely used and is much expensive than other motors. The motor controller–inverter system converts the power of the battery or the fuel cell DC power to AC power to control AC and BPM motors by insulated gate bipolar transistors (IGBTs) serving as the high power switching devices.

6.3.4.3 Auxiliary Systems in Fuel Cell Vehicles

Auxiliary systems in FCVs such as pumps, air conditioners, various sensors and gauges in the electric drive systems can work at voltages of 12, 140, 300 V or at the standard voltage of 42 V. The auxiliary systems as well as other systems must maintain high efficiency, low electromagnetic interface (EMI), electromagnetic compliance (EMC), and low cost. The design change/optimization of FCV varies based on the manufacturers and vehicle models. Basic design rules for hybrid FCV is to consider how to construct the energy management systems, electric motors, motor controller, and auxiliary systems as mention above. By downsizing the related electric drive systems and components, cost reduction is possible.

6.4 Control of Hybrid Fuel Cell System for Electric Vehicles

According to the FCV components described in Section 6.2, there are three major control modules of FCVs: drivetrain control including power control, motor/inverter control, and fuel cell control including a fuel processor. Using a fuel processor may make the system very complex. The detailed control descriptions of fuel cell processor are out of scope of this book, however, a simplified control of fuel cell processor will be described.

6.4.1 Drivetrain Control

Drivetrain control manages all signals of the driver and system operating condition signals such as key states (start-up or shutdown), accelerator pedal position, select gear or brake position, master cylinder pressure, temperature, displays of speed, torque, current, mileage, and so on. Based on the power demand of the electric motor on the road condition and vehicle capacity, the desired current signal is calculated through the main microprocessor, and then this calculated current signal is fed to the fuel cell control and power control modules. Since the drivetrain control is closely related to the power control in FCV, the following section will be helpful for the understanding of the drivetrain control.

6.4.2 Power Control

1. Power control: Power control module controls the power flow between the fuel cell system, the ES (battery or ultracapacitor), and the drivetrain, based on the motor power command and the energy level of the ES. Three power control modes are given as follows [24]:
    i. Standstill mode: It is an idle mode. Neither the fuel cell system nor the ES is inactive.
    ii. Braking mode: The fuel cell system is inactive, but the regenerative braking energy is absorbed into the ES until the ES is fully charged.
    iii. Traction mode: There are two cases in the traction model. One is the hybrid mode and the other is the sole mode. In the hybrid mode, if the command motor input power P_{comm} is greater than the fuel cell total rated power P_{fc}, the hybridization mode is active. So, the fuel cell system produces the rated power within its optimal operating region and the remaining power ($P_{\text{comm}} - P_{\text{fc}}$) is covered by the ES system. In the sole mode, if the command motor input power is less than the fuel cell-rated power, the energy difference between the fuel cell and the motor is absorbed by the ES system until it reaches its maximum charging level. In this case, the fuel cell system is the only source to drive the vehicle.

Once being fully charged, the ES system alone drives the vehicle until the energy level of the ES system reaches its minimum level.

2. Inverter control: Nowadays, the real-time microprocessor makes possible the advanced inverter switching method like SVPWM and vector control for AC induction motors. SVPWM is a special technique to determine the switching sequence of the upper level power of the three power transistors in a three-phase voltage source inverter. It can not only generate less harmonic distortions in the output voltages or current in the winding of the motor load, but also provides more efficient use of the DC input voltage, when compared with the sinusoidal PWM. For vector control of an AC induction machine, the machine has to be modeled in detail. In Appendices C and E, induction machine modeling, vector control, and SVPWM for HEV applications are described in detail. In Appendix D, explanation for the coordinate transformation of induction machine modeling and vector control is given. Here, indirect and direct field-oriented control schemes are introduced briefly. Since the time of the introduction to the field-oriented control, the indirect field-oriented control method has become more popular, due to its feasibility, for achieving a reliable and accurate speed and torque control than the direct method. The direct scheme electrically determines the rotor flux position using field angle sensors, while the indirect scheme determines the rotor flux from the calculation of the slip speed of the rotor. This field-oriented control is based on three major factors: (1) the machine current and voltage space vectors, (2) the transformation of a three-phase speed and time-dependent system into a two coordinate time invariant system, and (3) effective PWM pattern generation [28]. Because of these factors, AC machine can be modeled like DC machine and can achieve a good transient and steady-state control performance. Field-oriented controlled machines have two components: the torque component (aligned with the q coordinate) and the flux component (aligned with the *d* coordinate). In a conventional indirect vector control mode shown in Figure 6.12, the d-axis current producing the flux is controlled to be constant and the q-axis current producing the torque is controlled to have the machine to operate at the speed at which the machine supplies the maximum output power. Torque can be controlled by regulating i_{qs}^{e} and slip speed $\omega_e - \omega_r$. Rotor flux can be controlled by i_{ds}^{e} [27]. The main disadvantage of the indirect vector control is that it is too sensitive to motor parameters, and therefore, the accuracy of the control gain is highly required (Figure 6.15).

6.4.3 Fuel Cell Control

First of all, a fuel cell has a continuous supply of reactants adjusted by the load current. Hence, the internal states (humidity, temperature, and pressure)

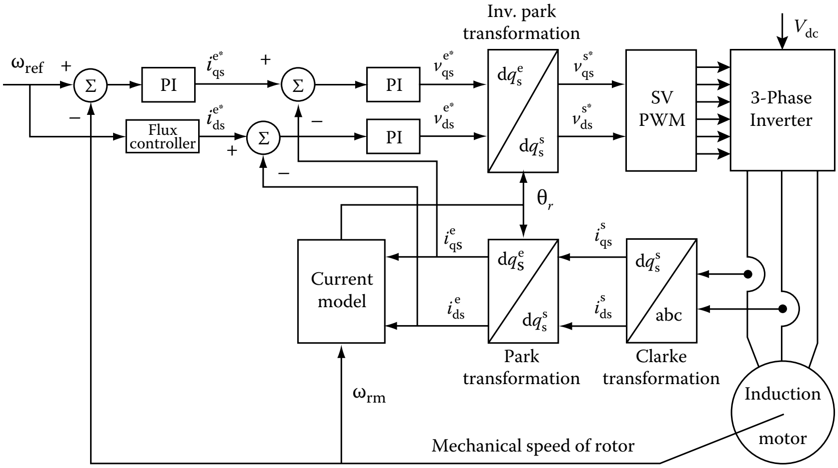

FIGURE 6.15
Indirect vector control scheme for induction machine. (From Toluyat, H. and Campbell, S., *DSP-Based Electromechanical Motion Control*, CRC Press, Boca Raton, FL, 2006. With permission.)

and external inputs (hydrogen and oxygen) have to be properly controlled to prevent from reactant starvation. The temperature of a fuel cell system reaches the steady state through the humidity controller and the temperature controller. The energy for the cold start-up of the fuel cell can be supplied by the backup battery (Figure 6.16).

Using a microprocessor or a DSP, the internal states and internal input can be controlled. The control scheme is shown in Figure 6.16. In Figure 6.16, control commands are issued for opening and closing the hydrogen solenoid valve and purge valve of the system. The speed of the air compressor varies according to the current demand. The speed of the cooling fan is controlled to regulate the fuel cell stack temperature through air compressor. The fuel cell operating temperature is maintained at 65°C by varying the speed of the cooling fan. In addition, the pressure difference between the anode and the cathode can be minimized to prolong the stack life by controlling the actuator on both anode and cathode sides.

6.4.4 Fuel Processor or Reformer

In [30], a simple model of a reformer that generates hydrogen through reforming methanol was introduced. Using a second-order transfer function model, the mathematical form of the fuel flow response to an input step of methanol flow is given as follows:

$$\frac{q_{H_2}}{q_{methanol}} = \frac{CV}{\tau_1\tau_2 s^2 + (\tau_1 + \tau_2)s + 1} \tag{6.9}$$

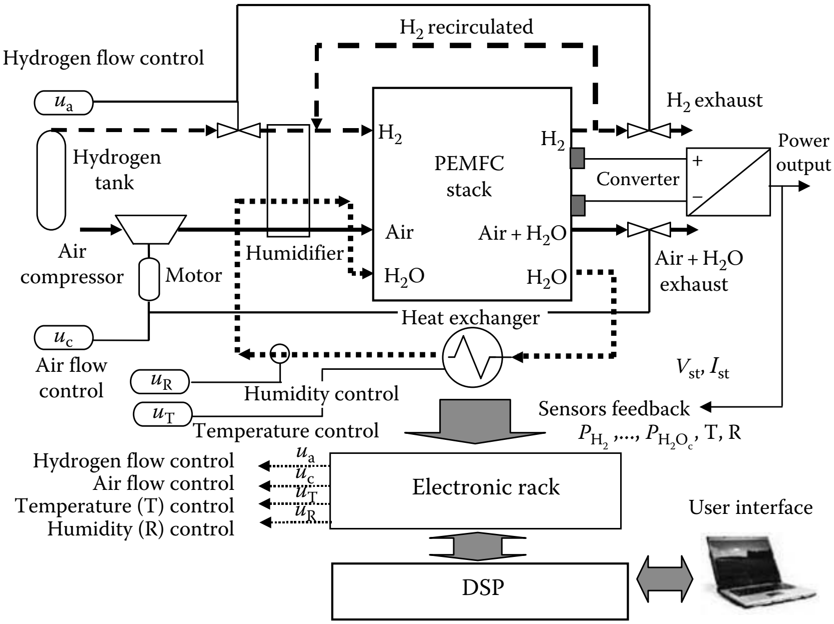

FIGURE 6.16
Simplified experiment setup for the PEMFC control. (From Na, W. and Gou, B., *IEEE Trans. Energy Convers.*, 23(1), 179, 2008. With permission.)

where

q_{H_2}, hydrogen flow rate [mol/s]
q_{methanol}, methanol flow rate [mol/s]
CV, conversion factor [kmol of hydrogen per mole of methanol]
τ_1, τ_2, reformer time constant [s]

A proportional integral (PI) controller determines the methanol flow into the reformer by controlling the hydrogen flow according to the current as shown in Figure 6.14. The oxygen flow is determined by the hydrogen–oxygen flow ratio r_{H-O} (Figure 6.17).

6.5 Fault Diagnosis of Hybrid Fuel Cell System

Fault diagnosis is to detect, isolate, and identify an impending or incipient failure condition—the affected component in the hybrid fuel cell system is still operational even though at a degraded mode. In this section, fault

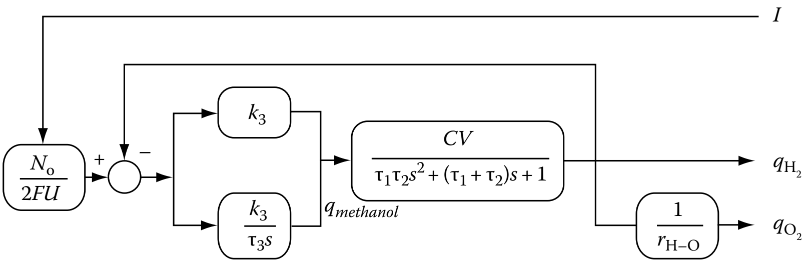

FIGURE 6.17
Reformer and reformer controller model. (From El-Sharkh, M.Y. et al., *IEEE Trans. Power Deliv.*, 19(4), 2022, 2004. With permission.) *Note: I*, stack current [A]; N_o, number of series of fuel cells in the stack; *F*, Faraday's constant [C/kmol]; *U*, fuel utilization factor; k_3, PI controller gain; τ_3, PI controller time constant; q_{O_2}, oxygen flow rate [mol/s]; r_{H-O}, hydrogen–oxygen flow ratio.

diagnostic issues and procedures will be described by using a practical system Nexa fuel cell stack of 1.2 kW [31].

6.5.1 Fuel Cell Stack

The 1.2 kW Nexa fuel cell stack output voltage varies with power, ranging from ~43 V without load to ~26 V with full load. During operations, the fuel cell stack voltage is monitored for fault diagnosis, control, and safety purposes. A cell voltage checker (CVC) system monitors the performance of individual cell pairs and detects the presence of a poor cell. The Nexa unit will shut down if a cell failure or a potentially unsafe condition is detected in the fuel cell stack.

6.5.2 Hydrogen Supply System

The fuel-supply system monitors and regulates the hydrogen supply to the fuel cell stack. The main concern of the fuel (hydrogen) supply system is the safety of hydrogen supply for the fuel cell. The fuel supply operation is taken into account in the following components:

- A pressure transducer monitors fuel delivery conditions to ensure an adequate fuel supply is present for Nexa system operation.
- A pressure relief valve protects downstream components from overpressure conditions.
- A solenoid valve provides isolation from the fuel supply when not in operation.
- A pressure regulator maintains appropriate hydrogen supply pressure to the fuel cell.

- A hydrogen leak detector monitors the hydrogen levels near the fuel delivery subassembly. Warning and shutdown alarms are implemented for product safety.
- The accumulation of nitrogen and water on the anode side degrades the fuel cell performance monitored by the purge cell voltage, and a hydrogen purge valve at the stack outlet is periodically opened to flush out inert constituents in the anode and to restore performance.

Only a small amount of hydrogen purges from the system, less than one percent of the overall fuel consumption rate. Purged hydrogen is discharged into the cooling air stream before it leaves the Nexa system. Hydrogen quickly diffuses into the cooling air stream and is diluted to a level much less than the lower flammability limit (LFL). The hydrogen leak detector, situated in the cooling air exhaust, ensures that flammable limits are not reached.

6.5.3 Air, Humidifier, and Water Management Systems

Like the anode side, the cathode side needs two actuators to control both the pressure and the air flow. These two actuators can minimize the pressure difference between the anode side and the cathode side, and control the air flow through the compressor because the fuel cell output voltage is largely dependent on the air flow.

Oxidant air has to be humidified for proper operation of fuel cells. Excess product water may cause flooding, which results in loss of cell potential. So, excess water needs to be evaporated passively into the surrounding environment, or alternatively, product water can be drained and collected through the water management system. However, small amount of water also causes membrane drying, which is one of the reasons to reduce cell potential. By monitoring the cell potential during the operation, flooding and drying will be alarmed.

6.5.4 Hydrogen Diffusion and Cooling Systems

The hydrogen quickly diffuses into the cooling air and is diluted to levels far below the LFL of hydrogen. For safety purpose, a hydrogen sensor is located within the cooling air outlet stream and it provides feedback to the control system. The control system generates warning and alarm signals if the hydrogen concentration approaches 25% of the LFL. The LFL of hydrogen is defined to be the smallest amount of hydrogen that will support a self-propagating flame when mixed with air and ignited. At concentrations less than the LFL, there is insufficient fuel present to support combustion. The LFL of hydrogen is 4% by volume.

6.5.5 Safety Electronics System

Unusual or unsafe operating conditions result in either a warning or alarm, and may cause an automatic shutdown, depending on the severity. During a warning, the Nexa power module continues to operate and the controller attempts to remedy the condition. During an alarm, the controller initiates a controlled shutdown sequence. There are two kinds of error levels [4].

First level errors

- Lower cell voltage: Alarm if one cell voltage drops below 0.3 V.
- Stack overload: It varies on the stack power capacity. If 125%–150% rate current is drawn, an alarm signal is activated.
- High temperature: The temperature exceeds 87.4°C.

Second level errors
These cases enforce the system to disconnect all power supply from the system components and all valves are set to their initial conditions.

- High-level hydrogen: According to the hydrogen sensor, when the hydrogen level is 15% over the LFL, an early alarm is triggered, and when 25% over the LFL, an error signal is turned on.
- Pressure difference protection: If the pressure difference between the anode and cathode sides is over 0.5 bar, an error signal is initiated.

References

1. J. Larminie and A. Dicks, *Fuel Cell Systems Explained*, New York: Wiley, 2002.
2. K. Rajashekrara, Propulsion system strategies for fuel cell vehicles, SAE paper 2000-01-0369, 2000.
3. F. Barbir and T. Gomez, Efficiency and economics of PEM fuel cells, *International Journal of Hydrogen Energy*, 22(10/11), 1027–1037, 1997.
4. C.A. Anderson, M.O. Christensen, A.R. Korsgaad, M. Nielsen, and P. Pederson, Design and control of fuel cells system for transport application, Aalborg University, Project Report, 2002.
5. J. Purkrushpan and H. Peng, *Control of Fuel Cell Power Systems: Principles, Modeling, Analysis and Feedback Design*, Germany: Springer, 2004.
6. F. Barbir, *PEM Fuel Cells: Theory and Practice*, London: Elsevier Academic Press, 2005.
7. J. Hamelin, K. Abbossou, A. Laperriere, F. Laurencelle, and T.K. Bose, Dynamic behavior of a PEM fuel cell stack for stationary application, *International Journal of Hydrogen Energy*, 26, 625–629, 2001.
8. W. Na and B. Gou, Nonlinear control of PEM fuel cells by feedback linearization, *IEEE Transactions on Energy Conversion*, 23(1), 179–190, 2008.

9. J. Purkrushpan, A.G. Stefanopoulou, and H. Peng, Control of fuel cell breathing, *IEEE Control Systems Magazine*, 24(2), 30–46, 2004.
10. J. Purkrushpan, A.G. Stefanopoulou, and H. Peng, Modeling and control for PEM fuel cell stack system, *Proceedings of the American Control Conference*, Anchorage, AK, 2002, pp. 3117–3122.
11. J.C. Amphlett, R.M. Baumert, R.F. Mann, B.A. Peppy, P.R. Roberge, and A. Rodrigues, Parametric modeling of the performance of a 5-kW proton exchange membrane fuel cell stack, *Journal of Power Sources*, 49, 349–356, 1994.
12. J.C. Amphlett, R.M. Baumert, R.F. Mann, B.A. Peppy, and P.R. Roberge, Performance modeling of the Ballard Mark IV solid polymer electrolyte fuel cell, *Journal of Electrochemical Society*, 142(1), 9–15, 1995.
13. R.F. Mann, J.C. Amphlett, M.A. Hooper, H.M. Jesen, B.A. Peppy, and P.R. Roberge, Development and application of a generalized steady-state electrochemical model for a PEM fuel cell, *Journal of Power Sources*, 86, 173–180, 2000.
14. M.J. Khan and M.T. Labal, Dynamic modeling and simulation of a fuel cell generator, *Fuel Cells*, 1, 97–104, 2005.
15. M.J. Khan and M.T. Labal, Modeling and analysis of electro chemical, thermal, and reactant flow dynamics for a PEM fuel cell system, *Fuel Cells*, 4, 463–475, 2005.
16. M.Y. El-Sharkh, A. Rahman, M.S. Alamm, A.A. Sakla, P.C. Byrne, and T. Thomas, Analysis of active and reactive power control of a stand-alone PEM fuel cell power plant, *IEEE Transactions on Power Delivery,* 19(4), 2022–2028, 2004.
17. P. Famouri and R.S. Gemmen, Electrochemical circuit model of a PEM fuel cell, *IEEE Power Engineering Society General Meeting,* 3, 13–17, 2003.
18. A. Sakhare, A. Davari, and A. Feliachi, Fuzzy logic control of fuel cell for standalone and grid connection, *Journal of Power Sources,* 135(1–2), 165–176, 2004.
19. P. Almeida and M. Godoy, Neural optimal control of PEM fuel cells with parametric CMAC network, *IEEE Transactions on Industry Applications,* 41(1), 237–245, 2005.
20. L.Y. Chiu, B. Diong, and R.S. Gemmen, An improved small-signal mode of the dynamic behavior of PEM fuel cells, *IEEE Transactions on Industry Applications*, 40(4), 970–977, 2004.
21. J. Sun and V. Kolmannovsky, Load governor for fuel cell oxygen starvation protection: A robust nonlinear reference governor approach, *IEEE Transactions on Control Systems Technology*, 3(6), 911–913, 2005.
22. W. Na and B. Gou, A Thermal Equivalent Circuit for PEM Fuel Cell Temperature Control Design, 2008 *IEEE International Symposium on Circuits and Systems*, Seattle, WA, May 2008.
23. W. Yang, B. Bates, N. Fletcher, and R. Pow, Control challenges and methodologies in fuel cell vehicle development, SAE paper 98C054, 1998.
24. A. Emadi, S.S. Williamson, and A. Khaligh, Power electronics intensive solutions for advanced electric, hybrid electric, and fuel cell vehicular power systems, *IEEE Transactions on Power Electronics*, 21(3), 567–577, 2006.
25. C.C. Chan, The state of the art of electric, hybrid, and fuel cell vehicles, *Proceedings of the IEEE*, 95(4), 704–718, 2007.
26. Z.Q. Zhu and D. Howe, Electrical machines and drives for electric, hybrid, and fuel cell vehicles, *Proceedings of the IEEE* 95(4), 746–765, 2007.
27. C.M. Ong, *Dynamic Simulation of Electric Machinery*, Upper Saddle River, NJ: Prentice Hall, 1997.

28. Texas Instruments Literature Number BPRA073, Field Oriented Control of 3-Phase AC motors, February 1998.
29. H. Toluyat and S. Campbell, *DSP-Based Electromechanical Motion Control*, Boca Raton, FL: CRC Press, 2006.
30. K.H. Hauer, Analysis tool for fuel cell vehicle hardware software (control) with an application to fuel economy comparisons of alternative system designs, PhD dissertation, Department of Transportation Technology and Policy, University of California, Davis, CA, 2001.
31. Ballard Power Systems Inc., *Nexa TM Power Module User's Manual MAN5100078*, Burnaby, BC, Canada: Ballard Power Systems Inc., October 2005.

7

Application of Fuel Cells in Utility Power Systems and Stand-Alone Systems

7.1 Introduction

Fuel cells ranging from subkilowatt portable power units to multimegawatt stationary power plants are emerging to deliver clean and efficient power. This new technology is suitable for producing heat and power for residential, commercial, and industrial customers. Because of high fuel conversion efficiency, combined heat and power generation flexibility, friendly siting characteristics, negligible environmental emissions, and lower carbon dioxide emissions, fuel cells are considered at the top of the desirable technologies for a broad spectrum of power generation applications. Among the available fuel cells, the polymer electrolyte membrane fuel cell (PEMFC) is seen as the system of choice for portable, vehicular, and residential applications.

In the United States, the Federal Energy Regulatory Commission has issued several rules and Notices of Proposed Rulemaking to set the road map for the utility deregulation. The California crisis has drawn great attention and sparked intense discussion within the utility industry. One possible solution is to rejuvenate the idea of integrated resource planning and promote the distributed generation (DG) via traditional or renewable generation facilities for the deregulated utility systems. The technology challenges of PEMFCs relating to the low-temperature operation include water management, heat removal, and anode poisoning by trace amounts of CO present in hydrocarbon-derived fuels.

Fuel cell is the most promising renewable generation technology for the residential and small commercial users. Fuel cells are static energy conversion devices directly converting the chemical energy of fuel into electrical energy. Compared with conventional power generation systems, they have many advantages, such as high efficiency, zero or low emission (of pollutant gases), and flexible modular structure. Fuel cell is a promising energy form that is expected to play an important role in future DG applications.

It is desirable for these renewable generation facilities to be interconnected with the utility grid to perform peak shaving, demand reduction, and to serve as emergency and standby power supply. However, the emerging integration problems including control strategy design, energy management, mismatch between the utility tie protection and the equipment protection, etc., need to be studied and solved. Fuel cell DGs can either be connected to a utility power system for network reinforcement or installed in a remote area to supply stand-alone power. This chapter is aimed to introduce the applications of fuel cells to the utility power systems and stand-alone applications.

7.2 Utility Power Systems and Residential Applications

One of the most important applications of fuel cells is utility power systems. The frequent occurrence of faults or big disturbances in power distribution systems causes the problem of loss of power supply; the energy transfer through the transmission network from generation plants in remote areas increase the energy cost. It is desirable to install renewable generation facilities near the customers to avoid the frequent occurrence of loss of power supply and the high energy cost. This section will discuss the technologies of fuel cell installation in the distribution systems.

7.2.1 Modeling and Control of PEMFC-Distributed Generation System

Wang et al. [1] proposed a typical configuration of fuel cell DG system, shown in Figure 7.1. The system configuration ratings and parameters are given in Table 7.1. PEMFC power plant consists of 10 parallel-connected fuel cell arrays. Each array is rated at 48 kW, for a total of 480 kW. A boost converter is used to adapt the output voltage of each fuel cell array to the DC bus voltage. In addition, a three-phase six-switch inverter is used to convert the power available at the dc bus to ac power. Following the inverter, a LC filter is applied, which is followed by a transformer to increase the ac voltage from 208 V to 12.5 kV, the voltage level of the utility grid.

The parameters used in this structure are given in Table 7.1.

7.2.1.1 Modeling of PEMFCs

To simplify the analysis, the following assumptions are made [2]:

1. One-dimensional treatment.
2. Ideal and uniformly distributed gases.
3. Constant pressures in the fuel cell gas flow channels.
4. The fuel is humidified and the oxidant is humidified air. Assume that the effective anode water vapor pressure is 50% of the saturated vapor pressure while the effective cathode water pressure is 100%.
5. The fuel cell works under 100°C and the reaction product is in liquid phase.

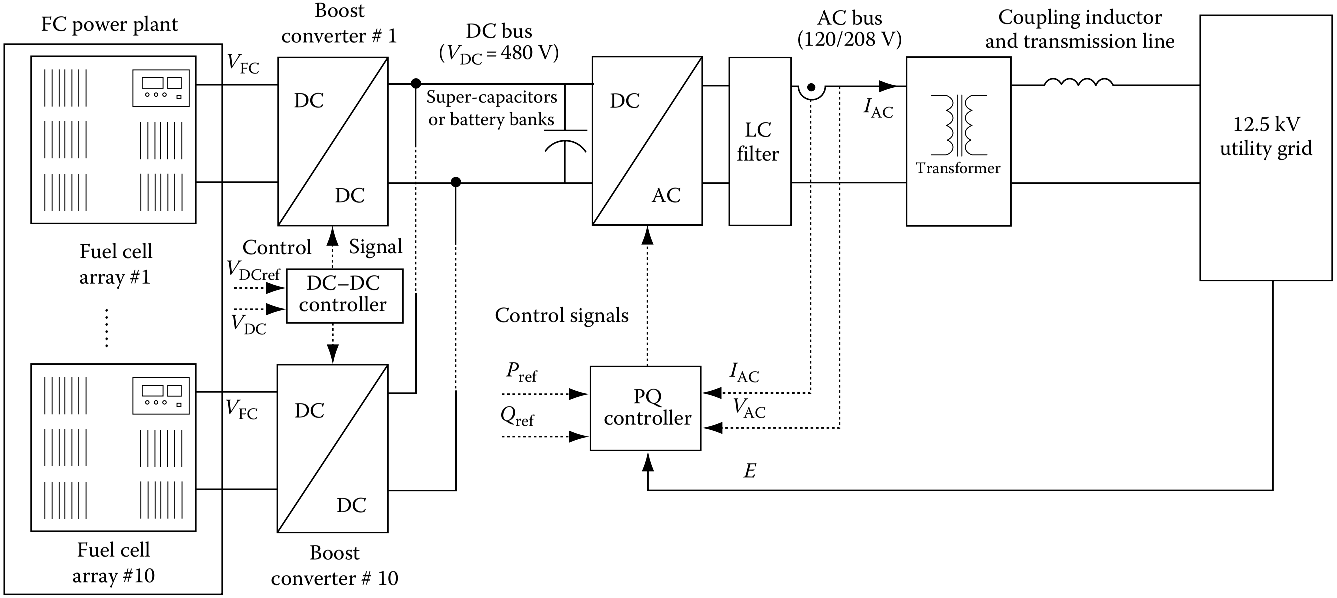

FIGURE 7.1
Block diagram of a fuel cell DG system. (From Wang, C. et al., *IEEE Trans. Energy Conver.*, 21, 586, 2006. With permission.)

TABLE 7.1

Configuration Parameters of the Proposed System

PEMFC power plant	216 V/480 kW Ten 48 kW fuel cell arrays are connected in parallel
PEMFC array	216 V/48 kW, consisting of 8 (series) × 12 (parallel) 500 W fuel cell stacks
Boost DC–DC converter	200 V/480 V, 50 kW each 10 units connected in parallel
3-Phase DC–AC inverter	480 V DC/208 V AC, 500 kW
LC filter	$L_f = 0.15$ mH, $C_f = 306.5\,\mu$F
Step-up transformer	$V_n = 208$ V/12.5 kV, $S_n = 500$ kW $R_1 = R_2 = 0.005$ p.u., $X_1 = X_2 = 0.025$ p.u.
Coupling inductor	$X = 50\ \Omega$
Transmission line	0.5 km ACSR 6/0 $R = 2.149\ \Omega$/km, $X = 0.5085\ \Omega$/km
DC bus voltage	480 V
AC bus voltage	120/208 V

6. Thermodynamic properties are evaluated at the average stack temperature, temperature variations across the stack are neglected, and the overall specific heat capacity of the stack is assumed to be a constant.
7. Parameters for individual cells can be lumped together to represent a fuel cell stack.

7.2.1.2 Equivalent Electrical Circuit

According to the assumptions, the output voltage of fuel cell is given as

$$V_{out} = E - V_C - V_{act1} - V_{ohm} \tag{7.1}$$

where

$$E = E_0 + \frac{RT}{2F}\ln\left(p^*_{H_2} \cdot \sqrt{p^*_{O_2}}\right) - E_d$$

$$V_C = -\frac{RT}{zF}\ln\left(1 - \frac{I}{I_{limit}}\right)$$

$$V_{act1} = \eta_0 + a(T - 298)$$

$$V_{ohm} = IR_{ohm}$$

where

R is the gas constant, 8.3143 J/(mol · K)

E_0 is the standard reference potential at standard state, 298 K and 1 atm pressure

T is the temperature (in Kelvin)

$p^*_{H_2}$ is the effective value of partial pressure of hydrogen

$p^*_{O_2}$ is the effective value of partial pressure of oxygen

I is the fuel cell current (A)

I_{limit} is the limitation current (A)

z is the number of electrons participating

F is the Faraday constant (96,487 C per mole)

R_{ohm} is the conducting resistance between the membrane and electrodes.

η_0 is the temperature invariant part of V_{act} (in volts)

a are the constant terms in Tafel equation (in volts per Kelvin)

From Equation 7.1, we can get an equivalent circuit of the fuel cell voltage, as in Figure 7.2.

7.2.1.3 Energy Balance of the Thermodynamics

The net heat casing its temperature to vary, which is generated by the chemical reaction inside the fuel cell, can be expressed as follows:

$$\dot{p}_{net} = \dot{p}_{chem} - \dot{p}_{elec} - \dot{p}_{sens+latent} - \dot{p}_{loss} \tag{7.2}$$

where $\dot{p}_{net}$, $\dot{p}_{chem}$, $\dot{p}_{elec}$, $\dot{p}_{sens+latent}$, and $\dot{p}_{loss}$ are net energy of fuel cell, chemical energy, electrical energy, sensible and latent heat, and the heat loss, respectively. Their values are given in [2].

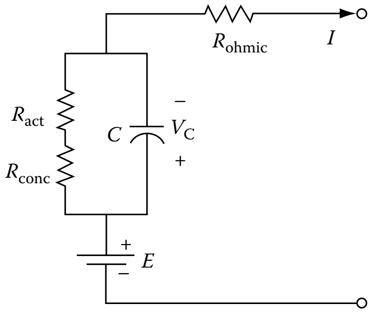

FIGURE 7.2
Equivalent electrical circuit of the double-layer charging effect inside the PEMFC.

7.2.1.4 Control Design for PEMFCs

Two controllers are designed for the boost DC–DC converter and the three-phase voltage source inverter.

7.2.1.4.1 Controller Design for the Boost DC–DC Converter

To design the controller for the boost DC–DC converter, we need to first build its state space model.

The equivalent circuit of the boost DC–DC converter is given in Figure 7.3.

The small signal state space model for the boost DC–DC converter is given as follows [1]:

$$\begin{bmatrix} \dot{i}_{L_{\mathrm{dd}}} \\ \dot{v}_{C_{\mathrm{dd}}} \end{bmatrix} = \begin{bmatrix} 0 & \dfrac{-(1-D)}{L_{\mathrm{dd}}} \\ \dfrac{1-D}{C_{\mathrm{dd}}} & \dfrac{-1}{RC_{\mathrm{dd}}} \end{bmatrix} x + \begin{bmatrix} \dfrac{X_2}{L_{\mathrm{dd}}} \\ \dfrac{-X_1}{C_{\mathrm{dd}}} \end{bmatrix} u$$

$$V_{\mathrm{dd\_out}} = \begin{bmatrix} 0 & 1 \end{bmatrix} \begin{bmatrix} i_{L_{\mathrm{dd}}} \\ v_{C_{\mathrm{dd}}} \end{bmatrix} \tag{7.3}$$

where X_1 and X_2 are the steady-state values of $i_{L_{\mathrm{dd}}}$ and $v_{C_{\mathrm{dd}}}$, respectively, and D is the pulse duty ratio at the rated operating point. Other variables are given in Figure 7.3.

A PI controller is designed based on Equation 7.3, whose parameters are given in Table 7.2.

7.2.1.4.2 Controller Design for the Three-Phase Voltage Source Inverter

A three-phase pulse-width modulation controller is designed for the inverter to satisfy voltage regulation as well as to achieve real and reactive power control. A voltage regulator is used in this design to take the error signals between the actual output voltage in *dq* frame ($V_{d,q}$) and the reference voltage

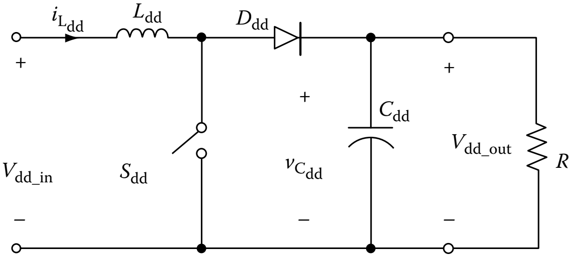

FIGURE 7.3
Boost DC–DC converter.

TABLE 7.2

Parameters of the Boost DC–DC Converter

L_{dd}	1.2 mH
C_{dd}	2500 μF
D_{N}	0.5833
R (equivalent load)	4.608 Ω
X_1	250 A
X_2	480 A
K_{di}	20
K_{dp}	0.02

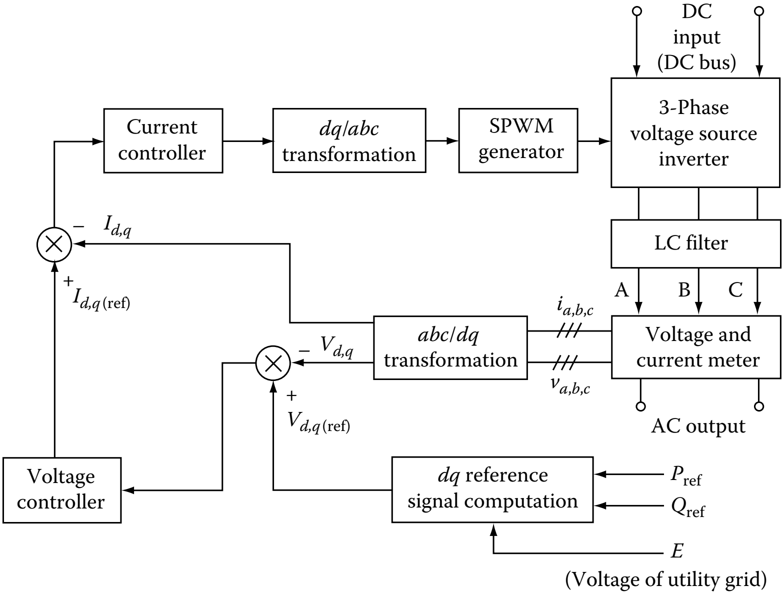

FIGURE 7.4
Overall control design for the three-phase voltage source inverter.

($V_{d,q(\mathrm{ref})}$) and generates the current reference signals ($I_{d,q(\mathrm{ref})}$) for the current control loop. The overall control design is given in Figure 7.4 [1].

7.2.2 Operation Strategies

In this section, we will introduce a concept of cogeneration of fuel cells for residential applications, proposed in [3]. Residential fuel cells have been launched recently. However, studies regarding hydrogen networks, hydrogen energy society, use of recovered heat from fuel cells in combined heat and power

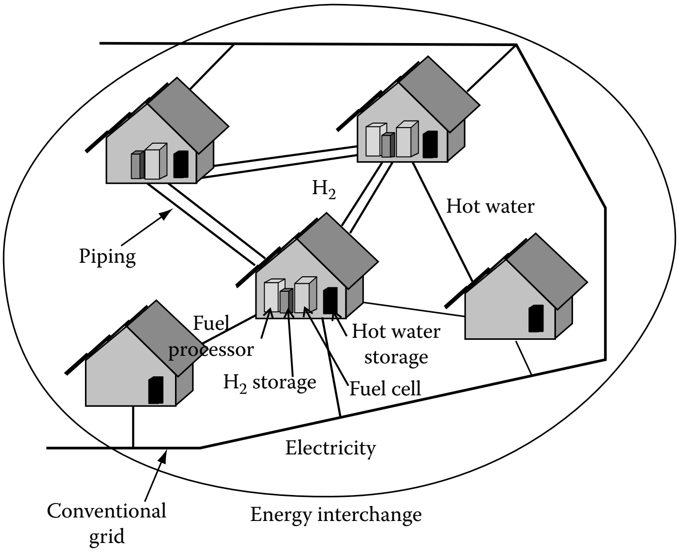

FIGURE 7.5
Example of proposed energy network for residential homes.

mode, and production and delivery of hydrogen are required. Neither a clear blueprint nor a clear path exists for achieving a future hydrogen energy society [4,5]. A cooperative and coordinated manner of operation and a hierarchical control of DG are necessary to avoid disorder and to sustain the reliability of power systems when a large number of DG systems are employed.

The concept of cogeneration via networked fuel cells is presented in Figure 7.5 [3]. Five homes are connected to the energy network, which provides the electricity interchangeable between the existing grid and fuel cells. Hot water piping is installed, and three homes are equipped with fuel cell stacks. Hydrogen is interchangeable between them via hydrogen piping. Two of these homes are also equipped with fuel processors that are constantly operated at their rated load without any interruption while producing hydrogen efficiently. The fuel cell stacks are operated depending on the load of the homes.

Based on the structure of the cogeneration network, four operation strategy (OS) rules were proposed and studied in [3].

OS Rule 0: The electricity dispatch of each fuel cell is generated to match the electricity demand of the home in which the fuel cell is installed. Electricity interchange is not available between them.

OS Rule 1: All the fuel cells equally share the total electricity demand of the homes.

OS Rule 2: A logic similar to that used for internal combustion engines and unit controls is applied. The fuel cells are switched on one by one as the electricity demand increases and vice versa.

OS Rule 3: The fuel cells are switched on one by one as the electricity demand increases, similar to Strategy 2; however, all the fuel cells, which are switched on, equally share the total electricity demand. In this strategy, Strategies 1 and 2 are combined.

Rule 0 is proposed as a baseline case of the analysis in this structure. Rule 1 deals with partial load operations, which provide higher electricity generation efficiencies and fuel cells can be operated for longer periods than in other Rules. Thus, Rule 1 provides efficient electricity supply rather than hot water supply. In Rule 2, the fuel cells are operated at partial load while the others at the rated load, which provides the highest heat recovery efficiency. This rule attempts to recover hot water (heat) from the fuel cells in the most efficient manner. Rule 3 is the intermediate one between Rules 1 and 2.

Details of this cogeneration concept and the simulation results can be found in [3].

7.3 Stand-Alone Application

The available power of a fuel cell power plant may not be able to meet load demand capacity, especially during peak demand or transient events encountered in stationary power plant applications. Normally, fuel cells need to work together with other sources to meet high load demand capacity. An ultracapacitor (UC) bank is commonly chosen for this purpose, which can supply a large burst of power, but it cannot store a significant amount of energy. Uzunoglu and Alam [6] proposed the modeling and control strategies for a combination of a fuel cell and an UC bank.

7.3.1 Dynamic Modeling of Fuel Cells and Ultracapacitor Bank

7.3.1.1 Modeling of Fuel Cell

A dynamic model was proposed in Figure 7.6 [6]. In this model, relationship between the molar flow of any gas (hydrogen) through the valve and its partial pressure inside the channel, and three significant factors—hydrogen input flow, hydrogen output flow, and hydrogen flow during the reaction—are considered.

Assuming constant temperature and oxygen concentration, the fuel cell output voltage can be expressed as follows:

$$V_{\text{cell}} = E + \eta_{\text{act}} + \eta_{\text{ohmic}}$$

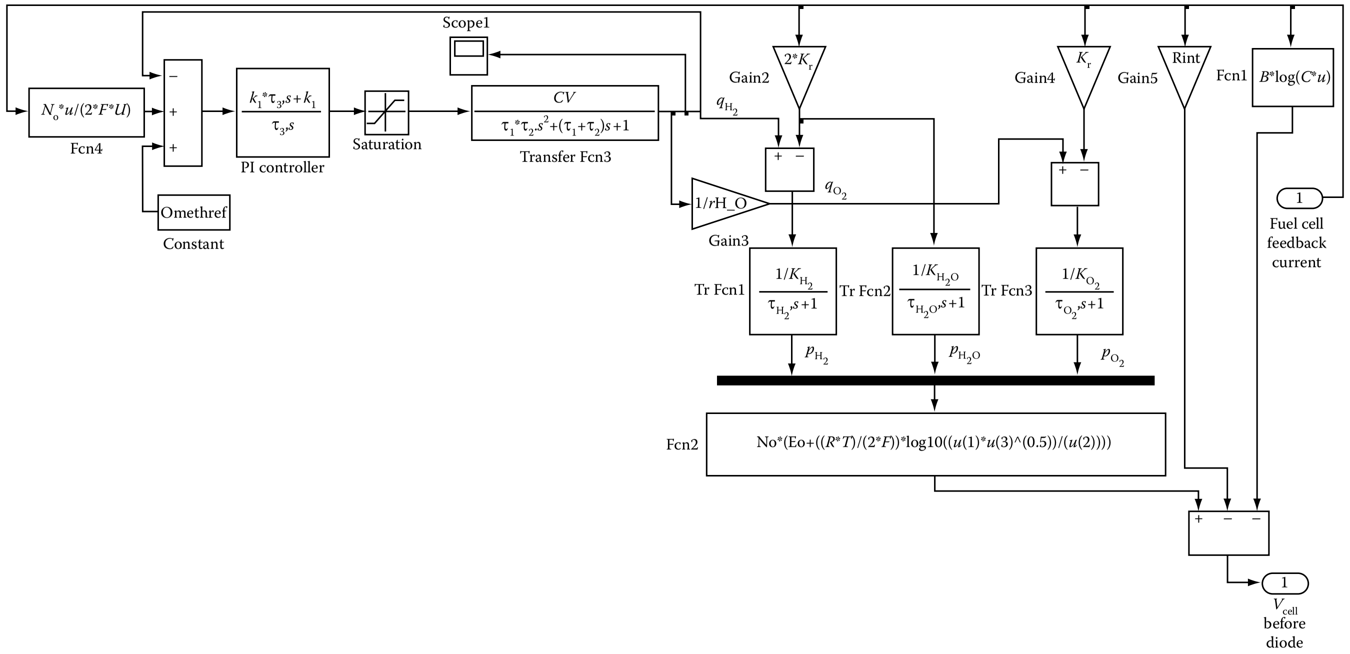

FIGURE 7.6
Dynamic model of fuel cell system.

where

$$\eta_{\text{act}} = -B\ln(CI'_{\text{FC}})$$

$$\eta_{\text{ohmic}} = -R^{\text{int}}I'_{\text{FC}}$$

and

$$E = N_0\left[E_0 + \frac{RT}{2F}\log\left[\frac{pH_2\sqrt{p_{O_2}}}{pH_2O}\right]\right]$$

The cell voltage is a sum of three voltages, which can be seen in Figure 7.6.

7.3.1.2 Modeling of Ultracapacitor Bank

The classical equivalent model of UC is given in Figure 7.7. It consists of an equivalent series resistance, an equivalent parallel resistance, and a capacitor. Due to the limited capacitor of an UC, a bank of UCs needs to be used via series and parallel connections.

7.3.2 Control Design of Combined Fuel Cell and Ultracapacitor Bank

In this structure, the fuel cell system and the UC bank are connected through a power diode, which is shown in Figure 7.8.

The fuel cell system, which decides the voltages of the UC bank and the load, prevents the power capability of the UC bank from being fully utilized. The power sharing between the fuel cell system and UC bank is determined by the total resistance between these two systems. The main control strategy for the combined system can be summarized as follows [6]:

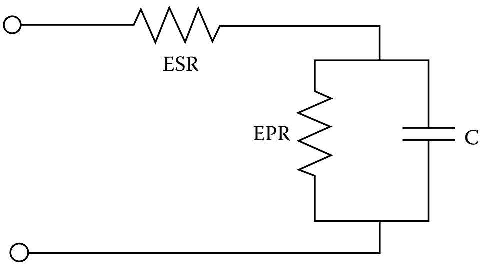

FIGURE 7.7
Classical equivalent model of ultracapicator.

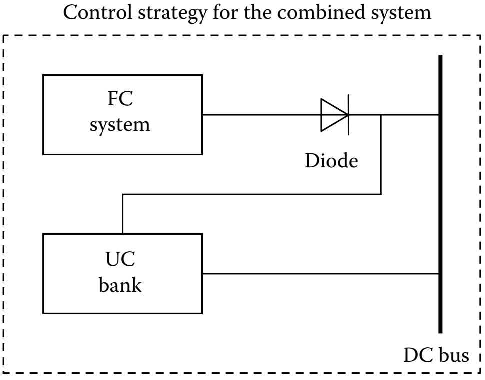

FIGURE 7.8
Combination of fuel cell system and UC Bank.

1. During low power demand periods (<5 kW), the fuel cell system generates up to its load limit and the excess power is used to charge the UC. The charging or discharging of the UC bank occurs according to the terminal voltage of the overall load requirements.
2. During high power demand periods (≥5 kW), the fuel cell system generates the rated power and the UC is discharged to meet the extra power requirements that cannot be supplied by the fuel cell system.
3. Short-time power interruptions in the fuel cell system can only be supplied by the UC bank.
4. The UC bank is designed to avoid overcharge or undercharge conditions.
5. About 75% of the initial energy stored in the UC bank can be utilized if the terminal load voltage is allowed to decrease to 50% of its initial value.

To realize the control system of the above mentioned combined system, PI controllers, ideal switching elements, and current and voltage sensors are used in the simulation model.

7.3.3 Active and Reactive Control for Stand-Alone PEMFC System

Based on the real power and reactive power of synchronized generators in power grids, a similar model for real power and reactive power control was proposed in [7].

Assume a lossless inverter and a small phase angle $\sin(\delta) \cong \delta$, using the output voltage and the output power and electrochemical relationships, the relationship between output voltage phase angle δ and hydrogen flow qH_2 is obtained:

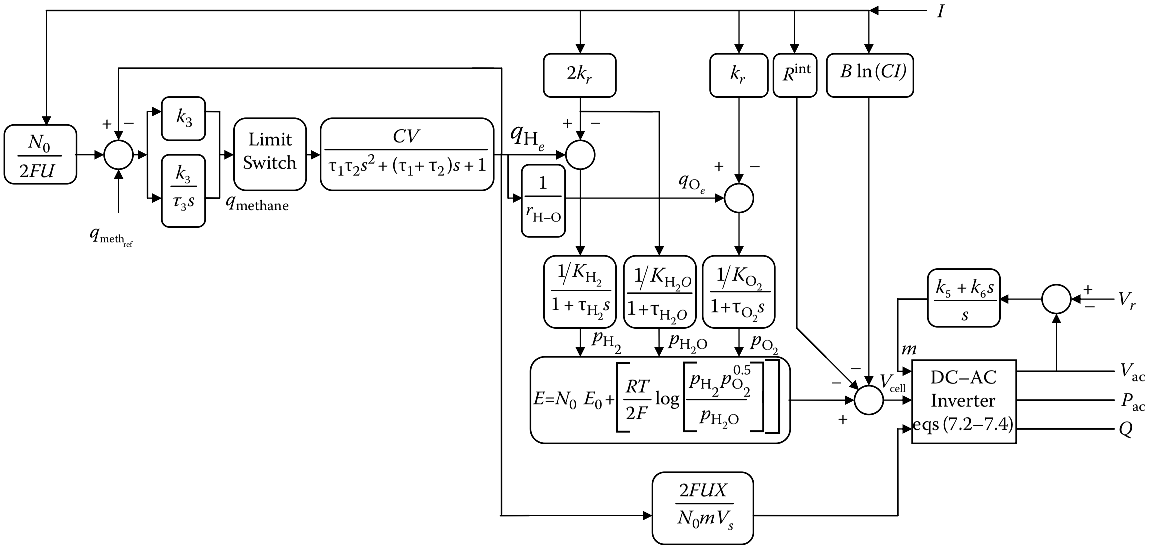

FIGURE 7.9
Real power and reactive power control for fuel cell system. (From El-Sharkh, M. et al., *IEEE Trans. Power Syst.*, 19(4), 2004. With permission.)

$$\delta = \frac{2FUX}{mV_s N_o} q\mathrm{H}_2$$

As we know, for synchronized generators, to increase the amount of steam input to the turbine can increase the output power, which is used to control the output power of synchronized generators. A similar scenario can be adopted to control the output power from the fuel cell system, the only difference is that there is no speed change, which can affect the frequency.

In the fuel cell system, the frequency is fixed at 60 Hz by the inverter. Figure 7.9 shows that the amount of hydrogen flow can be controlled manually or automatically according to the methane reference signal and the current feedback signal, respectively, and the current feedback signal is proportional to the terminal load. A limit switch is added to control the amount of hydrogen, which simulates the actual switch setting of the fuel cell system. Using the methane reference signal, $q_{\mathrm{meth}_{\mathrm{ref}}}$, the operator can manually set the power output from the fuel cell system to a value less than the maximum value set by the limit switch.

For a synchronized generator, controlling its reactive power is achieved by controlling the excitation voltage, which controls the generator output voltage and the amount of reactive power flowing in or out of the generator. In the fuel cell system, the reactive power can be controlled by the modulation index m. The modulation index controls the terminal voltage value, which also controls the reactive power output from the fuel cell system. The modulation index m can be set manually using the voltage reference signal V_r.

References

1. C. Wang, M.H. Nehrir, and H. Gao, Control of PEM fuel cell distributed generation systems, *IEEE Transactions on Energy Conversion*, 21, 586–595, 2006.
2. C. Wang, M.H. Nehrir, and S.R. Shaw, Dynamic models and model validation for PEM fuel cells using electrical circuits, *IEEE Transactions on Energy Conversion*, 20(2), 442–451, June 2005.
3. A. Hirohisa, Y. Shigeo, I. Yoshiro, K. Junji, M. Tetsuhiko, Y. Hiroshi, M. Akinobu, and I. Itaru, Operational strategies of networked fuel cells in residential homes, *IEEE Transactions on Power Systems*, 21(3), 1405–1414, 2006.
4. Fuel cell project team, Senior Vice-Minister Meeting: Report of Fuel Cell Project Team, Japanese Government (in Japanese), 2002.
5. U.S. Department of Energy, DOE releases long-term Hydrogen Posture plan, *Fuel Cells Bulletin*, 2004 (5), May 2004.
6. M. Uzunoglu and M.S. Alam, Dynamic modeling, design, and simulation of a combined PEM fuel cell and ultracapacitor system for stand-alone residential applications, *IEEE Transactions on Energy Conversation*, 21(3), 767–775, 2006.
7. M.Y. El-Sharkh, A. Rahman, M.S. Alam, A.A. Sakla, P.C. Byrne, and T. Thomas, Analysis of active and reactive power control of a stand-alone PEM fuel cell power plant, *IEEE Transactions on Power Systems*, 19(4), 2022–2028, 2004.

8

Control and Analysis of Hybrid Renewable Energy Systems

8.1 Introduction

Due to its capacity and operating characteristics, fuel cells normally work together with other alternative sources, for instance, the wind and the solar. Several main issues, including system configuration design, control methods, and power conditioning system design, need to be considered. Hybrid renewable energy power systems (HREPSs) combine two or more energy conversion devices, or two or more fuels for the same device, that when integrated, overcome limitations inherent in either. Characteristics of distributed energy resources are (1) normally located at or near the point of use, (2) locational value, and (3) distribution voltage [1].

The advantages of hybrid renewable energy systems are [1]:

- *Enhanced reliability*: Incorporating heat, power, and highly efficient devices (fuel cells, advanced materials, cooling systems, etc.) can increase overall efficiency and conserve energy for a hybrid system when compared with individual technologies.
- *Lower emissions*: HREPS can be designed to maximize the use of renewable resources, resulting in a system with lower emissions than traditional fossil-fueled technologies.
- *Acceptable cost*: HREPS can be designed to achieve desired attributes at the lowest acceptable cost, which is the key to market acceptance.

Different alternative energy sources can complement each other to some extent; multisource hybrid alternative energy systems (with proper control) have great potential to provide higher quality and more reliable power to customers than a system based on a single resource. Because of this feature, hybrid energy systems have caught worldwide research attention [2–12].

8.1.1 Wind Power

Wind power has been available for centuries as a source of mechanical power, and since the 1890s as a source of electrical power. Producing power from the wind is now more important than ever. It is currently one of the fastest growing sources of renewable energy in the United States with an approximately 30% annual increase over the last several years.

As a result of recent advances in technology, wind is becoming economically competitive with fossil fuels for power generation, especially in areas where electricity is expensive [13]. Lighter and stronger materials allow for greater energy capture and increase the lifespan of mechanical components. The newer generation of power and control electronics used in the conversion of wind to electricity includes the insulated gate bipolar transistor (IGBT) and the digital signal processor (DSP). The latest IGBTs have both faster switching times and higher power ratings than previous generations, and the modern DSPs have more computing power and higher speeds than previous digital controllers. Faster switching and higher speed processing means higher quality power is generated with less harmonic distortion. Higher power ratings and greater computing capability in a single chip allow for reduction in total number of electronic components, which means smaller, less expensive systems.

Technological advances are not the only reason for the recent growth in the wind industry. Today, we are much more aware of the environmental and political problems that are associated with using fossil fuels than we were a few decades ago. Although there is a wide spectrum of positions on environmental issues such as air pollution, global warming, and holes in the ozone layer, the debate now centers on the extent of the damage, not whether the damage is actually occurring. No one seriously believes that humans are not doing at least some damage to our environment. We will inevitably have to address this problem. Wind is obviously a much more environment-friendly source of energy than fossil fuels. No harmful emissions are produced and no water is consumed when generating power from the wind. One fact not widely known is that fossil fuel power generation consumes as much as 39% of the domestic freshwater used in the United States [14,15]. In the drier areas of the country, for example west Texas, optimizing water usage is critical for the sustainability and future growth of the populated areas, both urban and agricultural.

In addition to the environmental advantages of wind over fossil fuels, there are also political benefits to using wind power. Wind is both plentiful and renewable—the fuel is free and does not need to be conserved. There is more than enough wind available within our own borders to meet all our power demands far into the future. With the continued development and expansion of electric and hydrogen powered vehicles, we could reduce the amount of time, effort, and money spent on securing our foreign oil and gas supplies, which are also part of the hidden costs of fossil fuels. By producing a larger portion of the country's required power from domestically available resources, we could greatly reduce the potential for problems related to international politics.

8.1.2 Hybrid Power

The energy content of the wind varies with the cube of the wind speed. From Newton's laws, it is known that the kinetic energy of a given mass is proportional to the square of the velocity. Added to this is the fact that increasing the speed of the wind also increases the mass of the wind passing through a given plane proportionally. The result is that doubling the wind speed yields an eightfold increase in available energy.

However, the main disadvantage of the wind as a source of energy is its inherent variability. Wind energy comes in a form that typically varies with time. The energy can be collected only when it is available, which makes it unsuitable as a primary source. The traditional solution to this problem, particularly for isolated rural systems, is to supplement the wind turbine with a diesel generator; however, the wind–diesel combination does not entirely eliminate the problems associated with fossil fuel use.

8.1.3 Fuel Cell Power

An alternate remedy is to supplement the wind with hydrogen fuel cells, which offer the availability lacking in the wind while retaining many of the advantages. Wind turbines are efficient for the collection of energy, while fuel cells are efficient at producing electrical energy from hydrogen. Moreover, fuel cells continue to operate efficiently under part load conditions, while the efficiency of diesel generators drops substantially when operating away from the rated capacity.

Pure hydrogen is a clean, nonpolluting fuel. But it should be noted that the source of the hydrogen is an important consideration for a truly renewable power source. Hydrogen is potentially renewable if an electrolyzer is used with renewable sources like wind or solar power. Effectively, water (for the electrolyzer) is the only required fuel for such systems. Also, the hydrogen generated from electrolysis is generally of much greater purity than hydrogen from steam reformation of hydrocarbons.

Fuel cells alone could supply clean energy reliably, but at a much higher cost than the wind. Fuel cells typically cost three to five times more per kilowatt of generating capacity than wind turbines at present, and they require fuel [16]. An integrated system would use wind and fuel cells in a complementary fashion, offering the chance to provide steady renewable power at a lower cost. This can be achieved when hydrogen is generated by an electrolyzer and stored whenever wind power exceeds the load demand. Such a hybrid system could be connected to the utility network, adding reliability and security to it through distributed generation. A stand-alone version of the system could also provide power on demand for locations that are remote from the utility grid.

In this chapter, we introduce several typical designs of hybrid renewable energy systems.

8.2 Hybrid System Consisting of Wind and Fuel Cell Sources

8.2.1 Hybrid System Simulation Components and Equations

Figure 8.1 illustrates the hybrid wind turbine–fuel cell system model considered in a recent study [17], and Table 8.1 contains the associated system parameters and their values. The system is modeled using MATLAB® and

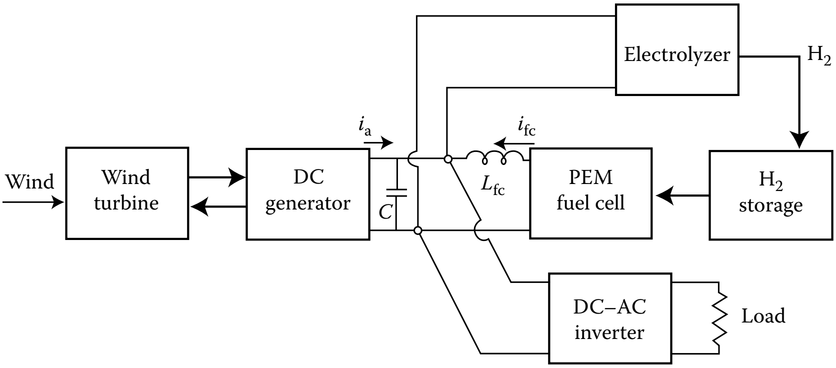

FIGURE 8.1
Complete hybrid wind turbine–fuel cell system.

TABLE 8.1

Parameter List for Wind Turbine–Fuel Cell System

Parameter	Value	Description
R	3.25 m	Wind turbine rotor radius
θ_P	2°	Fixed pitch of rotor blades
J_{eq}	$85\,\mathrm{kg \cdot m^2}$	Drivetrain moment of inertia
B_{eq}	$0.5\,\mathrm{N \cdot m \cdot s/rad}$	Drivetrain damping factor
N	14	Gearbox ratio
R_a	2.639 Ω	Armature resistance
L_a	34.6 mH	Armature inductance
R_f	335 Ω	Field winding resistance
L_f	156 H	Field winding inductance
K_g	0.08912	Generator constant
K_f	56	Field circuit voltage gain
N	220	Number of cells in fuel cell stack
A_C	$136.7\,\mathrm{cm^2}$	Cell-active area
V_A	$6.495\,\mathrm{cm^3}$	Volume of anode
V_C	$12.96\,\mathrm{cm^3}$	Volume of cathode
L_{fc}	25 mH	System interconnection inductance
C	25 mF	System interconnection capacitance

Simulink® software and is similar to that previously described by Iqbal [18] with some modifications and corrections. In particular, the following changes were made to the simulation model presented in [18]:

- Fuel cell stack equations replaced with a model provided by the U.S. Department of Energy (DoE) [19,20], with the DoE fuel cell controller modified to regulate stack voltage instead of fuel utilization.
- DC load replaced with a DC–AC inverter and AC load model.
- A wind turbine and fuel cell system interconnection (not specified by Iqbal), consisting of a filter capacitor and inductor, was added.
- Mathematical errors in the wind turbine model derivation were corrected.

A description of each of the subsystems and the governing equations is presented next.

8.2.1.1 Wind Turbine Subsystem

Wind energy is converted to electricity through the variable speed turbine and DC generator. The point wind speed u_i, as measured by an anemometer, is first translated to an effective wind speed u_e for use in the wind turbine model to account for the variations in forces and torque applied to the entire swept area of the turbine rotor. The effective wind speed is found by using a spatial filter in state-space form [21]:

$$\begin{aligned} \mathrm{d}u_1/\mathrm{d}t &= -\,0.6467u_iu_1 - 0.084335u_i^2u_2 + u_i \\ \mathrm{d}u_2/\mathrm{d}t &= u_1 \end{aligned} \tag{8.1}$$

where u_1 and u_2 are the state variables used to calculate the effective wind speed:

$$u_\mathrm{e} = 0.2242u_iu_1 + 0.084335u_i^2\,u_2 \tag{8.2}$$

The power coefficient C_P is the ratio of the mechanical power removed from the wind to the total power available in the wind passing through the turbine. The instantaneous C_P for a given wind turbine geometry is based on the tip speed ratio λ [22], which is the ratio of the speed of the rotor blade tip to the incoming wind speed: λ is one of the defining quantities used to determine the aerodynamic performance of a wind turbine. The tip speed ratio is thus given by

$$\lambda = \omega R/V_0 \tag{8.3}$$

where
ω is the rotational speed of the turbine
R is the rotor radius [22]

By allowing the rotor to change its speed as the wind speed changes, λ can be held constant, which means the C_P also remains constant, an important factor for maximum energy capture. A typical maximum C_P for real wind turbines is 0.4 due to losses.

The corresponding torque coefficient C_q may be found by

$$C_q = C_P/\lambda \tag{8.4}$$

The aerodynamic torque T_w induced on the rotor is defined as

$$T_w = (1/2)\rho\pi R^3 u_e^2\, C_q(\lambda)\cos^2(\theta) \tag{8.5}$$

where C_q is a function of λ. The θ in Equation 8.5 refers to the yaw misalignment angle between the wind velocity and the turbine axis. In [17], the yaw misalignment is assumed to be zero. The following equation is used to determine the torque coefficient C_q from the manufacturer's data for the considered wind turbine:

$$C_q(\lambda) = -0.0281 + 0.0385\lambda - 0.0046\lambda^2 + 0.000148\lambda^3 \tag{8.6}$$

The maximum value of C_q corresponds to a tip speed ratio of approximately 5.8. The torque calculation is subject to modification due to unsteady aerodynamics. The expected torque T_{we} on the rotor shaft is calculated from the aerodynamic torque T_w using a lead-lag filter in state-space form as given by [21]:

$$\begin{aligned} \mathrm{d}T_1/\mathrm{d}t &= -0.0793 u_e T_1 + T_w \\ T_{we} &= -0.0293 u_e T_1 + 1.37 T_w \end{aligned} \tag{8.7}$$

Finally, the equation describing the complete drivetrain torque balance on the wind turbine side is given as

$$J_{eq}(\mathrm{d}\omega/\mathrm{d}t) + B_{eq}\omega = T_{we} - NT_e \tag{8.8}$$

where

J_{eq} is the equivalent moment of inertia for the drivetrain

B_{eq} is the equivalent frictional damping coefficient

T_e is the electrical torque from the generator, which is multiplied by the gearbox ratio N (the gearbox is used to step up the shaft speed of the generator)

Wind speed input to the model is introduced as a constant speed, a step change in speed, or a variable speed profile. The variable speed wind is simulated by the SNwind v1.0 program, originally developed at Sandia National Laboratories and subsequently modified by the National Renewable Energy Laboratory. The SNwind program generates full-field turbulent wind data in three dimensions for specified meteorological conditions. The desired conditions for the SNwind simulation are given in an input parameter file.

The parameters include turbulence intensity, turbulence spectral model, average wind speed at a reference height, and height of the turbine rotor hub.

8.2.1.2 DC Generator Subsystem

A 5 kW DC generator with a separately excited field circuit is assumed to be used for converting the mechanical energy from the wind turbine to electrical energy. The armature circuit is connected to an external load through a commutator and brushes for unidirectional current flow. The DC generator provides good speed and torque regulation over a wide operating range and is more easily implemented for variable speed operation than an AC generator.

The field circuit is a series *R–L* circuit independent of the armature circuit. The differential equation describing the field circuit is

$$\mathrm{d}i_\mathrm{f}/\mathrm{d}t = (1/L_\mathrm{f})(K_\mathrm{f}V_\mathrm{fi} - R_\mathrm{f}i_\mathrm{f}) \tag{8.9}$$

where

i_f is the field current

R_f is the field winding resistance

L_f is the field inductance

V_fi is the input voltage to the field controller and is multiplied by the gain K_f to give the actual voltage V_f applied to the field circuit as

$$V_\mathrm{f} = K_\mathrm{f}\ V_\mathrm{fi} \tag{8.10}$$

The armature circuit located on the rotor is also modeled as an inductance and a resistance in series with a voltage. The voltage E_a across the armature, also called the air gap voltage, is related to the current in the field windings by the equation:

$$E_\mathrm{a} = K_\mathrm{g}\omega_\mathrm{m}(206.7i_\mathrm{f}^3 - 760.75i_\mathrm{f}^2 + 982.3i_\mathrm{f} + 5.26) \tag{8.11}$$

Equation 8.11 is derived from the generator saturation characteristics provided by the manufacturer: K_g is a constant that depends on the construction of the generator–rotor size, number of rotor turns, and other details, and ω_m is the generator rotor speed, which is *N* times faster than the wind turbine rotor speed ω as a result of the gearbox ratio. The differential equation describing the armature circuit is

$$\mathrm{d}i_\mathrm{a}/\mathrm{d}t = (1/L_\mathrm{a})\left[E_\mathrm{a} - i_\mathrm{a}(R_\mathrm{L} + R_\mathrm{a})\right] \tag{8.12}$$

where

i_a is the armature current

R_a is the armature resistance

L_a is the armature inductance

Equation 8.12 is similar to Equation 8.9 for the field circuit; however, the equivalent load resistance R_L is added to the armature resistance R_a in the case of the armature circuit. The electrical torque generated is found by dividing the electrical power (voltage E_a times the armature current i_a) in the armature circuit by the generator rotor speed so that

$$T_e = E_a i_a / \omega_m \tag{8.13}$$

8.2.1.3 Wind Turbine and DC Generator Controller

The controllers used for the generator portion of the combined wind–fuel cell system model in [17] are discrete-time proportional–integral–derivative (PID) controllers derived by the backward difference method. The backward difference method is based on Euler's method, and is unconditionally stable [23]. The general transfer function for the controller is [24]:

$$G(z) = (q_0 + q_1 z^{-1} + q_2 z^{-2})/(1 - z^{-1}) \tag{8.14}$$

The form of the controller used in the simulation is

$$y(k) = y(k-1) + q_0 e(k) + q_1 e(k-1) + q_2 e(k-2) \tag{8.15}$$

where

$e(k)$ is the error (controller input) signal

$y(k)$ is the controller output signal

The q terms are obtained from the PID constants:

$$\begin{aligned} q_0 &= K_p\,[1 + (T_d/T_s)] \\ q_1 &= K_p\,[(T_s/T_i) - 2(T_d/T_s) - 1] \\ q_2 &= K_p (T_d/T_s) \end{aligned} \tag{8.16}$$

where K_p, T_i, and T_d are the proportional, integral, and derivative constants, respectively. A sampling time of T_s is used for the controller. The original form of the controller used by Iqbal was retained; only the gains were adjusted. All PID control parameters are listed in Table 8.2.

For the below rated wind speed condition, the wind turbine is operated in a variable speed mode. The lambda-controller attempts to maintain a constant tip speed ratio of $\lambda = 6.5$ by adjusting the field voltage applied to the generator. The value of $\lambda = 6.5$ rather than the optimal value of 5.8 was used for convenience, since proper regulation to this lambda value then results in a rotor speed (in rad/s) that is simply twice the wind speed (in m/s). Above the rated wind speed of $u_e = 8$ m/s, the wind turbine is regulated by the omega-controller to a constant rotor speed of $\omega = 16$ rad/s. Again, control is achieved by adjusting the generator field voltage.

TABLE 8.2

Parameter List for Discrete- and Continuous-Time PID Controllers

Parameter	Value	Description
K_p	0.003	Omega-control proportional constant
T_i	5	Omega-control integral constant
T_d	1	Omega-control derivative constant
T_s	0.25	Omega-control sample period
K_{plm}	2.5×10^{-4}	Lambda-control proportional constant
T_{ilm}	0.08	Lambda-control integral constant
T_{dlm}	0	Lambda-control derivative constant
T_{slm}	0.25	Lambda-control sample period
K_{pfc}	4	Fuel flow-control proportional constant
K_{ifc}	1	Fuel flow-control integral constant
K_{dfc}	1	Fuel flow-control derivative constant

8.2.1.4 Polymer Electrolyte Membrane Fuel Cell Subsystem

This is described here for the sake of completeness. The model of the PEMFC in [17] begins with the ideal potential defined by the Nernst equation as described in Larminie and Dicks [25], which relates the concentrations of reactants and products to the potential difference produced by an electrochemical reaction under equilibrium conditions. The fuel cell model provided by the DoE for the 2001 Future Energy Challenge student design competition [19,20], was then used to construct the cell voltage equation as

$$V = N\left[OCV + \frac{RT}{2F}\ln\left(\frac{PH_2(PO_2/P_{std})^{1/2}}{PH_2O}\right) - L\right] \tag{8.17}$$

which has also been previously described in Chapter 3.

The actual voltage produced by the PEMFC is derived by subtracting the irreversible losses L from the ideal potential defined above [25]. These irreversible losses fall into four primary categories: activation losses, ohmic losses, concentration losses, and internal current losses. The voltage losses L can be described by

$$L = (i + i_n)r + a\ln\left(\frac{i + i_n}{i_o}\right) - b\ln\left(1 - \frac{i + i_n}{i_l}\right) \tag{8.18}$$

as discussed in Chapter 3.

The partial pressures of hydrogen, oxygen, and water are defined as the three state variables of the system. Also, since water management affects the fuel cell's performance, humidifiers are used on both anode and cathode

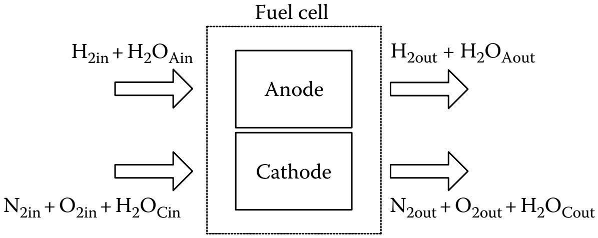

FIGURE 8.2
Illustration of gases flow of the PEMFC.

sides to control the humidity inside the cell. The consideration of water on the cathode side is more complicated than on the anode side because it includes not only the water supplied from the humidifiers, but also the by-product of the reaction.

Figure 8.2 is an illustration depicting how these gases flow in and out of the cell.

Based on the ideal gas law $PV = nRT$, the partial pressure of each gas is proportional to the amount of the gas in the cell, which is equal to the gas inlet flow rate minus gas consumption and gas outlet flow rate. Thus the state equations are

$$\begin{aligned}\frac{\mathrm{d}PH_2}{\mathrm{d}t} &= \frac{RT}{V_A}\left(H_{2in} - H_{2used} - H_{2out}\right)\\ \frac{\mathrm{d}PO_2}{\mathrm{d}t} &= \frac{RT}{V_C}\left(O_{2in} - O_{2used} - O_{2out}\right)\\ \frac{\mathrm{d}PH_2O_C}{\mathrm{d}t} &= \frac{RT}{V_C}\left(H_2O_{Cin} + H_2O_{Cproduced} - H_2O_{Cout}\right)\end{aligned} \tag{8.19}$$

where

H_{2in}, O_{2in}, and H_2O_{Cin} are the inlet flow rates of hydrogen, oxygen, and water on cathode side, respectively
H_{2out}, O_{2out}, and H_2O_{Cout} are the outlet flow rates of each gas

Furthermore, H_{2used}, O_{2used}, and $H_2O_{Cproduced}$ represent usage and production of the gases, which are related to output current I by

$$H_{2used} = 2O_{2used} = H_2O_{Cproduced} = 2K_rI = 2K_rA_ci \tag{8.20}$$

where

$K_r = N/4F$ in mol/C
A_c is the cell-active area in cm^2
i is the current density in A/cm^2

Since the inlet flow rates and output current are measurable, the outlet flow rates can be defined by the equations:

$$\begin{aligned} H_{2\text{out}} &= (\text{Anode}_{\text{in}} - 2K_r A_c i)FH_2 \\ O_{2\text{out}} &= (\text{Cathode}_{\text{in}} - K_r A_c i)FO_2 \\ H_2O_{\text{Cout}} &= (\text{Cathode}_{\text{in}} + 2K_r A_c i)FH_2O_C \end{aligned} \tag{8.21}$$

where

Anode_{in} and $\text{Cathode}_{\text{in}}$ are the summations of anode inlet flow and cathode inlet flow, respectively, as defined in Figure 8.2

FH_2, FO_2, and FH_2O_C are the pressure fractions of each gas inside the fuel cell

For this DoE model

$$\begin{aligned} FH_2 &= \frac{PH_2}{P_{\text{op}}} \\ FO_2 &= \frac{PO_2}{P_{\text{op}}} \\ FH_2O_C &= \frac{PH_2O_C}{P_{\text{op}}} \end{aligned} \tag{8.22}$$

where it is assumed that the cell pressure remains constant at P_{op}, a steady-state operating pressure of 101 kPa.

8.2.1.5 Fuel Cell Controller

A continuous PID controller adjusts the fuel flow rate of the hydrogen at the fuel cell inlet to control the fuel cell stack voltage. The controller transfer function is described by

$$G(s) = K_{\text{pfc}} + (K_{\text{ifc}}/s) + sK_{\text{dfc}} \tag{8.23}$$

Again, the controller parameter values are listed in Table 8.2.

The flow rate for the air in the simulations performed in [17] was fixed at a large enough value that is more than sufficient to match the hydrogen flow needed to satisfy the given fuel cell current demands. The fuel flow controller's objective is to regulate the inverter input voltage to a steady-state value of 200 V after the stack is activated to supplement the available wind power. If the voltage starts to fall below this value, the hydrogen flow rate is increased to compensate. If the voltage starts to rise above this value (when the wind power is sufficient to supply the load), the flow rate signal is reduced by the controller, and fuel cell current drops to zero.

8.2.1.6 Electrolyzer Subsystem

When the available wind power is insufficient to supply the load, the fuel cell delivers additional electricity by converting the stored hydrogen. But if the wind is strong enough to completely supply the load, the fuel cell becomes inactive, and any excess wind energy can then be sent to the electrolyzer to recharge the hydrogen storage.

The unipolar Stuart electrolyzer's operation is governed by the equation:

$$X_{H_2} = 5.18e^{-6} i_{elec} \tag{8.24}$$

where

X_{H_2} is the flow rate of hydrogen in mol/s

i_{elec} is the current through the electrolyzer [26], which is equivalent to 0.0128 moles per second per ampere

8.2.1.7 Equivalent Load and System Interconnection

For the hybrid wind–fuel cell system described in [17], the equivalent load is in parallel with a filter capacitor *C*. A series inductor L_{fc} is used to allow for a voltage difference at the interconnection of the DC generator and the fuel cell during transient events. The combined current from each subsystem flows to the load. The capacitor and inductor are ideal components and consume no real power. Figure 8.3 illustrates the details of this interconnection.

The next equation shows the calculation for the current i_{fc} drawn from the fuel cell through the inductor as

$$i_{fc} = (1/L_{fc})\int (V_{stack} - V_L)\, dt + i_{fc}(0) \tag{8.25}$$

where

V_{stack} and V_L are the stack voltage and load voltage, respectively

$i_{fc}(0)$ is the inductor's initial current

V_L is equal to the voltage of the DC generator and is calculated by

$$V_L = (1/C)\int \{i_a + i_{fc} - (V_L/R_L)\} dt + V_L(0) \tag{8.26}$$

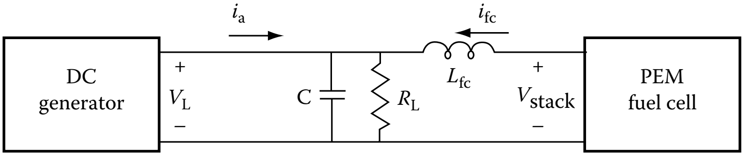

FIGURE 8.3
Equivalent load resistance with interconnecting capacitor and inductor.

where

i_a is the armature current from the generator

$V_L(0)$ is the initial voltage of the capacitor

R_L is the equivalent load resistance representing the DC–AC inverter and AC load [27]

8.2.2 Simulation Results

Simulation runs were conducted with the wind–fuel cell system model in [17] for above- and below-rated wind speed (8 m/s) conditions and for loads that were greater than and less than the available wind power. The different operating conditions simulated in these runs correspond to step changes in wind speed and equivalent load resistance and then to a more realistic wind speed profile.

8.2.2.1 Below-Rated Wind Speed Conditions (Wind Power > Load)

The fuel cell is not producing power when the available wind is greater than the load. For this case, it is assumed that the system is in operation at a wind speed of 6 m/s with an equivalent load resistance R_L of 30 Ω. Figure 8.4 shows the response of the rotor speed and inverter input voltage for a step change (at 10 s) in the input wind speed from 6 to 8 m/s. The lambda-controller regulates the rotor speed to 12 and 16 rad/s for these two wind speeds.

Figure 8.5 shows the response of the rotor speed and inverter input voltage for a subsequent step change in R_L from 30 to 20 Ω with 8 m/s wind. The load resistance change emulates a change in the demand or the addition of

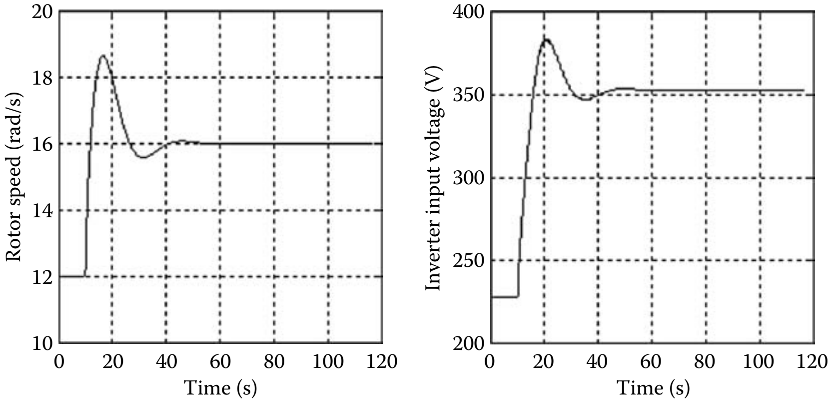

FIGURE 8.4
System response to step change in (below-rated) wind speed (wind turbine generator only).

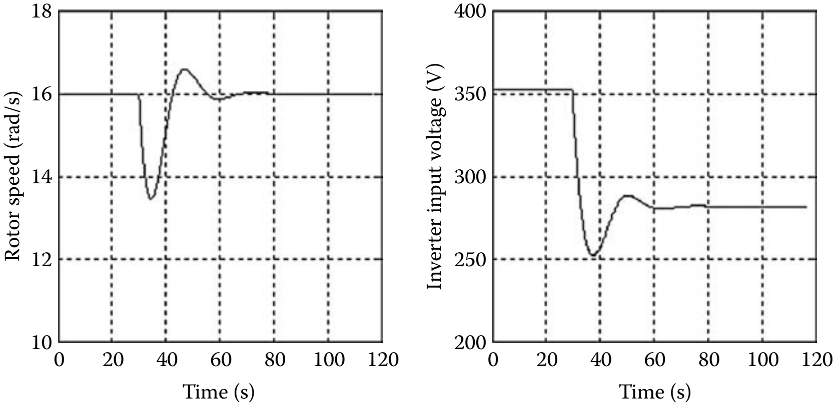

FIGURE 8.5
System response to step change in load resistance (wind turbine generator only).

the electrolyzer to take advantage of the "excess" available power. Note again the effective regulation of the rotor speed provided by the lambda-controller to 16 rad/s.

8.2.2.2 Above-Rated Wind Speed Conditions (Wind Power > Load)

For this case, the fuel cell is again not producing power, and R_L is 20 Ω. It is assumed that the system is in operation at a wind speed of 8 m/s. Figure 8.6 shows the response of the rotor speed and inverter input voltage for a step increase (at 30 s) in the input wind speed from 8 to 10 m/s. Note the rotor speed is now regulated by the omega-controller to 16 rad/s as the input wind speed exceeds the rated value.

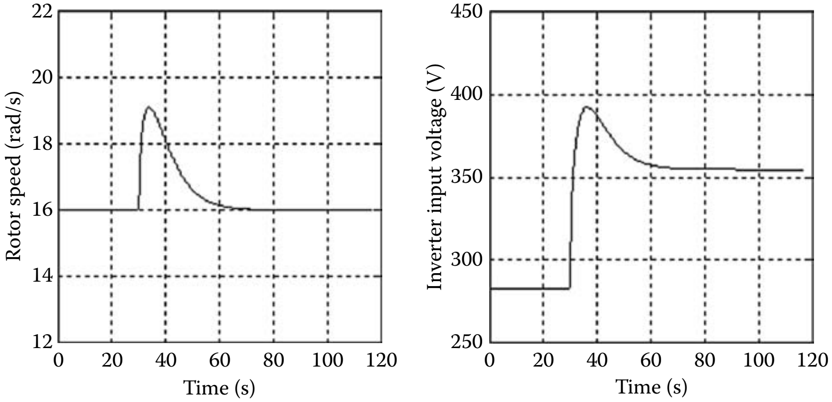

FIGURE 8.6
System response to step change in (above-rated) wind speed (wind turbine generator only).

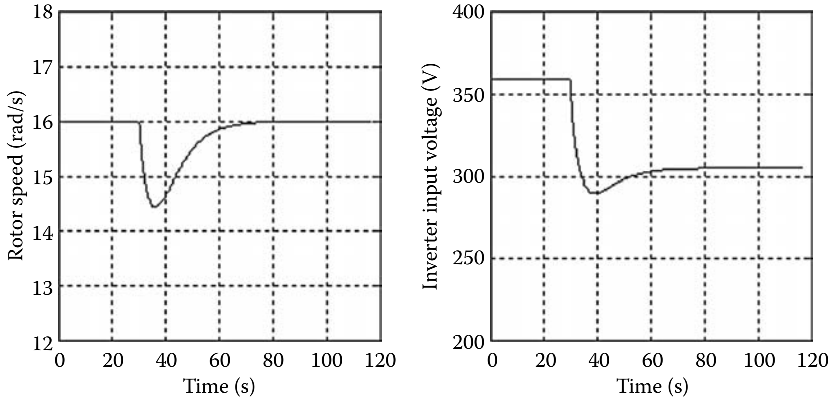

FIGURE 8.7
System response to step change in load resistance (wind turbine generator only).

Figure 8.7 shows the response of the rotor speed and inverter input voltage for a subsequent step change in the equivalent load resistance from 20 to 15 Ω. Note again the effective regulation of the rotor speed provided by the omega-controller to 16 rad/s.

8.2.2.3 Below-Rated Wind Speed Conditions (Wind Power < Load)

For this case, the wind power is insufficient to meet the load so the fuel cell produces the additional power needed to ensure a minimal inverter input voltage. It is assumed that the combined system is in operation at 6 m/s wind speed with an equivalent load resistance of 15 Ω. Figure 8.8 shows the response of the rotor speed, inverter input voltage, generator current, and fuel cell current for a step decrease (at 10 s) in input wind speed from 6 to 5 m/s. Note the regulation of the rotor speed provided by the lambda-controller to 12 and 10 rad/s-respectively, for these two wind speeds, as well as the regulation of the inverter input voltage with a maximum undershoot of 1.8%. It is preferred, but not essential, for the voltage deviation to be kept at ±3% of the nominal value; the inverter will further regulate the actual output delivered to the load. Two hundred volts (200 V) is deemed the minimal voltage for effective operation of an inverter to produce utility-quality 115 V_{rms} output.

Figure 8.9 shows the response of the rotor speed, inverter input voltage, generator current, and fuel cell current for a subsequent step change in R_L from 15 to 20 Ω. The decrease in the demand results in a corresponding drop in the fuel cell current. Note again the effective regulation of the inverter input voltage provided by the fuel cell controller to 200 V with a 3.8% maximum overshoot and a 3.6% maximum undershoot, as the current drawn from the fuel cell is reduced.

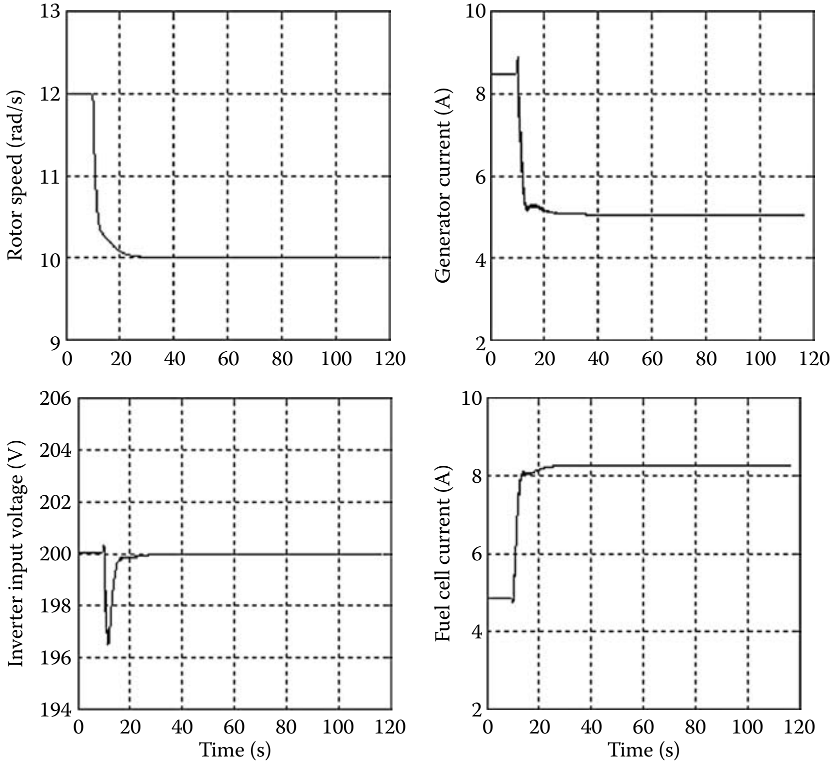

FIGURE 8.8
System response to step change in wind speed (combined system).

8.2.2.4 Turbulent Wind, Below-Rated Wind Speed Conditions (Wind Power < Load)

For this case, the wind speed is established by the SNwind-generated profile. The mean wind speed is set to 5 m/s, and the turbulence characteristics are determined by the SNwind input file parameters. The actual mean wind speed generated is 4.705 m/s. Figure 8.10 shows the response of the rotor speed, inverter input voltage, generator current, and fuel cell current for an initial equivalent load resistance of 15 Ω. Since the fuel cell is active, the fuel cell controller attempts to regulate the inverter input voltage to 200 V. The lambda-controller seeks to maintain an average rotor speed of 9.41 rad/s for the changing wind.

We can also see in Figure 8.10 that the generator and fuel cell currents are complementary. As the wind speed decreases, the generator current decreases and the fuel cell current increases accordingly. The combined current from the generator and the fuel cell is shown in Figure 8.11 along with

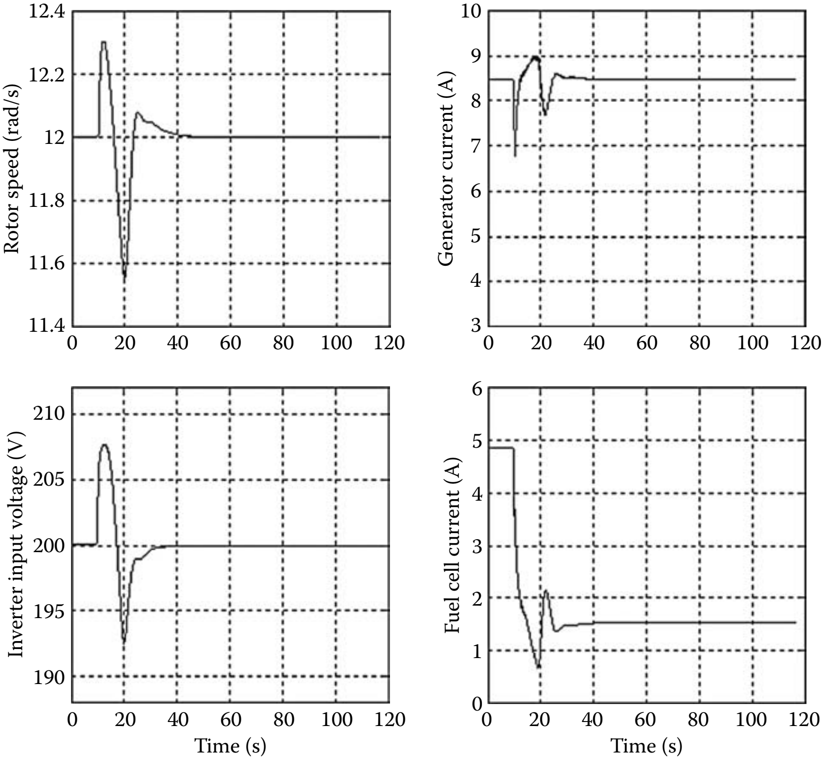

FIGURE 8.9
System response to step change in load resistance (combined system).

the wind profile for the same case. With the voltage regulated to 200 V and an initial average combined current of 13.33 A, the system attempts to provide a constant power of 2.67 kW to the load.

Then at 30 s, a 33% step change in the value of R_L from 15 to 20 Ω is applied. The fuel cell controller again regulates the inverter input voltage to 200 V. The maximum overshoot is 4.5%, and the maximum undershoot is 5%. The lambda-controller seeks to maintain an average rotor speed of 9.41 rad/s for the changing wind conditions, corresponding to the desired lambda value of 6.5.

Figure 8.10 also shows that the generator current maintains an average value of approximately 4.25 A after a step change in equivalent load resistance, while the fuel cell current's average value drops from approximately 9.08 to 5.75 A. With the inverter input voltage regulated to 200 V and a step change in the average combined current (fuel cell plus generator current) from 13.33 to 10 A as shown in Figure 8.11, the power output to the load changes from 2.67 to 2 kW.

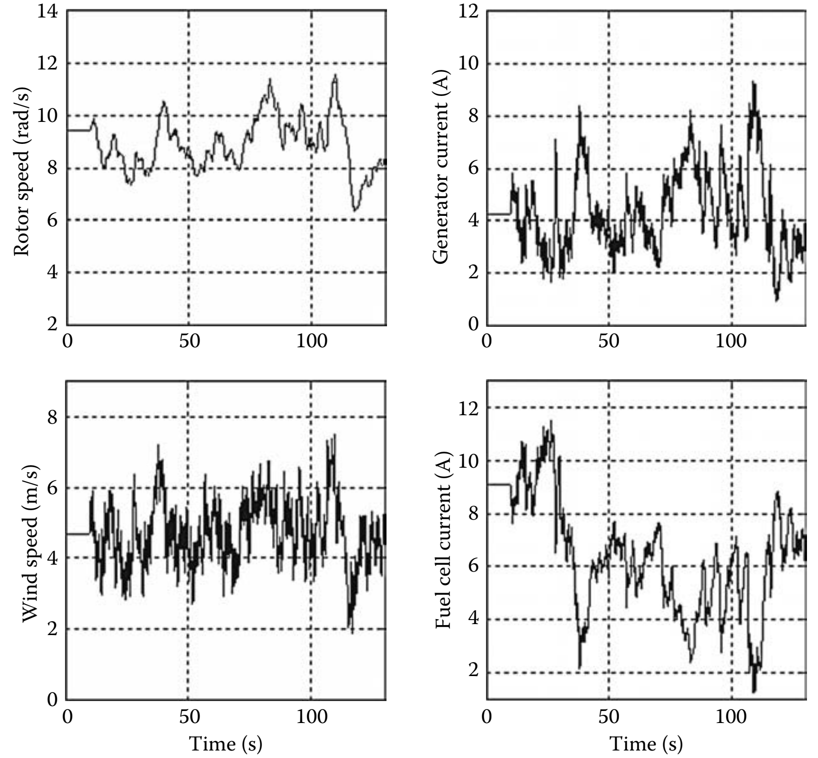

FIGURE 8.10
System response to changing wind speed profile (combined system).

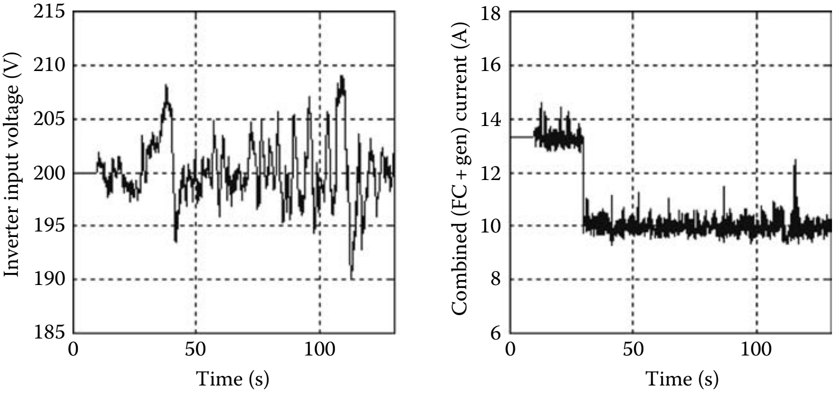

FIGURE 8.11
Inverter input voltage and fuel cell plus generator combined current response (combined system).

8.2.3 Conclusions

Wind is a renewable energy resource that is growing in importance as a means to address the national and global issues of air pollution, grid reliability, dependence on foreign oil, climate change, etc. However, the wind varies over time and there is less of it (on average) at sites around major load centers, which are two of the technical and economic challenges to the establishment of power generation facilities relying solely on the wind. But hybrid systems, such as wind turbine–fuel cell systems, have the potential to rectify these shortcomings and also make possible the greater decentralization of electric power generation in the United States, thus easing the transmission and distribution system's bottlenecks while increasing its overall reliability and security without sacrificing the quality of power delivered to the customer. Furthermore, wind turbine–fuel cell systems can achieve these results in an environment-friendly manner without producing harmful emissions.

The study by Carter and Diong [17] described the development of a simulation model and the associated control schemes for a small-scale, prototype wind turbine–fuel cell system that will enable the further study and optimization of the performance, sizing, cost, etc., of such hybrid systems. For this study, models of a variable speed wind turbine and DC generator, a PEMFC, and an electrolyzer unit were combined to simulate a regenerative hybrid wind–fuel cell AC power generating system. The system model with appropriately designed controllers was then exercised and found to perform effectively, both below and above the rated wind speed of 8 m/s, for delivering power to an AC load and/or electrolyzer while regulating the necessary minimal inverter input DC voltage of 200 V. Simulations of this model have also shown that the system responds adequately to significant changes in wind speed (both step and turbulent) and load demand for various representative cases.

The simulations indicated that such a hybrid system can be made to deliver utility-grade electricity reliably and effectively from the combined energy sources. These results are encouraging from the standpoint of utilizing regenerative hybrid wind turbine–fuel cell systems as a means to address some of the current challenges such as air pollution, grid reliability, dependence on foreign oil, and climate change facing the electric power industry, the nation and the world.

8.3 Hybrid Renewable Energy Systems for Isolated Islands

The output power of wind turbine generators is mostly fluctuating and has an effect on system frequency. Senjyu et al. [28] tried to solve this problem by using hybrid renewable energy systems. Its configuration is given in Figure 8.11.

Where P_s is the power supply to load, P_g is generating power of diesel, P_{fc} is the actual generating power of fuel cell, P_w is the output power of wind turbine, and P_r is the power flowing to aqua electrolyzer.

This system consists of wind generators, diesel generators, fuel cell generators, and aqua electrolyzers. The aqua electrolyzers are used to absorb the rapidly fluctuating output power from wind turbine generators and generate hydrogen as fuel for fuel cells. The power supplied to the load is P_s.

8.3.1 Simulation Models

To simulate the proposed system configuration as shown in Figure 8.12, the simulation model as shown in Figure 8.13 is used to test it.

It should be noted that the wind power is modeled as an input power to the load. A detailed model and control method for the wind turbine are not presented in the paper [28].

8.3.2 Control Methods

From Figure 8.13, we can see that the PI controller is applied to the fuel cell, the electrolyzer and the diesel generator, which are shown in Figures 8.14 through 8.16.

8.3.3 Simulation Results

In this simulation study, four cases, whose conditions are shown in Table 8.3, have been simulated. The gains of the PI controllers for each case are shown

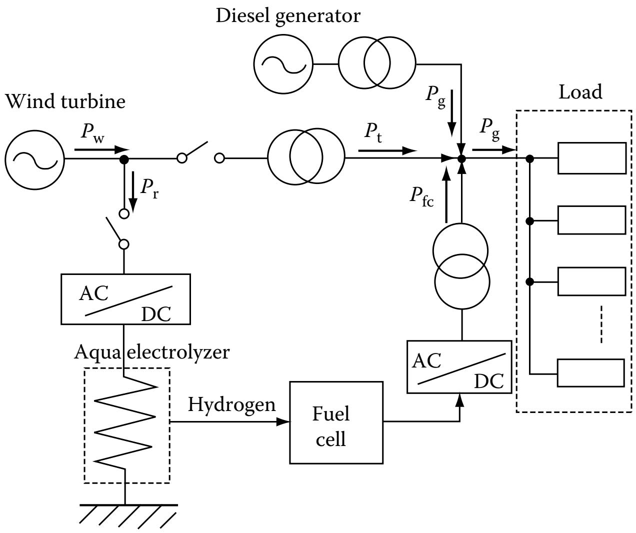

FIGURE 8.12
System configuration.

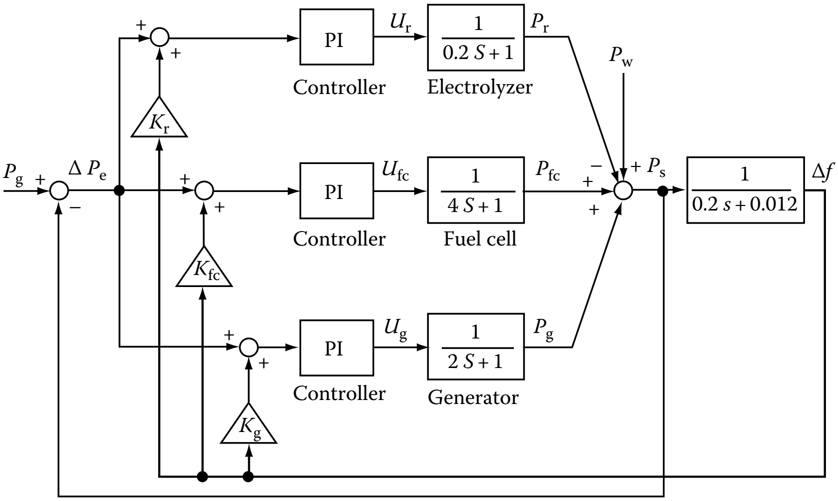

FIGURE 8.13
Simulation model.

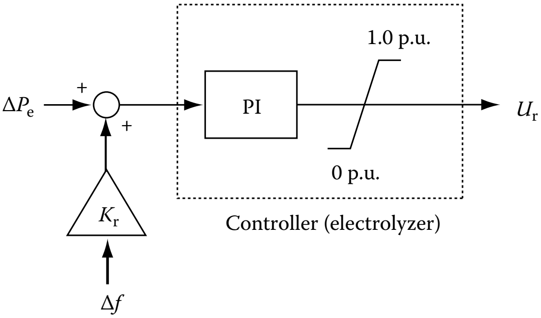

FIGURE 8.14
PI controller for electrolyzer.

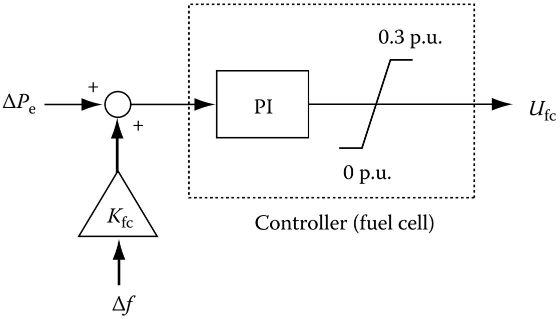

FIGURE 8.15
PI controller for fuel cell.

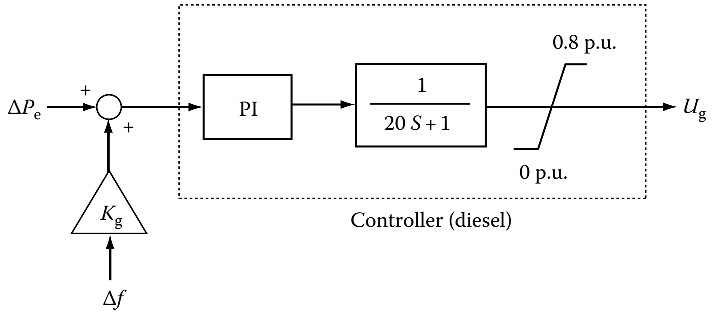

FIGURE 8.16
PI controller for diesel generator.

TABLE 8.3
Four Cases of Simulations

	Case 1	Case 2	Case 3	Case 4
Diesel generators	○	○	○	○
Fuel cells	×	○	○	×
Aqua electrolyzers	×	○	○	×
Batteries	×	×	×	○
Wind turbines	○	○	Δ	○

Note: ○, means the corresponding components in the left column are contained in the case; ×, means the corresponding components in the left column are not contained in the case; Δ, means that Case 3 uses the same equipments as Case 2, but the total generated power from the wind turbine is used for electrolysis.

in Table 8.4. These parameters are determined by the trial-and-error method such that the supply error and the frequency deviation of power system are small. In Case 1, the system consists of only diesel generators and wind turbines; the system of Case 2 consists of diesel generators, fuel cell generators, wind turbines, and aqua electrolyzers, which is the system proposed in [28]. The system of Case 3 uses the same equipment as the system of Case 2. The system of Case 4 consists of diesel generators, wind turbines, and batteries. In Case 4, the supply power is represented as follows:

$$P_s = P_w + P_g + P_b \tag{8.27}$$

where P_b is the charge or discharge power of the batteries.

Simulation results for Case 1, Case 2, Case 3, Case 4-1 and Case 4-2 have been given in Figures 8.17 through 8.21, respectively.

8.3.4 Remarks and Discussion

From the above simulations, Table 8.5 shows the feature of each power supply system, from Cases 1 to 4. Among these four cases, Case 1 simulation system

TABLE 8.4

Gain Values in PI Controllers

Case	Equipment	Proportional Gain	Integral Gain
Case 1	Diesel	4.7	1.3
	Diesel	4.7	2.5
Case 2	Fuel cell	11.5	3.7
	Electrolyzer	16.8	5.8
Case 3	Diesel	8.7	5.7
	Fuel cell	5.5	2.3
Case 4	Diesel	4.7	2.3
	Battery	1.4	0.4

is the most inexpensive system, but it cannot supply high-quality power to load demand when output power of wind turbines changes suddenly. Case 3 can supply very high-quality power to load demand when the output power of wind turbines changes suddenly, but this system is not an effective system since all the total output power generated from wind turbine generators is used only in electrolysis.

In addition, this system needs a large capacity of diesel generators, fuel cell generators, aqua electrolyzers, and a fuel tank. The Case 4 simulation system can supply high-quality power to load demand. However, this system is very costly since this system needs a large battery capacity. In addition, the battery charges and discharges many times, which makes the lifetime of the battery very short. The Case 2 simulation system is a more effective and inexpensive system compared with the systems in Cases 3 and 4, and maintains the load frequency of the system in Case 1. However, the configuration of Case 2 is expensive compared with the system in Case 1.

8.4 Power Management of a Stand-Alone Wind/Photovoltaic/Fuel Cell Energy System

Due to the ever increasing energy consumption, the soaring cost, the exhaustible nature of fossil fuel, and the worsening global environment, the power industry has become more and more interested in green (renewable and fuel cell-based energy sources) power generation systems [29]. As we know, wind and solar power generation are two of the most promising renewable power generation technologies. The growth of wind and photovoltaic (PV) power generation systems has exceeded the most optimistic estimation [30–32]. Fuel cells also show great potential to be green power sources of the future because of many merits they have (such as high efficiency, zero or low emission of pollutant gases, and flexible modular structure) and the rapid progress in fuel

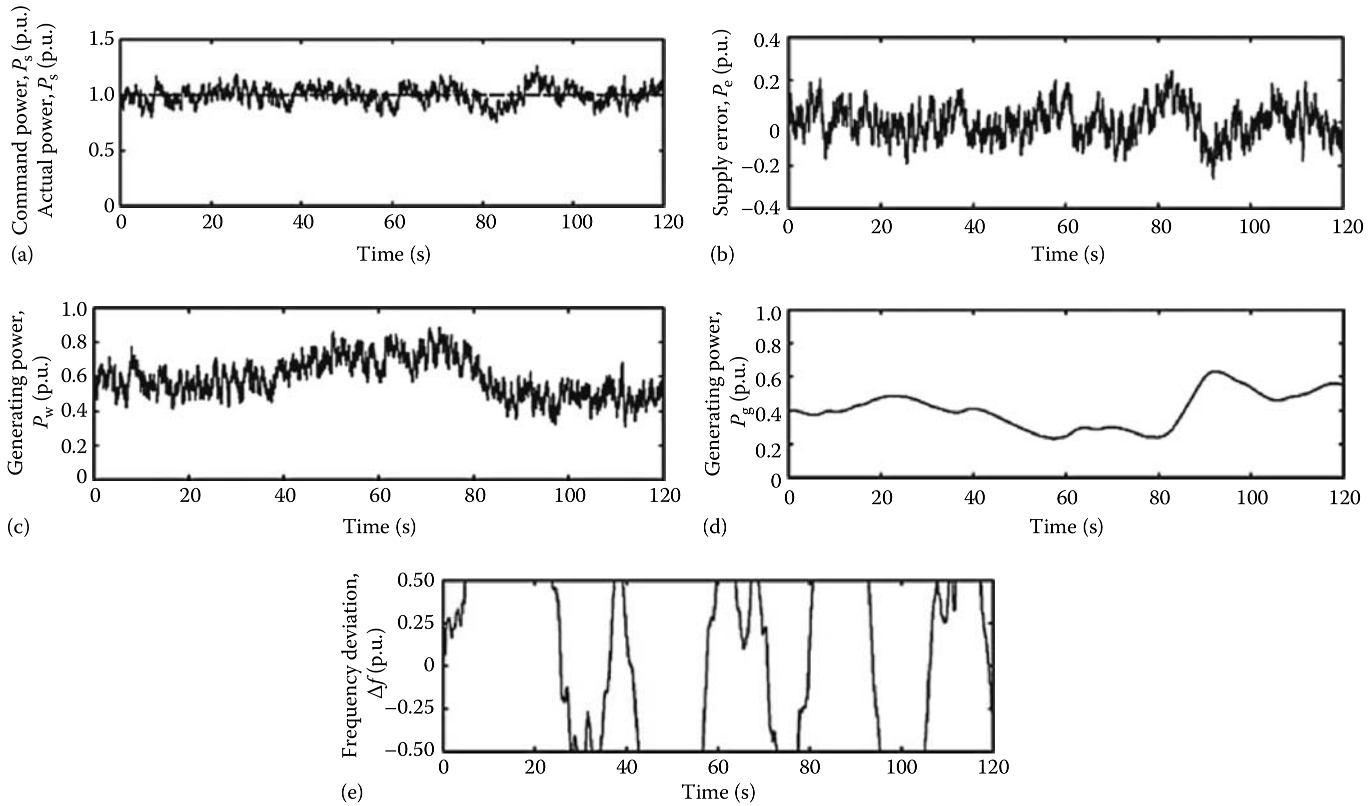

FIGURE 8.17
Simulation results of proposed system (Case 1). (a) Demand power P_s^* and supply power P_s. (b) Error in supply demand ΔP_e. (c) Generating power of wind turbine P_w. (d) Generating power of diesel generator P_g. (e) Frequency deviation of power systems Δf.

cell technologies. However, each of the aforementioned technologies has its own drawbacks. For instance, wind and solar power are highly dependent on climate while fuel cells need hydrogen-rich fuel. Nevertheless, because different alternative energy sources can complement each other to some

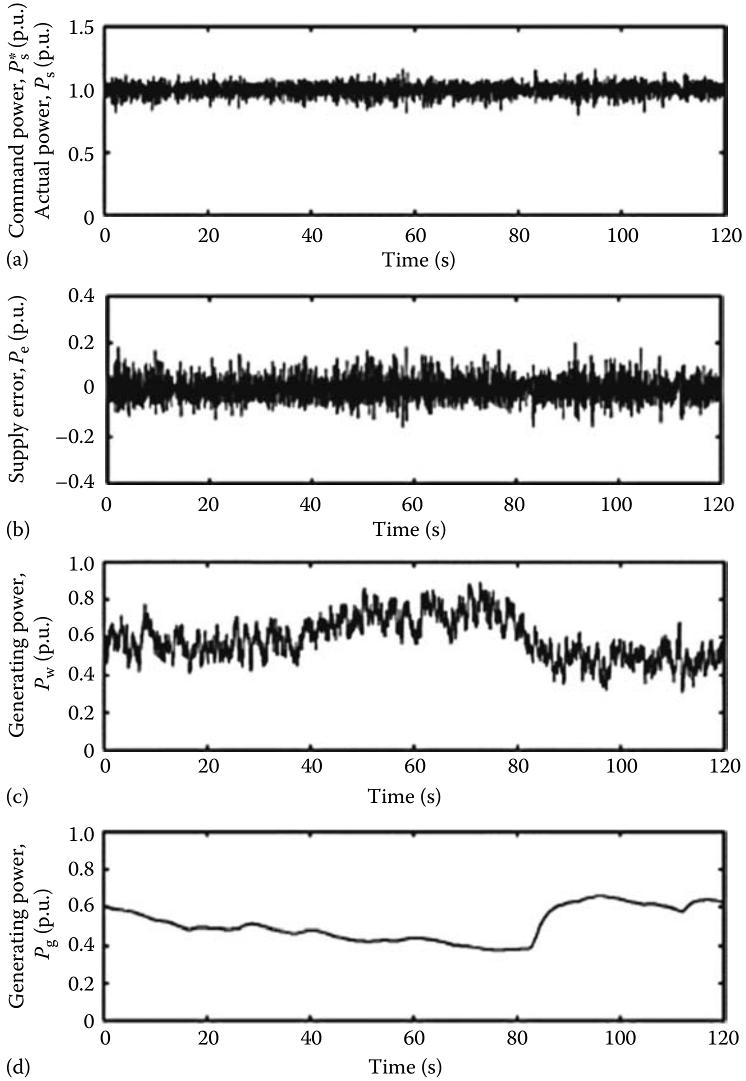

FIGURE 8.18
Simulation results of proposed system (Case 2). (a) Demand power P_s^* and supply power P_s. (b) Error in supply demand ΔP_e. (c) Generating power of wind turbine P_w. (d) Generating power of diesel generator P_g. (e) Generating power of fuel cell P_{fc}. (f) Input power to aqua electrolyzers P_r. (g) Fuel tank capacity. (h) Frequency deviation of power systems Δf.

(*continued*)

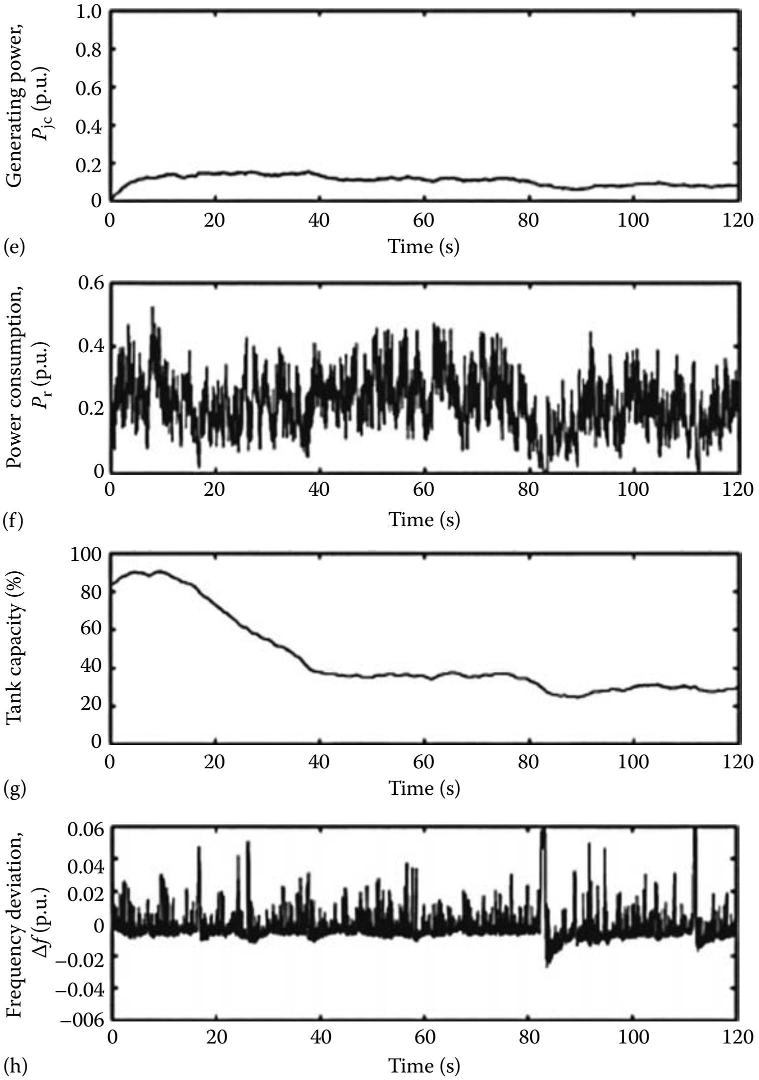

FIGURE 8.18 (continued)

extent, multisource hybrid alternative energy systems (with proper control) have great potential to provide higher quality and more reliable power to customers than a system based on a single resource. Because of this feature, hybrid energy systems have caught worldwide research attention [2–12].

Many alternative energy sources including wind, PV, fuel cell, diesel system, gas turbine, and microturbine can be used to build a hybrid energy system [2–12]. Nevertheless, the major renewable energy sources used and reported are wind and PV power [2–12]. Due to the intermittent nature of wind and solar energies, stand-alone wind and PV energy systems normally require energy storage devices or some other generation sources to form a hybrid system. The storage device can be a battery bank, supercapacitor bank, superconducting magnetic energy storage, or a fuel cell–electrolyzer system.

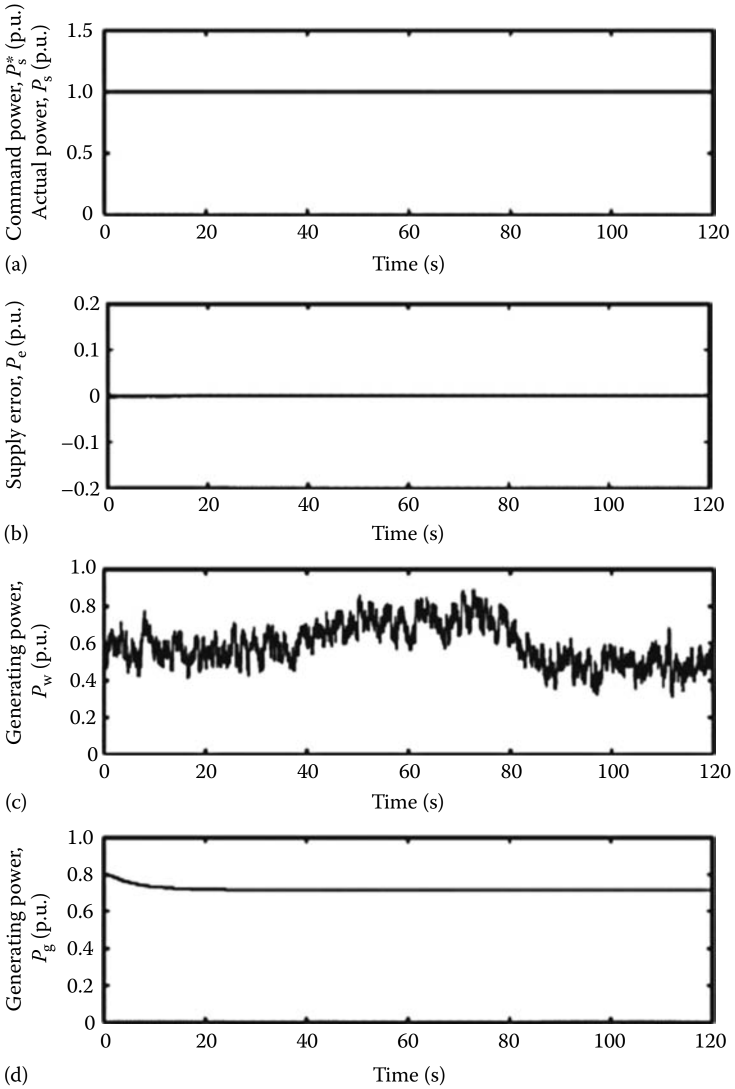

FIGURE 8.19

Simulation results for Case 3. (a) Demand power P_s^* and supply power P_s. (b) Error in supply demand ΔP_e. (c) Generating power of wind turbine P_w. (d) Generating power of diesel generator P_g. (e) Generating power of fuel cell P_{fc}. (f) Input power to aqua electrolyzers P_r. (g) Fuel tank capacity. (h) Frequency deviation of power systems Δf.

(*continued*)

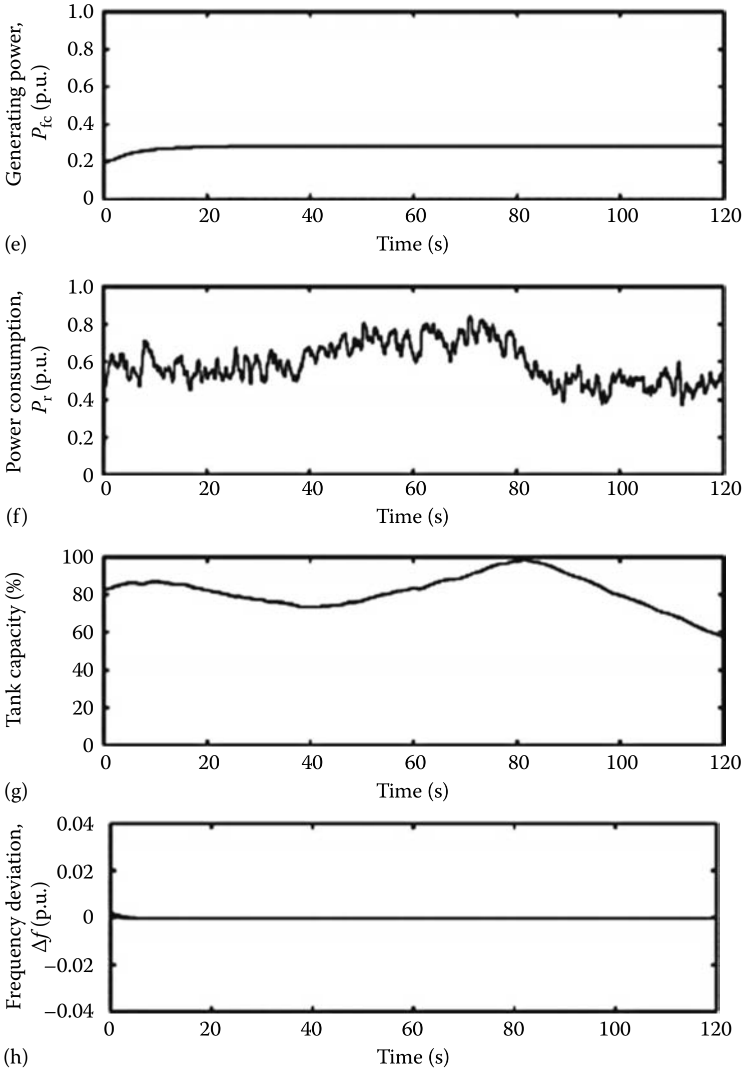

FIGURE 8.19 (continued)

Wang and Nehrir [29] proposed a stand-alone hybrid alternative energy system consisting of wind, PV, fuel cell, electrolyzer, and battery. Wind and PV are the primary power sources of the system to take full advantage of renewable energy, and the fuel cell–electrolyzer combination is used as a backup and a long-term storage system. A battery bank is also used in the system for short-time backup to supply transient power. The different energy/storage sources in the proposed system are integrated through an AC link bus. The details of the system configuration, system unit sizing, and

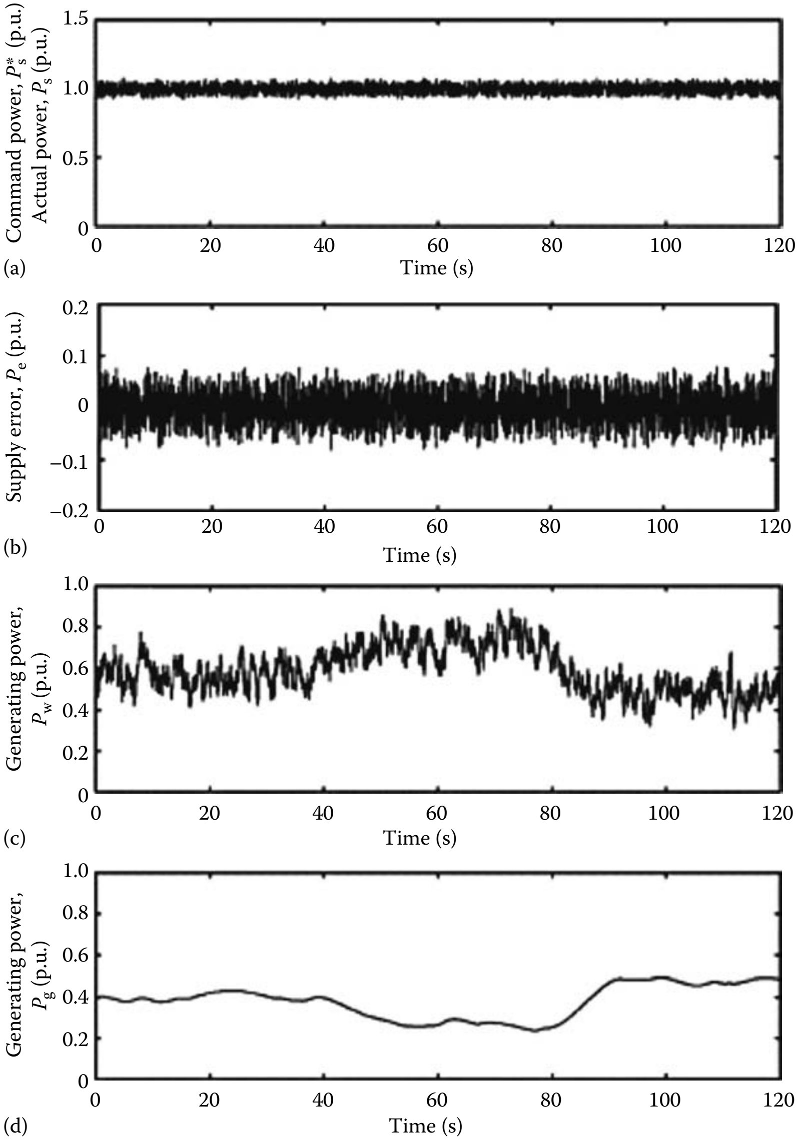

FIGURE 8.20
Simulation results for Case 4-1. (a) Demand power P_s^* and supply power P_s. (b) Error in supply demand ΔP_e. (c) Generating power of wind turbine P_w. (d) Generating power of diesel generator P_g. (e) Generating power of fuel cell P_{fc}. (f) Battery capacity. (g) Frequency deviation of power systems Δf.

(*continued*)

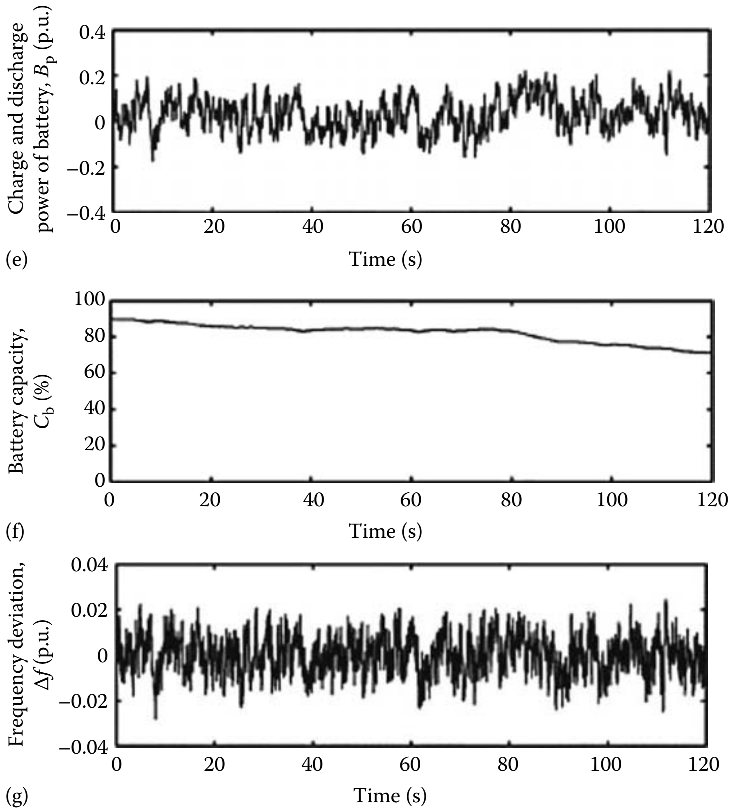

FIGURE 8.20 (continued)

the characteristics of the major system components are also discussed in the paper. An overall power management strategy is designed for the system to coordinate the power flows among the different energy sources. Simulation studies have been carried out to verify the system performance under different scenarios using practical load profile and real weather data.

8.4.1 System Configuration

The system configuration for the proposed hybrid alternative energy system is shown in Figure 8.22. The wind and PV power play the primary roles in this design while the fuel cell–electrolyzer combination serves as a backup and storage system. If there is excess wind and/or solar generation, the electrolyzer starts to produce hydrogen, which is then delivered to the hydrogen storage tanks. On the other hand, when there is a deficit in power generation, the fuel cell stack will begin to produce energy using hydrogen from the reservoir tanks, or in case they are empty, from the backup hydrogen tanks. The design also uses a battery bank to supply transient power to load transients, ripples, and spikes. Different energy sources are connected to the AC bus through appropriate power electronic interfacing circuits. Detailed system design can be found in [29].

In the design, DC–AC converters are used for the wind energy, solar energy, fuel cell stack because this hybrid renewable energy system is used

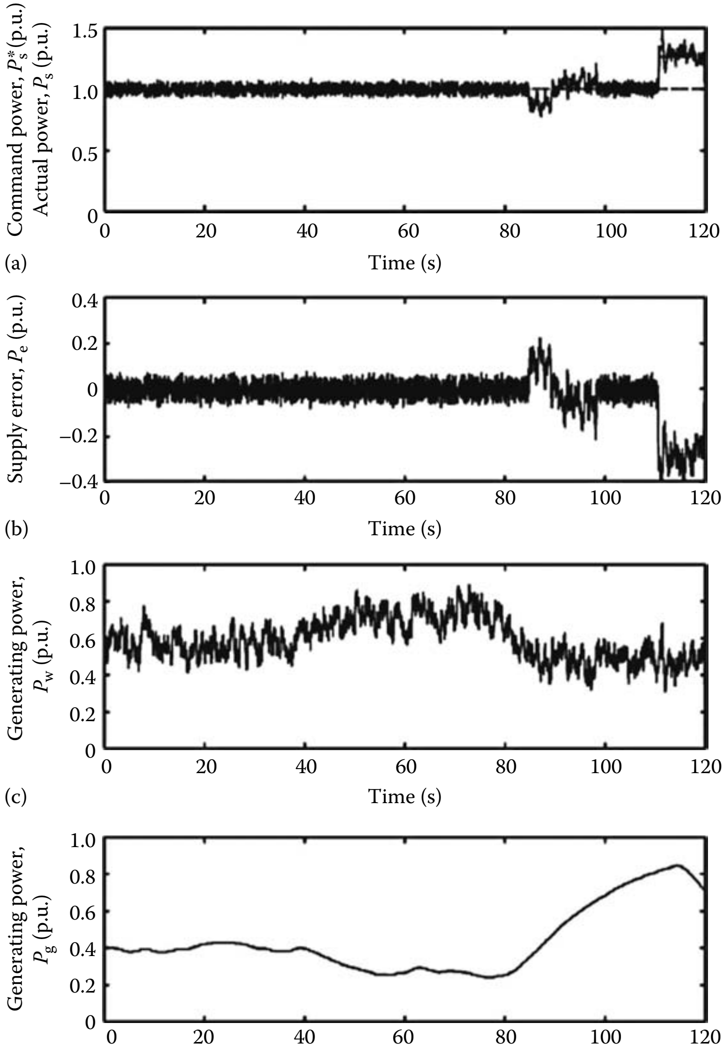

FIGURE 8.21
Simulation results for Case 4-2. (a) Demand power P_s^* and supply power P_s. (b) Error in supply demand ΔP_e. (c) Generating power of wind turbine P_w. (d) Generating power of diesel generator P_g. (e) Generating power of fuel cell P_{fc}. (f) Battery capacity. (g) Frequency deviation of power systems Δf.

(*continued*)

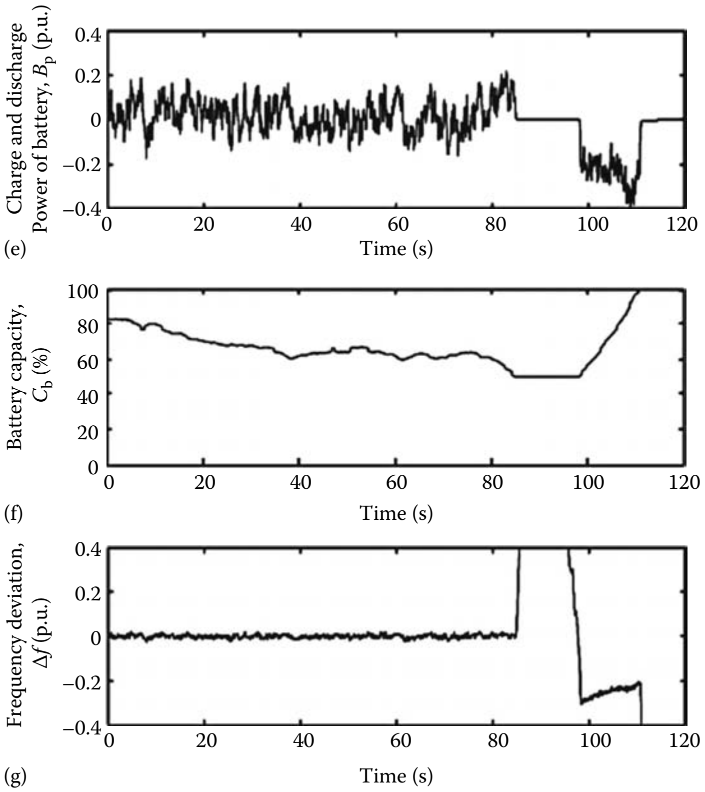

FIGURE 8.21 (continued)

TABLE 8.5

Simulation Results for Each Case

	Effective Utilization of Wind Energy	Quality of Electric Power	Cost
Case 1	○	×	◎
Case 2	○	○	○
Case 3	×	◎	Δ
Case 4	○	○	×

Note: ×, means "not available" or "very costly"; ○, means "available"; Δ, has the same meaning as in Table 8.3; ◎, means "most" or "the best."

in utility power systems. The details of the components in the system can be found in [29].

8.4.2 Power Management Strategies

In the overall control scheme shown in Figure 8.23, the wind energy conversion system is controlled by a pitch angle controller, while a PV electricity

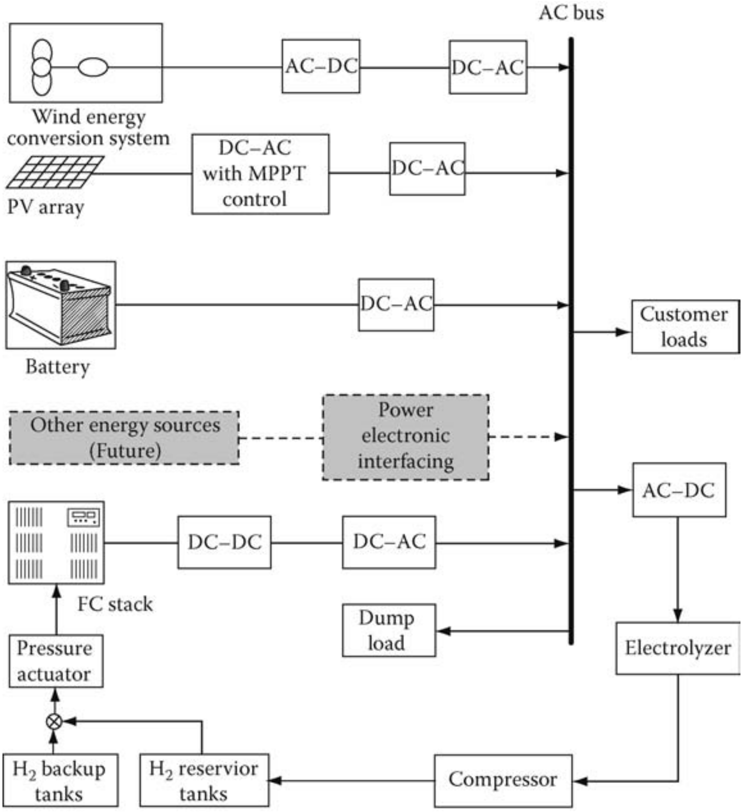

FIGURE 8.22
System configuration of hybrid renewable energy system.

generation unit is controlled by a maximum power point tracking controller. The wind energy conversion system and PV electricity generation unit are the main energy sources to feed the load. The power difference between the generation sources and the load demand is calculated as

$$P_{\text{net}} = P_{\text{wind}} + P_{\text{PV}} - P_{\text{load}} - P_{\text{sc}} \tag{8.28}$$

where P_{sc} is the self-consumed power for the operating system.

Two modes are needed to be considered in the operations: excess mode and deficit mode.

1. Excess mode

When the power difference between the generation and the demand P_{net} is larger than zero, the excess wind and PV-generated power P_{net} is supplied to the electrolyzer to generate hydrogen that is delivered to the hydrogen storage tanks through a gas compressor. The power balance equation becomes

$$P_{\text{wind}} + P_{\text{PV}} = P_{\text{load}} + P_{\text{elec}} + P_{\text{comp}}, \qquad P_{\text{net}} > 0, \tag{8.29}$$

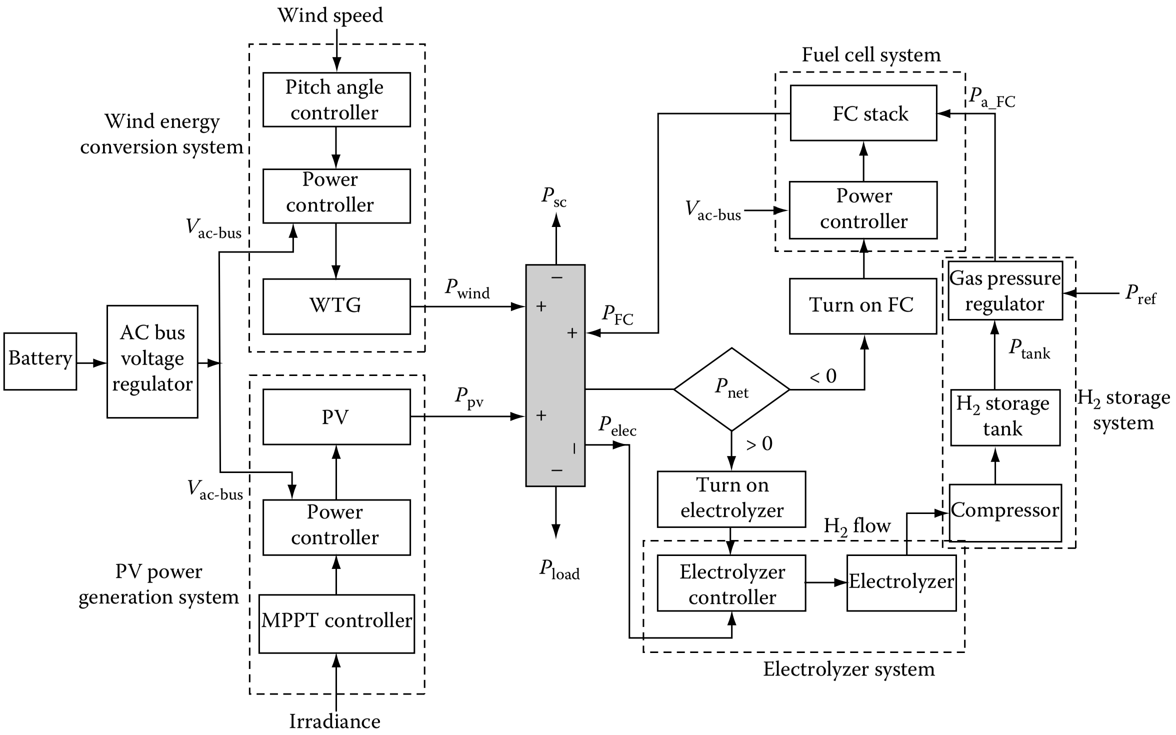

FIGURE 8.23
Block diagram of the overall control scheme for the proposed hybrid alternative energy system. (From Wang, C. and Nehrir, M.H., *IEEE Trans. Energ. Convers.*, 23(3), 957, 2008. With permission.)

where

P_{elec} is the power consumed by the electrolyzer to generate hydrogen

P_{comp} is the power consumed by the gas compressor

2. Deficit mode

When there is a deficit in power generation ($P_{\text{net}} < 0$), the fuel cell stack begins to produce energy for the load using hydrogen stored in the tanks. The power balance equation is

$$P_{\text{wind}} + P_{\text{PV}} + P_{\text{FC}} = P_{\text{load}}, \quad P_{\text{net}} < 0 \tag{8.30}$$

where P_{FC} is the power generated by the fuel cell stack.

8.4.3 Simulation Results

The proposed wind/PV/fuel cell–electrolyzer energy system has been developed using MATLAB/Simulink. In order to verify the system performance under different situations, simulation studies have been carried out using practical load demand data and real weather data (wind speed, solar irradiance, and air temperature). The system is designed to supply electric power demand of five houses in the southwestern part of Montana. A typical hourly average load demand for a house in the Pacific Northwest regions provided in [33], is used in this simulation study. The total hourly average load demand profile of five houses over 24 h is shown in Figure 8.24. The weather data are obtained from the online records of the weather station at Deer Lodge, Montana, affiliated to the Pacific Northwest Cooperative Agricultural Weather Network (AgriMet) [34].

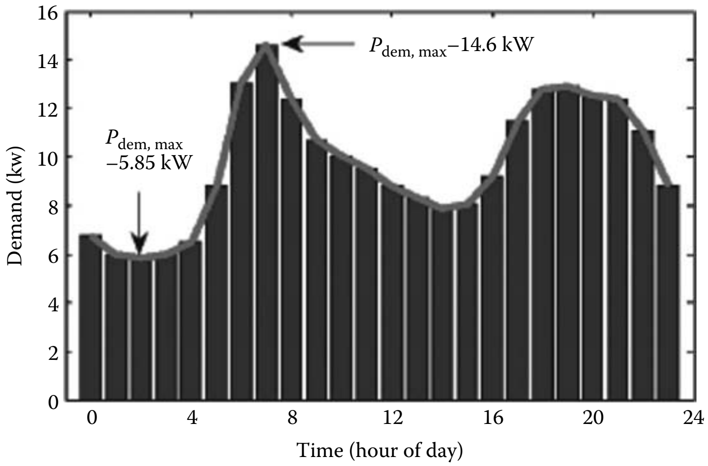

FIGURE 8.24
Hourly average demand of five typical homes in the Pacific Northwest area.

Simulation studies are conducted for the proposed power management scheme during a typical winter day and a summer day. The load demand is kept the same for the two cases.

1. Winter scenario

The weather data for the winter scenario simulation were collected on February 1, 2006. Figure 8.25 shows the output power from the wind energy conversion unit in the hybrid energy system over the 24 h simulation period. Figure 8.26 shows the effect of temperature upon the PV performance. Used by the electrolyzer to generate H_2, the available power profile over the 24 h simulation period is given in Figure 8.27. The corresponding DC voltage applied to the electrolyzer and the electrolyzer current are shown in Figure 8.28. Figure 8.29 shows the actual power delivered by the fuel cell stack.

2. Summer scenario

The output power from the wind energy conversion system and the PV array in the hybrid energy system over the 24 h simulation period are shown in Figures 8.30 and 8.31, respectively. When $P_{\text{net}} > 0$, there is excess power available for H_2 generation. Figure 8.32 shows the H_2 generation rate over the simulation period. When $P_{\text{net}} > 0$, the sum of the wind and the PV-generated power is not sufficient to supply the load demand. Under this scenario, the fuel cell stack turns on to supply the power shortage using the H_2 stored in the storage tank. Figure 8.33 shows the corresponding H_2 consumption rate. Figure 8.34 shows the tank pressure variations over the 24 h simulation period for the summer scenario study.

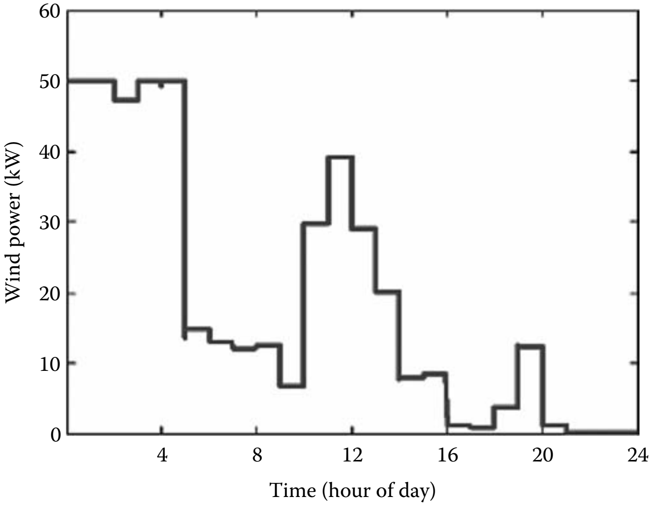

FIGURE 8.25
Wind power for the winter scenario study.

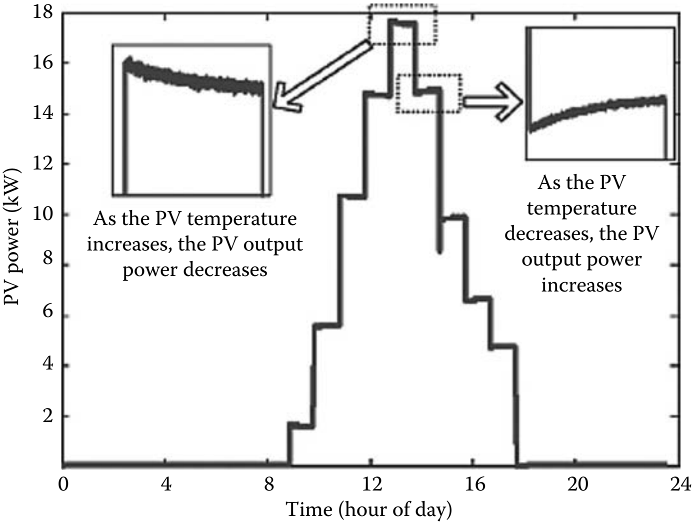

FIGURE 8.26
PV power for the winter scenario.

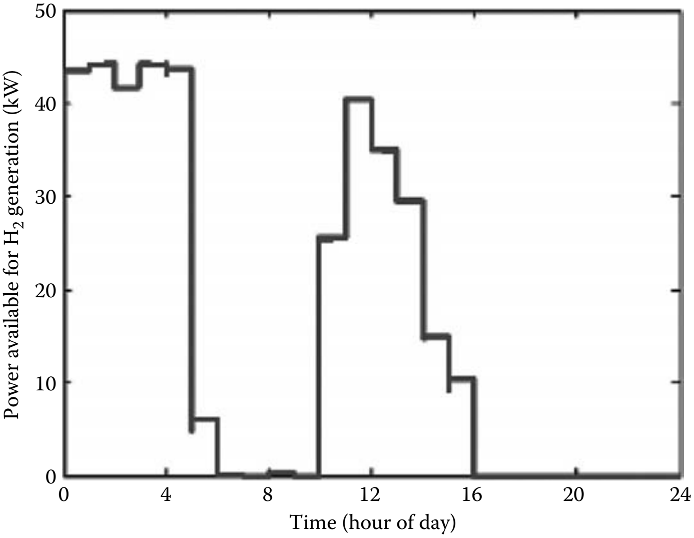

FIGURE 8.27
Power available for H_2 generation for the winter scenario study.

8.4.4 Summary

This section proposes an AC-linked stand-alone wind/PV/fuel cell alternative energy system. The wind and PV generation systems serve as the main power generation sources, the electrolyzer acts as a dump load using any

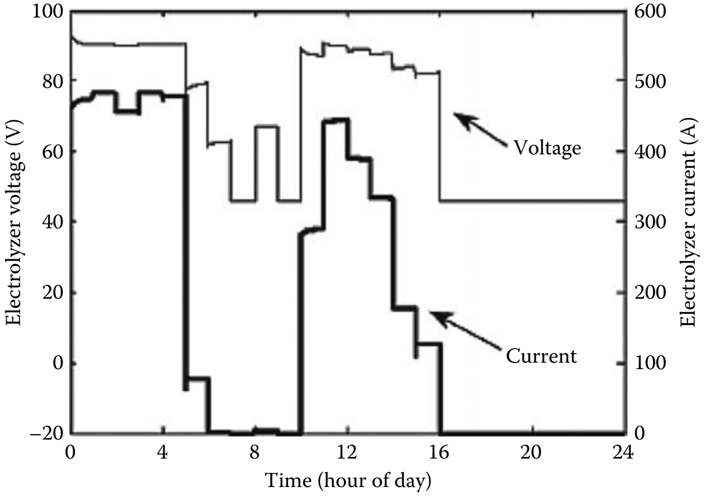

FIGURE 8.28
Electrolyzer voltage and current for the winter scenario.

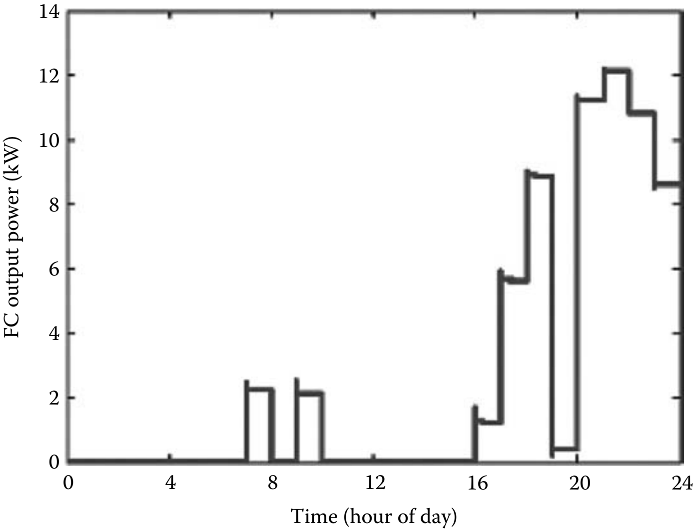

FIGURE 8.29
Power supplied by the fuel cell stack for the winter scenario study.

excess power available to produce hydrogen, and the fuel cell system serves as the backup and supplies power to the system when there is power deficit. The characteristics of the main components in the system including the WECS, PV, fuel cell, and electrolyzer are provided, and the overall control and power management strategy for the proposed hybrid energy system is

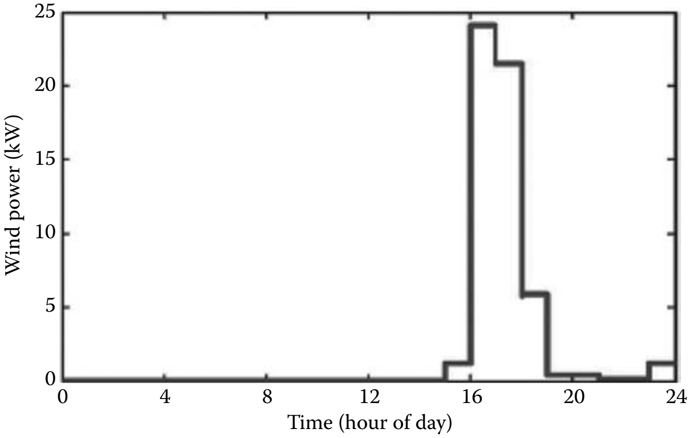

FIGURE 8.30
Wind power generated for the summer scenario study.

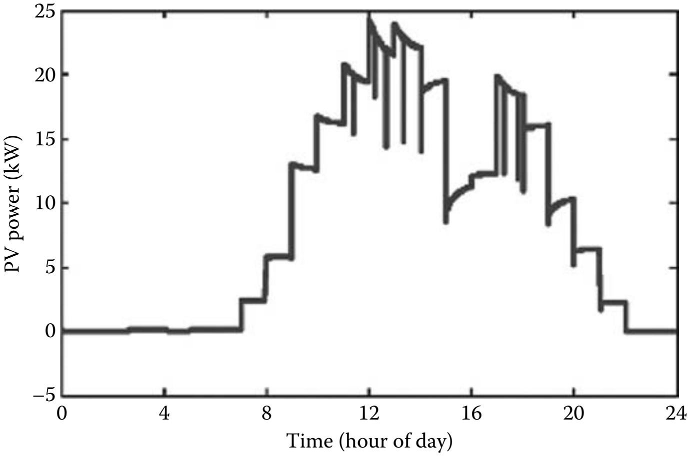

FIGURE 8.31
PV power generated for the summer scenario study.

described. The simulation model of the hybrid system has been developed using MATLAB/Simulink. Simulation studies have been carried out to verify the system performance under different scenarios (winter and summer) using the practical load profile in the Pacific Northwest regions and the real weather data collected at Deer Lodge, MT. The simulation results show the effectiveness of the overall power management strategy and the feasibility of the proposed hybrid alternative energy system.

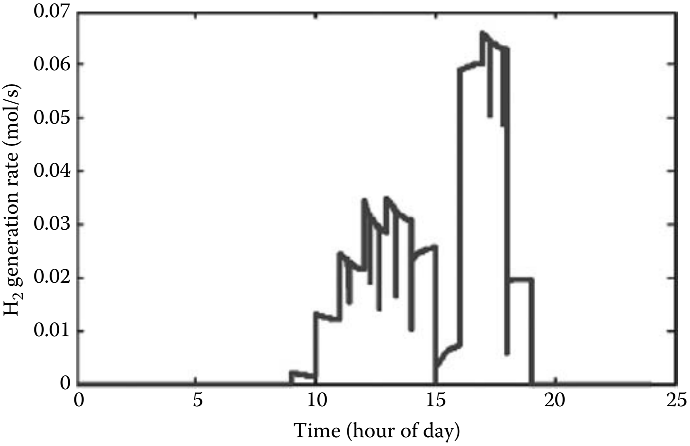

FIGURE 8.32
H_2 generation rate for the summer scenario study.

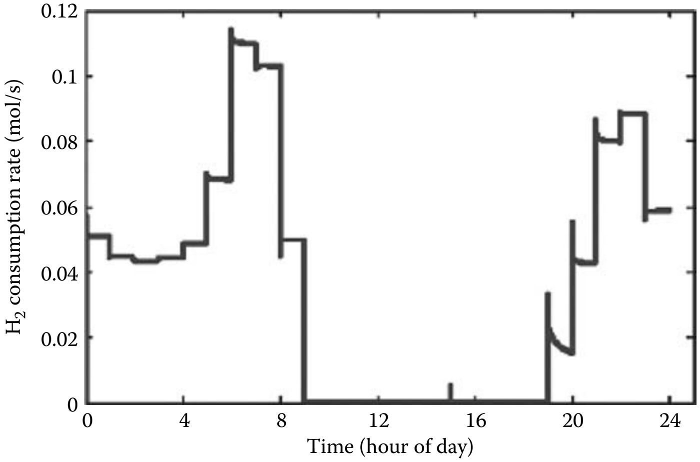

FIGURE 8.33
H_2 consumption rate for the summer scenario study.

8.5 Hybrid Renewable Energy Systems in Load Flow Analysis

Power distribution system is one of the three parts in power grids. Traditional power distribution systems normally consist of a power source (substation) at the root of the feeder and loads along the feeder. Load flow analysis is a

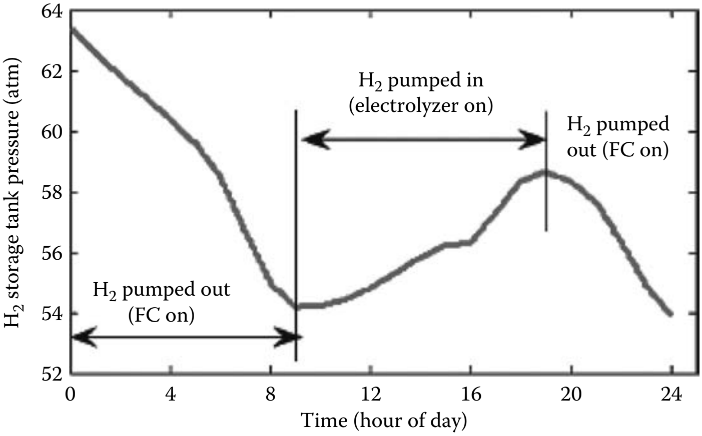

FIGURE 8.34
Tank pressure over 24 h for the summer scenario study.

powerful tool for distribution automation (DA) and demand-side management (DSM). Several typical load flow algorithms have been proposed for traditional power distribution systems.

With the advent of distributed generators (DGs), the advantages of distributed generators make them to be a promising source to be installed in power distribution systems. The installation of distributed generators in distribution systems may cause the reverse power flow and power injections to the feeder. The problems involving the integration of DA, DGs, and DSM are not easy to deal with. Furthermore, the installation of DGs in distribution feeders and the participation in system operations, make it necessary to restudy the problems including power flow, power quality, ferroresonance, voltage control, loss reduction, protection device coordination, voltage flicker, etc. Since voltage profiles are directly related to power quality and customer satisfaction, an efficient and robust three-phase load flow method with the considerations of DGs should be developed first [35].

This chapter serves as a brief introduction to load flow analysis with the considerations of DGs. In order to achieve that goal, a brief introduction to load flow analysis and its typical algorithms is provided first.

8.5.1 Load Flow Analysis for Power Distribution Systems

Load flow analysis has been well developed for power transmission systems. Typical approaches include Gauss–Seidel approach, Newton–Raphson, and fast decoupled approaches. All these approaches can be directly applied to power distribution systems. However, due to its own characteristics of radial structure, new approaches have also been developed for power distribution systems.

Four typical load flow analysis approaches have been developed for power distribution systems: Gauss–Seidel approach, Newton–Raphson approach, DistFlow approach, and a Rigid approach. In this section, we provide a brief introduction to these three approaches.

1. Gauss–Seidel approach

For transmission networks, the Gauss–Seidel algorithm is a basic iterative numerical procedure with a merit of simple procedure. It can be directly used for power distribution systems. The Gauss–Seidel algorithm is an iterative numerical procedure which attempts to find a solution to the system of linear equations by repeatedly solving the linear system until the iteration solution is within a predetermined acceptable bound of error. It is a robust and reliable load flow method that provides convergence to extremely complex power systems. The iterative procedure of Gauss–Seidel algorithm is given as follows:

$$V_k^{(i+1)} = \frac{1}{Y_{kk}}\left(\frac{P_k - iQ_k}{(V_k^{\,i})^*} - \sum_{n=1}^{N} Y_{kn} V_n^{(i)}\right) \tag{8.31}$$

where

$V_k^{(i+1)}$ and $V_k^{(i)}$ are the voltage values at bus k for $(i + 1)$th and ith iterations
P_k and Q_k are the real power and reactive power injection at bus k
Y_{kk} and Y_{kn} are the elements in the admittance matrix

2. Newton–Raphson approach

One of the disadvantages of Guass–Seidel approach is that each bus is handled independently, that is, each correction to a bus requires subsequent correction to all the buses to which it is connected. However, Newton–Raphson approach is based on the idea of calculating the corrections while considering all the interactions.

To solve a nonlinear equation $f(x) = b$, Newton's method is used to drive the error in the function $f(x)$ to zero by making the adjustment Δx to the independent variable associated with the function.

The Taylor expansion of the function $f(x)$ about a specific x^0 is

$$f(x^0) + \left.\frac{\mathrm{d}f(x)}{\mathrm{d}x}\right|_{x=x^0} \Delta x + \varepsilon = b \tag{8.32}$$

By setting the error ε to zero, we get

$$\Delta x = \left(\left.\frac{\mathrm{d}f(x)}{\mathrm{d}x}\right|_{x=x^0}\right)^{-1} \left[b - f(x^0)\right] \tag{8.33}$$

The above equation is the calculation of the adjustment for each iteration.

Applying the above idea to power systems could obtain the Newton–Raphson method derivation for power flow analysis.

For each bus i, we have the following power balance equation:

$$P_i + jQ_i = V_i I_i^* \tag{8.34}$$

where

$P_i + jQ_i$ is the complex power of bus i

V_i and I_i are the voltage and injection current phasors of bus i

The variables are the voltage magnitudes $|V_i|$ and voltage angles θ_i. Thus we need to write the power balance equation as follows:

$$P_i + jQ_i = V_i\left(\sum_{k=1}^{N} Y_{ik}V_k\right)^* = |V_i|^2 Y_{ii}^* + \sum_{\substack{k=1\\k\neq i}}^{N} Y_{ik}^* V_i V_k^* \tag{8.35}$$

Obtaining the derivative of the above equation and considering the real and imaginary parts of this equation, we obtain the following:

$$\begin{aligned} \Delta P_i &= \sum_{k=1}^{N}\frac{\partial P_i}{\partial\theta_k}\Delta\theta_k + \sum_{k=1}^{N}\frac{\partial P_i}{\partial|V_k|}\Delta|V_k| \\ \Delta Q_i &= \sum_{k=1}^{N}\frac{\partial Q_i}{\partial\theta_k}\Delta\theta_k + \sum_{k=1}^{N}\frac{\partial Q_i}{\partial|V_k|}\Delta|V_k| \end{aligned}, \quad i = 1, 2, \ldots, N \tag{8.36}$$

According to Equation 8.36, we can obtain the adjustment calculation for iteration:

$$\Delta X = [J]^{-1}\Delta Z \tag{8.37}$$

where

$$\Delta X = \begin{bmatrix} \Delta\theta_1 \\ \Delta|V_1| \\ \Delta\theta_2 \\ \Delta|V_2| \\ \vdots \end{bmatrix}; \quad \Delta Z = \begin{bmatrix} \Delta P_1 \\ \Delta Q_1 \\ \Delta P_2 \\ \Delta Q_2 \\ \vdots \end{bmatrix}; \quad [J] = \begin{bmatrix} \dfrac{\partial P_1}{\partial\theta_1} & \dfrac{\partial P_1}{\partial|V_1|} & \cdots \\ \dfrac{\partial Q_1}{\partial\theta_1} & \dfrac{\partial P_1}{\partial|V_1|} & \cdots \\ \vdots & \vdots & \vdots \end{bmatrix}$$

For details of Newton–Raphson method of power flow analysis, the readers can refer any book on power system analysis or calculations.

3. DistFlow approach

This approach has been developed by Mesut E. Baran and Felix F. Wu, for the purpose of solving the optimal capacitor placement.

According to the structural nature of radial distribution systems, the power flow equations, called the DistFlow equations, of a radial distribution system, comprise branch flow equations and the associated terminal conditions for each lateral including the main feeder which is treated as the zeroth lateral. They are of the following form:

$$x_{ki+1} = f_{ki+1}(X_{ki}, u_{ki+1}), \quad k = 0, 1, \ldots, l \tag{8.38}$$

$$x_{k0} = x_{0k}; \quad x_{kn} = x_{kn_2} = 0, \quad i = 0,1,\ldots,nk-1 \tag{8.39}$$

where

$$X = \left[x_i^{\mathrm{T}} \cdots x_l^{\mathrm{T}} x_0^{\mathrm{T}} \right]^{\mathrm{T}}$$

$$x_k = \left[x_{k0}^{\mathrm{T}} \cdots x_{kn}^{\mathrm{T}} \right]^{\mathrm{T}}$$

For a radial distribution system consisting of a main feeder and m primary laterals, we need to solve the following $2(m + 1)$ equations:

$$\begin{aligned} P_{0n} &= \hat{P}_{on}(Z_{00}, Z_{10}, \ldots, Z_{k0}, |V_{00}|) = 0 \\ P_{kn_k} &= \hat{P}_{kn_k}(Z_{00}, Z_{10}, \ldots, Z_{j0}, |V_{00}|) = 0\,, \quad j \le k, \text{ and } k = 1, 2, \ldots, m \\ Q_{kn_k} &= \hat{Q}_{kn_k}(Z_{00}, Z_{10}, \ldots, Z_{j0}, |V_{00}|) = 0 \end{aligned} \tag{8.40}$$

Or in vector form:

$$H(Z) = 0 \tag{8.41}$$

where $Z = \lfloor Z_{10}{}^{\mathrm{T}} \cdots Z_{l0}{}^{\mathrm{T}} Z_{00}{}^{\mathrm{T}} \rfloor$ is the state variable vector.

Using Newton–Raphson method, one can solve this load flow problem:

Step 1: For a given estimate Z^0, calculate the mismatch of $H(Z^0)$.

Step 2: Build the Jacobian matrix $J(Z^0) = \partial H / \partial Z|_{Z=Z^0}$.

Step 3: Solution of the following system of equations to update the state Z:

$$J(Z^0)\Delta Z^0 = -H(Z^0)$$

Details of DistFlow method can be referred in [36,37].

8.5.2 Modeling of Distributed Generators in Load Flow Analysis

Modeling distributed generators in load flow analysis is an important problem for the distribution system operations and control. Some efforts have been made to solve parts of the problems [38–40]. Feijoo and Cidras [40] proposed some useful DG models for distribution load flow. Some works have been proposed to satisfy some of those requirements [41–43]. Chen et al. [41] used the Gauss implicit Z-matrix method to solve the three-phase load flow problem. Transformer and cogenerator were also modeled for rigorous system analysis. The Gauss method is traditionally used for the load flow solution of general meshed networks; however, distribution systems typically have a radial or weakly meshed structure. Therefore, research reveals some new ideas to deal with the special network characteristics of distribution feeders [42,43]. Cheng and Shirmohammadi [42] proposed a compensation-based technique, where the forward/backward sweep algorithm was adopted in the solution scheme. A sensitivity matrix, used to calculate the incremental relation between the voltage magnitude and current injections, was derived and used for voltage-specific generator bus. A direct-approach technique for solving the three-phase distribution power flow which fully exploits network characteristic of distribution feeder was proposed in [43]. Two developed matrices, the bus-injection to branch-current (BIBC) matrix and the branch-current to bus-voltage (BCBV) matrix, and matrix multiplications are utilized to obtain power flow solution. However, the integration of different types of DGs was not proposed in [43].

Figure 8.35 shows an example of a combination of DGs for distribution systems. Fuel cell, PV cell, and wind turbine forming a hybrid renewable energy system, connect to the distribution network through a static power converter and a power system interface.

Teng [35] proposed three models of DGs for load flow analysis.

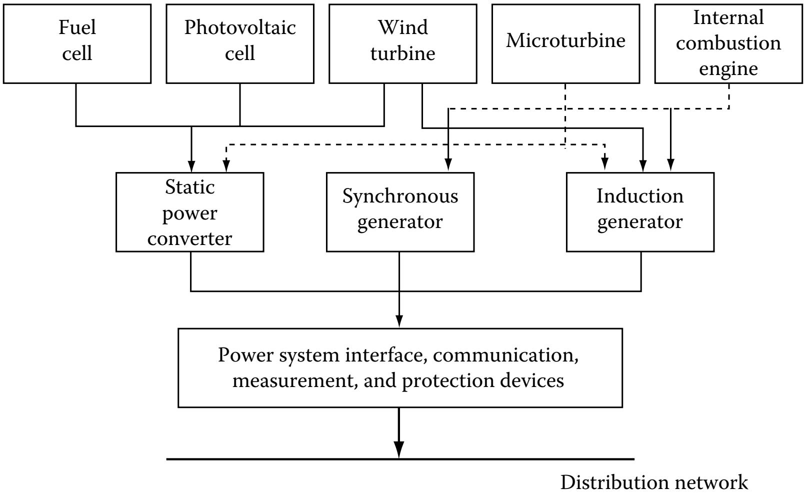

FIGURE 8.35
An example of combination of DGs.

8.5.2.1 Several Models for Distributed Generators

1. Constant power factor model

Constant power factor model is a commonly used model in power systems. It is applicable for the controllable DGs, such as synchronous generator-based DGs and power electronic-based DGs. In this model, the values of real power output $P_{i,g}$ and the power factor $pf_{i,g}$ of the DG need to be specified. Once these two values are given, the reactive power of the DG and its injected current can be calculated accordingly:

$$Q_{i,g} = P_{i,g} \tan\left[\cos^{-1}(pf_{i,g})\right] \tag{8.42}$$

$$I_{i,g} = \left(\frac{P_{i,g} + jQ_{i,g}}{V_{i,g}^{k}} \right) \tag{8.43}$$

where $Q_{i,g}$, $I_{i,g}$, and $V_{i,g}^{k}$ are the reactive power, injected current, and the output voltage at the *k*th iteration of the DG, respectively.

2. Variable reactive power model

DGs using induction generators as the power conversion devices act nearly like variable reactive power generators. A typical example is the induction generator-based wind turbine, whose real power output can be calculated by the wind turbine power curve. The reactive power consumed by a wind turbine can be represented as a function of its real power [40]:

$$Q_{i,g}^{1} = -Q_0 - Q_1 P_{i,g} - Q_2 {P_{i,g}}^{2} \tag{8.44}$$

where Q_0, Q_1, and Q_2 are experimentally obtained.

According to the equivalent circuit given in Figure 8.36, the reactive power output can be calculated as

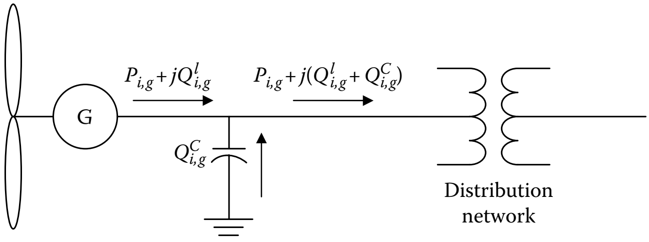

FIGURE 8.36
Equivalent circuit of induction generator-based wind turbine.

$$Q_{i,g} = Q_{i,g}^{1} + Q_{i,g}^{c} \tag{8.45}$$

3. Constant voltage model

This model is normally used for large-scale controlled DGs. The real power output and bus voltage magnitude are specifically valued. For the three methods introduced in Section 8.4.1, the reactive power output value needs to be calculated for iterations:

$$\Delta Q_{i,g}^{k,m} = V_{i,g}^{\text{mis}} \left(2\left|X_g\right|\right)^{-1} \tag{8.46}$$

$$V_{i,g}^{\text{mis}} = \left(\left|V_{i,g}^{\text{spec}}\right|\right)^2 - \left(\left|V_{i,g}^{k,m}\right|\right)^2 \tag{8.47}$$

$$\left[X_g\right] = \text{img}\left([\text{BCBV}_i][\text{BIBC}_i]\right) \tag{8.48}$$

where

$\Delta Q_{i,g}^{k,m}$ is the required reactive power variation for the mth inner iteration and the kth outer iteration

$V_{i,g}^{\text{mis}}$ is the square voltage mismatch between the specified voltage and the calculated voltage for the mth inner iteration and the kth outer iteration

$[\text{BIBC}_i]$ is the column vector of [BIBC] corresponding to bus i

$[\text{BCBV}_i]$ is the row vector of [BCBV] corresponding to bus i

Two matrices [BIBC] and [BCBV] are defined as follows:

1. [BIBC] describes the relationship between current injections [I] and branch currents [B].

$$[B] = [\text{BIBC}][I] \tag{8.49}$$

2. [BCBV] describes the relationship between branch currents [B] and bus voltages [V]:

$$[V_0] - [V] = [\text{BCBV}][B] \tag{8.50}$$

Applying the three load flow analysis models to the load flow analysis, one can calculate the state of distribution systems.

8.5.2.2 Test Results

The proposed models have been implemented using Borland C++ language on a Windows-XP-based Pentium-III PC. The following feeder is used for the test (Figure 8.37).

Tables 8.6 and 8.7 show the load data and line length for this feeder, respectively. Figure 8.38 shows the bus voltage profiles for phases A, B, and C without DG installation. Figure 8.38 also shows that this feeder is unbalanced, and therefore a three-phase load flow analysis can give an exact solution.

In a test two WTs are replaced by power converter-based fuel cells and operated at constant voltage, and the voltage profiles from the simulation as shown in Figure 8.39 can be obtained. In this case, the specified voltage

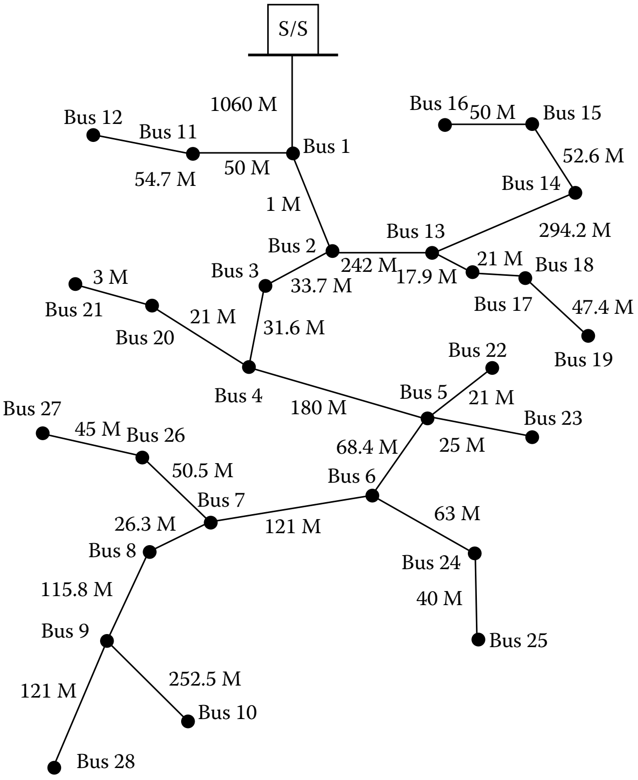

FIGURE 8.37
Test feeder.

TABLE 8.6

Load Data of Test Feeder

Bus Number	Phase A		Phase B		Phase C	
	P (kW)	Q (kVAR)	P (kW)	Q (kVAR)	P (kW)	Q (kVAR)
1	139.9	90.4	31.9	20.6	31.9	20.6
2	0	0	0	0	0	0
3	28.4	48.3	56.0	−0.4		
4	154.1	73.8	74.6	24.5	74.6	24.5
5	101.5	76.2	101.5	76.2	183.4	124.7
6			29.9	69.9	75.5	9.1
7	26.1	12.6	26.1	12.6	84.0	40.7
8			37.7	67.1	77.0	0.9
9	105.0	20.2	34.6	56.2		
10	84.0	63.0	84.0	63.0	141.5	98.7
11	113.2	61.1	113.2	61.1	212.4	109.1
12	165.1	91.3	81.4	46.1	81.4	46.1
13	367.3	133.3	367.3	133.3	367.3	133.3
14	30.5	13.9	30.5	13.9	108.9	58.3
15			75.3	85.9	88.8	−6.5
16	20.5	33.2	104.6	39.6		
17	74.4	64.6	34.0	1.1		
18	67	44.8	14.2	0.2		
19			67.5	109.5	128.5	−3.7
20	98.4	33.6	36.2	13.1	36.2	13.1
21	7.8	8.8	11.5	−2.4		
22	29.9	16.1	73.9	49.1	29.9	16.1
23	173.7	68.3	72.1	34.9	72.1	34.9
24			47.9	−3.5	75.4	69.7
25	88.2	23.2	26.0	48.5		
26	75.7	19.0	75.7	19.0	207.0	51.9
27	23.5	1.2			87.2	66.3
28	79.5	49.3	79.5	49.3	187.7	130.4
Total demand	2053.7	1046.2	1787.1	1088.4	2350.7	1038.2

magnitude at the furthest bus 28 is 0.97 p.u. Therefore, from Figure 8.39A, it can be seen that the voltages at Bus 28 are 0.97 p.u. and the unbalanced condition of this feeder is improved. Figure 8.39B shows the voltage profiles for Buses 1–10. The proposed DG constant voltage model was used in the load flow analysis, and the results are displayed in Figure 8.39.

TABLE 8.7

Line Length of Test Feeder

Line Number	From Bus	To Bus	Length (m)
1	S/S	1	1060
2	1	2	1
3	2	3	33.7
4	3	4	31.6
5	4	5	180
6	5	6	68.4
7	6	7	121
8	7	8	26.3
9	8	9	115.8
10	9	10	252.5
11	1	11	50
12	11	12	54.7
13	2	13	242
14	13	14	294.2
15	14	15	52.6
16	15	16	50
17	13	17	17.9
18	17	19	21
19	18	19	47.4
20	4	20	21
21	20	21	3
22	5	22	21
23	5	23	25
24	6	24	63
25	24	25	40
26	7	26	50.5
27	26	27	45
28	9	28	121

8.5.2.3 Summary

This section proposed the mathematical models of DGs for the application in the three-phase distribution load flow program. According to the characteristics of power output, DGs can be specified as constant power factor model, constant voltage model, or variable reactive power model in the load flow analysis. Test results show that the proposed method can be used to analyze the penetration of DGs into distribution feeders effectively and efficiently. Besides, the structures of the proposed matrices and the performance of the original load flow method are maintained. The proposed BIBC and BCBV matrices have the potential to be applied in other applications such as asymmetrical short-circuit current calculation, optimal capacitor placement, feeder reconfiguration problem, and so on.

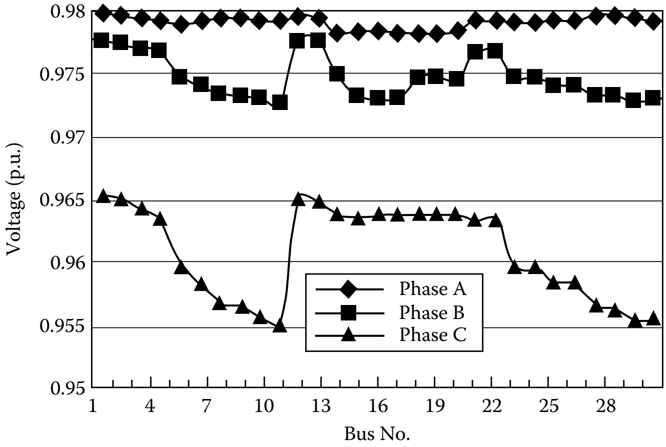

FIGURE 8.38
Voltage profiles of test feeder without DG installation.

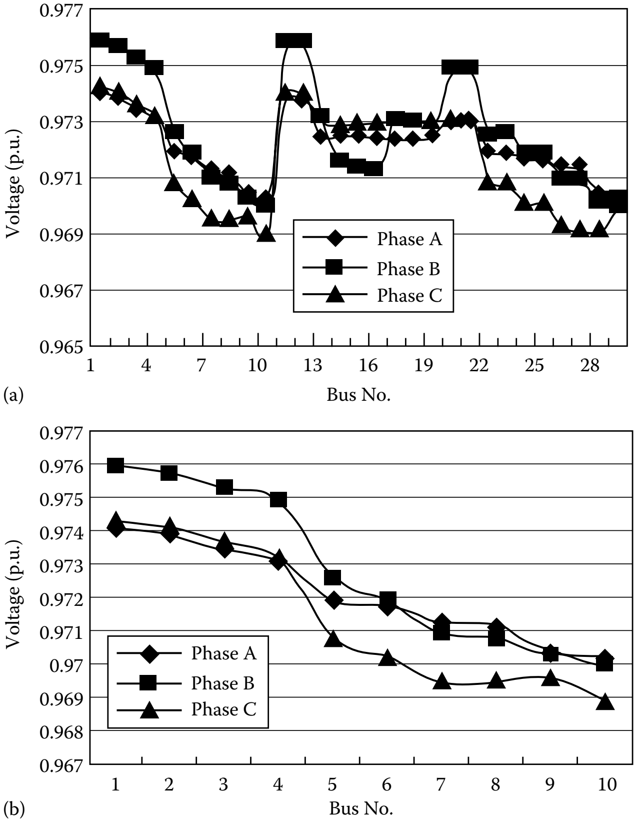

FIGURE 8.39
Voltage profiles of DGs operated in constant voltage model. (a) Bus voltage profiles of test feeder. (b) Bus voltage profiles for Buses 1–10.

References

1. G.D. Burch, *Hybrid Renewable Energy Systems*. http://www.netl.doe.gov/publications/proceedings/01/hybrids/Gary%20Burch%208.21.01.pdf.
2. K. Agbossou, M. Kolhe, J. Hamelin, and T.K. Bose, Performance of a stand-alone renewable energy system based on energy storage as hydrogen, *IEEE Transactions on Energy Conversation*, 19(3), 633–640, 2004.
3. D.B. Nelson, M.H. Nehrir, and C. Wang, Unit sizing and cost analysis of stand-alone hybrid Wind/PV/fuel cell systems, *Renewable Energy*, 31(10), 1641–1656, 2006.
4. S.H. Chan, H.K. Ho, and Y. Tian, Multi-level modeling of SOFC-gas turbine hybrid system, *International Journal of Hydrogen Energy*, 28(8), 889–900, 2003.
5. L.A. Torres, F.J. Rodriguez, and P.J. Sebastian, Simulation of a solarhydrogen-fuel cell system: Results for different locations in Mexico, *International Journal of Hydrogen Energy*, 23(11), 1005–1010, 1998.
6. F. Bonanno, A. Consoli, A. Raciti, B. Morgana, and U. Nocera, Transient analysis of integrated diesel-wind-photovoltaic generation systems, *IEEE Transactions on Energy Conversation*, 14(2), 232–238, 1999.
7. K. Strunz and E.K. Brock, Stochastic energy source access management: Infrastructure-integrative modular plant for sustainable hydrogenelectric co-generation, *International Journal of Hydrogen Energy*, 31, 1129–1141, 2006.
8. E.S. Abdin, A.M. Osheiba, and M.M. Khater, Modeling and optimal controllers design for a stand-alone photovoltaic-diesel generating unit, *IEEE Transactions on Energy Conversation*, 14(3), 560–565, 1999.
9. F. Giraud and Z.M. Salameh, Steady-state performance of a gridconnected rooftop hybrid wind-photovoltaic power system with battery storage, *IEEE Transactions on Energy Conversation*, 16(1), 1–7, 2001.
10. W.D. Kellogg, M.H. Nehrir, G. Venkataramanan, and V. Gerez, Generation unit sizing and cost analysis for stand-alone wind, photovoltaic, and hybrid wind/PV systems, *IEEE Transactions on Energy Conversation*, 13(1), 70–75, 1998.
11. H. Sharma, S. Islam, and T. Pryor, Dynamic modeling and simulation of a hybrid wind diesel remote area power system, *International Journal of Renewable Energy Engineering*, 2(1), 19–25, 2000.
12. R. Chedid, H. Akiki, and S. Rahman, A decision support technique for the design of hybrid solar-wind power systems, *IEEE Transactions on Energy Conversation*, 13(1), 76–83, 1998.
13. D.L. Elliott and M.N. Schwartz, *Wind Energy Potential in the United States, National Renewable Energy Laboratory (NREL)*, 1993. http://www.nrel.gov/wind/wind_potential.html (current May 2004).
14. P. Gipe, *Wind Energy Comes of Age*, New York: John Wiley & Sons, 1995.
15. S.S. Hutson, N.L. Barber, J.F. Kenny, K.S. Linsey, D.S. Lumia, and M.A. Maupin, Estimated use of water in the United States in 2000, Reston, VA: U.S. Geological Survey, Circular 1268, 46 pp., 2004.
16. American Wind Energy Association (AWEA), *Wind Energy Fast Facts, AWEA*. http://www.awea.org/pubs/factsheets/FastFacts2003.pdf (current May 2004).
17. W. Carter and B. Diong, Model of regenerative fuel cell-supported wind turbine AC power generating system, *Proceedings of IEEE Industry Applications Society Annual Meeting*, Seattle, WA, October 2004.

18. M.T. Iqbal, Modeling and control of a wind fuel cell hybrid energy system, *Renewable Energy*, 28(2), 223–237, 2003.
19. Grainger Center for Electric Machinery and Electromechanics, University of Illinois at Urbana-Champaign, *The 2001 International Future Energy Challenge*. http://www.energychallenge.org/.
20. L.-Y. Chiu, B. Diong, and R. Gemmen, An improved small-signal model of the dynamic behavior of PEM fuel cells, To appear in *IEEE Transactions Industry Applications*, 40(4), July/August 2004.
21. W.E. Leithead, S.A. De La Selle, and D. Reardon. Classical control of active pitch regulation of constant speed horizontal axis wind turbine, *International Journal of Control*, 55(4), 845–876, 1992.
22. D.M. Eggleston and F.S. Stoddard, *Wind Turbine Engineering Design*, New York: Kluwer Academic Publishers, 1987.
23. E.W. Weisstein, Euler backward method. From *MathWorld—A Wolfram Web Resource*. http://mathworld.wolfram.com/EulerBackwardMethod.html (current May 2004).
24. R. Isermann, *Digital Control Systems*, vol. 2, 2nd ed., Berlin, Germany: Springer-Verlag, 1989.
25. J. Larminie and A. Dicks, *Fuel Cell Systems Explained*, Chichester, U.K.: John Wiley & Sons, Inc., 2000.
26. K. Sapru, N.T. Stetson, and S.R. Ovshinsky, Development of a small scale hydrogen production storage system for hydrogen applications, *Proceedings of Intersociety Energy Conversion Engineering Conference,* Honolulu, HI, Vols. 3 & 4, 1997.
27. N. Mohan, T.M. Undeland, and W.P. Robbins, *Power Electronics: Converters, Applications, and Design*, New York: John Wiley & Sons, Inc., 1995.
28. T. Senjyu, T. Nakaji, K. Uezato, and T. Funabashi, A hybrid power system using alternative energy facilities in isolated Island, *IEEE Transactions on Energy Conversion*, 20(2), 406–414, June 2005.
29. C. Wang and M.H. Nehrir, Power management of a stand-alone wind/photovoltaic/fuel cell energy system, *IEEE Transactions on Energy Conversion*, 23(3), 957–967, 2008.
30. Global Wind 2007 report, Global Wind Energy Council. [Online] http://www.gwec.net/index.php?id = 90.
31. *Wind Power Today—FederalWind ProgramHighlights*. NREL, DOE/GO-102005-2115, April 2005.
32. *Trends in Photovoltaic Applications: Survey Report of Selected IEA Countries between 1992 and 2004*, International Energy Agency Photovoltaics Power Systems Programme (IEA PVPS), September 2005.
33. J. Cahill, K. Ritland, and W. Kelly, *Description of Electric Energy Use in Single Family Residences in the PacificNorthwest 1986–1992*, Portland, OR: Office Energy Resour, Bonneville Power Admin, December 1992.
34. http://www.usbr.gov/pn/agrimet/webaghrread.html, 2006 [Online].
35. J.H. Teng, Modeling distributed generations in three-phase distribution load flow, *IET Generation, Transmission & Distribution*, 2(3), 330–340, 2008.
36. M.E. Baran and F.F. Wu, Optimal sizing of capacitors placed on a radial distribution system, *IEEE Transactions on Power Delivery*, 4(1), 735–743, 1989.
37. H. Chiang and M.E. Baran, On the existence and uniqueness of load floa solution for radial distribution power networks, *IEEE Transactions on Circuits and Systems*, 37(3), 410–416, 1990.

38. M. Rabinowitz, Power systems of the future, *IEEE Power Engineering Review*, 20(1), 5–16, 2000.
39. S. Persaud, B. Fox, and D. Flynn, Impact of remotely connected wind turbines on steady state operation of radial distribution networks, *IEE Proceedings—Generation, Transmission and Distribution*, 147(3), 157–163, 2000.
40. A.E. Feijoo and J. Cidras, Modeling of wind farms in the load flow analysis, *IEEE Transactions on Power Systems*, 15(1), 110–115, 2000.
41. T.H. Chen, M.S. Chen, T. Inoue, P. Kotas, E.A. Chebli, Three-phase cogenerator and transformer models for distribution system analysis, *IEEE Transactions on Power Delivery*, 6(4), 1671–1681, 1991.
42. C.S. Cheng and D. Shirmohammadi, A three-phase power flow method for real-time distribution system analysis, *IEEE Transactions on Power Systems*, 10(2), 671–679, 1995.
43. J.H. Teng, A direct approach for distribution system load flow solutions, *IEEE Transactions on Power Delivery*, 18(3), 882–887, 2003.

Appendix A: Linear Control

A.1 Introduction

Since this book is aimed at automotive and power industry engineers, as well as researchers and graduate students in the areas of renewable energy, circuits, and control, it has been assumed that the reader has some basic knowledge of differential equations, the Laplace transform, transfer functions, poles and zeros, and matrix algebra. Furthermore, it would be desirable for the reader to have taken a course on continuous-time linear control systems. But to make this book accessible to a wider audience, we include a brief review of linear systems and control in this appendix.

A.2 Linear Systems and Control

A.2.1 State Variables and State Equations

The "state variables" of a dynamic system are a "minimal" set of variables, usually denoted as $x_1(t)$, $x_2(t)$, …, $x_n(t)$, that can describe the system's dynamic behavior completely in terms of n first-order linear differential equations:

$$\begin{aligned}
\dot{x}_1(t) &= a_{11}x_1 + a_{12}x_2 + \cdots + a_{1n}x_n + b_{11}u_1 + \cdots + b_{1m}u_m \\
\dot{x}_2(t) &= a_{21}x_1 + a_{22}x_2 + \cdots + a_{2n}x_n + b_{21}u_1 + \cdots + b_{2m}u_m \\
\vdots \quad & \quad \vdots \\
\dot{x}_n(t) &= a_{n1}x_1 + a_{n2}x_2 + \cdots + a_{nn}x_n + b_{n1}u_1 + \cdots + b_{nm}u_m
\end{aligned} \tag{A.1}$$

where $u_i(t)$, $i=1, 2, \ldots, m$ represent the system's (control) "inputs," and the coefficients a and b are all (time-invariant) constants. These first-order linear differential equations are then known as the "state equations" of the dynamic system.

The system's "outputs," usually denoted by $y(t)$, are those variables that are measured (using sensors). If these depend linearly on the system's state variables and inputs, then they can be mathematically described by the equations:

$$\begin{aligned}
y_1(t) &= c_{11}x_1 + c_{12}x_2 + \cdots + c_{1n}x_n + d_{11}u_1 + \cdots + d_{1m}u_m \\
y_2(t) &= c_{21}x_1 + c_{22}x_2 + \cdots + c_{2n}x_n + d_{21}u_1 + \cdots + d_{2m}u_m \\
\vdots \quad & \quad \vdots \\
y_p(t) &= c_{p1}x_1 + c_{p2}x_2 + \cdots + c_{pn}x_n + d_{p1}u_1 + \cdots + d_{pm}u_m
\end{aligned} \tag{A.2}$$

where $p \le n$, and the coefficients c and d are all constants. Then, Equations A.1 and A.2 can be written much more compactly in vector–matrix form as

$$\begin{aligned} \dot{x}(t) &= Ax(t) + Bu(t) \\ y(t) &= Cx(t) + Du(t) \end{aligned} \tag{A.3}$$

where $\dot{x}(t)$, $x(t)$, $u(t)$, and $y(t)$ are $n \times 1$, $n \times 1$, $m \times 1$, and $p \times 1$ vectors of the state derivatives, state variables, inputs, and outputs, respectively, whereas A, B, C, and D are $n \times n$, $n \times m$, $p \times n$, and $p \times m$ matrices, respectively.

Example: State equations describing a mass–spring–damper system.

First note that a mass–spring–damper system's dynamic behavior is completely described by the second-order linear differential equation:

$$M\ddot{y}(t) + B\dot{y}(t) + Ky(t) = u(t) \tag{A.4}$$

where $y(t)$ represents the displacement of mass M when it is subject to force $u(t)$ as shown in Figure A.1; B and K are the system's damping and spring constants, respectively.

Let us define two new variables $x_1(t) = y(t)$ and $x_2(t) = \dot{y}(t)$ to be the system's state variables. Then, we can rewrite Equation A.4, after some simple algebra, equivalently as the following first-order linear differential equations that represent a second-order state equation description of this mass–spring–damper system:

$$\begin{aligned} \dot{x}_1(t) &= \dot{y}(t) = x_2(t) \\ \dot{x}_2(t) &= \ddot{y}(t) = -\frac{K}{M}x_1(t) - \frac{B}{M}x_2(t) + u(t) \end{aligned} \tag{A.5}$$

This can be expressed in vector–matrix form as

$$\begin{pmatrix} \dot{x}_1 \\ \dot{x}_2 \end{pmatrix} = \begin{pmatrix} 0 & 1 \\ -\frac{K}{M} & -\frac{B}{M} \end{pmatrix} \begin{pmatrix} x_1 \\ x_2 \end{pmatrix} + \begin{pmatrix} 0 \\ 1 \end{pmatrix} u \tag{A.6}$$

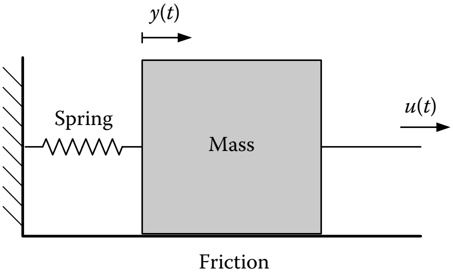

FIGURE A.1
Mass–spring–damper system.

A.2.2 Linear Approximation of a Nonlinear System

For a nonlinear dynamic system, it is also possible to define state variables and thereby obtain a set of state equations, although these will be nonlinear, for describing the dynamic behavior of that system. However, assuming that the system operates in a limited range, i.e., the variables do not change by much, about an operating or equilibrium point defined by the set of state variable and input values (x_0, u_0), we can approximate the system's behavior within that range (its small-signal behavior, using electrical engineering terminology) by a set of "linear" state equations. A standard procedure for doing so, via the mathematical concept of Taylor series expansion, can be found in many undergraduate control systems textbooks such as [1]. This same approximation technique has been applied to obtain the PEMFC linear model described in Section 3.5.1.

Example: Linear approximation of a generic second-order nonlinear system.

Suppose that we are given a second-order dynamic system, with state variables x_1, x_2, and a single input u, which is described by the nonlinear state equations:

$$\begin{aligned}\dot{x}_1(t) &= f_1\left(x_1, x_2, u\right)\\ \dot{x}_2(t) &= f_2\left(x_1, x_2, u\right)\end{aligned} \tag{A.7}$$

where f_1 and f_2 are some nonlinear functions. Denoting the system's operating point values to be (x_{10}, x_{20}, u_0), then a linear approximation of Equation A.7 is given as

$$\begin{aligned}\dot{x}_1(t) &= \left.\frac{\mathrm{d}f_1}{\mathrm{d}x_1}\right|_{x_{10},x_{20},u_0} x_1 + \left.\frac{\mathrm{d}f_1}{\mathrm{d}x_2}\right|_{x_{10},x_{20},u_0} x_2 + \left.\frac{\mathrm{d}f_1}{\mathrm{d}u}\right|_{x_{10},x_{20},u_0} u\\ \dot{x}_2(t) &= \left.\frac{\mathrm{d}f_2}{\mathrm{d}x_1}\right|_{x_{10},x_{20},u_0} x_1 + \left.\frac{\mathrm{d}f_2}{\mathrm{d}x_2}\right|_{x_{10},x_{20},u_0} x_2 + \left.\frac{\mathrm{d}f_2}{\mathrm{d}u}\right|_{x_{10},x_{20},u_0} u\end{aligned} \tag{A.8}$$

Note that the evaluation of the calculated partial derivatives at the operating point values will yield constant coefficients for x_1, x_2, and u in the equations.

A.2.3 Characteristic Equation, Characteristic Roots, and Eigenvalues of Linear System

For the linear dynamic system described by the state equations (Equation A.3), its input–output "transfer function" can be expressed as

$$\frac{Y(s)}{U(s)} = C(sI - A)^{-1}B + D \tag{A.9}$$

where s is the Laplace transform's complex frequency variable and I represents the identity matrix. Furthermore, the system's "characteristic roots" are given by the roots of the matrix determinant of $sI - A$ (an nth-order polynomial of s) equated to 0, i.e.,

$$|sI - A| = 0 \tag{A.10}$$

These n roots are also the "poles" of the system (subject to exact cancellation by the system's zeros) and can be obtained alternatively by finding the "eigenvalues" of the system matrix A.

A.2.4 Linear State Feedback Control

We consider a linear dynamic system described by the state equations (Equation A.3), where the control has the form:

$$u(t) = -Kx(t) \tag{A.11}$$

where the state feedback gain K is a vector (or a matrix in the multiple-input case) with constant elements. This form of control means that

1. All state variables can be, and are, measured.
2. The control is a linear combination of the state variables.
3. The closed-loop control system consisting of Equations A.3 and A.11 can now be described by

$$\dot{x}(t) = (A - BK)x(t) \tag{A.12}$$

4. The characteristic equation of the closed-loop system is then given by

$$|sI - (A - BK)| = 0$$

Now if the pair of matrices (A, B) are such that the open-loop system (Equation A.3) is completely state-controllable [1], then it is well known that the closed-loop system's characteristic roots can be "placed" anywhere in the complex s-plane (subject to the complex roots being in conjugate pairs), by appropriately choosing the elements of K. This state feedback gain design procedure is typically called "pole-placement" design.

Example: State feedback pole-placement for a generic second-order system.

Suppose that we are given a dynamic system that is described by the state equation:

$$\begin{pmatrix} \dot{x}_1 \\ \dot{x}_2 \end{pmatrix} = \begin{pmatrix} 0 & 1 \\ -a_0 & -a_1 \end{pmatrix} \begin{pmatrix} x_1 \\ x_2 \end{pmatrix} + \begin{pmatrix} 0 \\ 1 \end{pmatrix} u \tag{A.13}$$

This system's characteristic equation is then given by

$$s^2 + a_1 s + a_0 = 0 \tag{A.14}$$

with two eigenvalues (poles) that may be in undesirable locations, e.g., in the right-half s-plane, which corresponds to an unstable system. Since (A, B) is a completely controllable pair for this system, we can apply state feedback control to place the closed-loop system's poles at any other locations; but it is necessary to have the measured outputs $y(t) = x(t)$.

Then the needed state feedback gain is given by $K = (k_0 k_1)$, which means that the system under state feedback control is described by

$$\begin{pmatrix} \dot{x}_1 \\ \dot{x}_2 \end{pmatrix} = \begin{pmatrix} 0 & 1 \\ -[a_0 + k_0] & -[a_1 + k_1] \end{pmatrix} \begin{pmatrix} x_1 \\ x_2 \end{pmatrix} \tag{A.15}$$

This yields the characteristic equation:

$$s^2 + (a_1 + k_1)s + (a_0 + k_0) = 0 \tag{A.16}$$

so, the elements of K can therefore be chosen appropriately to obtain the desired characteristic equation that corresponds to have the closed-loop system's poles at those locations that would yield the desired system stability and performance characteristics.

Appendix B: Nonlinear Control

In nature, almost all systems are nonlinear systems, for example, fuel cell system, power grids, etc. Linear control is based on the linearized modeling of the system, which is accurate only at the operating point of linearization. To achieve better control performance, nonlinear modeling and nonlinear control need to be considered. Nonlinear modeling of fuel cell system is given previously in Chapter 3. This appendix provides a preliminary introduction to nonlinear control technique, especially the exact linearization approach [2–4].

B.1 Nonlinear Coordinate Transformation and Diffeomorphism

For a given set of nonlinear equations:

$$Z = \Phi(X) \tag{B.1}$$

where Z and X are vectors with $(n \times 1)$ dimension, Φ is a nonlinear vector function with $(n \times 1)$ dimension, the set of nonlinear transformation in Equation B.1 is called nonlinear coordinate transformation if the following two conditions are satisfied:

1. The inverse transformation of Φ exists, which means that Φ^{-1} exists.
2. Both Φ and Φ^{-1} are smooth vector functions, that is, the function of each component of both Φ and Φ^{-1} has continuous partial derivatives of any orders.

If the above two conditions are satisfied, the coordinate transformation $\Phi(X)$ is also called a diffeomorphism between two coordinate spaces.

From a geometric point view, the coordinate transformation $Z = \Phi(X)$ and $X = \Phi^{-1}(Z)$ can be considered as a mapping between two spaces with the same dimension X and Z.

B.2 Local Diffeomorphism

The above two conditions may be satisfied only for a neighborhood of a specific point X^0 rather than all points in the space. Local diffeomorphism is then defined on a certain domain.

A property of local diffeomorphism is given as follows:

Suppose $\Phi(X)$ is a smooth function defined on a certain subset S of space R^n. If the Jacobian matrix $\partial\Phi/\partial X$ at $X = X^0$ is nonsingular, $\Phi(X)$ is then a local diffeomorphism in an open subset S^0 including X^0.

B.3 Coordinate Transformation of Nonlinear Control Systems

Given a nonlinear control system:

$$\begin{cases} \dot{X} = f(X) + g(X)u \\ y = h(X) \end{cases} \tag{B.2}$$

where

$X \in R^n$ and $u \in R$ are state variable and control variable, respectively

$y \in R$ is the output variable

f and g are nonlinear function vectors

h is a nonlinear function

Let us select a local diffeomorphism $Z = \Phi(X)$. Then considering Equation B.2, we have

$$\dot{Z} = \frac{\mathrm{d}\Phi}{\mathrm{d}X} = \frac{\partial\Phi}{\partial X}\frac{\mathrm{d}X}{\mathrm{d}t} = \frac{\partial\Phi}{\partial X}\dot{X} = \frac{\partial\Phi}{\partial X}(f(X) + g(X)u)$$

And consider $X = \Phi^{-1}(Z)$; therefore, we get

$$\dot{Z} = \frac{\partial\Phi}{\partial X}[f(X) + g(X)u] = \frac{\partial\Phi}{\partial X}\left[f(\Phi^{-1}(Z)) + g(\Phi^{-1}(Z))u\right]$$

$$y = h(X) = h(\Phi^{-1}(Z))$$

Define

$$\tilde{f}(Z) = \frac{\partial\Phi}{\partial X}f(X)\bigg|_{X=\Phi^{-1}(Z)}$$

$$\tilde{g}(Z) = \frac{\partial\Phi}{\partial X}g(X)\bigg|_{X=\Phi^{-1}(Z)}$$

$$\tilde{h}(Z) = h(X)\big|_{X=\Phi^{-1}(Z)}$$

Then, we have

$$\begin{aligned} \dot{Z} &= \tilde{f}(Z) + \tilde{g}(Z)u \\ y &= \tilde{h}(Z) \end{aligned} \tag{B.3}$$

Equation B.3 represents the transformed nonlinear system using the selected local diffeomorphism.

B.4 Affine Nonlinear Control Systems

A control system is called affine nonlinear control system if it is nonlinear to state variable vector but linear to control variable vector. It has the following format:

$$\dot{X} = f(X) + \sum_{i=1}^{m} g_i(X)u_i$$

$$y = h(X)$$

where

$X \in R^n$ and $u \in R$ are state variable vector and control variable vector, respectively
$y \in R$ is the output variable
f and g are nonlinear function vectors
h is a nonlinear function

Nonlinear function vectors $f(X)$ and $g(X)$ are also called vector fields of state space.

B.5 Derived Mapping of Vector Fields

Derived mapping of vector fields is very important for exact linearization technique. Here is the definition—For a given diffeomorphism, $Z = \Phi(X)$ and a vector field $f(X)$, the Jacobian matrix of $\Phi(X)$ is $J_\Phi = (\partial\Phi/\partial X)$, then the derived mapping of $f(X)$ under the mapping $\Phi(X)$ is defined as

$$\Phi_*(f) = J_\Phi(X)f(X)\big|_{X=\Phi^{-1}(Z)}$$

The derived mapping of vector field $f(X)$ is a transformation that moves the vector field $f(X)$ from the state space to Z space based on the diffeomorphism $Z = \Phi(X)$.

B.6 Lie Derivative and Lie Bracket

Two essential geometric concepts of nonlinear systems are Lie derivative and Lie bracket, which are used in the application of exact linearization technique.

B.6.1 Lie Derivative

Given a differentiable scalar function $\xi(X) = \xi(x_1, x_2, \ldots, x_n)$ and a vector field $f(X)$ of X, a new scalar function, denoted by $L_f\xi(X)$, is obtained by the following operation:

$$L_f\xi(X) = \frac{\partial\xi(X)}{\partial X} f(X) = \sum_{i=1}^{n} \frac{\partial\xi(X)}{\partial x_i} f_i(X)$$

and called the Lie derivative of function $\xi(X)$ along the vector field $f(X)$.

B.6.2 Lie Bracket

Suppose two vector fields $f(X)$ and $g(X)$. The Lie bracket of $g(X)$ along $f(X)$ is defined by the following operation:

$$[f, g] = ad_f g = \frac{\partial g}{\partial X} f - \frac{\partial f}{\partial X} g$$

Since Lie bracket of $g(X)$ is a new vector field, it can be used to calculate the Lie bracket along $f(X)$ once more:

$$ad_f^{\,2} g(X) = [f, [f, g]](X)$$
$$\ldots$$
$$ad_f^{\,k} g(X) = [f, ad_f^{\,k-1} g](X)$$

The main operational rules of Lie bracket are

1. Lie bracket is skew-symmetric:

$$[f, g] = -[g, f]$$

2. If λ_1 and λ_2 are two real numbers, then

$$[f, \lambda_1 g_1 + \lambda_2 g_2](X) = \lambda_1 [f, g_1](X) + \lambda_2 [f, g_2](X)$$

3. If $\gamma(X)$ is another vector field, then

$$\left[f,[g,\gamma]\right]+\left[\gamma,[f,g]\right]+\left[g,[\gamma,f]\right]=0$$

4. If $f(X)$ and $g(X)$ are vector fields, $\xi(X)$ is a scalar function, then the Lie derivative of $\xi(X)$ along vector field $[f(X), g(X)]$ is

$$L_{[f,g]}\xi(X)=L_f L_g \xi(X)-L_g L_f \xi(X)$$

B.7 Involutivity of Vector Field Sets

Suppose k vector fields $g_1(X), \ldots, g_n(X)$, all with n-dimension, let us form the matrix:

$$G=\left[g_1(X) \quad g_2(X) \quad \cdots \quad g_k(X)\right]$$

If the matrix G has rank k at $X = X^0$ and the following augmented matrix:

$$\left[g_1(X) \quad g_2(X) \quad \cdots \quad g_k(X) \quad \left[g_i, g_j\right]\right]$$

has the same rank k at $X=X^0$ for any i and j where $1 \le i, j \le k$, then the vector field set $\{g_1, g_2, \ldots, g_k\}$ is called an involutive one or we say it has the property of involutivity.

B.8 Relative Degree of a Control System

Suppose a SISO nonlinear control system:

$$\begin{aligned}\dot{X} &= f(X)+g(X)u \\ y &= h(X)\end{aligned}$$

where $X \in R^n$, $u \in R$, $y \in R$, $f(X)$, and $g(X)$ are vector field items.

The above is said to have relative degree γ in a neighborhood Ω of $X = X^0$, if the following two conditions are satisfied:

1. The Lie derivative of the function $L_f^k h(X)$ along g equals zero in Ω, i.e.,

$$L_g L_f{}^k h(X) = 0, \quad k < \gamma - 1, \ \forall\ x \in \Omega$$

2. The Lie derivative of the function $L_f^{\gamma-1} h(X)$ along vector field $g(X)$ is not equal to zero in Ω, i.e.,

$$L_g L_f{}^{\gamma-1} h(X) \neq 0.$$

B.9 Exact Linearization Control

Exact linearization control design principle is to exactly linearize a nonlinear control system into a controllable linear system and to get the state nonlinear feedback control law based on the linear control system. Converting the obtained control law back to the original nonlinear space results in the nonlinear control design for the original control system.

B.9.1 Conditions of Exact Linearization

To introduce the conditions of exact linearization, we need to introduce the following theorem.

Frobenius Theorem

Consider the following partial differential equations set:

$$\frac{\partial h(X)}{\partial X}\left[Y_1(X) \ \ Y_2(X) \ \ \ldots \ \ Y_k(X)\right] = 0 \tag{B.4}$$

where $\partial h(X)/\partial X$ is the gradient vector of $h(X)$; $Y_1(X)$, $Y_2(X)$, …, $Y_k(X)$ are the n-dimensional vector fields defined on X space.

Suppose the matrix $[Y_1(X)\ Y_2(X)\ \ldots\ Y_k(X)]$ has rank k at $X = X^0$. If and only if the augmented matrix $[Y_1(X)\ Y_2(X)\ \ldots Y_k(X)\ [Y_i, Y_j]]$ still has rank k for all X in a neighborhood of X^0, there must exist $n - k$ scalar functions, defined in a neighborhood Ω of X^0, which are the solutions of Equation B.4, such that the Jacobian matrix $\partial h(X)/\partial X$ has rank $n - k$ at $X = X^0$.

The conditions proposed in Frobenius Theorem are actually the conditions of involutivity of a vector field $\{Y_1, Y_2, \ldots, Y_k\}$.

B.9.2 Nonlinear Control Design by Exact Linearization

Consider a SISO nth order nonlinear control system as follows:

$$\begin{aligned} \dot{X} &= f(X) + g(X)u \\ y &= h(X) \end{aligned} \tag{B.5}$$

We assume that the relative degree of the system $r = n$, then the system could be transformed into a controllable linear system:

$$\dot{Z} = AZ + Bv \tag{B.6}$$

where the matrix A and B are Brunovsky normal form, and Z and v are state variable vector and control variable, respectively.

This linearization can be generated by using the nonlinear state feedback:

$$u = -\frac{\alpha(X)}{\beta(X)} + \frac{1}{\beta(X)} v \tag{B.7}$$

where

$\alpha(X) = L_f{}^n h(X)$

$\beta(X) = L_g L_f{}^{n-1} h(X)$

And the diffeomorphism coordinate transformation:

$$Z = \Phi(X) = \begin{bmatrix} h(X) \\ L_f h(X) \\ \vdots \\ L_f{}^{n-1} h(X) \end{bmatrix} \tag{B.8}$$

The optimal control of the linear system in Equation B.6 is

$$v^* = -B^{\mathrm{T}} P^* Z(t)$$

where P^* is the solution of the Riccati matrix equation.

Considering the coordinate transformation $Z = \Phi(X)$, we can obtain the following nonlinear control law:

$$u = \frac{-\left(L_f{}^n h(X) + k_n{}^* L_f{}^{n-1} h(X) + \cdots + k_2{}^* L_f h(X) + k_1{}^* h(X)\right)}{L_g L_f{}^{n-1} h(X)}$$

The Brunovsky normal form is given as follows:

$$\dot{Z} = AZ + Bv$$

where

$$Z = \begin{bmatrix} z_1 \\ z_2 \\ \vdots \\ z_n \end{bmatrix}$$

$$A = \begin{bmatrix} 0 & 1 & 0 & \cdots & 0 & 0 \\ 0 & 0 & 1 & \cdots & 0 & 0 \\ \vdots & \vdots & \vdots & \vdots & \vdots & \vdots \\ 0 & 0 & 0 & \cdots & 0 & 1 \\ 0 & 0 & 0 & 0 & 0 & 0 \end{bmatrix}$$

$$B = \begin{bmatrix} 0 \\ 0 \\ \vdots \\ 0 \\ 1 \end{bmatrix}$$

Appendix C: Induction Machine Modeling and Vector Control for Fuel Cell Vehicle Applications

C.1 Voltage Equations of the Induction Machine

The idealized induction machine is shown in Figure C.1.

If the winding of the stator is sinusoidally distributed, then stator and rotor voltage equations are expressed as follows [6]:

$$\begin{aligned} V_{\mathrm{abcs}} &= R_{\mathrm{s}} i_{\mathrm{abcs}} + p\bar{\lambda}_{\mathrm{abcs}} \\ V_{\mathrm{abcr}} &= R_{\mathrm{r}} i_{\mathrm{abcr}} + p\bar{\lambda}_{\mathrm{abcr}} \end{aligned} \tag{C.1}$$

where $p = \mathrm{d}/\mathrm{d}t$, $V_{\mathrm{abcs}} = [V_{\mathrm{as}}\ V_{\mathrm{bs}}\ V_{\mathrm{cs}}]^{\mathrm{T}}$, $i_{\mathrm{abcs}} = [i_{\mathrm{as}}\ i_{\mathrm{bs}}\ i_{\mathrm{cs}}]^{\mathrm{T}}$, $\bar{\lambda}_{\mathrm{abcs}} = [\lambda_{\mathrm{as}}\ \lambda_{\mathrm{bs}}\ \lambda_{\mathrm{cs}}]^{\mathrm{T}}$, $V_{\mathrm{abcr}} = [V_{\mathrm{ar}}\ V_{\mathrm{br}}\ V_{\mathrm{cr}}]^{\mathrm{T}}$, $i_{\mathrm{abcr}} = [i_{\mathrm{ar}}\ i_{\mathrm{br}}\ i_{\mathrm{cr}}]^{\mathrm{T}}$, and $\bar{\lambda}_{\mathrm{abcs}} = [\lambda_{\mathrm{as}}\ \lambda_{\mathrm{bs}}\ \lambda_{\mathrm{cs}}]^{\mathrm{T}}$.

The s and r subscripts represent the equations in terms of stator and rotor windings.

The flux linkage equations are given as

$$\begin{bmatrix} \bar{\lambda}_{\mathrm{abcs}} \\ \bar{\lambda}_{\mathrm{abcr}} \end{bmatrix} = \begin{bmatrix} L_{\mathrm{s}} & L_{\mathrm{sr}} \\ L_{\mathrm{sr}}^{\mathrm{T}} & L_{\mathrm{r}} \end{bmatrix} \begin{bmatrix} i_{\mathrm{abcs}} \\ i_{\mathrm{abcr}} \end{bmatrix} \tag{C.2}$$

where

$$L_{\mathrm{s}} = \begin{bmatrix} L_{\mathrm{ls}} + L_{\mathrm{ms}} & -\frac{1}{2}L_{\mathrm{ms}} & -\frac{1}{2}L_{\mathrm{ms}} \\ -\frac{1}{2}L_{\mathrm{ms}} & L_{\mathrm{ls}} + L_{\mathrm{ms}} & -\frac{1}{2}L_{\mathrm{ms}} \\ -\frac{1}{2}L_{\mathrm{ms}} & -\frac{1}{2}L_{\mathrm{ms}} & L_{\mathrm{ls}} + L_{\mathrm{ms}} \end{bmatrix}, \quad L_{\mathrm{r}} = \begin{bmatrix} L_{\mathrm{lr}} + L_{\mathrm{mr}} & -\frac{1}{2}L_{\mathrm{mr}} & -\frac{1}{2}L_{\mathrm{mr}} \\ -\frac{1}{2}L_{\mathrm{mr}} & L_{\mathrm{ls}} + L_{\mathrm{mr}} & -\frac{1}{2}L_{\mathrm{mr}} \\ -\frac{1}{2}L_{\mathrm{mr}} & -\frac{1}{2}L_{\mathrm{mr}} & L_{\mathrm{ls}} + L_{\mathrm{mr}} \end{bmatrix}, \quad \text{and}$$

$$L_{\mathrm{sr}} = L_{\mathrm{sr}} \begin{bmatrix} \cos\theta_r & \cos\left(\theta_{\mathrm{r}} + \frac{2\pi}{3}\right) & \cos\left(\theta_{\mathrm{r}} - \frac{2\pi}{3}\right) \\ \cos\left(\theta_{\mathrm{r}} - \frac{2\pi}{3}\right) & \cos\theta_{\mathrm{r}} & \cos\left(\theta_{\mathrm{r}} + \frac{2\pi}{3}\right) \\ \cos\left(\theta_{\mathrm{r}} + \frac{2\pi}{3}\right) & \cos\left(\theta_r - \frac{2\pi}{3}\right) & \cos\theta_{\mathrm{r}} \end{bmatrix}$$

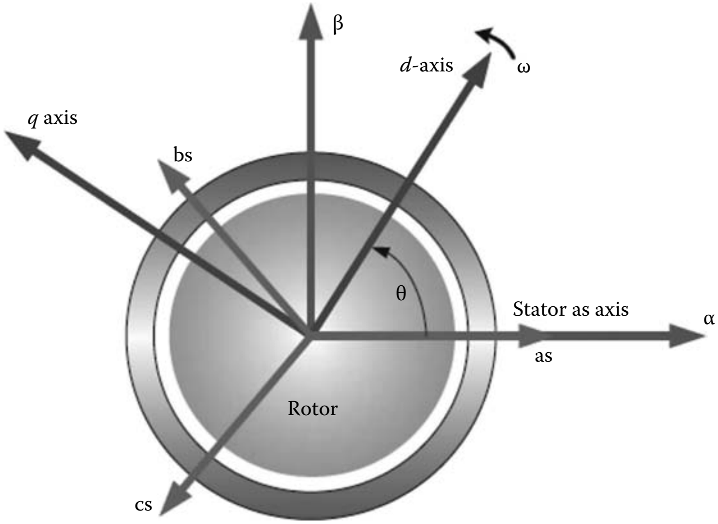

FIGURE C.1
Idealized induction machine. (Extracted from Liu, J., Modeling, analysis and design of integrated starter generator system based on field oriented controlled induction machines, PhD thesis, Ohio State University, Columbus, OH, 2005.)

where

L_{ms} is the stator magnetizing inductance
L_{mr} is the rotor magnetizing inductance
L_{ls} is the stator leakage inductance
L_{lr} is the rotor leakage inductance
L_{sr} is the mutual inductance between stator and rotor windings

C.2 Voltage Equations on the Stationary Reference Frame

Using the reference frame theory (Appendix D), we can transform the induction machine variables (voltage, current, and linkage) to another reference frame as long as the condition that $f_a + f_b + f_c = 0$ (f_a, f_b, and f_c are each phase v, i, and λ components) is satisfied. Using Park transformation, these three phases can be changed on the stationary reference frame:

$$f_s^s = f_{ds}^s + jf_{qs}^s = 2/3\left(f_a + f_b e^{j2\pi/3} + f_b e^{j4\pi/3}\right) \tag{C.3}$$

or equivalently

$$\begin{bmatrix} f_{ds}^s \\ f_{qs}^s \end{bmatrix} = 2/3 \begin{bmatrix} 1 & -1/2 & -1/2 \\ 0 & \sqrt{3}/2 & -\sqrt{3}/2 \end{bmatrix} \begin{bmatrix} f_a \\ f_b \\ f_c \end{bmatrix} \tag{C.4}$$

Simply we can write stator and rotor voltage equations:

$$\text{Stator voltage equation: } v_\mathrm{s}^\mathrm{s} = R_\mathrm{s} i_\mathrm{s}^\mathrm{s} + p\lambda_\mathrm{s}^\mathrm{s} \tag{C.5}$$

$$\text{Rotor voltage equation: } v_\mathrm{r}^\mathrm{r} = R_\mathrm{r} i_\mathrm{r}^\mathrm{r} + p\lambda_\mathrm{r}^\mathrm{r} \tag{C.6}$$

Assuming that there is a relationship between the stationary and the synchronous reference frames:

$$f_\mathrm{r}^\mathrm{s} = \mathrm{e}^{j\theta_\mathrm{r}} \cdot f_\mathrm{r}^\mathrm{r} \tag{C.7}$$

where $\theta_\mathrm{r} = \omega_\mathrm{r} t$ is the phase angle difference between the stationary and the synchronous reference frames:

$$v_\mathrm{r}^\mathrm{r} = R_\mathrm{r} i_\mathrm{r}^\mathrm{r} + p\lambda_\mathrm{r}^\mathrm{r} \tag{C.8}$$

$$\begin{aligned} v_\mathrm{r}^\mathrm{s}\mathrm{e}^{-j\theta_\mathrm{r}} &= R_\mathrm{r} i_\mathrm{r}^\mathrm{s}\mathrm{e}^{-j\theta_\mathrm{r}} + p\left(\lambda_\mathrm{r}^\mathrm{s}\mathrm{e}^{-j\theta_\mathrm{r}}\right) \\ &= R_\mathrm{r} i_\mathrm{r}^\mathrm{s}\mathrm{e}^{-j\theta_\mathrm{r}} + p\left(\lambda_\mathrm{r}^\mathrm{s}\mathrm{e}^{-j\theta_\mathrm{r}}\right) \\ &= R_\mathrm{r} i_\mathrm{r}^\mathrm{s}\mathrm{e}^{-j\theta_\mathrm{r}} + \mathrm{e}^{-j\theta_\mathrm{r}} p\lambda_\mathrm{r}^\mathrm{s} - p\left(\mathrm{e}^{-\theta_\mathrm{r}}\right)\lambda_\mathrm{r}^\mathrm{s} \\ &= R_\mathrm{r} i_\mathrm{r}^\mathrm{s}\mathrm{e}^{-j\theta_\mathrm{r}} + \mathrm{e}^{-j\theta_\mathrm{r}} p\lambda_\mathrm{r}^\mathrm{s} - \omega_\mathrm{r}\mathrm{e}^{-\theta_\mathrm{r}}\lambda_\mathrm{r}^\mathrm{s} \\ \Rightarrow \quad v_\mathrm{r}^\mathrm{s} &= R_\mathrm{r} i_\mathrm{r}^\mathrm{s} + \left(p - j\omega_\mathrm{r}\right)\lambda_\mathrm{r}^\mathrm{s} \end{aligned} \tag{C.9}$$

So the voltage equations on the stationary frame are

$$\text{Stator voltage equation: } v_\mathrm{s}^\mathrm{s} = R_\mathrm{s} i_\mathrm{s}^\mathrm{s} + p\lambda_\mathrm{s}^\mathrm{s} \tag{C.10}$$

$$\text{Rotor voltage equation: } v_\mathrm{r}^\mathrm{s} = R_\mathrm{r} i_\mathrm{r}^\mathrm{s} + (p - j\omega)\lambda_\mathrm{r}^\mathrm{s} \tag{C.11}$$

C.3 Voltage Equations on the Synchronous Reference Frame

$\lambda_\mathrm{s}^\mathrm{s} = L_\mathrm{s} i_\mathrm{s}^\mathrm{s} + L_\mathrm{m} i_\mathrm{r}^\mathrm{s}$ (L_s, stator self-inductance; L_m, mutual inductance):

$$\lambda_\mathrm{r}^\mathrm{s} = L_\mathrm{r} i_\mathrm{r}^\mathrm{s} + L_\mathrm{m} i_\mathrm{s}^\mathrm{s} \quad (L_\mathrm{s}\text{, rotor self-inductance}) \tag{C.12}$$

By substituting Equation C.12 into Equations C.10 and C.11, the *d*–*q* model voltage equations on the stationary frame can be derived:

$$\begin{bmatrix} v_{d\mathrm{s}} \\ v_{q\mathrm{s}} \\ v_{d\mathrm{r}} \\ v_{q\mathrm{r}} \end{bmatrix} = \begin{bmatrix} R_\mathrm{s} + L_\mathrm{s}p & 0 & L_\mathrm{m}p & 0 \\ 0 & R_\mathrm{s} + L_\mathrm{s}p & 0 & L_\mathrm{m}p \\ L_\mathrm{m}p & \omega_\mathrm{r}L_\mathrm{m} & R_\mathrm{r} + L_\mathrm{r}p & \omega_\mathrm{r}L_\mathrm{r} \\ -\omega_\mathrm{r}L_\mathrm{m} & L_\mathrm{m}p & -\omega_\mathrm{r}L_\mathrm{r} & R_\mathrm{r} + L_\mathrm{r}p \end{bmatrix} \begin{bmatrix} i_{d\mathrm{s}} \\ i_{q\mathrm{s}} \\ i_{d\mathrm{r}} \\ i_{q\mathrm{r}} \end{bmatrix} \tag{C.13}$$

The voltage equations on the stationary frame can be transferred on the synchronous frame using the relationship given in

$$\begin{aligned} f_{\mathrm{s}}^{\mathrm{e}} &= \mathrm{e}^{-j\theta_{\mathrm{e}}} f_{\mathrm{s}}^{\mathrm{s}} \\ f_{\mathrm{r}}^{\mathrm{e}} &= \mathrm{e}^{-j\theta_{\mathrm{e}}} f_{\mathrm{r}}^{\mathrm{s}} \end{aligned} \tag{C.14}$$

where θ_{e} is the synchronous angular velocity.

The stator voltage equation becomes

$$\begin{aligned} v_{\mathrm{s}}^{\mathrm{s}} &= R_{\mathrm{s}} i_{\mathrm{s}}^{\mathrm{s}} + p\lambda_{\mathrm{s}}^{\mathrm{s}} \\ \mathrm{e}^{j\theta_{\mathrm{e}}} v_{\mathrm{s}}^{\mathrm{e}} &= R_{\mathrm{s}} i_{\mathrm{s}}^{\mathrm{e}} \mathrm{e}^{j\theta_{\mathrm{e}}} + p\left(\mathrm{e}^{j\theta_{\mathrm{e}}} \lambda_{\mathrm{s}}^{\mathrm{e}}\right) \\ &= R_{\mathrm{s}} i_{\mathrm{s}}^{\mathrm{e}} \mathrm{e}^{j\theta_{\mathrm{e}}} + j\omega_{\mathrm{e}} \mathrm{e}^{j\theta_{\mathrm{e}}} \lambda_{\mathrm{s}}^{\mathrm{e}} + \mathrm{e}^{j\theta_{\mathrm{e}}} p\lambda_{\mathrm{s}}^{\mathrm{e}} \\ \Rightarrow \quad v_{\mathrm{s}}^{\mathrm{e}} &= R_{\mathrm{s}} i_{\mathrm{s}}^{\mathrm{e}} + (p + j\omega_{\mathrm{e}})\lambda_{\mathrm{s}}^{\mathrm{e}} \end{aligned} \tag{C.15}$$

The rotor voltage equation becomes

$$\begin{aligned} v_{\mathrm{r}}^{\mathrm{s}} &= R_{\mathrm{r}} i_{\mathrm{r}}^{\mathrm{s}} + \left(p - j\omega_{\mathrm{r}}\right)\lambda_{\mathrm{r}}^{\mathrm{s}} \\ \mathrm{e}^{j\theta_{\mathrm{e}}} v_{\mathrm{r}}^{\mathrm{e}} &= R_{\mathrm{r}} i_{\mathrm{r}}^{\mathrm{e}} \mathrm{e}^{j\theta_{\mathrm{e}}} + \left(p - j\omega_{\mathrm{r}}\right)\left(\lambda_{\mathrm{r}}^{\mathrm{e}} \mathrm{e}^{j\theta_{\mathrm{e}}}\right) \\ &= R_{\mathrm{r}} i_{\mathrm{r}}^{\mathrm{e}} \mathrm{e}^{j\theta_{\mathrm{e}}} + \left(p + j\omega_{\mathrm{e}} - j\omega_{\mathrm{r}}\right)\lambda_{\mathrm{r}}^{\mathrm{e}} \mathrm{e}^{j\theta_{\mathrm{e}}} \\ \Rightarrow \quad v_{\mathrm{r}}^{\mathrm{e}} &= \lambda_{\mathrm{r}}^{\mathrm{e}} R_{\mathrm{r}} i_{\mathrm{r}}^{\mathrm{e}} + \left(p + j\left(\omega_{\mathrm{e}} - \omega_{\mathrm{r}}\right)\right) \\ &= R_{\mathrm{r}} i_{\mathrm{r}}^{\mathrm{e}} + \left(p + j\omega_{\mathrm{sl}}\right)\lambda_{\mathrm{r}}^{\mathrm{e}} \end{aligned} \tag{C.16}$$

where the slip speed is defined as

$$\omega_{\mathrm{sl}} = \omega_{\mathrm{e}} - \omega_{\mathrm{r}} \tag{C.17}$$

and the linkage flux equations can be expressed as

$$\begin{aligned} \lambda_{\mathrm{s}}^{\mathrm{e}} &= L_{\mathrm{s}} i_{\mathrm{s}}^{\mathrm{e}} + L_{\mathrm{m}} i_{\mathrm{r}}^{\mathrm{e}} \\ \lambda_{\mathrm{r}}^{\mathrm{e}} &= L_{\mathrm{r}} i_{\mathrm{r}}^{\mathrm{e}} + L_{\mathrm{m}} i_{\mathrm{s}}^{\mathrm{e}} \end{aligned} \tag{C.18}$$

Using Equations C.16 and C.17, the voltage equation can be described using current, resistance, reactance, and speeds:

$$\begin{bmatrix} v_{ds}^{\mathrm{e}} \\ v_{qs}^{\mathrm{e}} \\ v_{dr}^{\mathrm{e}} \\ v_{qr}^{\mathrm{e}} \end{bmatrix} = \begin{bmatrix} R_{\mathrm{s}} + L_{\mathrm{s}} p & -\omega_{\mathrm{e}} L_{\mathrm{s}} & L_{\mathrm{m}} p & -\omega_{\mathrm{e}} L_{\mathrm{m}} \\ \omega_{\mathrm{e}} L_{\mathrm{m}} & R_{\mathrm{s}} + L_{\mathrm{s}} p & \omega_{\mathrm{e}} L_{\mathrm{m}} & L_{\mathrm{m}} p \\ L_{\mathrm{m}} p & -\omega_{\mathrm{sl}} L_{\mathrm{m}} & R_{\mathrm{r}} + L_{\mathrm{r}} p & -\omega_{\mathrm{sl}} L_{\mathrm{r}} \\ \omega_{\mathrm{sl}} L_{\mathrm{m}} & L_{\mathrm{m}} p & \omega_{\mathrm{sl}} L_{\mathrm{r}} & R_{\mathrm{r}} + L_{\mathrm{r}} p \end{bmatrix} \begin{bmatrix} i_{ds}^{\mathrm{e}} \\ i_{qs}^{\mathrm{e}} \\ i_{dr}^{\mathrm{e}} \\ i_{qr}^{\mathrm{e}} \end{bmatrix} \tag{C.19}$$

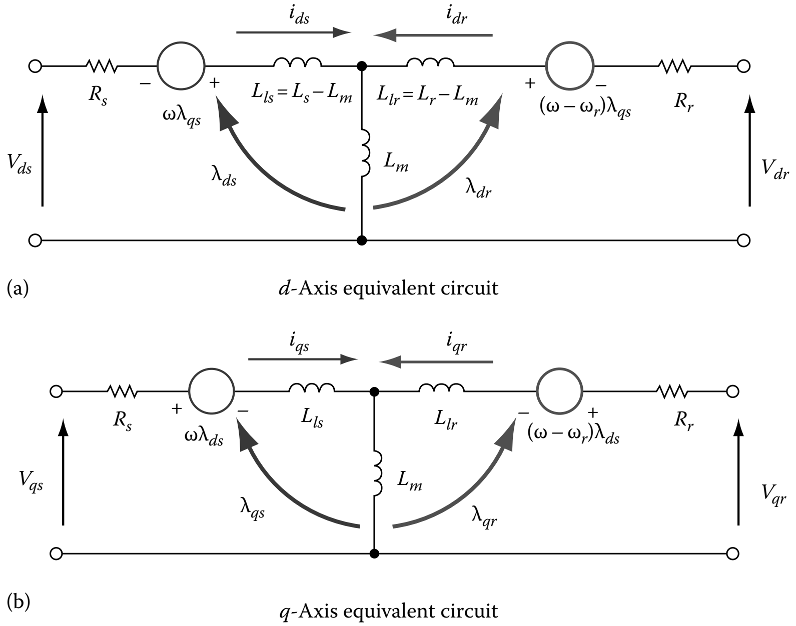

FIGURE C.2 Dynamic *d–q* equivalent circuit. (a) *d*-Axis equivalent circuit, (b) *q*-Axis equivalent. (Extracted from Liu, J., Modeling, analysis and design of integrated starter generator system based on field oriented controlled induction machines, PhD thesis, Ohio State University, Columbus, OH, 2005.)

C.4 *d–q* Equivalent Circuit

Figure C.2 shows the equivalent circuits in arbitrary reference frame. According to the definition of rotor speed ω on the reference frame, we can obtain the dynamic *d–q* model in a difference frame. When the rotating speed of the reference frame is zero, $\omega=0$, the dynamic *d–q* model in the stationary reference frame can be obtained. When the rotating speed of the reference frame is synchronous speed $\omega=\omega_e$, the dynamic *d–q* model in the synchronous rotating reference frame is obtained.

C.5 Dynamic Induction Machine Model in the State Space Form

In order to obtain state space equation about the induction machine, let us consider:

$$\begin{bmatrix} i_{ds}^{e} \\ i_{qs}^{e} \\ \lambda_{dr}^{e} \\ \lambda_{qr}^{e} \end{bmatrix} = \begin{bmatrix} 1 & 0 & 0 & 0 \\ 0 & 1 & 0 & 0 \\ L_{m} & 0 & L_{r} & 0 \\ 0 & L_{m} & 0 & L_{r} \end{bmatrix} \begin{bmatrix} i_{ds}^{e} \\ i_{qs}^{e} \\ i_{dr}^{e} \\ i_{qr}^{e} \end{bmatrix} \tag{C.20}$$

By inversing the Equation C.20, the following equation is obtained:

$$\begin{bmatrix} i_{ds}^{e} \\ i_{qs}^{e} \\ i_{dr}^{e} \\ i_{qr}^{e} \end{bmatrix} = \begin{bmatrix} 1 & 0 & 0 & 0 \\ 0 & 1 & 0 & 0 \\ -L_{m}/L_{r} & 0 & 1/L_{r} & 0 \\ 0 & -L_{m}/L_{r} & 0 & 1/L_{r} \end{bmatrix} \begin{bmatrix} i_{ds}^{e} \\ i_{qs}^{e} \\ \lambda_{dr}^{e} \\ \lambda_{qr}^{e} \end{bmatrix} \tag{C.21}$$

By substituting Equation C.21 into Equation C.18, a new voltage equation is written as follows:

$$\begin{aligned} \begin{bmatrix} v_{ds}^{e} \\ v_{qs}^{e} \\ v_{dr}^{e} \\ v_{dr}^{e} \end{bmatrix} &= \begin{bmatrix} R_{s} & -\sigma\omega_{e}L_{s} & 0 & -\omega_{e}L_{m}/L_{s} \\ -\sigma\omega_{e}L_{s} & R_{s} & \omega_{e}L_{m}/L_{s} & 0 \\ -L_{m}R_{r}/L_{r} & 0 & R_{r}/L_{r} & -\omega_{sl} \\ 0 & -L_{m}R_{r}/L_{r} & \omega_{sl} & R_{r}/L_{r} \end{bmatrix} \begin{bmatrix} i_{ds}^{e} \\ i_{qs}^{e} \\ \lambda_{dr}^{e} \\ \lambda_{qr}^{e} \end{bmatrix} \\ &+ \begin{bmatrix} \sigma L_{s} & 0 & L_{m}/L_{r} & 0 \\ 0 & \sigma L_{s} & 0 & L_{m}/L_{r} \\ 0 & 0 & 1 & 0 \\ 0 & 0 & 0 & 1 \end{bmatrix} p \begin{bmatrix} i_{ds}^{e} \\ i_{qs}^{e} \\ \lambda_{dr}^{e} \\ \lambda_{qr}^{e} \end{bmatrix} \end{aligned} \tag{C.22}$$

where $\sigma = 1 - (L_{m}^{2}/L_{s}L_{r})$.

By defining

$$A = \begin{bmatrix} R_{s} & -\sigma\omega_{e}L_{s} & 0 & -\omega_{e}L_{m}/L_{s} \\ -\sigma\omega_{e}L_{s} & R_{s} & \omega_{e}L_{m}/L_{s} & 0 \\ -L_{m}R_{r}/L_{r} & 0 & R_{r}/L_{r} & -\omega_{sl} \\ 0 & -L_{m}R_{r}/L_{r} & \omega_{sl} & R_{r}/L_{r} \end{bmatrix};$$

$$B = \begin{bmatrix} \sigma L_{s} & 0 & L_{m}/L_{r} & 0 \\ 0 & \sigma L_{s} & 0 & L_{m}/L_{r} \\ 0 & 0 & 1 & 0 \\ 0 & 0 & 0 & 1 \end{bmatrix}$$

the state space equation can be obtained using the above definition:

$$\frac{\mathrm{d}}{\mathrm{d}t}\begin{bmatrix} i_{ds}^{\mathrm{e}} \\ i_{qs}^{\mathrm{e}} \\ \lambda_{dr}^{\mathrm{e}} \\ \lambda_{qr}^{\mathrm{e}} \end{bmatrix} = -B^{-1}A\begin{bmatrix} i_{ds}^{\mathrm{e}} \\ i_{qs}^{\mathrm{e}} \\ \lambda_{dr}^{\mathrm{e}} \\ \lambda_{qr}^{\mathrm{e}} \end{bmatrix} + B^{-1}\begin{bmatrix} v_{ds}^{\mathrm{e}} \\ v_{qs}^{\mathrm{e}} \\ v_{dr}^{\mathrm{e}} \\ v_{qr}^{\mathrm{e}} \end{bmatrix} \tag{C.23}$$

$$\frac{\mathrm{d}}{\mathrm{d}t}\begin{bmatrix} i_{ds}^{\mathrm{e}} \\ i_{qs}^{\mathrm{e}} \\ \lambda_{dr}^{\mathrm{e}} \\ \lambda_{qr}^{\mathrm{e}} \end{bmatrix} = \begin{bmatrix} -\left(\frac{R_{\mathrm{s}}}{\sigma L_{\mathrm{s}}} + \frac{L_{\mathrm{m}}^2}{\sigma L_{\mathrm{s}} T_{\mathrm{r}} L_{\mathrm{r}}}\right) & \omega_{\mathrm{e}} & \frac{K}{T_{\mathrm{r}}} & \omega_{\mathrm{r}} K \\ -\omega_{\mathrm{e}} & -\left(\frac{R_{\mathrm{s}}}{\sigma L_{\mathrm{s}}} + \frac{L_{\mathrm{m}}^2}{\sigma L_{\mathrm{s}} T_{\mathrm{r}} L_{\mathrm{r}}}\right) & -\omega_{\mathrm{r}} K & \frac{K}{T_{\mathrm{r}}} \\ \frac{L_{\mathrm{m}}}{T_{\mathrm{r}}} & 0 & -\frac{1}{T_{\mathrm{r}}} & \omega_{\mathrm{sl}} \\ 0 & \frac{L_{\mathrm{m}}}{T_{\mathrm{r}}} & -\omega_{\mathrm{sl}} & -\frac{1}{T_{\mathrm{r}}} \end{bmatrix}\begin{bmatrix} i_{ds}^{\mathrm{e}} \\ i_{qs}^{\mathrm{e}} \\ \lambda_{dr}^{\mathrm{e}} \\ \lambda_{qr}^{\mathrm{e}} \end{bmatrix} + \begin{bmatrix} \frac{1}{\sigma L_{\mathrm{s}}} & 0 \\ 0 & \frac{1}{\sigma L_{\mathrm{s}}} \\ 0 & 0 \\ 0 & 0 \end{bmatrix}\begin{bmatrix} v_{ds}^{\mathrm{e}} \\ v_{qs}^{\mathrm{e}} \end{bmatrix} \tag{C.24}$$

where $K = L_{\mathrm{m}}/\sigma L_{\mathrm{s}} L_{\mathrm{r}}$ and $T_{\mathrm{r}} = L_{\mathrm{r}}/R_{\mathrm{r}}$.

C.6 Torque Equation

To derive torque equation, let us consider the following voltage equation:

$$v = Ri + Lpi + G_{\mathrm{m}} i \tag{C.25}$$

where

$$R = \begin{bmatrix} R_{\mathrm{s}} & 0 & 0 & 0 \\ 0 & R_{\mathrm{s}} & 0 & 0 \\ 0 & 0 & R_{\mathrm{r}} & 0 \\ 0 & 0 & 0 & R_{\mathrm{r}} \end{bmatrix}; \quad L = \begin{bmatrix} L_{\mathrm{s}} & 0 & L_{\mathrm{m}} & 0 \\ 0 & L_{\mathrm{s}} & 0 & L_{\mathrm{m}} \\ L_{\mathrm{m}} & 0 & L_r & 0 \\ 0 & L_{\mathrm{m}} & 0 & L_{\mathrm{r}} \end{bmatrix}; \quad v = \begin{bmatrix} v_{ds}^{\mathrm{e}} \\ v_{qs}^{\mathrm{e}} \\ 0 \\ 0 \end{bmatrix}$$

$$G_{\mathrm{m}} = \begin{bmatrix} 0 & -\omega_{\mathrm{e}} L_{\mathrm{s}} & 0 & -\omega_{\mathrm{e}} L_{\mathrm{s}} \\ \omega_{\mathrm{e}} L_{\mathrm{s}} & 0 & \omega_{\mathrm{e}} L_{\mathrm{m}} & 0 \\ 0 & -(\omega_{\mathrm{e}} - \omega_{\mathrm{r}}) L_{\mathrm{m}} & 0 & -(\omega_{\mathrm{e}} - \omega_{\mathrm{r}}) L_{\mathrm{r}} \\ (\omega_{\mathrm{e}} - \omega_{\mathrm{r}}) L_{\mathrm{m}} & 0 & (\omega_{\mathrm{e}} - \omega_{\mathrm{r}}) L_{\mathrm{r}} & 0 \end{bmatrix}; \quad i = \begin{bmatrix} i_{d\mathrm{s}}^{\mathrm{e}} \\ i_{q\mathrm{s}}^{\mathrm{e}} \\ i_{d\mathrm{r}}^{\mathrm{e}} \\ i_{q\mathrm{r}}^{\mathrm{e}} \end{bmatrix}$$

By multiplying voltage equation by $1.5i^{\mathrm{T}}$, the power equation can be obtained as follows:

$$P = 1.5 i^{\mathrm{T}} v = 1.5\left(i^{\mathrm{T}} R i + i^{\mathrm{T}} L p i + i^{\mathrm{T}} G_m i\right) \tag{C.26}$$

In Equation C.26, $1.5i^{\mathrm{T}}v$ is the motor input power and $1.5i^{\mathrm{T}}Ri$ is the copper loss. The item $1.5i^{\mathrm{T}}Lpi$ represents the rate of exchange of magnetic field energy between windings and $1.5i^{\mathrm{T}}G_m i$ represents the rate of energy converted to mechanical work. Hence, the mechanical power can be defined as

$$\begin{aligned} P_{\mathrm{m}} &= 1.5 i^{\mathrm{T}} G_{\mathrm{m}} i \\ &= 1.5\left(i^{\mathrm{T}} \omega_{\mathrm{r}} G_{\mathrm{e}} i + i^{\mathrm{T}} \omega_{\mathrm{r}} G_{\mathrm{r}} i\right) \\ &= 1.5 i^{\mathrm{T}} \omega_{\mathrm{r}} G_{\mathrm{r}} i \end{aligned} \tag{C.27}$$

where

$$G_{\mathrm{e}} = \begin{bmatrix} 0 & -L_{\mathrm{s}} & 0 & -L_{\mathrm{m}} \\ L_{\mathrm{s}} & 0 & L_{\mathrm{m}} & 0 \\ 0 & -L_{\mathrm{m}} & 0 & -L_{\mathrm{r}} \\ -L_{\mathrm{m}} & 0 & L_{\mathrm{r}} & 0 \end{bmatrix}, \quad G_{\mathrm{r}} = \begin{bmatrix} 0 & 0 & 0 & 0 \\ 0 & 0 & 0 & 0 \\ 0 & -L_{\mathrm{m}} & 0 & L_{\mathrm{r}} \\ L_{\mathrm{m}} & 0 & L_{\mathrm{r}} & 0 \end{bmatrix}$$

Since G_{e} is skew-symmetric ($G_{\mathrm{e}}^{\mathrm{T}} = -G_{\mathrm{e}}$), $i^{\mathrm{T}}\omega_{\mathrm{r}}G_{\mathrm{e}}i$ is not considered when calculating the mechanical power, P_{m}.

The torque is obtained by dividing the power by the mechanical speed:

$$\begin{aligned} T_{\mathrm{e}} &= \frac{P_{\mathrm{m}}}{\omega_{\mathrm{m}}} = 1.5 \frac{P}{2} i^{\mathrm{T}} G_{\mathrm{r}} i \\ &= 1.5 \frac{P}{2} L_{\mathrm{m}} \left(i_{q\mathrm{s}}^{\mathrm{e}} i_{d\mathrm{r}}^{\mathrm{e}} - i_{d\mathrm{s}}^{\mathrm{e}} i_{q\mathrm{r}}^{\mathrm{e}}\right) \\ &= 1.5 \frac{P}{2} \frac{L_{\mathrm{m}}}{L_{\mathrm{r}}} \left(i_{q\mathrm{s}}^{\mathrm{e}} \lambda_{d\mathrm{r}}^{\mathrm{e}} - i_{d\mathrm{s}}^{\mathrm{e}} \lambda_{q\mathrm{r}}^{\mathrm{e}}\right) \end{aligned} \tag{C.28}$$

where P is the pole of the machine.

The power in the *d*–*q* frame is

$$\begin{aligned}
P_{dq} &= v_{ds}^{s} i_{ds}^{s} + v_{qs}^{s} i_{qs}^{s} = \begin{bmatrix} v_{ds}^{s} & v_{qs}^{s} \end{bmatrix} \begin{bmatrix} i_{qs}^{s} \\ i_{qs}^{s} \end{bmatrix} \\
&= \frac{2}{3} \begin{bmatrix} v_{a} & v_{b} & v_{c} \end{bmatrix} \begin{bmatrix} i_{a} \\ i_{b} \\ i_{c} \end{bmatrix} \\
&= \frac{2}{3} \left(v_{a} i_{a} + v_{b} i_{b} + v_{c} i_{c} \right) \\
&= \frac{2}{3} P_{abc}
\end{aligned}$$

Then we get

$$P_{abc} = \frac{3}{2} P_{dq} \tag{C.29}$$

C.7 Slip Calculation

The fourth row in Equation C.22 is

$$p\lambda_{qr}^{e} = -\frac{1}{T_{r}} \lambda_{qr}^{e} + \frac{L_{m}}{T_{r}} i_{qs}^{e} - \omega_{sl} \lambda_{qr}^{e} \tag{C.30}$$

For the field orientation control or vector control, I_{ds} is aligned with the rotor flux and I_{qs} is responsible for torque production. I_{ds} is perpendicular to I_{qs} so that the flux and the torque can be controlled separately like a DC machine. Since the rotor flux linkage is only aligned with *d*-axis, the vector control condition is that $\lambda_{qr}^{e} = 0$. In Equation C.24, $p\lambda_{qr}^{e} = 0$, and Equation C.25 can be modified as

$$\begin{aligned}
\omega_{sl} \lambda_{dr}^{e} &= \frac{L_{m}}{T_{r}} i_{qs}^{e} \\
\Rightarrow \quad \omega_{sl} &= \frac{L_{m}}{T_{r}} \frac{i_{qs}^{e}}{\lambda_{dr}^{e}}
\end{aligned} \tag{C.31}$$

C.8 Calculation of the Rotor Flux λ_{dr}^{e} on *d*-Axis

The third row in Equation C.22 is

$$p\lambda_{dr}^{e} = -\frac{1}{T_{r}} \lambda_{dr}^{e} + \frac{L_{m}}{T_{r}} i_{ds}^{e} + \omega_{sl} \lambda_{qr}^{e} \tag{C.32}$$

Considering the vector control condition ($\lambda_{qr}^{e} = 0$), Equation C.32 can be rewritten as

$$\begin{aligned} p\lambda_{dr}^{e} + \frac{1}{T_r}\lambda_{dr}^{e} &= \frac{L_m}{T_r} i_{ds}^{e} \\ \Rightarrow \quad \lambda_{dr}^{e} &= \frac{L_m}{1+T_r p} i_{ds}^{e} \end{aligned} \tag{C.33}$$

Using the steady-state condition, Equation C.33 can be modified as

$$i_{ds}^{e} = \frac{\lambda_{dr}^{e}}{L_m} \tag{C.34}$$

which means that i_{ds}^{e} controls the rotor flux linkage.

C.9 Calculation of the Torque

Since $\lambda_{qr}^{e} = 0$, the torque equation (Equation C.28) becomes

$$T_e = 1.5 \frac{P}{2} \frac{L_m}{L_r} i_{qs}^{e} \lambda_{dr}^{e} \tag{C.35}$$

According to the vector control condition that the rotor flux is constant, i_{qs}^{e} controls the electromagnetic torque.

C.10 *d–q* Decoupling Control and Back Electromotive Force Compensation Control

From the first and second rows of Equation C.24, we can derive the voltage equations as follows, which have coupling terms due to the vector control condition, $\lambda_{qr}^{e} = 0$:

$$\begin{aligned} v_{ds}^{e} &= (R_s + \sigma L_s p) i_{ds}^{e} - \sigma L_s \omega_e i_{qs}^{e} \\ v_{qs}^{e} &= (R_s + \sigma L_s p) i_{qs}^{e} + \sigma L_s \omega_e i_{ds}^{e} + \omega_e \frac{L_m}{L_r} \lambda_{dr}^{e} \end{aligned} \tag{C.36}$$

The voltage equations (Equations C.36) have coupling terms ($\sigma L_s \omega_e i_{qs}^{e}$ and $\sigma L_s \omega_e i_{ds}^{e}$) and back electromotive force (EMF) term $(\omega_e (L_m/L_r)\lambda)$. These coupling and EMF terms must be controlled using decoupling control, namely the back EMF compensation control. Otherwise, this vector control cannot control i_q and i_d separately due to these coupling terms.

The new decoupling voltage equations are

$$\begin{aligned} \overline{v}_{ds}^{\mathrm{e}} &= v_{ds}^{\mathrm{e}} + \sigma L_{\mathrm{s}} \omega_{\mathrm{e}} i_{qs}^{\mathrm{e}} \\ \overline{v}_{qs}^{\mathrm{e}} &= v_{qs}^{\mathrm{e}} - \sigma L_{\mathrm{s}} \omega_{\mathrm{e}} i_{ds}^{\mathrm{e}} \end{aligned} \tag{C.37}$$

By using Equation C.37, Equation C.38 can be derived:

$$\begin{aligned} \overline{v}_{ds}^{\mathrm{e}} &= \left(R_{\mathrm{s}} + \sigma L_{\mathrm{s}} p\right) i_{ds}^{\mathrm{e}} \\ \overline{v}_{qs}^{\mathrm{e}} &= \left(R_{\mathrm{s}} + \sigma L_{\mathrm{s}} p\right) i_{qs}^{\mathrm{e}} + \omega_{\mathrm{e}} \frac{L_{\mathrm{m}}}{L_{\mathrm{r}}} \lambda_{dr}^{\mathrm{e}} \end{aligned} \tag{C.38}$$

To compensate the back EMF term $\omega_{\mathrm{e}}(L_{\mathrm{m}}/L_{\mathrm{r}})\lambda$, we add $-\omega_{\mathrm{e}}(L_{\mathrm{m}}/L_{\mathrm{r}})\lambda$ to $\overline{v}_{qs}^{\mathrm{e}}$. So the new compensation voltage becomes

$$\tilde{v}_{qs}^{\mathrm{e}} = \overline{v}_{qs}^{\mathrm{e}} - \omega_{\mathrm{e}} \frac{L_{\mathrm{m}}}{L_{\mathrm{r}}} \lambda_{dr}^{\mathrm{e}} \tag{C.39}$$

Finally new current equations, decoupling the coupling terms and compensating the back EMF, can be written as

$$\begin{aligned} \frac{\mathrm{d}}{\mathrm{d}t} i_{ds}^{\mathrm{e}} &= -\frac{R_{\mathrm{s}}}{\sigma L_{\mathrm{s}}} i_{ds}^{\mathrm{e}} + \frac{1}{\sigma L_{\mathrm{s}}} \overline{v}_{ds}^{\mathrm{e}} \\ \frac{\mathrm{d}}{\mathrm{d}t} i_{qs}^{\mathrm{e}} &= -\frac{R_{\mathrm{s}}}{\sigma L_{\mathrm{s}}} i_{qs}^{\mathrm{e}} + \frac{1}{\sigma L_{\mathrm{s}}} \overline{v}_{qs}^{\mathrm{e}} \end{aligned} \tag{C.40}$$

Appendix D: Coordinate Transformation

D.1 *abc* Phase to *qd0* Reference Frame Transformation

$$f_{qd0}=\begin{bmatrix} f_q \\ f_d \\ f_o \end{bmatrix}=Tf_{abc}=T\begin{bmatrix} f_a \\ f_b \\ f_c \end{bmatrix}$$
$$\begin{bmatrix} f_a \\ f_b \\ f_c \end{bmatrix}=T^{-1}\begin{bmatrix} f_q \\ f_d \\ f_o \end{bmatrix} \tag{D.1}$$

where

$$T=\frac{2}{3}\begin{bmatrix} \cos\theta & \cos(\theta-\gamma) & \cos(\theta+\gamma) \\ \sin\theta & \sin(\theta-\gamma) & \sin(\theta+\gamma) \\ 1/2 & 1/2 & 1/2 \end{bmatrix};\ \gamma=\frac{2\pi}{3}$$

$$T^{-1}=\begin{bmatrix} \cos\theta & \sin\theta & 1 \\ \cos(\theta-\gamma) & \sin(\theta-\gamma) & 1 \\ \cos(\theta+\gamma) & \sin(\theta+\gamma) & 1 \end{bmatrix};\ \theta\text{, arbitrary angle}$$

D.2 Synchronous Reference Frame

Assuming that q-axis is rotating with synchronous speed $\omega_e = 2\pi f_e$, the phase angle difference between q- and a-axes is

$$\theta=\theta_e=\omega_e t \tag{D.2}$$

The phase angle difference is shown in Figure D.1.

Using Equation D.1, the synchronous reference frame q- and d-axes are

$$\begin{aligned} f_q^e &= \frac{2}{3}\left[(f_a+f_b\cos\gamma+f_c\cos\gamma)\cos\theta_e+(f_b\sin\gamma-f_c\sin\gamma)\sin\theta_e\right] \\ &= \frac{2}{3}\left(f_a-\frac{1}{2}f_b-\frac{1}{2}f_c\right)\cos\theta_e+\frac{1}{\sqrt{3}}(f_b-f_c)\sin\theta_e \end{aligned} \tag{D.3}$$

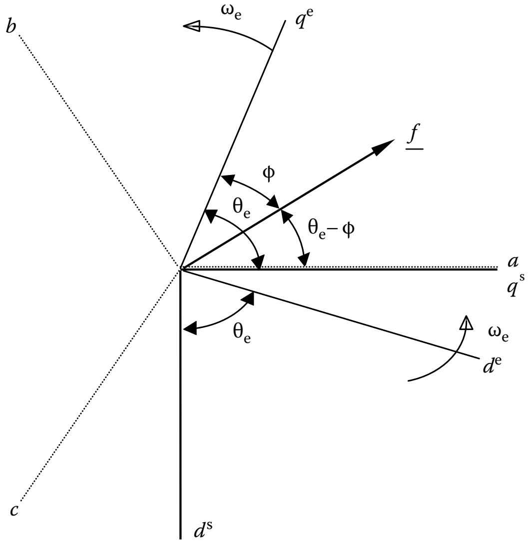

FIGURE D.1
The space vectors between *abc*- and *dq*-axes. (From Na, W., A study on the output voltage control strategies of 3-phase PWM inverter for an uninterruptible power supply, Korea master thesis, Kwangwoon University, Seoul, 1997. With permission.)

$$\begin{aligned} f_d^e &= \frac{2}{3}\left[(f_a + f_b\cos\gamma + f_c\cos\gamma)\sin\theta_e + (-f_b\sin\gamma + f_c\sin\gamma)\cos\theta_e\right] \\ &= \frac{2}{3}\left(f_a - \frac{1}{2}f_b - \frac{1}{2}f_c\right)\sin\theta_e - \frac{1}{\sqrt{3}}(f_b - f_c)\cos\theta_e \end{aligned} \tag{D.4}$$

As long as the condition $f_a + f_b + f_c = 0$ is satisfied, Equations D.3 and D.4 can be converted to Equations D.5 and D.6, respectively, with two variables:

$$\begin{aligned} f_q^e &= f_a\cos\theta_e + \frac{1}{\sqrt{3}}(f_b - f_c)\sin\theta_e \\ &= f_a\cos\theta_e + \frac{1}{\sqrt{3}}(f_a + 2f_b)\sin\theta_e \end{aligned} \tag{D.5}$$

$$\begin{aligned} f_d^e &= f_a\sin\theta_e - \frac{1}{\sqrt{3}}(f_b - f_c)\cos\theta_e \\ &= f_a\sin\theta_e - \frac{1}{\sqrt{3}}(f_a + 2f_b)\sin\theta_e \end{aligned} \tag{D.6}$$

D.3 Stationary Reference Frame

Assuming that q-axis is aligned with the a-axis ($\theta = 0$), the synchronous frame q- and d-axes are

$$\begin{aligned} f_q^{\mathrm{e}} &= \frac{2}{3}(f_a + f_b \cos\gamma + f_c \cos\gamma) \\ &= \frac{2}{3}\left(f_a - \frac{1}{2} f_b - \frac{1}{2} f_c\right) \end{aligned} \tag{D.7}$$

$$\begin{aligned} f_d^{\mathrm{e}} &= \frac{2}{3}(-f_b \sin\gamma + f_c \sin\gamma) \\ &= -\frac{1}{\sqrt{3}}(f_b - f_c) \end{aligned} \tag{D.8}$$

For the condition $f_a + f_b + f_c = 0$, we obtain

$$f_q^{\mathrm{s}} = f_a \tag{D.9}$$

$$f_d^{\mathrm{s}} = -\frac{1}{\sqrt{3}}(f_b - f_c) = -\frac{1}{\sqrt{3}}(f_a + 2f_b) \tag{D.10}$$

D.4 Transformation between Synchronous Frame and Stationary Frame

Using Equation D.11, the stationary reference frame can be converted to the synchronous reference frame:

$$\begin{bmatrix} f_q^{\mathrm{e}} \\ f_d^{\mathrm{e}} \end{bmatrix} = \begin{bmatrix} \cos\theta & -\sin\theta \\ \sin\theta & \cos\theta \end{bmatrix} \begin{bmatrix} f_q^{\mathrm{s}} \\ f_d^{\mathrm{s}} \end{bmatrix} \tag{D.11}$$

Using Equation D.12, the stationary reference frame can be converted to the synchronous reference frame:

$$\begin{bmatrix} f_q^{\mathrm{s}} \\ f_d^{\mathrm{s}} \end{bmatrix} = \begin{bmatrix} \cos\theta & \sin\theta \\ -\sin\theta & \cos\theta \end{bmatrix} \begin{bmatrix} f_q^{\mathrm{e}} \\ f_d^{\mathrm{e}} \end{bmatrix} \tag{D.12}$$

Appendix E: Space Vector Pulsewidth Modulation

As mentioned in Chapter 7, space vector pulsewidth modulation (SVPWM) provides the maximum sinusoidal phase voltage $V_{\max} = 0.57735V_{\mathrm{dc}}$, which is 15.5% higher than sinusoidal PWM [8]. Before we discuss SVPWM, the concept of the space voltage vectors in the inverter must be understood first with the help of the following voltage equations.

The voltages in Figure E.1 can be written as

$$\begin{aligned} v_{\mathrm{A}a} &= L_{\mathrm{f}} \frac{\mathrm{d}}{\mathrm{d}t} i_{\mathrm{A}a} + v_{\mathrm{C}a} \\ v_{\mathrm{A}b} &= L_{\mathrm{f}} \frac{\mathrm{d}}{\mathrm{d}t} i_{\mathrm{A}b} + v_{\mathrm{C}b} \\ v_{\mathrm{A}c} &= L_{\mathrm{f}} \frac{\mathrm{d}}{\mathrm{d}t} i_{\mathrm{A}c} + v_{\mathrm{C}c} \end{aligned} \tag{E.1}$$

where L_{f} is inductance of LC filter, and other voltages and currents can be found in Figure E.1.

The voltages in the stationary reference frame have the same form as those in Equation E.1:

$$\begin{aligned} v_{\mathrm{A}q}^{\mathrm{s}} &= L_{\mathrm{f}} \frac{\mathrm{d}}{\mathrm{d}t} i_{\mathrm{A}q}^{\mathrm{s}} + v_{\mathrm{C}q}^{\mathrm{s}} \\ v_{\mathrm{A}d}^{\mathrm{s}} &= L_{\mathrm{f}} \frac{\mathrm{d}}{\mathrm{d}t} i_{\mathrm{A}d}^{\mathrm{s}} + v_{\mathrm{C}d}^{\mathrm{s}} \end{aligned} \tag{E.2}$$

The space vector form of Equation E.2 is

$$V_{\mathrm{A}q}^{\mathrm{s}} = L_{\mathrm{f}} \frac{\mathrm{d}}{\mathrm{d}t} I_{\mathrm{A}q}^{\mathrm{s}} + V_{\mathrm{C}q}^{\mathrm{s}} \tag{E.3}$$

The right-hand side in Equation E.3, capacitor voltage $V_{\mathrm{C}q}^{\mathrm{s}}$ in space vector form is

$$V_{\mathrm{C}q}^{\mathrm{s}} = V^{*} \mathrm{e}^{j\theta} \tag{E.4}$$

where θ is an arbitrary phase angle in the space vector.

In order to obtain the space voltage vectors in the inverter system given in Figure E.1, the switching function of each leg in the inverter can be defined as

$$S_a, S_b, S_c = \begin{cases} 0, & \text{Negative leg is ON} \\ 1, & \text{Positive leg is ON} \end{cases} \tag{E.5}$$

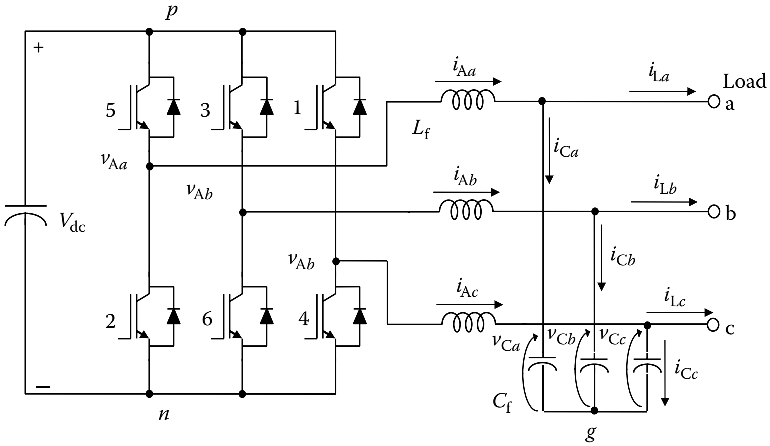

FIGURE E.1
Three phase inverter with LC filter. (From Na, W., A study on the output voltage control strategies of 3-phase PWM inverter for an uninterruptible power supply, Korea master thesis, Kwangwoon University, Seoul, 1997. With permission.)

From the neutral ground point *g*, using the switching function in Equation E.5, the new inverter output voltages are

$$\begin{aligned} v_{Aa} &= S_a V_{dc} + v_{ng} \\ v_{Ab} &= S_b V_{dc} + v_{ng} \\ v_{Ac} &= S_c V_{dc} + v_{ng} \end{aligned} \tag{E.6}$$

where v_{ng} is the potential difference between the negative point *n* and the neural ground *g*, and V_{dc} is DC link input voltage of the inverter.

The new voltage equations in Equation E.6 in the stationary reference frame are

$$\begin{aligned} v_{Aq}^{s} &= V_{dc} S_q \\ v_{Aq}^{s} &= V_{dc} S_d \end{aligned} \tag{E.7}$$

According to the coordinate transformations given in Appendix D,

$$\begin{aligned} S_q &= \frac{2}{3}\left(S_a - \frac{1}{2} S_b - \frac{1}{2} S_c \right) \\ S_d &= \frac{1}{\sqrt{3}} (S_b - S_c) \end{aligned} \tag{E.8}$$

And according to the switching function S_a, S_b, and S_c, the eight difference states should exist. The detailed changes of the switching function are displayed in Table E.1, and the calculation of the switching time will be explained as follows.

TABLE E.1

The Changes of Switching Function according to Switching States

Voltage Vector	Conducting Switches			S_a	S_b	S_c	S_q	S_d
V_0	2	4	6	0	0	0	0	0
V_1	6	1	2	1	0	0	$\frac{2}{3}$	0
V_2	1	2	3	1	1	0	$\frac{1}{3}$	$-\frac{1}{\sqrt{3}}$
V_3	2	3	4	0	1	0	$-\frac{1}{3}$	$-\frac{1}{\sqrt{3}}$
V_4	3	4	5	0	1	1	$-\frac{2}{3}$	0
V_5	4	5	6	0	0	1	$-\frac{1}{3}$	$\frac{1}{\sqrt{3}}$
V_6	5	6	1	1	0	1	$\frac{1}{3}$	$\frac{1}{\sqrt{3}}$
V_7	1	3	5	1	1	1	0	0

The SVPWM technique is a special technique of determining the switching state sequence of the inverter. The inverter has eight possible switching states. As shown in Figure E.2, those states are mapped on the d–q axis. There are six valid voltage space vectors (V_1–V_6) and two null or zero voltage vectors (V_0, V_7) shown in Table E.1. Null or zero voltage vector occurs when all upper switches are ON simultaneously and other bottom switches are OFF, or all upper switches are OFF and other bottom switches are ON. This case leads to short the load, and therefore zero voltage output is generated.

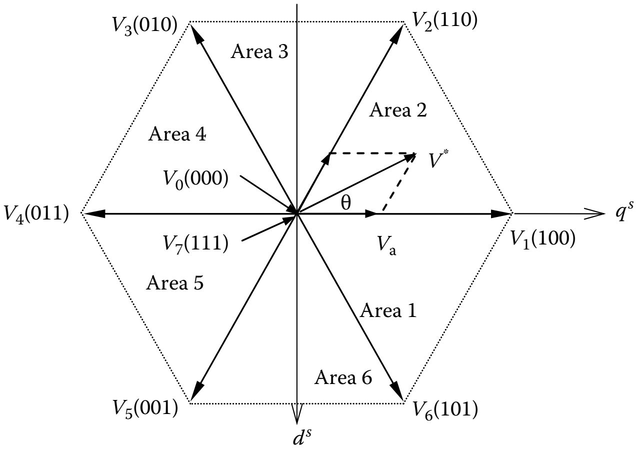

FIGURE E.2
Space vector diagram.

For example, assuming that the reference voltage vector V^* be in the area I, to generate the PWM output voltage, the adjacent voltage vectors V_1 and V_2 need to be used [6]. The switching cycle can be calculated using [9]

$$\int_0^{T_c} V^* \mathrm{d}t = \int_0^{V_a} V_1 \mathrm{d}t + \int_{V_a}^{V_a+V_b} V_2 \mathrm{d}t + \int_{V_a+V_b}^{T_s} (V_0 \quad \text{or} \quad V_7)\mathrm{d}t \tag{E.9}$$

or

$$V^* \cdot T_c = V_1 \cdot t_a + V_2 \cdot t_b + (V_0 \quad \text{or} \quad V_7) \cdot T_0 \tag{E.10}$$

where

$$\begin{aligned} T_a &= \frac{V_a}{V_1} T_c \\ T_b &= \frac{V_b}{V_2} T_c \\ T_0 &= T_c - (T_a + T_b) \end{aligned} \tag{E.11}$$

In order to minimize the switching frequency of each inverter leg, the switching pattern is arranged in a way shown in Figure E.3. By doing so, the symmetrical pulse pattern for two consecutive T_c intervals is created.

In Figure E.3, $T_s = 2T_c = 1/f_s$ (f_s, switching frequency) is the sampling frequency [6], and as shown in Figure E.3, during the first half period, the switching sequence has to be (000 → 100 → 110 → 111) and in the following second period, the switching sequence has to be in reverse (111 → 110 →

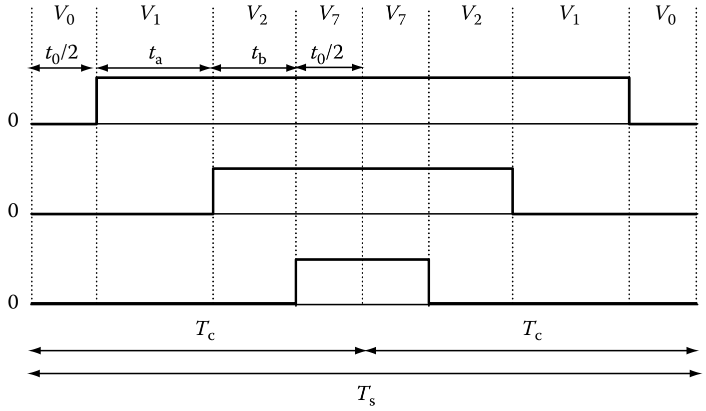

FIGURE E.3
Symmetrical pulse pattern for the three-phase inverter. (From Bose, B.K., *Modern Power Electronics and AC Drives*, Prentice Hall, Upper Saddle River, NJ, 2002. With permission.)

100 → 000). The zero and null voltage vectors (V_0, V_7) need to be replaced efficiently such that minimal output harmonics and torque ripple can be produced [9].

References

1. K. Ogata, *Modern Control Engineering*, Upper Saddle River, NJ: Prentice-Hall, 2002.
2. A. Isidori, *Nonlinear Control System: An Introduction*, 3rd ed., New York: Springer-Verlag, 1995.
3. D. Cheng, T.J. Tarn, and A. Isidori, Global linearization of nonlinear system via feedback, *IEEE Transactions on AC*, 30(8), 808–811, 1985.
4. Q. Lu, Y. Sun, and S. Mei, *Nonlinear Control Systems and Power System Dynamics*, London: Kluwer Academic Publishers, 2001.
5. J. Liu, Modeling, analysis and design of integrated starter generator system based on field oriented controlled induction machines, PhD thesis, Ohio State University, Columbus, OH, 2005.
6. B.K. Bose, *Modern Power Electronics and AC Drives*, Upper Saddle River, NJ: Prentice Hall PTR, 2002.
7. W. Na, A study on the output voltage control strategies of 3-phase PWM inverter for an uninterruptible power supply, Korea master thesis, Kwangwoon University, Seoul, 1997.
8. R. Valentine, *Motor Control Electronics Handbook*, New York: McGraw-Hill, 1998.
9. H.W.V.D. Broeck, H.C. Skudelny, and G.V. Stanke, Analysis and realization of a pulse modulator based on voltage space vectors, *IEEE Transactions on Industry Applications*, 24(1), 142–150, 1988.

Index

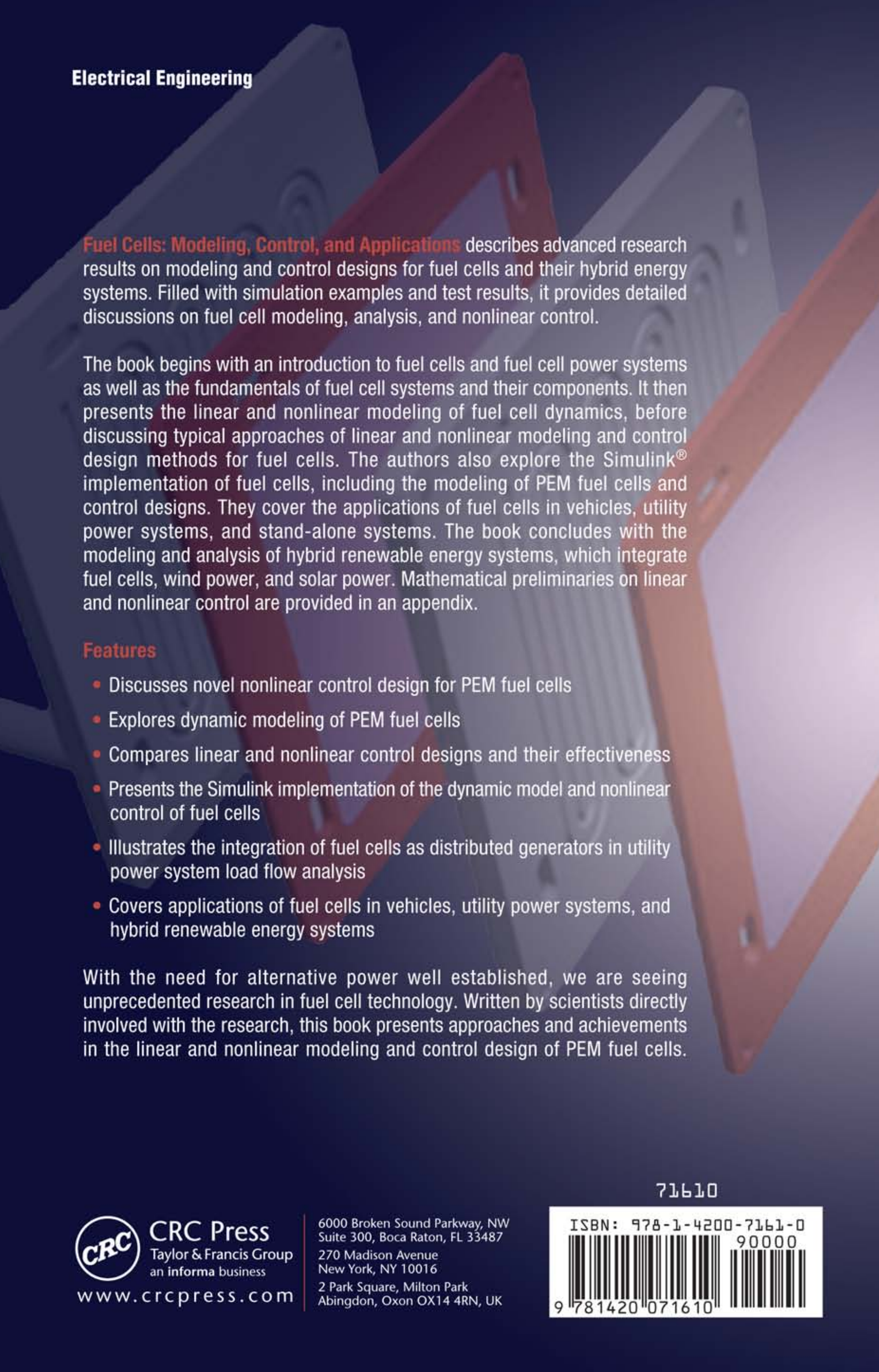

Electrical Engineering

Fuel Cells: Modeling, Control, and Applications describes advanced research results on modeling and control designs for fuel cells and their hybrid energy systems. Filled with simulation examples and test results, it provides detailed discussions on fuel cell modeling, analysis, and nonlinear control.

The book begins with an introduction to fuel cells and fuel cell power systems as well as the fundamentals of fuel cell systems and their components. It then presents the linear and nonlinear modeling of fuel cell dynamics, before discussing typical approaches of linear and nonlinear modeling and control design methods for fuel cells. The authors also explore the Simulink® implementation of fuel cells, including the modeling of PEM fuel cells and control designs. They cover the applications of fuel cells in vehicles, utility power systems, and stand-alone systems. The book concludes with the modeling and analysis of hybrid renewable energy systems, which integrate fuel cells, wind power, and solar power. Mathematical preliminaries on linear and nonlinear control are provided in an appendix.

Features

- Discusses novel nonlinear control design for PEM fuel cells
- Explores dynamic modeling of PEM fuel cells
- Compares linear and nonlinear control designs and their effectiveness
- Presents the Simulink implementation of the dynamic model and nonlinear control of fuel cells
- Illustrates the integration of fuel cells as distributed generators in utility power system load flow analysis
- Covers applications of fuel cells in vehicles, utility power systems, and hybrid renewable energy systems

With the need for alternative power well established, we are seeing unprecedented research in fuel cell technology. Written by scientists directly involved with the research, this book presents approaches and achievements in the linear and nonlinear modeling and control design of PEM fuel cells.

71610

CRC Press
Taylor & Francis Group
an **informa** business
www.crcpress.com

6000 Broken Sound Parkway, NW
Suite 300, Boca Raton, FL 33487
270 Madison Avenue
New York, NY 10016
2 Park Square, Milton Park
Abingdon, Oxon OX14 4RN, UK

ISBN: 978-1-4200-7161-0
90000
9 781420 071610